Dissertation zur Erlangung des Doktorgrades
der Fakultät für Chemie und Pharmazie
der Ludwig-Maximilians-Universität München

Structure, Dynamics and Interactions in Porous Host-Guest Systems

Bastian Rühle
aus
Herrenberg, Deutschland

2013

Erklärung und Eidesstattliche Versicherung

Erklärung

Diese Dissertation wurde im Sinne von § 7 der Promotionsordnung vom 28. November 2011 von Herrn Prof. Dr. Thomas Bein betreut.

Eidesstattliche Versicherung:

Diese Arbeit wurde eigenständig und ohne unerlaubte Hilfe erarbeitet.

München, den 21. Mai 2013 ....

Bastian Rühle

Dissertation eingereicht am:	16.04.2013
1. Gutachter:	Prof. Thomas Bein
2. Gutachter:	Prof. Christoph Bräuchle
Mündliche Prüfung am:	13.05.2013

Danksagung

Als Erstes möchte ich meinem Doktorvater Professor Thomas Bein für die Möglichkeit danken, an den vielen interessanten und herausfordernden Projekten dieser Dissertation zu arbeiten. Ich konnte in meiner Zeit in seiner Gruppe sehr viel lernen, nicht nur über die faszinierende Welt poröser Materialien, sondern dank der herausragenden Ausstattung des Arbeitskreises auch über viele Charakterisierungsmethoden. Außerdem möchte ich mich für das von ihm entgegengebrachte Vertrauen und seine Unterstützung bedanken, sowohl wenn es um die Vertretung von Vorlesungsstunden ging, als auch bei der wissenschaftlichen Freiheit, die ich bei der Ausführung der Projekte hatte. Auch für die finanzielle Unterstützung während der ganzen Zeit und für die zahlreichen Möglichkeiten, verschiedene Konferenzen und Meetings zu besuchen, bin ich sehr dankbar. Diese erlaubten mir nicht nur immer wieder interessante Einblicke in andere Themengebiete, sondern eröffneten mir oft auch neue Sichtweisen auf die eigene Forschungsarbeit.

Außerdem gilt mein besonderer Dank Professor Christoph Bräuchle für die exzellente, langjährige Zusammenarbeit. Durch die gemeinsamen Kooperationen und die vielen interessanten Meetings konnte ich vieles lernen, nicht zuletzt natürlich über die faszinierenden Methoden der Einzelmolekülfluoreszenzmikroskopie. Ohne diese tolle Zusammenarbeit wäre ein großer Teil dieser Arbeit in dieser Form nicht möglich gewesen. Natürlich möchte ich mich bei ihm auch für das Übernehmen des Zweitgutachtens für diese Arbeit bedanken.

Professor Konstantin Karaghiosoff möchte ich ebenfalls für die tolle Kooperation und die vielen interessanten, lehrreichen und oft auch unterhaltsamen Besprechungen danken. Ohne seine wertvolle Hilfe, seine Expertise, und die Zeit, die er in die zahlreichen Messungen investiert hat (auch wenn es von unserer Seite aus teilweise sehr kurzfristig war), wäre das gemeinsame Projekt nicht das, was es heute ist.

Ein weiteres interessantes Projekt konnte dank der guten Kooperation mit Professor

Adelheid Godt von der Universität Bielefeld durchgeführt werden, wofür ich ebenfalls sehr dankbar bin.

Außerdem möchte ich mich bei meinen Kooperationspartnern aus Professor Christoph Bräuchles Gruppe bedanken, ohne die die gemeinsamen Projekte ebenfalls nicht möglich gewesen wären. Angefangen hatte die Kooperation mit Dr. Timo Lebold, dem ich für seinen Enthusiasmus für das gemeinsame Projekt und die zahlreichen Messungen danken möchte. Die Kooperation wurde mit Melari Davies fortgesetzt, der ich besonders dankbar bin für all die viele Arbeit und Zeit die sie in unsere gemeinsamen Projekte investiert hat, ihr ständiges Interesse, ihre Unterstützung, ihre Motivation, ihre Geduld, ihre ständige Bereitschaft, auch kurzfristig und jederzeit an den Projekten zu arbeiten (auch wenn es manchmal später wurde) und natürlich für die vielen tollen Diskussionen in München und auf verschiedenen Konferenzen (on- und off-topic). Ich wünsche ihr und ihrer jungen Familie alles Gute für die Zukunft. Außerdem möchte ich mich noch bei Dr. Florian Feil und Dr. Stephan Mackowiak für ihre Hilfe bei verschiedenen Messungen bedanken.

Aus der eigenen Gruppe möchte ich mich für die Kooperationen bei Florian Hinterholzinger und Dr. Stefan Wuttke bedanken, die mir durch ihr Wissen über und ihren Enthusiasmus für MOFs die Möglichkeit gegeben haben, an neuen herausfordernden Projekten zu arbeiten und mit denen ich nicht nur viele interessante und hilfreiche Diskussionen zu den gemeinsamen Projekten führen, sondern auch außerhalb der Uni viel Spaß haben konnte. Stefan möchte ich hierbei für die vielen Gespräche zu den unterschiedlichsten Themen danken, sei es nun über MOFs, Bücher, Filme, oder über verschiedenste andere Dinge. Meinem langjährigen Bürokollegen Flo gilt neben dem Dank für die exzellente wissenschaftliche Zusammenarbeit auch besonderer Dank für die zahlreichen lustigen Tage und Abende im Büro und bei Konferenzen, sowie natürlich dafür, dass er mir als Neuankömmling an der LMU von Anfang an alle Dinge gezeigt und erklärt hat. In diesem Zusammenhang möchte ich mich auch gleich bei der ganzen Gruppe dafür bedanken, dass ich als “Preiß” so nett aufgenommen wurde und so eine gute Zeit hier in München verbringen konnte. Das gilt nicht nur den ehemaligen und jetzigen Mitgliedern der MesoBio Subgroup, Anderl, Axel, Valentina, Stefan, Christian, Alex und Cindy, mit denen ich nicht nur bei den gemeinsamen Meetings und Konferenzen, sondern auch so oft sehr viel Spaß hatte, sondern auch der Klinikum-Mittagessensgruppe Keili, Sonni, Jörg, Mirjam, Fabi, Mona und Markus, sowie meinen Kollegen Benni, Flo Auras, Alesja, Dana, Johann, Dina, Karin, Yujing und Yan, sowie allen, die ich hier aus Platzgründen nicht namentlich erwähnt habe.

Ich denke und hoffe ihr alle erinnert euch selbst noch an die gute Zusammenarbeit und die vielen schönen gemeinsamen Erlebnisse. Aus dem Kollegium möchte ich mich noch ganz besonders bei Hans, Norma, Mona, Halina und Fabi für die vielen schönen gemeinsamen (Spiele-)Abende mit leckerem Essen, sowie insbesondere bei Hans für die schönen Wander- und Skiausflüge ins Zillertal bedanken.

Außerdem geht mein Dank an Markus und Steffen für ihre Hilfe bei TEM-Aufnahmen und dafür, dass ich so viel über REM während meiner Zeit hier lernen konnte. Keili und Fabi möchte ich nicht nur für IT-Support, sondern allgemein für die interessanten Gespräche und die gute Zeit danken. Tina gilt besonderer Dank dafür, dass sie sich um alles rund um die Labore so hervorragend gekümmert und uns Doktoranden damit einen Haufen Zeit und Arbeit erspart hat. Ebenso möchte ich mich bei Regina für ihre exzellente Hilfe bei allen administrativen Dingen bedanken, und natürlich für ihre Geduld und ihr Verständnis für mein Unverständnis für Bürokratie, was mir ebenfalls einiges an Zeit und Nerven erspart hat. Dank gilt natürlich auch meiner Bachelor-Studentin Tanja, sowie meinen Praktikanten Lisa, Claudia und Nitin. Für finanzielle Unterstützung während der Arbeit möchte ich mich bei CeNS, NIM und der DFG (SFB749 und SFB1032) bedanken.

Besonderer Dank gilt meiner Familie für die Unterstützung über all die Jahre. Mein Bruder war immer für mich da und hat mir stets geholfen wo er nur konnte. Gleiches gilt natürlich auch für meine Eltern. Ihre persönliche und finanzielle Unterstützung und die Tatsache, dass sie mein Interesse an der Wissenschaft geweckt und von Anfang an gefördert haben machten diese Arbeit überhaupt erst möglich. Danke.

Abstract

Porous host–guest systems play an important role in a variety of applications. The nature and structure of the host, the dynamics of guests inside the host, and the interaction of the guests with the host are of great importance and define the scope of application of the porous system. Often, these properties are interdependent. For example, the porous structure of the host can have a strong influence on the dynamics of guest species diffusing inside the porous framework. At the same time, interactions of the guest species with the pore walls can play an important role for determining diffusion dynamics. Lastly, the nature and structure of the porous host often define the kinds of interactions that can be implemented for a certain guest species.

Introducing fluorescent guests into host systems enables us to extract detailed information about the structure and the dynamics of guest molecules inside the porous material. In order to be able to fully understand and utilize these complex materials, often a hierarchical patterning of the structures can be beneficial. On the other hand, tailoring the interactions of guest molecules with the host structure can help us to understand and develop new detection and sensor concepts or to endow porous materials with new, interesting properties, such as chemiluminescence.

In this work, two different kinds of porous host materials were used, namely porous silica and metal–organic frameworks (MOFs). While the studies with porous silica were mainly focused on hierarchical patterning and on gathering information about the structure and the diffusion dynamics, studies involving MOFs were more focused on employing specific host–guest interactions to create materials with new, interesting properties.

In collaboration with the group of Prof. Bräuchle (LMU), mesoporous silica thin films acting as model systems were investigated. A way to achieve in-plane alignment of cylindrical mesopores in mesoporous silica thin films was shown on a macroscopic scale. The alignment was achieved by introducing a preferential direction on the sub-

strate during thin film formation. The influence of various experimental parameters was investigated and found to have a strong influence on the alignment. Using fluorescent guests as probe molecules inside these systems provided deep insights into the structure of the host on a nanoscale level. Moreover, the dynamics of guests inside the host could be studied.

In a second project, which was also carried out together with the group of Prof. Bräuchle, the approach was extended and charged fluorescent dyes were incorporated into the host material. This enabled us to directly influence the movement of the guest species and to achieve a separation of differently charged guests. Moreover, the experiments provided information about the dynamics of charged guest species inside the porous host structure under the influence of electric fields on a single molecule level.

The third project described in this thesis is focused on the synthesis and characterization of a chemiluminescent MOF. The well-known concept of peroxyoxalate chemiluminescence was used to achieve this goal, with the luminescent compound, a diphenyl anthracene moiety, being an integral part of the framework structure. We also investigated the stability of the metal–organic framework under the conditions of the chemiluminescence reaction.

A fourth project, carried out in collaboration with Prof. Karaghiosoff (LMU), dealt with the investigation of a new detection concept based on the tailored interaction of guests with porous host structures. Here, MOFs were used as the porous hosts. We found that upon incorporation of a fluorescent guest into a MOF structure, the fluorescence was almost completely quenched. When exposed to another guest (the analyte molecule) that acts as a strongly coordinating ligand for the metal centers in the MOF, the framework could be decomposed and fluorescence was switched back on. The feasibility of this new detection concept in the field of MOFs was demonstrated by developing a novel fluoride detector whose sensitivity exceeded the ones of commonly used commercially available fluoride detection methods in aqueous solutions.

Hierarchical patterning of thin silica films played the main role in the fifth project. Here, different ways to obtain patterned films with periodic features on different length scales were investigated. The patterning was achieved by a combination of various top-down and bottom-up strategies, including soft templating, hard templating, soft lithography and photolithography. The properties of the resulting structures were compared and their advantages and disadvantages were discussed. Such films could provide a platform for investigation of different movement modes of macromolecules

inside constrained geometries and could also prove beneficial for miniaturization of macromolecule separation.

The sixth and last part is also focused on patterning, but here different methods for pattern creation of lipid-bilayer coated mesoporous silica nanoparticles were studied. Such patterns could be interesting for studying cell–receptor interactions or for the specific spatial control of cell behavior. The patterning was achieved by endowing the nanoparticles with functional groups through anchoring of functionalized lipids to the supported lipid bilayer membrane and binding them to patterned substrates of complementary functionality. In this context, biocompatible reactions that can be carried out under mild conditions were investigated for the attachment of the nanoparticles to the surface, namely an EDC/NHS mediated amide bond formation, a Michael addition of thiols to maleimide groups, and the binding of thiols to gold.

Zusammenfassung

Poröse Wirt–Gast Systeme spielen eine wichtige Rolle für eine Vielzahl von Anwendungen. Die Art und Struktur des Wirtsystems, die Dynamik von Gastmolekülen im Wirtsystem, und die Wechselwirkungen der Gäste mit den Wirten sind von großer Bedeutung und bestimmen maßgeblich die Anwendungsgebiete der porösen Systeme. In der Regel können diese Eigenschaften allerdings nicht unabhängig voneinander betrachtet werden. Beispielsweise kann die interne Porenstruktur und -geometrie einen starken Einfluss auf die Dynamik der Diffusion von Gastspezies im Inneren des porösen Systems haben. Ebenso kann die Wechselwirkung der Gäste mit den Porenwänden die Diffusionsdynamik maßgeblich bestimmen. Letztendlich wird auch die Art und Struktur des porösen Wirts oftmals die Art der Wechselwirkungen mitbestimmen, die mit unterschiedlichen Gästen auftreten können.

Das Einbringen von fluoreszierenden Gästen in die Wirtsysteme ermöglicht es, detaillierte Informationen über die Struktur und Dynamik der Gastmoleküle im Inneren des porösen Systems zu erhalten. Um ein besseres Verständnis zu erlangen und um diese komplexen Systeme bestmöglich einsetzen zu können ist in vielen Fällen eine hierarchische Strukturierung von Vorteil. Andererseits kann die Abstimmung der Wechselwirkungen zwischen Gastmolekülen und Wirtstruktur ein besseres Verständnis für die Entwicklung neuer Detektions- und Sensorkonzepte fördern oder es ermöglichen, poröse Materialien mit neuen, interessanten Eigenschaften wie beispielsweise Chemolumineszenz auszustatten.

Im Rahmen dieser Arbeit wurden zwei verschieden Arten von porösen Materialien verwendet – poröse Silikatsysteme und metall–organische Gerüstverbindungen (MOFs). Während sich die Untersuchungen mit porösen Silikaten vor allem um hierarchische Strukturierung drehten und Informationen über die Struktur und Diffusionsdynamik lieferten, beschäftigten sich die Studien mit MOFs eher damit, spezifische Wirt–Gast Wechselwirkungen zur Schaffung von Materialien mit interessanten Eigen-

schaften zu untersuchen.

In Zusammenarbeit mit der Gruppe von Prof. Bräuchle (LMU) wurden mesoporöse Silikatfilme als Modellsysteme untersucht. Es wurde eine Möglichkeit aufgezeigt, wie eine makroskopische Ordnung zylindrischer Mesoporen in einer Ebene parallel zum Substrate erreicht werden kann. Die Ausrichtung der Mesoporen erfolgte durch das Schaffen einer Vorzugsrichtung auf dem Substrat während der Bildung der dünnen Schichten. Der Einfluss verschiedener experimenteller Faktoren wurde untersucht, und es wurde festgestellt, dass diese einen starken Einfluss auf die Ausrichtung haben können. Das Einbringen fluoreszenter Gastmoleküle in diese Systeme ermöglichte tiefe Einblicke in die Struktur der Wirtsmaterialien auf einer nanoskopischen Ebene. Zusätzlich konnte auch die Dynamik der Gäste in den Wirtsystemen untersucht werden.

In einem zweiten Projekt, welches ebenfalls in Zusammenarbeit mit der Gruppe von Prof. Bräuchle durchgeführt wurde, wurde dieser Ansatz weiter verfolgt und ausgedehnt, indem geladene fluoreszierende Farbstoffmoleküle in die Wirtsysteme eingebracht wurden. Dies ermöglichte es, die Bewegung der Gastspezies direkt zu beeinflussen und eine Auftrennung unterschiedlich geladener Spezies zu erreichen. Des Weiteren lieferten diese Experimente Aufschluss über die Dynamik geladener Gastspezies in der porösen Wirtstruktur unter dem Einfluss elektrischer Felder auf Einzelmolekülebene.

Das dritte Projekt das in dieser Dissertation beschrieben wird drehte sich um die Synthese und Charakterisierung eines chemolumineszenten MOFs. Hierzu wurde das bekannte Konzept der Peroxyoxalat-Chemolumineszenz verwendet, wobei die lumineszierende Komponente, ein Diphenylanthracen-Derivat, einen integraler Bestandteil der Gerüststruktur darstellte. Im Rahmen dieses Projekts wurde auch die Stabilität der metall–organischen Gerüstverbindung unter den Bedingungen der Chemolumineszenzreaktion untersucht.

Ein viertes Projekt, das in Zusammenarbeit mit Prof. Karaghiosoff (LMU) durchgeführt wurde, beschäftigte sich mit der Untersuchung eines neuen Detektionskonzepts, das auf der maßgeschneiderten Wechselwirkung zwischen Gästen und porösen Wirtsystem beruht. In diesem Projekt wurden MOFs als poröse Systeme verwendet. Es konnte gezeigt werden, dass als Folge der Aufnahme eines fluoreszierenden Gastmoleküls in die MOF-Struktur die Fluoreszenz der Gäste praktisch vollständig ausgelöscht wurde. Nachdem das System den Analytmolekülen, welche stark koordinierende Liganden für die Metallzentren des MOFs darstellen, ausgesetzt wurde, wurde die poröse Gerüstverbindung zersetzt und die Fluoreszenz der Gäste konnte dadurch erneut eingeschaltet werden. Als Beispiel einer möglichen Umsetzung dieses für MOFs neuartigen Detekti-

onskonzepts wurde ein Fluorid-Nachweis entwickelt dessen Sensitivität besser war als die bisher standardmäßig verwendeter kommerzieller Fluoridnachweise in wässrigen Lösungen.

Die hierarchische Strukturierung dünner Silikatfilme war Gegenstand eines fünften Projekts. Es wurden verschiedene Möglichkeiten untersucht, wie eine periodische Strukturierung auf unterschiedlichen Längenskalen erreicht werden kann. Für die Strukturierung wurden verschiedene "top-down" und "bottom-up" Strategien wie "soft templating", "hard templating", "soft lithography" und Photolithographie verwendet. Die Eigenschaften der resultierenden Strukturen wurden verglichen und ihre Vor- und Nachteile wurden diskutiert. Solche Filme könnten eine Plattform zur Untersuchung verschiedener Bewegungsmodi von Makromolekülen in eingeschränkten Geometrien bereitstellen und könnten für die Miniaturisierung von Makromolekültrennverfahren eine wichtige Rolle spielen.

Der sechste und letzte Teil beschäftigte sich ebenfalls mit Strukturierung, allerdings wurden hier unterschiedliche Methoden zur Erzeugung von Strukturen aus lipidschichtbedeckten Silikatnanopartikeln untersucht. Solche Strukturen könnten eine interessante Rolle für die Untersuchung von Zell–Rezeptor Wechselwirkungen oder für die spezifische, räumliche Steuerung und Kontrolle von Zellverhalten spielen. Die Strukturierung wurde dadurch erreicht, dass die Nanopartikel mit funktionellen Gruppen ausgestattet wurden welche an strukturierte Substrate komplementärer Funktionalität angebunden werden konnten. Hierfür wurden bioverträgliche Reaktionen die unter milden Bedingungen durchgeführt werden können untersucht, so wie eine EDC/NHS-vermittelte Amidbindungsbildung, eine Michael-Addition von Thiolen an Maleimidgruppen, und das Anbinden von Thiolen an Gold.

Contents

Chapter 1

. . . . . .

Introduction

Parts of this chapter are based on a review article by B. Rühle, M. Davies, T. Bein, and C. Bräuchle, which has been accepted for publication in *Zeitschrift für Naturforschung B*.

1.1 Porous Silica Compounds

Porous silica compounds are used in a wide variety of applications, including molecular sieves and filters[1,2], catalysts[3], ion exchangers[4], nanosensors[5] or drug-delivery-systems[6,7]. They are appreciated for their large pore volume, large surface area, and high chemical and structural flexibility and tunability. These properties allow us to tailor the morphology and interaction chemistry of the porous host systems according to the demands of the desired applications. However, in order to be able to efficiently design and synthesize new materials with the envisioned properties, a thorough understanding of the microscopic nature and structure of the host systems and their interactions with guest molecules is of great importance. There are many techniques that can help to gain an overview of the average, bulk properties of these porous systems, such as NMR[8], electron microscopy[9], X-ray diffraction, and neutron scattering measurements[10]. However, there are often heterogeneities at a nanoscopic or microscopic level that cannot be assessed with bulk methods, but still play an important role for host–guest interactions and can help us to improve our understanding of the porous host systems. While these heterogeneities can be random, there are also cases in which they reflect intrinsic characteristics of the materials, such as phase separation or domain boundaries. In order to be able to extract such information, single molecule

spectroscopy or microscopy measurements are highly desirable.

In this chapter, the synthesis, formation mechanism and functionalization of sol-gel-derived porous silica compounds, will be briefly described, especially focusing on the evaporation-induced self-assembly (EISA) process for the formation of thin silica films. A brief introduction into single molecule microscopy is given, discussing some technical requirements and important aspects of this technique. We then give an overview of selected cooperative studies performed in the groups of Prof. Bräuchle and Prof. Bein at the Ludwig-Maximilians-University Munich, characterizing the details of diffusional dynamics of molecules in different mesoporous materials. These experiments will be introduced by a fundamental study that opened up new ways of understanding the interactions of hosts and guests by combining information from transmission electron microscopy with the diffusion dynamics obtained from single molecule microscopy studies. We will also present a selection of fluorescence microscopy studies from other groups that helped elucidating important aspects of porous silica compounds and heterogeneous catalysis such as diffusion properties, reactivity, morphology, intergrowth, accessibility and catalyst deactivation. In the end, we will give a short outlook on the potential of porous silica hosts in drug delivery applications.

1.1.1 Synthesis of Porous Silica Materials

Micro- and mesoporous silica materials are usually synthesized by a bottom-up approach, in which small organic molecules or surfactants act as a template for the porous structure of the silica framework. Early and prominent examples of this process include the use of alkylammonium ions to control the pore size and periodicity of zeolites, as demonstrated by researchers at the Mobil Oil Corporation in the 1960s.[11] The templating process results in porous, crystalline solids with a well-defined 1-, 2-, or 3-dimensional network of periodically arranged micropores. Later, this approach was further extended to longer-chain alkylammonium ions,[12] which yielded a periodic array of mesopores that were approximately 4 nm in diameter or larger, and gave rise to the development of the MCM (Mobil Crystalline Material) family of mesoporous silica compounds. The amphiphilic nature (i.e., the presence of hydrophilic and hydrophobic parts within one molecule) of the surfactant that acts as the structure-directing agent (SDA) allows for a spontaneous assembly of the latter into micelles, resembling a liquid crystalline phase that gives rise to the periodic porous structure. Meanwhile, a variety of other surfactants have been employed to extend the pore-size and structural diversity even further,[13,14] for example non-ionic triblock-copolymers for the synthesis

of the Santa Barbara Amorphous (SBA) type materials.[15]

The synthesis strategies mentioned above were originally designed for the synthesis of porous particles that are used in a wide variety of different fields. However, in certain applications such as membranes, low dielectric constant interlayers and sensors, thin films rather than particles are desired. In some of the first approaches that yielded stable, supported mesoporous silica films a substrate was introduced into a silica/surfactant/solvent systems in which the initial surfactant concentration was high enough that a micellar phase could be formed (i.e., higher than the critical micelle concentration, cmc).[16–18] These approaches allowed for the nucleation of hexagonal silica-surfactant mesophases on the substrate with pores oriented parallel to the substrate surface, and further growth and coalescence over a longer period of time resulted in continuous films. However, these films are often macroscopically inhomogeneous and feature granular textures on micrometer length scales. Another approach that yields very homogeneous films even on macroscopic length scales is the evaporation-induced self-assembly (EISA) approach, introduced by Brinker *et al.* in 1999.[19] This synthesis strategy employs a homogeneous solution of soluble, inorganic building blocks such as alkoxysilanes (typically tetraethylorthosilicate (TEOS)) and surfactant molecules at concentrations lower than the cmc in a volatile solvent mixture, often comprised of ethanol and water. When coating this solution onto a substrate, preferential evaporation of the volatile solvent leads to an increase in concentration of the surfactant and the non-volatile silica precursor in water. This increase in surfactant concentration in turn leads to a spontaneous self-assembly of silica-surfactant micelles, which further organize into liquid-crystalline mesophases. By altering the molar ratios and chemical nature of the solvent mixture, the silica source, and the surfactant, differently arranged porous mesophases such as 2D-hexagonal, 3D-hexagonal, cubic, and lamellar structures can be obtained.[20,21] In order for the self-assembly process to occur, the silica condensation has to be suppressed or slowed down during the film deposition step by adjusting the pH to a value close to the isoelectric point of colloidal silica (pH $\approx$ 2).[19] This allows for the cooperative silica-surfactant self-assembly and results in as-deposited films exhibiting liquid-crystalline (i.e., semi-solid) behavior. Only after subsequent aging, thermal treatment, or exposure to acid or base catalysis the silica network solidifies in its final pore geometry.

The liquid-crystalline nature of freshly formed films was confirmed by the fact that tensile stress developed during the mesophase thin film deposition is much lower than that of a similar silica sol prepared without surfactants.[19,22] Moreover, under certain

conditions freshly deposited films could be transformed to a different mesophase (e.g., from lamellar to cubic).[20] Further proof of a structurally flexible material after deposition and deeper insight into the mechanism of mesophase formation and film organization during the EISA process was gained by different groups through *in situ* grazing incidence small-angle X-ray scattering (GISAXS) experiments.[22–24] Grosso *et al.*[23] investigated the influence of various experimental parameters on the film formation and organization of films prepared by dip-coating from a silica sol with cetyltrimethylammonium bromide (CTAB) as the SDA. They found that – under otherwise identical conditions – the CTAB-to-TEOS ratio plays the main role in determining the structure of the resulting films. By adjusting this ratio to 0.08, 0.10, or 0.12, 2D-hexagonal, 3D-hexagonal, or cubic phases could be obtained. They also found that the degree of condensation of the silica species present in the solution (and hence the water content and the aging time of the sol prior to deposition) can have a strong effect on mesophase organization, where the highest degree of organization seems to correlate with a rather high condensation rate. Combining *in situ* XRD measurements with interferometry suggested a formation mechanism that includes the formation of micelles at the film/air interface, a morphological change from elongated to spherical micelles in the case of 3D-hexagonal and 3D-cubic structures, and the existence of a 3D-hexagonal intermediate phase prior to the formation of a 3D-cubic structure. In the case of the other structures (i.e., 2D-hexagonal and 3D-hexagonal), the authors also observed a transient peak in their XRD patterns. However, unlike in the case of the 3D-cubic structure, they did not attribute this transient peak to a real intermediate structure.

A similar system (namely a silica sol with CTAB as the SDA yielding a 2D-hexagonal mesophase) was also investigated by Doshi *et al.*[22], who carried out time-resolved *in situ* GISAXS studies combined with gravimetric analysis to study the self-assembly of a slowly evaporating film maintained in a horizontal geometry under controlled environmental conditions. This experiment allowed the authors to derive structural and compositional information simultaneously under steady-state conditions. They proposed a mechanism for the formation of the 2D-hexagonal mesophase that included four distinct successive stages during the EISA process, namely an isotropic, a lamellar, a correlated micellar, and finally a 2D-hexagonal geometry, each identified by their respective 2D GISAXS pattern (see Figure 1.1).

At the beginning, there are no reflections visible, indicating the lack of any periodic arrangement. Hence, this pattern was assigned to the isotropic phase. In the subse-

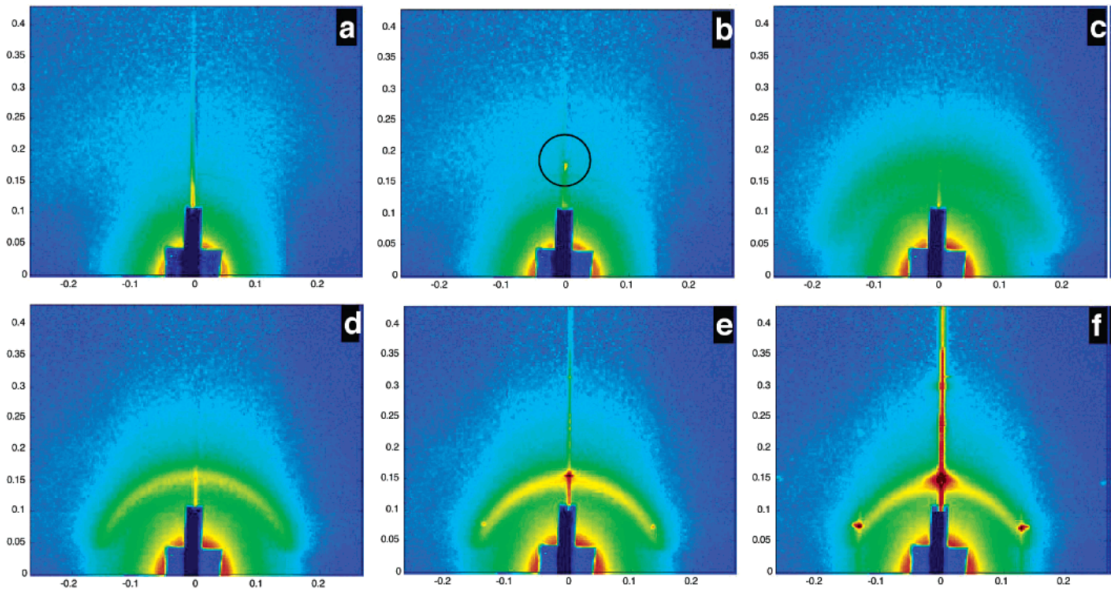

Figure 1.1: GISAXS patterns obtained at different points in time during the formation of a CTAB-templated, 2D-hexagonal thin silica film. The patterns correspond to the following phases: (a) the isotropic phase, (b) the lamellar mesophase, (c,d) the correlated micellar, and (e,f) the hexagonal mesophase. Figure adapted from Reference 22.

quent phase, a single Bragg reflex can be seen which indicates – in combination with the absence of out-of-plane reflections and combined with the spot orientation and d-spacing – a smectic ordering parallel to the substrate surface. The appearance of such a lamellar phase is unexpected from the bulk phase diagram and the authors attributed it to an interfacial effect. Interestingly, this intermittent lamellar phase could only be observed in the presence of a silica precursor and did not appear under similar conditions when no TEOS was added to the precursor solution. At later stages, the lamellar diffraction spot disappears and a broad, diffuse arc appears concomitantly at larger q-values. This pattern can be explained by the presence of spherical or cylindrical micelles showing a low degree of spatial correlation and hence it was assigned to the correlated micellar phase. Over time, the scattering intensified and the width of the arc and its radius decreased. This was attributed to an enhancement of spatial correlation of micelles resulting from their increasing number density and conceivably from their positioning by regular undulations of the lamellar mesophase. Finally, three well-defined Bragg spots defining adjacent 60° central angles with respect to the origin are observed, which can be assigned to a 2D-hexagonal mesophase (*p6mm*) with tube axes oriented parallel to the substrate. Moreover, the authors also observed a disorder-to-order transformation during the EISA process using X-ray reflectivity

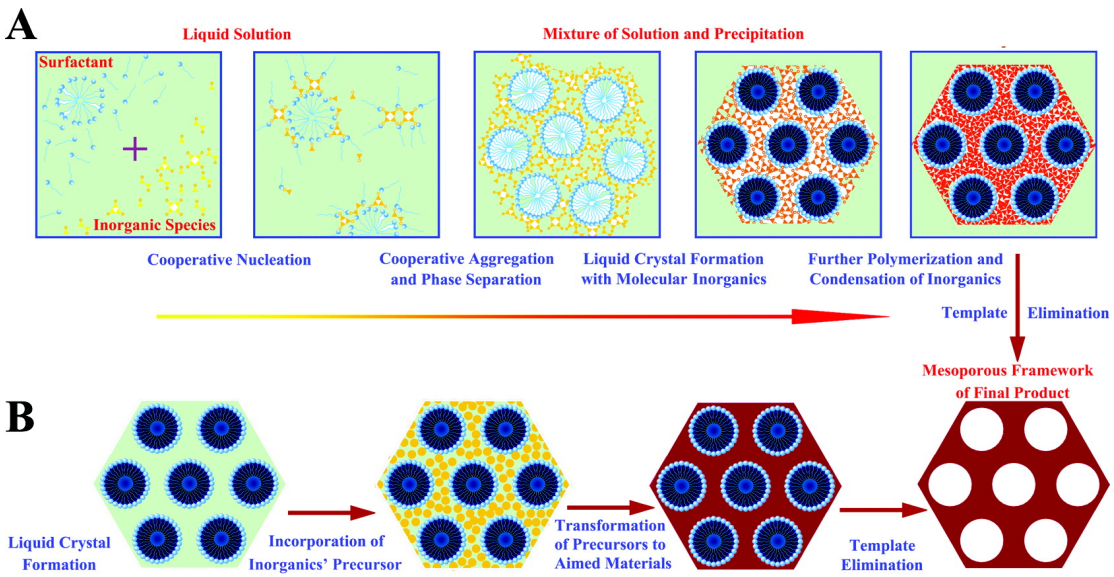

Figure 1.2: Two synthetic strategies of mesoporous materials: (A) cooperative self-assembly. (B) "true" liquid-crystal templating process. Figure adapted from Reference 28.

data and electron microscopy. This transition seems to start at the solid-liquid and at the liquid-air interfaces, and then propagates to the middle of the film. Similar observations were also made by other groups and for other surfactants, e.g., non-ionic triblock-copolymers.[20,23,25]

Besides the cooperative mechanism discussed above, in which surfactant molecules and inorganic species combine first to form hybrid intermediate species which then further self-assemble into the final structures, a liquid crystal templating (LCT) mechanism is discussed for some systems, which suggests that first a stable surfactant mesophase develops, around which the inorganic building blocks are assembled.[14,26,27] Both mechanisms are summarized in Figure 1.2. The exact nature of the mechanism that occurs during thin film synthesis most probably depends on the chemical parameters and processing conditions, and often a combination of both mechanisms might operate.

Studies on the mechanism during film growth were also recently published by C. Jung *et al.* who reported on the *in situ* visualization of domain growth in the self-assembly of silica nanochannels using fluorescence microscopy and atomic force microscopy (AFM).[29] They could observe well-ordered silica nanochannels with domain sizes of up to $\approx 0.3\,\mathrm{mm}$ and showed that transient lamellar structures precede the formation of hexagonal layers. Furthermore they discussed that the layer growth follows

two distinct pathways (for details see Reference 29).

1.1.2 Thin Film Deposition and Functionalization Techniques

There are several techniques available for the preparation of thin films, of which a selection is depicted schematically in Figure 1.3.[30] Out of these, the EISA process described above is compatible with the chemical solution deposition methods, i.e., spin-coating, dip-coating, spray-coating, and meniscus-coating. These are widely employed, because they are cheap and do not require expensive and sophisticated equipment, but rather rely on techniques that are already commonly used in industrial processes. Moreover, they offer a good degree of control over the experimental conditions before and during the self-assembly process.

However, these methods usually do not result in a macroscopic in-plane alignment of the mesopores, most probably due to the lack of a preferential direction during the self-assembly process. Since there are many applications that could greatly benefit from mesopore alignment on a macroscopic scale, such as nanofluidics and nanoreactors[31], oriented growth of nanowires[32], and optoelectronic devices[33], a lot of effort was put into developing methods that can help achieving this goal. These methods include the use of microtrenches[34,35], external electric[36,37] and magnetic[38] fields, substrate surface modification[18,39,40], and shear flow control[41,42]. However, these approaches often require specialized equipment or impose constraints on the applicable substrates or surfactants. That is why we recently investigated another technique, namely guided growth in PDMS microchannels[43], which is described in more detail in Chapter 3 of this thesis.

Wu *et al.*[34] and Daiguji *et al.*[35] demonstrated that microtrenches that introduce a spatial confinement during the EISA process can influence the mesopore alignment. The trenches were produced by top-down lithographic methods either by directly using the pattern generated from the resist[34], or by transferring the pattern into the substrate *via* reactive ion etching[35]. In both cases, the spatial confinement led to a preferential alignment of mesopores inside the trenches. Wu *et al.* showed in their studies that the alignment depends critically on the aspect ratio of the microtrenches, while Daiguji *et al.* also found an influence of the composition of the precursor solution, the relative humidity during coating and aging, and the chemical properties of the trench sidewalls on mesopore alignment. However, both methods require a clean room and a photolithography or even an electron beam lithography setup, rendering these approaches costly and time-consuming. Trau et al investigated the use of electric

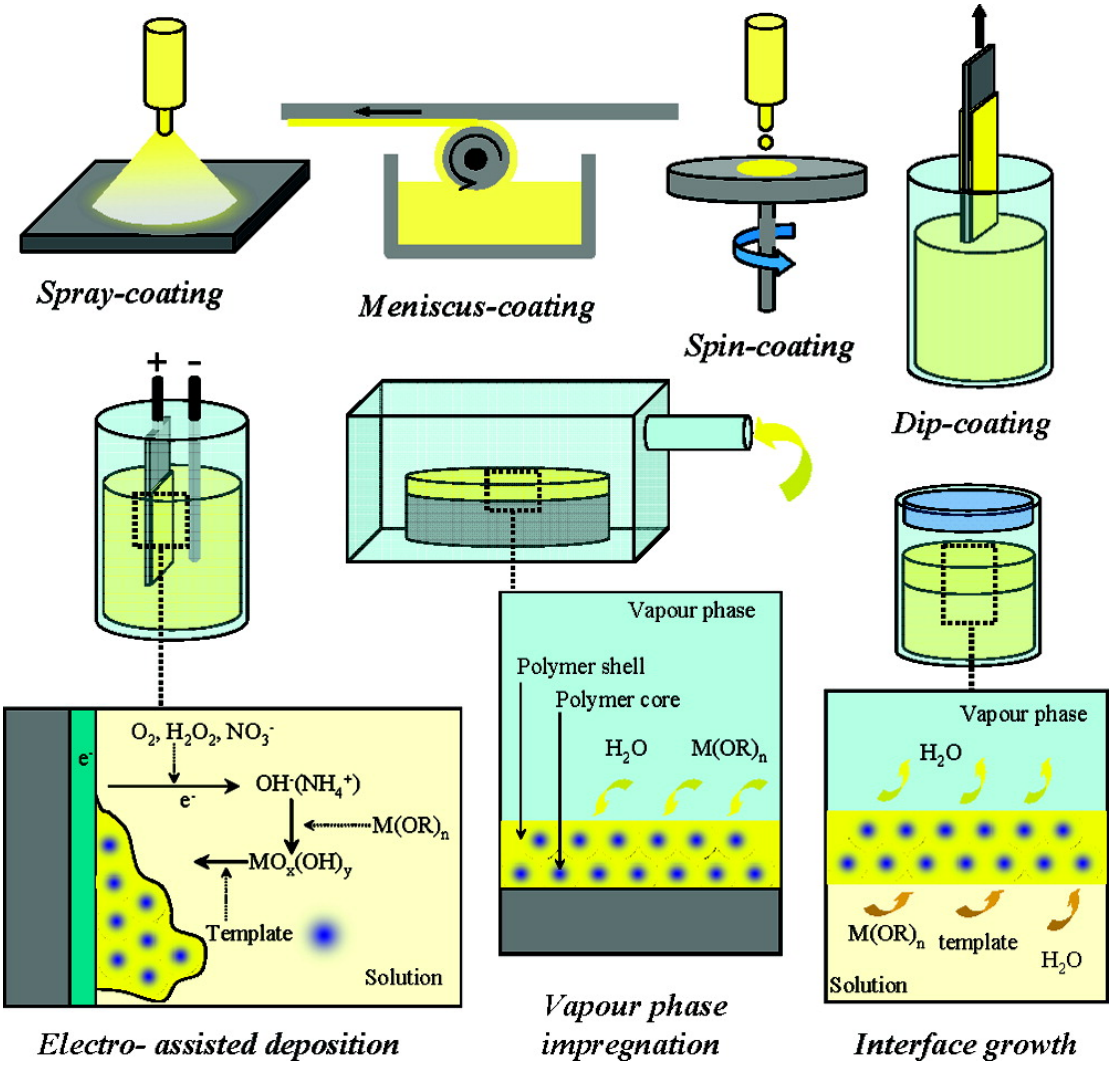

Figure 1.3: Various processing methods used to prepare mesostructured thin films. Figure adapted from Reference 30.

fields to induce mesopore alignment.[37] The authors used strong electric fields in combination with a microfluidic system to achieve mesopore alignment. They attributed the alignment effect to both the confined geometry and the presence of the electric field. However, the necessity of strong electric fields at the order of 1500 $\mathrm{V\,cm^{-1}}$ might limit the applicability of the technique. Furthermore, it also narrows down the choice of the substrate to non-conducting materials and the choice of the template to charged or ionic surfactants, typically resulting in mesoporous silica thin films with small pore sizes. Tolbert *et al.* demonstrated that magnetic fields instead of electric fields could also be used to trigger mesopore alignment.[38] They oriented a silicate-surfactant liquid crystal phase in an 11.7 T magnetic field by heating the samples

above their anisotropic-to-isotropic phase transition temperatures, followed by slow cooling (5 °C per hour in 3 °C to 5 °C steps) in the magnetic field and subsequent polymerization of the silica by acidic or acidic-thermal treatment. While this approach also allows for a perpendicular alignment of the mesochannels with respect to the substrate plane, it requires very specialized equipment. Another approach was pursued by Yang *et al.* and Miyata *et al.*, who deposited thin silica films on mica[18] or single-crystal silicon wafers[39] and found that the crystallographic orientation of the substrate surface can influence the mesopore alignment to a certain degree. Miyata *et al.* also suggested another way to introduce mesopore alignment by substrate surface modification, namely by creating a thin polyimide layer on the substrate and subjecting it to a rubbing treatment that can help to align the polymeric chains.[40] This alignment is passed on to the micellar structure of the surfactant molecules and can lead to a macroscopic alignment of the mesopores. The exact formation mechanism that leads to the alignment seems to depend on the matching of the chain length of the hydrophobic part of the surfactant to the chemical structure of the polyimide underlayer.[44,45] Zhao *et al.*[41] and Naik *et al.*[42] demonstrated that the shear flow exerted on films during dip coating can also influence mesopore alignment to some degree, but the correlation length of the obtained mesostructure might be low in these cases.

Besides macroscopic ordering and mesopore alignment, chemical functionalization of the pore walls of the porous materials is of great importance for many applications, since these determine the host–guest interactions of the system.[46–48] There is a large variety of synthesis strategies that lead to functionalized porous materials,[30] of which the co-condensation approach and the chemical grafting approach will be briefly discussed here. In the co-condensation approach, organically modified building blocks (such as functionalized aryl or alkyltriethoxysilanes) are mixed with the inorganic building blocks and the templates in a one-pot reaction.[49,50] During the self-assembly process, the functionalized silica species will hydrolyze and condense together with the other inorganic silica precursors, resulting in a random incorporation into the silica framework. Another commonly used approach is the post-synthetic grafting of organically modified silica species onto the porous materials. In this approach, the unfunctionalized porous material is first obtained with a standard synthesis protocol, and subsequently subjected to silica species that bear functional groups and that exhibit reactivity towards the free hydroxyl groups present at the surface of the silica pore walls. While the co-condensation approach is simpler and has the advantage of a more homogeneous distribution of the functional groups within the material and its

channels, the presence of functionalized silica species during the synthesis can interfere with the delicate formation mechanism of the porous structure and may result in a less well-defined (or, at high loadings, a completely amorphous) material with reduced hydrothermal stability.[51]

1.1.3 Characterization of Host–Guest Interactions with Single Molecule Microscopy Techniques

Knowing the interactions between the mesoporous host and the guest molecules is essential for many applications. To investigate these interactions, single molecule microscopy (SMM) is a powerful technique. While measurements of ensemble diffusion of molecules in porous hosts provide information about the overall behavior of the guest in the host, tracking of individual molecules provides insights into the heterogeneity and the mechanistic details of molecular diffusion as well as the structure of the host. With SMM experiments, Zürner *et al.* and Kirstein *et al.* show how single dye molecules can be used as nanoscale probes to map out the structure of mesoporous silica channel systems prepared as thin films *via* the cooperative self-assembly of surfactant molecules with polymerizable silicate species.[52,53] The dye molecules act as beacons while they diffuse through the different structural phases of the host: the structure of the trajectories, the diffusivities and the orientation of single molecules are distinctive for molecules traveling in the lamellar and the hexagonal mesophases.[54] These experiments reveal unprecedented details of the host structure, its domains and the accessibility as well as the connectivity of the channel system. In these studies, mostly strongly fluorescent and photostable molecules are used, e.g. terrylenediimide (TDI) derivatives, which can be easily incorporated into mesopores and then individually observed travelling in the host.

The idea that a single molecule can act as a direct reporter of its environment was pioneered in 1989 by Moerner[55] and Orrit[56], who were the first reporting on the optical detection of single fluorophores in a solid matrix at liquid-helium temperatures. Since then, Single Molecule Microscopy (SMM) was continuously improved (e.g. adapting it to room temperature) and now plays a growing role in chemistry, biology, physics and materials science.[57–61] In the following, the basic principles of SMM will be explained.

1.1.4 Principle of Single Molecule Fluorescence Microscopy

Nowadays, there are different types of microscopes available for single molecule experiments, such as confocal, total internal reflection fluorescence (TIRF) or wide-field epi-fluorescence microscopes. All these techniques are based on the detection of fluorescence light, which can provide an excellent signal-to-noise (or signal-to-background) ratio. In this chapter we will focus mainly on studies that employ wide-field epi-fluorescence microscopy (schematic setup see Figure 1.4.a). The samples are excited with a laser beam that is focused on the back focal plane of the microscope objective: this results in a cylindrical excitation volume, depicted in Figure 1.4.a. Since the concentration of the fluorescent dye molecules is kept extremely low ($\leq 10^{-10}$ M) single molecules can be detected by their individual fluorescence spots imaged onto the CCD camera. The imaging is done with an objective with a high numerical aperture (NA = 1.4). The numerical aperture NA is defined as:

$$NA = n \sin \alpha \tag{1.1}$$

with n being the refractive index of the medium (e.g. oil) in which the objective lens is working, and α the half collection angle of the objective. The higher the NA, the higher is the light collection efficiency of the objective and thus the number of the collected photons. The emitted fluorescence passes a dichroic mirror and a fluorescence filter to get separated from the exciting laser wavelength. The signal is detected by a back-illuminated, cooled electron multiplying charge-coupled device (EMCCD) camera. The position of a single molecule which acts as a point light source can be determined by fitting a two-dimensional Gaussian distribution (Figure 1.4.b) to the signal on the detector chip, according to

$$I = A_0 e^{\frac{-(x-x_0)^2}{2\sigma^2}} e^{\frac{-(y-y_0)^2}{2\sigma^2}} \tag{1.2}$$

where I is the recorded fluorescence intensity, A_0 the amplitude of the signal and σ the width of the Gaussian curve. x_0 and y_0 are the coordinates of the peak position. The position accuracy corresponds to the standard error of the fitting parameters x_0 and y_0 and depends on the photon noise, the error due to the finite pixel size of the detector and the background. Moreover, the position accuracy depends on the fluorescence intensity of a single molecule since Δx is inversely proportional to the square root of the number of collected photons. Thus, in SM experiments one tries

to get as many photons as possible from a single fluorescent molecule. This can be achieved by the use of the proper optical system as described above, as well as by using molecules with high fluorescent quantum yield and high photostability so that they can be excited with high excitation intensities. In this way the position of a single fluorescent molecule like TDI can be determined with an accuracy of typically 5 nm or less.

This striking resolution needs to be clearly distinguished from the resolution of the microscope that describes the smallest distance Δx of two objects that can still be distinguished from one another (see Figure 1.4.c). This distance is roughly equal to the full width at half maximum of the signal and is given by Abbe's law and the Rayleigh criterion (Figure 1.4.c). It follows that the higher the NA, the smaller the minimum distance Δx of two objects that can be resolved. By using visible light (e.g., 633 nm), the lateral resolution is about 300 nm. SMM, however, overcomes this resolution limit, since the samples in these studies are prepared on a single molecule level, meaning a very low fluorescent dye concentration (of about $10^{-10} - 10^{-11}$ M) as mentioned above. Hence, the probability of two molecules coming closer to each other than 300 nm is very low.

In order to investigate the diffusion behavior of single molecules incorporated into porous hosts, movies of many images in time series (i.e. frames) were collected. Then, the position of the molecules was determined in each individual frame and connected frame-by-frame to give a SM trajectory. This trajectory gives detailed information about the pathway of the molecule within the pores and thus the structure of the host. Such movies can be found in the Supplementary Material of articles by J. Kirstein *et al.*[53] or A. Zürner *et al.*[52]. The main features of the technique are also summarized in Section 2.1.

1.1.5 Structural analysis by combining TEM and SMM studies

To learn more about host–guest interactions, e.g., how a single fluorescent dye molecule travels through linear or strongly curved regions of a mesoporous channel system, a combination of electron microscopic mapping and optical single-molecule tracking experiments were performed by Zürner *et al.*[52] In this study, an extremely thin mesoporous silica film with a 2D-hexagonal pore arrangement and a pore to pore distance of about 7 nm was synthesized on a silicon nitride membrane (Si_3N_4 membrane). In order to correlate fluorescence and structural features, a fluorescent terrylenediimide (TDI) derivative and 280 nm polystyrene beads were added to the synthesis solution

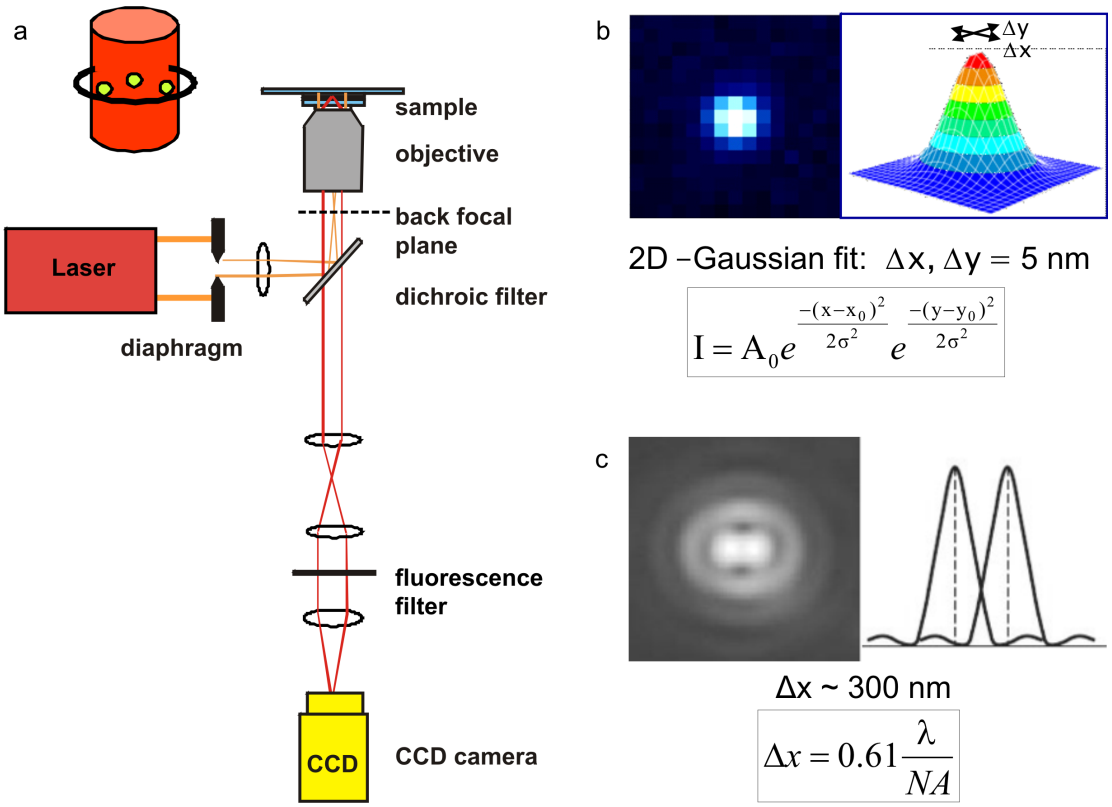

Figure 1.4: (a) Schematic setup of wide-field epi-fluorescence microscopy (the cylinder depicts the excitation volume of the microscope). (b) The fluorescence intensity distribution of a single molecule can be fitted by a two-dimensional Gaussian curve according to the equation. The peak position x_0 and y_0 can be determined with an accuracy down to typically 5 nm or less. (c) Demonstration of the Rayleigh criterion which describes the smallest distance Δx of two objects that can still be resolved by the optical system.

of the mesoporous silica. The polystyrene beads were used as markers and allowed the authors to overlay the transmission electron microscopy (TEM) images with the SMM images. Fast Fourier transform (FFT) directors obtained from a FFT analysis of regions in the TEM images (black bars in Figure 1.5.a) indicate parallel aligned channels with strongly curved areas and domain boundaries. By overlaying the SM trajectory over the TEM images it can be clearly seen that the molecule diffuses along the pores. This was the first direct proof that the molecular diffusion pathway through the pore system correlates with the pore orientation of the two-dimensional hexagonal structure (Figure 1.5). Changes of the molecular diffusional movement (and even stopping at less ordered regions) in the channel structure, repulsion by domain boundaries with different channel orientations, or lateral motions between "leaky" channels allow a molecule to explore different parallel channels within an otherwise well-ordered

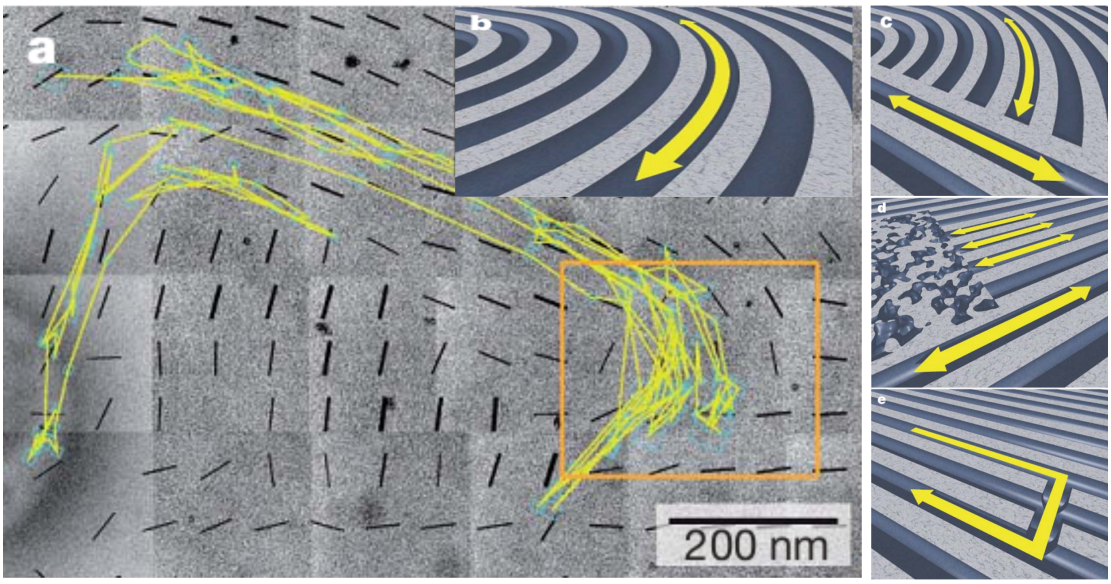

Figure 1.5: (a) Overlay of a single-molecule trajectory (yellow) and multiple TEM images of the silica film (grey) stitched together to provide a macroscopic overview of the sample. The pathway of the molecule is influenced by the domain architecture of hexagonally ordered mesoporous silica pores. Domain boundaries and the local orientation of the pores (black bars) are indicated by the fast Fourier transform of the TEM images. (b-e) Schematic representations of structural elements and molecular movements found in hexagonal mesoporous silica films. Figures adapted from Reference 52.

periodic structure. This striking heterogeneity of diffusion behavior only becomes apparent through single molecule experiments, whereas TEM provides static information only. Moreover, TEM images correspond to an average over the thickness of the film, and while giving a good indication about the general local architecture, they cannot show single defects such as closed channels or open neighboring channels, which can be detected by SMM. In a subsequent study, we applied the knowledge that SMM can characterize the structural properties of the mesoporous structure in a non-invasive and direct way and optimized the synthesis conditions that lead to porous silica thin films with highly oriented mesopores (see Chapter 3).

1.1.6 Silica filaments for applications in bioanalytics

A further approach to control the mesoporous structure is the confined synthesis of mesoporous silica inside porous anodic alumina membranes[48,62,63] *via* the EISA process. Feil *et al.*[48] synthesized template-free, chemically functionalized mesoporous silica filaments with 4 nm pore diameter and used SMM to investigate the translational and orientational dynamics of TDI dye molecules (see chemical structure in

Figure 1.6) and dye-functionalized (Cy3 and Cy5) double-stranded DNA (ds-DNA). In order to introduce a homogeneous chemical functionalization of the porous host with nitrile groups (10 mol % with respect to the silica source), a co-condensation of the silica matrix with (2-cyanoethyl)triethoxysilane was performed. The template was then removed by Soxhlet extraction. Afterwards, amino groups were grafted to the channel walls to favor the uptake of the negatively charged DNA constructs. The samples were loaded with the desired guest molecules at a concentration appropriate for single molecule studies.

First, TDI dye molecules were incorporated into nitrile functionalized mesoporous channels and studied by SMM. While the TDI molecules remained immobile in the mesopores under air atmosphere, diffusion inside the pores could be detected in the presence of a saturated chloroform/water atmosphere acting as a lubricant phase. To ensure that the observed diffusion of single TDI molecules occurs in the mesoporous channels of the host material and not on the surface, a 0.4 nm thin layer of gold was deposited on the surface of the sample by thermal evaporation. This way, the fluorescence of all molecules on the surface of the glass substrate was quenched and only molecules inside the mesoporous host remained fluorescent (Figure 1.6.a). Their positions could be correlated to the transmission optical images of the filaments (Figure 1.6.b). Furthermore, the trajectories of the molecules were highly structured due to the confinement in the columnar mesopores (Figure 1.6.c and Figure 1.6.d) and provided detailed information about the host structure, such as domain size (up to about 10 µm) and the presence of defects. The next step was to load DNA into mesopores. The functionalization of the pores and thus the interaction between host and guest turned out to play an important role for achieving this goal. The authors observed no loading in unfunctionalized or mono-functionalized mesopores, but only in bi-functionalized samples. The loading process took about 2 weeks, and movement of the DNA molecules was only detectable under a high humidity atmosphere. The DNA was labeled with Cy3 (donor) and Cy5 (acceptor) dyes to check its integrity by measuring the Förster resonance energy transfer (FRET) signal. FRET is strongly distance-dependent, and in the case of DNA denaturation, the two single strands will be separated and no FRET signal in the red channel is expected. Feil *et al.*[48] observed Cy3 fluorescence in the green channel (right) and emission of fluorescing Cy5 molecules upon FRET in the red channel (left) (Figure 1.6.e). This demonstrates that the ds-DNA strands were still intact after loading into the mesoporous channels. Furthermore the trajectories were highly structured and quite linear over up to 7 µm. In

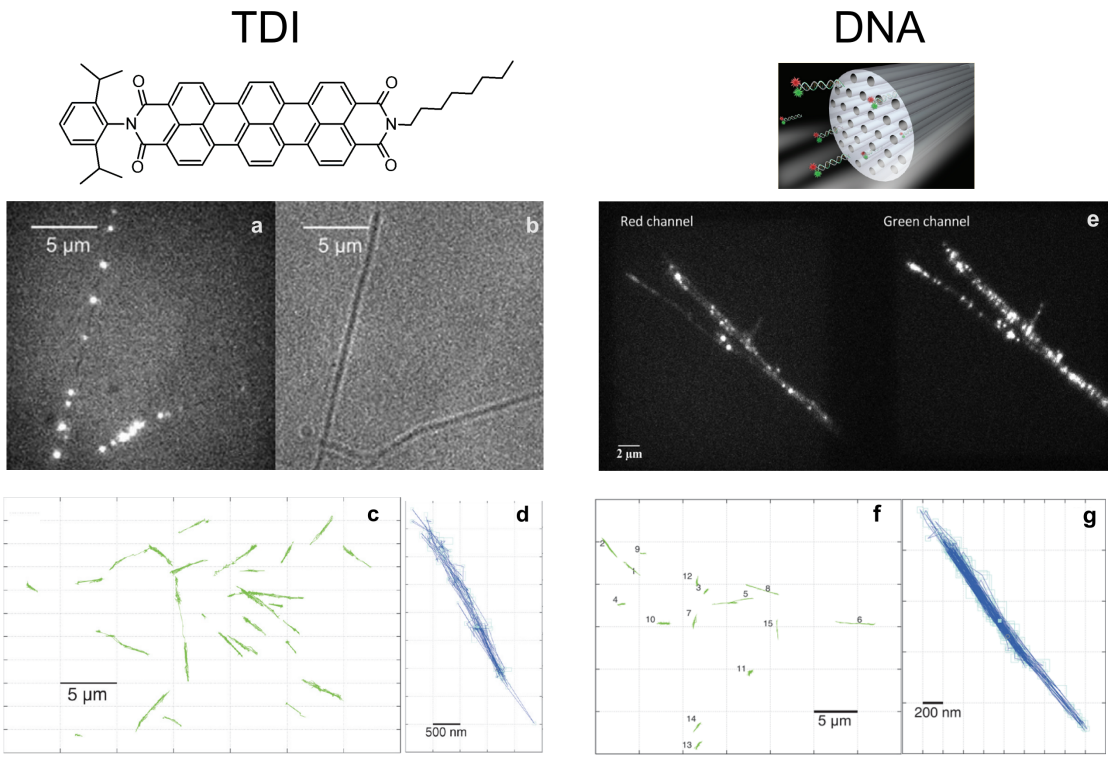

Figure 1.6: (a) Fluorescence image of single TDI molecules within filament channels. Molecules located on the cover glass are quenched with a coated gold layer. (b) The positions of the bright spots are perfectly correlated to the structure of the filaments displayed in the optical transmission image. (c) Overview of several linear shaped single molecule trajectories. (d) Example of a single TDI molecule trajectory. (e) FRET experiment of Cy3-Cy5 labeled ds-DNA strands inside the mesoporous filaments structure. Left: red channel showing the red emission of fluorescing Cy5 molecules after FRET. This means that the ds-DNA strands are still intact. Right: green channel showing Cy3 fluorescence. (f) Overview of several single molecule trajectories of ds-DNA strands. (g) Example of a ds-DNA molecule trajectory. Figures adapted from Reference 48.

addition, the diffusion constant for ds-DNA and also for TDI was obtained by fitting the linear part of the plots of the mean square displacement (MSD) vs. time with the one-dimensional form of the Einstein-Smoluchowski equation, $MSD = 2Dt$.

Figure 1.7 shows the single molecule diffusion analysis of ds-DNA and TDI molecules in mesoporous filaments. The results indicate that while the larger DNA molecules took much longer to be loaded into the mesoporous channels compared to the smaller TDI molecules, they moved nearly as fast once they were inside the mesopores. The single molecule diffusion coefficients of the DNA molecules have a mean value of $\langle D \rangle = 5.9 \times 10^4\,\mathrm{nm^2\,s^{-1}}$ for saturated H_2O vapor pressure at room temperature, while TDI molecules have a diffusion constant of $\langle D \rangle = 1.1 \times 10^5\,\mathrm{nm^2\,s^{-1}}$.

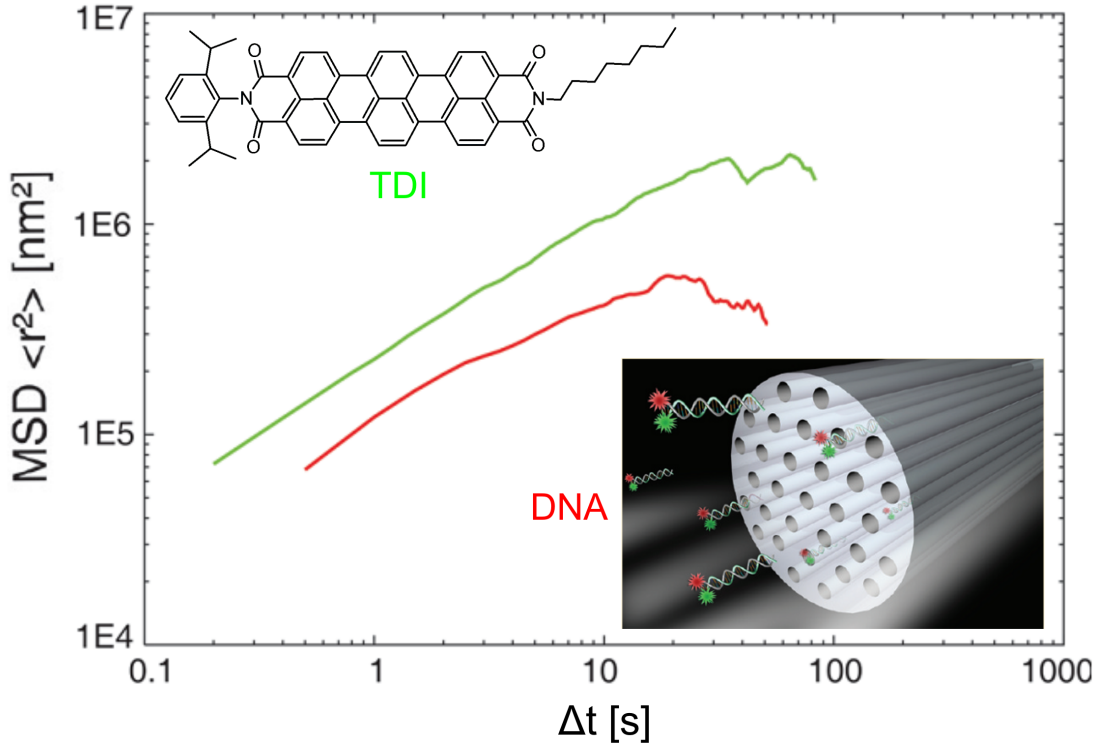

Figure 1.7: Single molecule diffusion analysis of TDI and ds-DNA molecules in mesoporous filaments. Comparison of the average MSD plots of TDI (green) and ds-DNA (red) molecules. The MSDs of the DNA molecules are about two times lower than the MSDs of TDI. Furthermore, the difference in size of the observed guest molecule is reflected by the shape of their MSDs. While the mean MSD plot of the small TDI molecules is nearly linear (which suggests normal diffusion) over the observed time range, the mean MSD plot of the ds-DNA molecules bends for longer time intervals (due to the confined diffusion in the mesopores). This indicates that the larger DNA molecules respond more strongly to the confinement in the filaments than the TDI molecules. Figures adapted from Reference 48.

This work shows once more how important it is to investigate host–guest interactions with SMM to provide a solid basis for a thorough understanding of the interactions within a porous material. Furthermore, the right functionalization of the highly structured collinear pore walls plays an important role for applications in bioanalytics and drug-delivery (see Section 1.1.12).

1.1.7 Diffusion in Thin Silica Films

Very interesting work on single molecule diffusion studies of different guest species in silica thin films was also done by Higgins *et al.* In early studies, they investigated the nanoscale properties, the heterogeneity, and the diffusion behavior of dye molecules

in dense (organically modified) sol-gel silica films at the single molecule level.[64–67] Later, Fu *et al.*[68] and Ye *et al.*[69] extended the approach to porous silica thin films. By incorporating fluorescent dyes into the surfactant phase of the mesoporous silica thin films and comparing their diffusional movement to that of dye molecules loaded into template-free films after calcination, striking differences in the dynamics could be observed. The measurements revealed that the dye molecules were relatively mobile in the as-synthesized (i.e., surfactant-containing) films, but appeared to be entrapped at fixed locations after being loaded into the calcined (i.e., template-free) films. Upon re-hydrating the calcined films under high humidity conditions, the dye molecules became mobile again. These results indicate that the surfactant phases of the as-synthesized material and the hydrated pores of the calcined material after exposure to high humidity behave like fluid-filled domains, providing a "lubricant" phase that enables mass transport of the dye inside the porous host. The authors used fluorescence imaging and single-point fluorescence time transients in their studies (see Figure 1.8). These fluorescence correlation spectroscopy (FCS) methods are interesting for diffusion studies as they feature a high time resolution and hence allow for the investigation of rapid processes. Moreover, FCS measurements are independent of photobleaching which can limit the amount of available data in other techniques. However, no structural information of the porous host can be obtained, and a model for the possible mode of motion needs to be provided.

In contrast to those studies, Bräuchle *et al.* investigated the diffusional processes of various fluorescent dye molecules in the nanoporous network of sol-gel-glasses[70] and in mesoporous materials[71] with the direct method of single molecule tracking. Furthermore, they showed diffusional and orientational dynamics of various single dye molecules in nanostructured host–guest-materials[72] and the switchable mobility of single TDI molecules in networks of long unidimensional nanochannels[73]. In these studies, a more direct observation of the mobility of the dye molecules could be achieved by the optical tracking and polarization techniques than in the FCS studies of Higgins *et al.*[64–69].

1.1.8 Diffusion Phenomena, Morphology, Intergrowth and Accessibility in Porous Catalyst Particles

Investigations of diffusion processes and identifying diffusion barriers for molecules inside porous compounds play a major role in many heterogeneous catalysis processes.

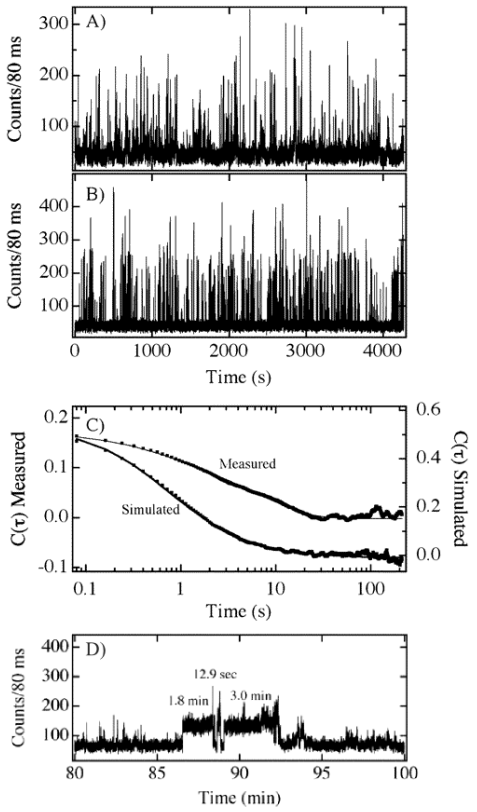

Figure 1.8: (A) Representative fluorescence time transient recorded for Nile Red in an as-synthesized mesoporous silica film. (B) Simulated time transient obtained by using a molecular areal density of 0.6 molecules/µm^2 and $D = 3 \times 10^{-10}\,\mathrm{cm^2\,s^{-1}}$. (C) Autocorrelations (points) and fits (lines) for the data shown in parts A and B. (D) Expanded section of a representative time transient showing long-term adsorption events in an as-synthesized film. Each of the three designated events is labeled with the measured desorption time. Figures adapted from Reference 68.

If the intraparticle diffusion is too slow or if there are substantial diffusion barriers, a depletion of substrate molecules can occur, and only a fraction of the catalytically active particle is actually used. Hence, visualizing, measuring and quantifying diffusion processes is crucial to provide a better understanding and to make a rational design and improvement of the porous catalysts possible. De Cremer *et al.* showed how single molecule fluorescence spectroscopy could be used to visualize and quantify the effects of mass transfer limitations on the overall catalytic efficiency in a spatially resolved fashion.[74] As a model system, the authors chose mesoporous Ti-MCM-41 particles which catalyze the epoxidation of a fluorescent dye (PBD-bodipy), resulting in a spectral shift of the excitation and emission maximum of the products. Hence, the emission of the reaction products could be spectrally separated from the educts,

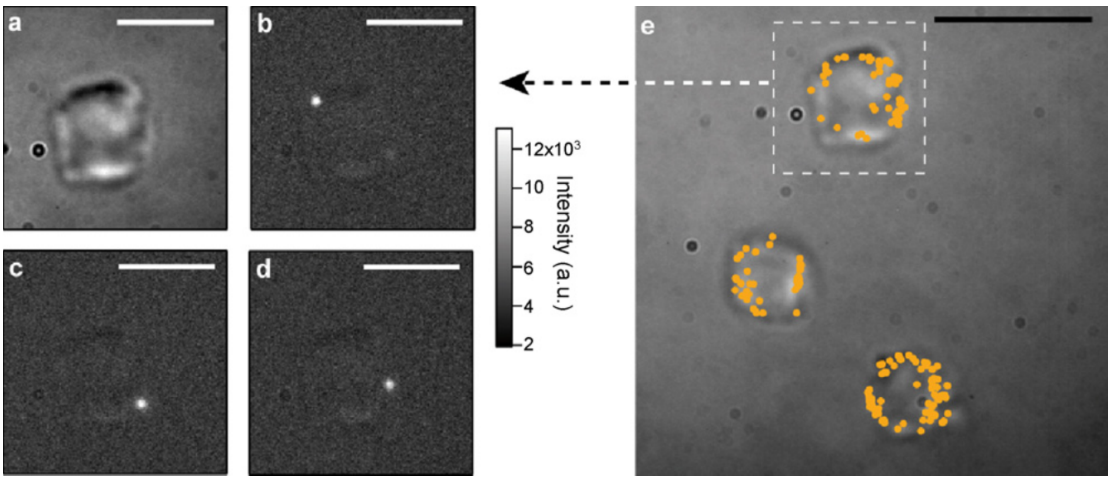

Figure 1.9: (a) Transmission image of an individual Ti-MCM-41 particle. (b-d) Three representative examples of fluorescent bursts due to the formation of a single product molecule in the Ti-MCM-41 catalyzed epoxidation of the PBD-bodipy probe. The white scale bars in panels (a-d) represent a distance of 3 µm. (e) Transmission image of three Ti-MCM-41 particles on which the positions where reactions were observed over a time span of 140 s are highlighted by a yellow mark. The black scale bar represents a distance of 5 µm. Figures adapted from Reference 74.

and single turnover events could be subjected to a spatial and temporal analysis (see Figure 1.9), giving quantitative information about the catalytic process.

Karawacki *et al.* showed that the decomposition of template molecules in zeolite-type crystals yields light-absorbing and fluorescent intermediates, which the authors used to elucidate the three-dimensional intergrowth structure by means of *in situ* optical and fluorescence microscopy during heating.[75] In another study, also by Karawacki *et al.*, the authors related the intergrowth structure of zeolites to internal and outer-surface molecular diffusion barriers.[76] In their study, they used a combination of confocal fluorescence microscopy, electron backscatter diffraction from samples prepared by focused ion beam sectioning, transmission electron microscopy imaging and diffraction, atomic force microscopy and X-ray photoelectron spectroscopy to study a wide range of coffin-shaped MFI-type zeolite crystals, and presented an overview of the morphology-dependent MFI-type intergrowth structures. Sommer *et al.* used a Brønsted acid catalyzed oligomerization of styrene derivatives to study the intergrowth structure and the active site accessibility in etched SSZ-13 zeolites by confocal fluorescence microscopy.[77] The authors found a high degree of heterogeneity in the density of defects and the catalytic activity among different crystals within one SSZ-13 batch.

1.1.9 Catalytic Reactivity Mapping in Porous Silica Compounds

Another interesting application of single molecule spectroscopy is the mapping of catalytically active sites within porous materials. Roeffaers *et al.* used the liquid phase acid-catalyzed self-condensation of furfuryl alcohol in dioxane as a reporter reaction for imaging the catalytic activity of active sites in individual zeolite crystals.[78,79] After the condensation of the furfuryl alcohol, the reaction products entrapped in the pores are sufficiently fluorescent to be detected with a confocal microscope. When polarized excitation light is used, the efficiency of excitation and emission is strongly orientation-dependent, since the linear oligomeric products have transition dipole moments of absorption and emission parallel to the long molecular axis. This anisotropy allows conclusions about the orientation of the emissive product molecules and hence the channel orientations within the zeolite crystals.[78] In another study, Roeffaers *et al.* demonstrated the use of the same self-condensation reaction to study the reactive sites within ZSM-22 and ZSM-5 crystals with a new technique they called NASCA (nanometer accuracy by stochastic catalytic reactions) microscopy.[79] In this technique, 2D-Gaussian functions are fitted to the (diffraction-limited) emission spots of the fluorescent product molecules, and from these data, a high-resolution image is reconstructed that gives valuable information about the catalytic activity at different locations within the crystal (see Figure 1.10).

Kox *et al.* investigated the catalytic conversion of various thiophenes over individual ZSM-5 crystals, using a combination of X-ray absorption, UV/Vis and fluorescence microspectroscopy.[80] The authors discuss spatial heterogeneities in product formation and the alignment of distinct reaction products within the pores, and visualize the three-dimensional distribution of reaction products within the crystals, showing the influence of crystal intergrowth and concurrent diffusion barriers. Chung *et al.* studied the coke formation during the aromatization of paraffin and olefin hydrocarbons over ZSM-5 in a space and time-resolved manner.[81] In this study, polarization dependent *in situ* UV/Vis micro-spectroscopy and confocal fluorescence microscopy were used to show how large poly-aromatics mainly grow in alignment with the zeolite straight channels and how these techniques can be used to reveal spatial heterogeneities of the photo-excited coke compounds. Buurmans *et al.* used Nile Blue A and a Brønsted acid-catalyzed thiophene oligomerization that yields a fluorescent product to selectively stain different components and investigate Brønsted acidity and catalytic activity in fluid catalytic cracking (FCC) particles,[82] while Karreman *et al.* used a fluorostyrene oligomerization (also yielding a fluorescent product) in an integrated laser and elec-

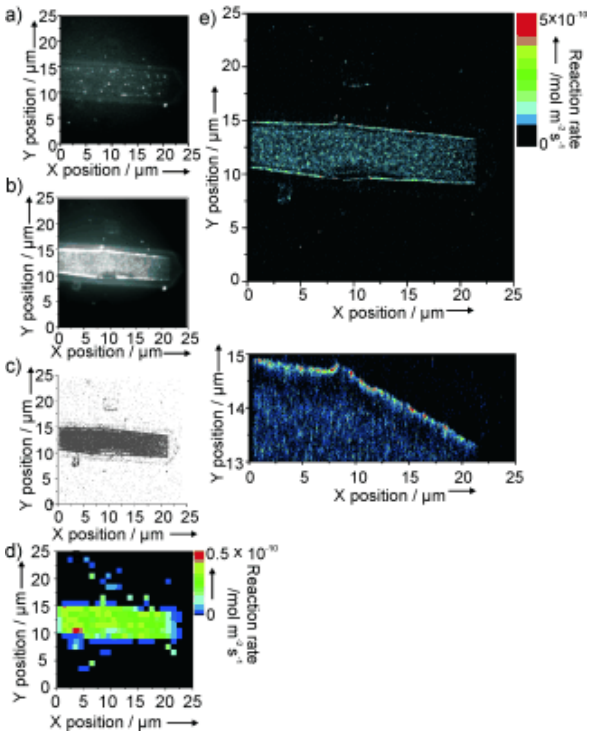

Figure 1.10: (a) Individual fluorescent product molecules on a ZSM-5 crystal. The contours of the crystal are visible because of a small amount of unfiltered scattered light. (b) Accumulated and diffraction-limited image of all reactions observed during the time course of the recorded movie (80 s, 800 frames). (c) Reconstructed image obtained after mathematical fitting of all reaction events observed in the 800-frame movie. (d) Resolved reaction map (1x1 µm^2) reconstructed using the data in (c). (e) Similar resolved reaction map (top) calculated for 20x20 nm^2 pixels with a zoom (bottom) at the upper part of the active rim. Figure adapted from Reference 79.

tron microscopy study to investigate and characterize these industrially important catalysts.[83] Stavitsky *et al.* also used fluorescence generated through oligomerization of various styrene derivatives for time- and space-resolved optical and fluorescence investigations of the shape selectivity and catalytic activity within the pores of ZSM-5 crystals,[84] and Kox *et al.* used a styrene oligomerization reaction in a combined *in situ* optical and fluorescence microscopy study of ZSM-5 featuring micro and mesoporosity (introduced through desilication) for investigating the intergrowth structure and catalytic activity trends.[85] Domke *et al.* introduced a technique for tracing catalytic conversion on single zeolite crystals in 3D with nonlinear Raman- and two-photon spectromicroscopy.[86] The authors used these techniques to gain mechanistic insights into the alkene activation and glycol etherification catalyzed by large crystal H-beta zeolites.

1.1.10 Catalyst Deactivation

Catalyst deactivation is a very important issue in industrial processes. One of the most important deactivation mechanisms in acid heterogeneous catalysis and for zeolites in particular is a deactivation due to coke formation. In this process, heavy byproducts that are formed during the catalytic reaction cover the active sites or block the pore network of the zeolite, resulting in a partial or total loss of catalytic activity. Fluorescence microscopy in combination with other techniques can help to obtain a more detailed picture of the individual processes that happen inside the pores of porous materials employed in industrial applications. Ruiz-Martinez *et al.* studied the deactivation process of FCC catalyst particles containing zeolite Y or ZSM-5 by sulfur compounds[87], and Mores *et al.* investigated the deactivation of H-ZSM-5/silicalite-1 zeolite composites[88]. Parvulescu *et al.* focused on another important industrial process, namely the etherification of biomass-based alcohols with olefins over beta zeolites.[89] Confocal fluorescence microscopy studies allowed the authors to observe the interaction between the reactants and the catalyst particles in a space-resolved manner (see also Figure 1.11). The results indicate that the etherification of alcohols with long linear alkenes takes place at the external surface of the catalyst particles, and that alkenes were found mainly responsible for the coke formation and blockage of the external surface, which results in a loss of catalytic activity.

1.1.11 Electrophoretic Translocation of Macromolecules through Nanopores

Besides catalysis, porous systems have great potential in analytics and diagnosis. In recent years, a large interest arose in studying the electrically driven translocation of single macromolecules through nanopores. Some of the first examples that demonstrated the feasibility of this endeavor were published by Bezrukov *et al.* in 1994[90] and Kasianowicz *et al.* in 1996[91]. Both groups demonstrated that macromolecules such as polyethylene glycol or polynucleotides could be translocated through natural channel-forming peptides incorporated into a lipid bilayer membrane by applying an electric field across the latter, and that the translocation events could be detected on a single molecule basis. The detection scheme is based on the fact that the macromolecules block the pore during the translocation event, which causes a drop of the ionic current through the pore. The duration and magnitude of the ionic current blockade is characteristic for the length distribution of the individual macromolecules. These findings

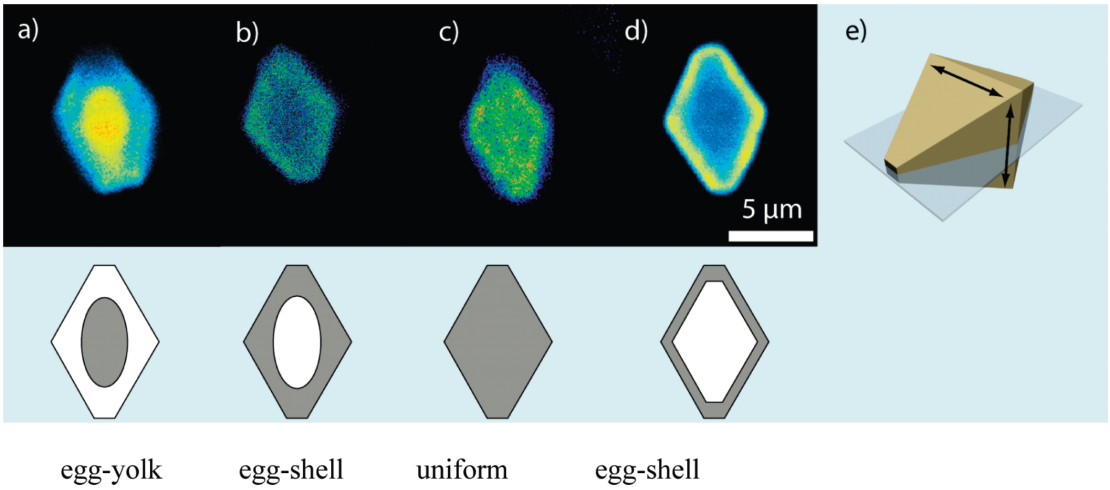

Figure 1.11: Fluorescence intensity maps of an individual H-Beta zeolite crystal recorded with a laser excitation of 488 nm (detection at 510 – 550 nm). Samples were taken after 3 h of reaction at 140 °C with (a) glycerol, (b) ethylene glycol, (c) 1,3-propylene glycol, and (d) 1,2-propylene glycol. (e) Schematic representation of the slice at which the confocal fluorescence measurements have been performed, with the arrows indicating the direction of the pores. Figures adapted from Reference 89.

sparked a large interest in such systems, arising from their potential application in cheap and fast third-generation genome sequencing through single-nucleotide identification.[92,93] However, employing protein pores embedded in lipid membranes can be problematic due to the limited robustness and stability of this biological system, since it is known that high voltages can lead to rupture of lipid membranes.[94] Several groups have tackled these challenges by using different kinds of artificially fabricated solid-state nanopores.[95,96] Besides excellent stability over a wide temperature and voltage range, these artificial pores also have other advantages over biological pores, such as fixed pore position, rapid response to environmental changes, and controllable pore size down to the nanometer level[97]. Typically, such pores are fabricated by drilling a hole into a thin substrate such as silicon nitride with an electron microscope or *via* focused ion beam (FIB) lithography.

Chen *et al.* extended this approach by coating a silicon nitride substrate that has a single pore drilled through it with a very thin mesoporous silica film (see Figure 1.12).[98] This thin film features "kinked" mesopores that cause up to fivefold reduction in translocation velocity, which has been identified as one of the critical issues in DNA sequencing. The thin film was prepared through the EISA process using Brij56 as the structure-directing agent, resulting in a cubic structure with an average pore diameter of around 4 nm and pore window sizes of about 2.6 nm. The authors used

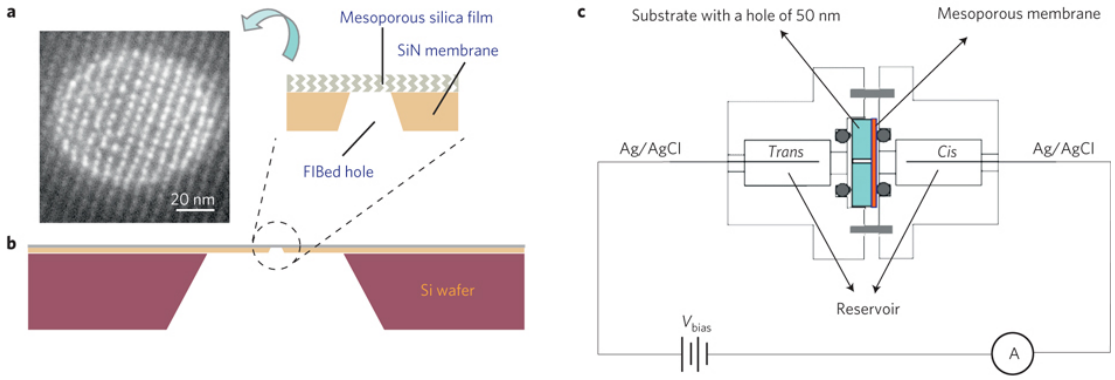

Figure 1.12: (a) TEM plan-view image of a free-standing *Fmmm* film suspended over a sub-100-nm-diameter aperture formed by FIB. The orientation is along [001]. (b) Schematic of the experimental platform showing the free-standing film suspended over an aperture formed in a silicon nitride window by FIB. Nanopores are tortuous in the direction normal to the film surface. (c) Schematic of the electrochemical cell for carrying out voltage-driven DNA-translocation experiments. Figure adapted from Reference 98.

thermal atomic layer deposition (ALD) of TiO_2 to further reduce the pore aperture size down to 2.3 nm (one layer) or 2.0 nm (two layers) or to form an aminopropyl silane monolayer using the molecular precursor aminopropyl trimethoxysilane (APTMS). Reduction of the pore window size down to 2.3 nm resulted in a threefold reduced dsDNA translocation time, while after a pore window size reduction down to 1.9 – 2.0 nm (i.e., below the diameter of dsDNA) no DNA translocation events could be observed. When APTMS was used in the ALD process, the pore aperture size was reduced to approximately 1.4 nm, and while again no translocation events could be observed for dsDNA, ssDNA ($poly(dA)_{100}$) caused current-blockage events indicative of successful ssDNA translocation.

Other work done in this field focuses on single molecule fluorescence detection in zero-mode waveguides[99–101] or in submicrometer-sized fluidic channels[102], on very thin silica capillaries for sensing applications and investigating molecular transport[103], or on DNA electrophoresis in a monodisperse porous medium obtained from closely packed silica beads[104].

1.1.12 Outlook: Mesoporous Silica in Drug Delivery Applications

An intriguing perspective for mesoporous silica materials is their use as carriers in drug delivery applications, where they are employed to encapsulate various drugs or even

RNA or DNA fragments and release them specifically at a target site. Especially the controlled release of cytotoxic antineoplastic drugs for cancer treatment in malignant cells could greatly enhance the efficacy of these drugs and simultaneously reduce the detrimental side effects of a chemotherapeutic treatment. In order to devise such systems, a great amount of control over the chemical properties of the porous silica materials as well as detailed knowledge about their behavior upon cell internalization and during the triggered release are of great importance. In the following, three examples are given that demonstrate how chemically modified mesoporous silica thin films or particles can be used in combination with single molecule microscopy studies to achieve this goal.

In a recent study, Lebold *et al.* demonstrated the feasibility of mesoporous silica thin films for the encapsulation and release of the anticancer drug doxorubicin, which is already widely used in clinical chemotherapy.[105] The authors investigated the influence of different templates (Pluronic P123, CTAB, and Brij56) and pore functionalizations on the drug dynamics inside the mesopores on a single molecule level. In thin films templated by the non-ionic triblock-copolymer Pluronic P123, a mobile sub-population of doxorubicin molecules could be observed at high drug loading rates, presumably due to the formation of doxorubicin dimers. However, the diffusional pathways of the drug inside the channel system were not very well structured. With the ionic template CTAB, the population of mobile molecules was about 10 %, and the trajectories indicating the diffusional movement of the drug showed a high degree of orientation. Interestingly, when the non-ionic block copolymer Brij56 was used, all molecules were immobile inside the film, presumably due to interactions of the guests with free hydroxyl groups at the channel surface, which were not shielded by an ionic counterpart (as in the case of the ionic template CTAB), and which were in close proximity to the guest molecules due to the smaller pore width (compared to silica thin films templated by Pluronic P123). This assumption is backed up by the fact that a mobile population could be recovered in the Brij56-templated samples by chemically modifying the silica pore walls with propyl groups. This leads to a hydrophobization of the inner pore surface through a shielding of the hydroxyl groups, resulting in weaker interactions between the drug and the host matrix and hence a structured movement of the drug inside the porous host. Based on these findings, it was shown that the release kinetics of doxorubicin into cell medium could be controlled by varying the template and the pore functionalization within the porous host, and that doxorubicin released from the film could be used to induce cell death in human cervical cancer (HeLa)

cells. These findings suggest that for future applications, mesoporous silica structures could be used either in the form of film coatings for implants, e.g., for the delivery of immunosuppressive drugs to diminish rejection, or in the form of nanoparticles for drug-delivery applications.

Inspired by the previously described experiments, Lebold *et al.* further investigated ways to control the mobility of oligonucleotides (siRNA and dsDNA) within the nanochannels of mesoporous silica particles.[47] In order to do so, the authors focused on SBA-15 particles that were functionalized with aminopropyl, cyanoethyl and phenyl groups and compared them to unfunctionalized particles. They found that unfunctionalized and cyanoethyl-functionalized particles could not be loaded with siRNA, presumably due to the repulsive interaction of the negatively charged oligonucleotides with these functional groups. However, when adjusting the surface polarity of the silica pore walls by functionalization with aminopropyl groups, the unfavorable repulsive interactions are reduced, favorable interactions of the positively charged amino groups and the siRNA are created, and the particles could be loaded with siRNA. Moreover, the functionalized particles could also be loaded with dsDNA, ranging from 20 up to 90 base pairs in length. A detailed analysis of the movement of single oligonucleotides guest molecules revealed that the diffusion dynamics critically depend on the length of the oligonucleotides, and that long DNA sequences have a higher tendency to get immobilized at adsorption sites inside the porous framework. The stability of the oligonucleotides inside the porous silica host was proven for all nucleotides by Förster resonance energy transfer (FRET) experiments. The obtained information is of great importance for the design of mesoporous silica nanoparticles that can be used in gene therapy or gene silencing and for drug carriers featuring controlled retarded release of a drug over a prolonged period of time, generating a "depot effect".

In order to tackle the challenge of controlled release at a target site, the groups of Prof. Bein and Prof. Bräuchle investigated a variety of different ways to enclose a drug inside porous silica particles and to release it as a result of specific external stimuli, including pH changes,[107,108] temperature changes,[109] the presence of certain enzymes,[110] and changes in the redox potential.[111] In a recent paper, Schlossbauer *et al.* demonstrated the cascaded photoinduced release of various model drugs from multifunctional core-shell mesoporous silica particles sealed with a supported lipid bilayer.[106] In this study, the model drugs propidium iodide, phalloidine, and small dye-labeled antibody fragments (chromobodies) were incorporated into multifunctional core-shell mesoporous silica particles[112,113], carrying amino groups in the inner shell and thiol

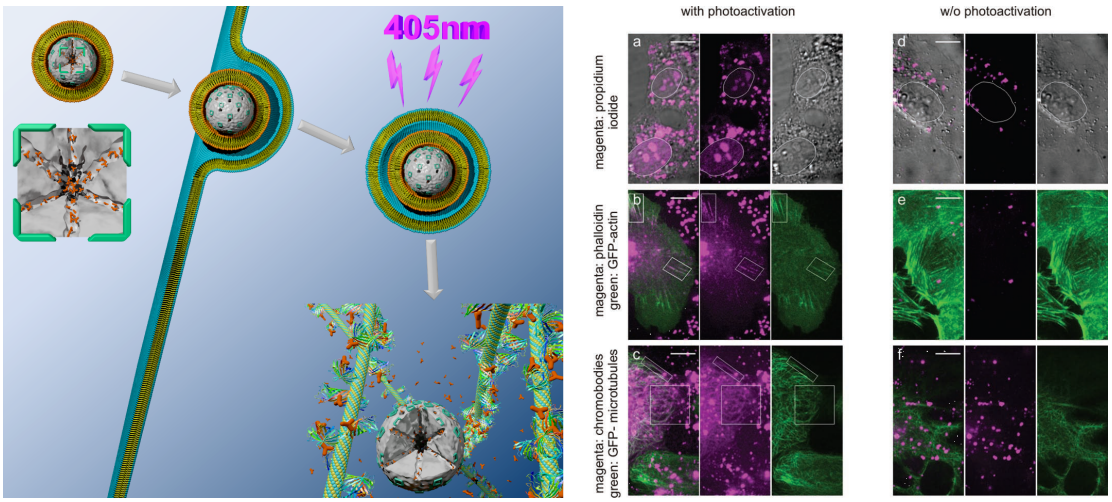

Figure 1.13: Cascaded photoinduced release of various model drugs from multifunctional core-shell mesoporous silica particles sealed with a supported lipid bilayer. Left: Schematic representation of the process. Right: Confocal microscopy of living HuH7 cells exposed to the colloidal mesoporous silica nanoparticles carrying a photosensitizer and loaded with model drugs, sealed by a SLB. (a) Superposition of the transmitted light image of HuH7 cells with the PI fluorescence (left panel) and the PI fluorescence alone (center panel) and the transmitted light image (right panel). Propidium iodide stains the nucleus of the cell. (b) Alexa Fluor 647-labeled phalloidin fluorescence (shown in magenta) and stably actin-GFP (GFP: green fluorescent protein) expressing HuH7 cell (shown in green on the left panel), the phalloidin fluorescence channel alone (shown in magenta in the center panel) and the actin-GFP fluorescence channel (shown in green in the right panel). (c) Chromeo642-labeled chromobodies (magenta) released from the particles stain the microtubules of stably microtubule-GFP expressing HuH7 cells (green) (left panel). The chromobody channel is displayed in the center panel, the separated actin-GFP channel is shown in the right panel. (d-f). In case of the non-photoactivated samples, no labeled cell structure was observed. Scale bar: 10 µm. Figures adapted from Reference 106.

groups on the outer surface. This orthogonal, site-selective functionalization allowed for the specific covalent binding of a photosensitizer (Protoporphyrin IX) to the outer particle shell. Such photosensitizers are already used in photodynamic therapy to treat cancer. However, initial approaches of combining these photosensitizers with mesoporous silica as a drug carrier did not provide a covalent attachment, and could hence lead to uncontrolled leaching of the compounds from the particles, resulting in highly toxic effects on the cell. After covalent attachment of the photosensitizer and loading with drugs, the particles were sealed with a 1,2-dioleoyl-sn-glycero-3-phosphocholine (DOPC) supported lipid bilayer (SLB) membrane, constructed *via* a one-step solvent exchange route[114]. The formation of the SLB results in a tight encapsulation of the

cargo molecules, preventing premature release of the model drugs from the particle. When the SLB-coated particles come into contact with cells, they are taken up *via* endocytosis and end up in an endosome inside the cell (see also Figure 1.13). Upon illumination with light, the covalently bound photosensitizers produce highly reactive singlet oxygen that leads to the disintegration of the SLB around the particles.[106] Without the sealing, the model drugs can escape from the particles, but they are still trapped within the endosome. In a second step, the endosomal membrane is destroyed, which allows the model drugs to be released into the cytosol and reach their final destination. Strikingly, phototoxic effects (e.g., on microtubule motor proteins) were restricted to endosomes carrying nanoparticles, allowing for a "surgical" endosomal release without the global cell toxicity of common liquid-phase photosensitizers.

1.2 Metal–Organic Frameworks

1.2.1 Structure and Synthesis

Another class of porous materials that has attracted increasing attention over the past two decades are metal–organic frameworks (MOFs). The term MOF was first introduced by Yaghi *et al.*[115] in 1995 to describe a new class of hybrid materials that result from the interaction of organic and inorganic species to form three-dimensional porous frameworks (see Figure 1.14).[116,117] The combination of these two components – metal ions or clusters and organic linkers – provides a nearly infinite number of possible structures and properties.

MOFs owe much of their development to the interest in coordination chemistry and the resulting investigation of coordination polymers. Those are polymers that consist of metals and ligands, held together by coordinative bonds. A very early example of a coordination polymer is $[Fe(III)_4[Fe(II)(CN)_6]_3]$, or Prussian Blue, which can be dated back to the early 1700s and consists of a mixed-valent Fe(II)/Fe(III) network with cyanide ligands bridging the metal centers to form a 3D-cubic structure.[117] In 1989, Hoskins *et al.* extended the approach and synthesized a structure in which Cu(I) centers were linked by 4,4',4'',4'''-tetracyanotetraphenylmethane (tctpm) ligands in a three-dimensional network with diamond-like topology.[118] This provided the foundation for the use of tunable organic linkers in coordination polymers, and soon also other linkers such as bipyridyl-based donors were investigated. Bipyridyls are well-suited for the formation of coordination polymers, since they are good ligands for a

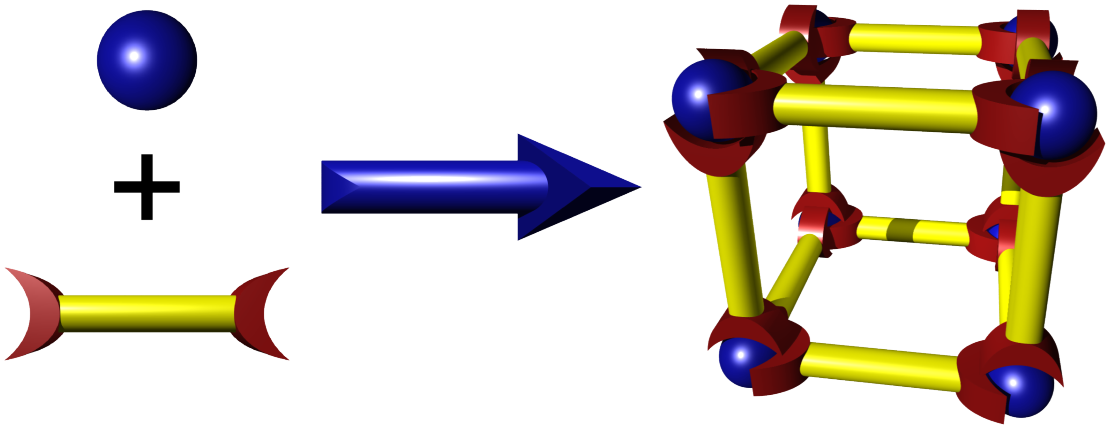

Figure 1.14: Schematic representation of the formation of a three-dimensional network consisting of metal ions or clusters (blue) and organic linker molecules (yellow), carrying functional groups (red).

variety of metals, have a linear and rigid topology, and have two coordination sites, which enables them to form 1, 2 or 3-dimensional networks.[119,120] In the mid-1990s, carboxylate-based ligands were added to the ever-growing toolbox of organic linkers that can be used to build three-dimensional coordinative structures,[121] and meanwhile a large variety of different ligands and metals are used to synthesize new MOF structures.

The vast number of theoretically possible framework structures resulting from the many possible combinations of organic linkers and metal ions can be made more comprehensible by the fact that functionalized linkers can often be substituted by larger ones as long as the connectivity to the inorganic building blocks is maintained. Using this approach, a series of "isoreticular" MOFs (IRMOFs) can be obtained (see Figure 1.15).[122–124] While the structures all share the same cubic topology, the pore and aperture size can be systematically increased by increasing the linker length. However, when the linkers become too large, interpenetrated (or catenated) structures can form, which results in smaller pores compared to the non-interpenetrated structures. While this imposes restrictions on the type and size of guest molecules that can be incorporated into the host structure, it can also have beneficial effects, for example in hydrogen storage applications.[125]

The reticular chemistry of MOFs is closely linked to the structural description using secondary building units (SBUs). The term SBUs is adapted from zeolite chemistry, where it is used to describe tetrahedral species like SiO_4, PO_4, AsO_4, and SO_4, associated with metallic cations in four-, five- or six-coordination. In MOF chemistry,

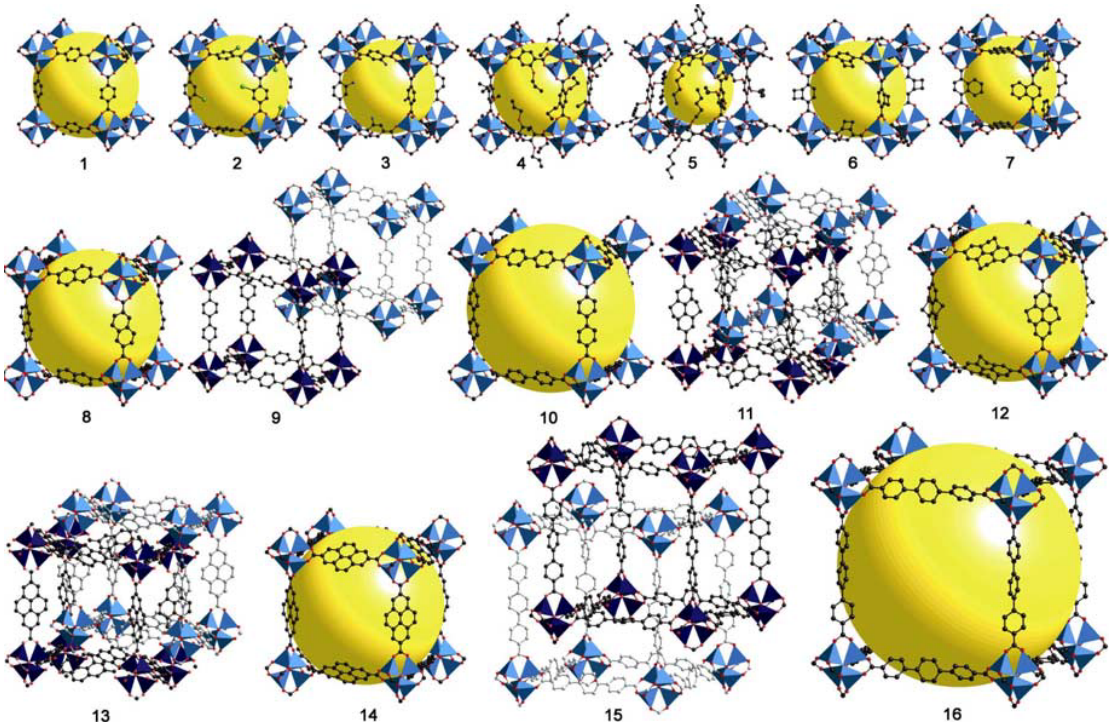

Figure 1.15: A large series of isoreticular metal–organic frameworks (IRMOFs), each sharing the same cubic topology. The linkers differ in length and functionality. With increasing linker length, the pore sizes become larger (yellow spheres), but also interpenetrated networks can form. Figure adapted from Reference 124.

the term refers to metal nodes and metal clusters arranged in an array to form more complex substructures. Some common SBUs in reticular MOF synthesis are shown in Figure 1.16.

Typically, MOFs are synthesized at relatively low temperature (below 250 °C). If the temperature during the synthesis is even below 100 °C, often classic synthesis strategies known from coordination chemistry are used, while above 100 °C, solvothermal synthesis routes are applied.[116] The most frequently used solvents for MOF synthesis include water, alcohols, dialkyl formamides and pyridine. The solubility of the metal precursors and the linkers are important for the choice of the right solvent. Other important synthesis parameters are the pH value (which is typically acidic) and the concentration of the precursors. For some syntheses, the addition of a modulator such as amines or benzoic acid can be beneficial. Moreover, the counter ions of the metal salts can play an important role due to their redox properties or their influence on the pH. Besides the "classical" synthesis approach, other routes are investigated, such as using microwave heating,[126,127] carrying out the synthesis in a biphasic solvent mixture

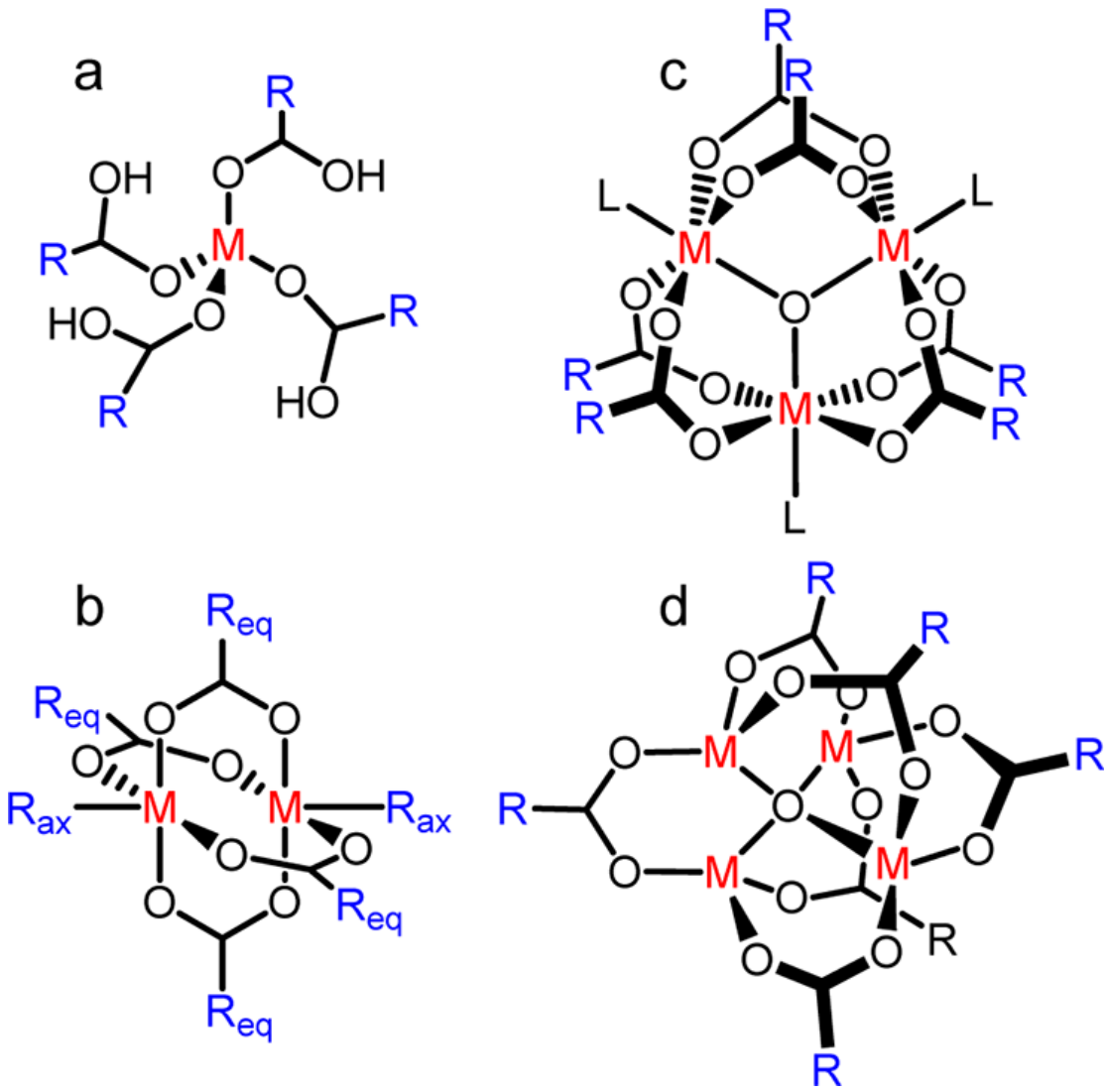

Figure 1.16: Some common SBUs used in reticular MOF synthesis: (a) A mononuclear tetrahedral center with four monodentate acetate ligands. (b) A dinuclear paddlewheel center with four bridging acetates and two axial ligands. (c) A trinuclear basic chromium acetate structure with six bridging acetates and three terminal ligands. (d) A tetranuclear basic zinc acetate structure with six bridging acetate ligands. Figure adapted from Reference 117.

with the product forming at the interface,[128] or even electrochemical approaches.[129] A striking feature of MOF synthesis is the fact that a periodic porous structure is formed without the need for adding any additional templates, as opposed to the synthesis of porous silica materials discussed in Section 1.1. The structure is rather determined by the coordinative geometry and connectivity of the inorganic and organic moieties, with the solvent acting as the template. Often, the solvent can be removed from the

final structure at low temperatures, keeping the framework intact and providing access to a highly porous material. In fact, the porosity (up to 90 % free volume) and surface area (up to over 6000 $m^2 g^{-1}$) of MOFs are often much higher than those of other porous materials.[130,131]

As already described for porous silica systems (see Section 1.1.2), there are two main concepts to endow a porous material with additional functionality. In the first approach, one of the building blocks is modified so that it carries a functional group (as for example in the co-condensation approach for functionalizing porous silica structures), in the second approach, the structure is synthesized first and then subjected to further transformations or post-synthetic modifications (PSMs).[132–134] These two concepts can in principle be applied analogously to MOFs. However, when following the first approach, finding the right synthesis conditions after replacing a linker molecule with a functionalized derivative can be tedious, especially if the functional group that shall be introduced can also coordinate the metal ions in the solution. Hence, the second approach, PSM, plays an important role for creating functionalized MOFs.

One of the conceptually simplest PSMs is an ion exchange. However, since the ions are embedded throughout the entire porous material, a complete exchange can take several days. A reversible anion exchange was shown by Fei *et al.* for copper and silver-based MOFs of the type M_2(4,4'-bipy)$_2$(EDS)·4H_2O (EDS = ethanedisulfonate) by stirring the MOF material in the corresponding salt solutions for several days.[135] A cation exchange could be demonstrated by Dinca *et al.*, who exchanged the charge-balancing Mn^{2+} guest ions in $Mn_3[(Mn_4Cl)_3(BTT)_8(CH_3OH)_{10}]_2$ (BTT = 1,3,5-benzenetristetrazolate) with Fe, Co, Ni, Cu, Zn, Li, and Cu by immersing the parent Mn MOF in concentrated methanolic solutions of the corresponding metal chloride salts for one month.[136]

Except for ion exchange, MOFs can in some cases also be post-synthetically modified by adding Lewis acids or Lewis bases. For Lewis acids, this was investigated for example by Wu *et al.*, who showed that titanium could be bound to free hydroxy groups of a hydroxy-functionalized binaphthyl bipyridine linker in a cadmium-based MOF after treatment with Ti(O^{i}Pr)$_4$,[137] while Kaye *et al.* demonstrated that chromium can bind *via* η^6 coordination to benzene rings in MOF-5.[138] For Lewis bases, the concept was demonstrated for example by Bae *et al.*, who showed that after removal of DMF from its axial positions of the Zn paddlewheel SBUs in a Zn-based MOF through heating under vacuum, pyridyl ligands could be grafted onto the unsaturated metal sites.[139]

Covalent PSMs on MOFs usually involve well-known organic reactions such as the formation of amide bonds between amine-functionalized linkers and organic anhydrides or isocyanates[140–142] or the azide–alkyne Huisgen cycloaddition ("click-reaction").[143–145]

1.2.2 Metal–Organic Frameworks in Sensor Applications

As discussed in the last section, MOFs feature an extremely high porosity, a huge structural variety and flexibility, and a high degree of tailorability. These properties make them interesting materials in a variety of applications, including gas storage and separation,[146–149] heterogeneous catalysis,[150–152] or even magnetic resonance imaging diagnostics.[153] Besides these applications, the potential of MOFs for detection and sensing of different analyte molecules has recently been investigated.[154,155] Important factors to consider for detection and sensing applications are sensitivity, selectivity, response time, material stability and reusability.

Due to their high porosity and surface area, MOFs are especially interesting for gas and vapor detection, since they concentrate analyte molecules in their interior which can lead to a high sensitivity.[155] Other factors that influence the sensitivity are the strength of the interaction of the analytes with the MOF scaffold, the dynamics of the analyte transport within the MOF, and the method of signal transduction. A large variety of different signal transduction schemes have been implemented for MOFs, including photo and radioluminescence, solvatochromism or vaporchromism, interferometry, localized surface plasmon resonance, and electromechanical sensors, such as quartz crystal microbalances, surface acoustic wave devices, or microcantilevers.

Photoluminescence describes the emission of light after bringing a molecule from its ground state to an excited state by absorption of a photon (see also Section 2.2), while in radioluminescence or scintillation the emission of short bursts of light are caused by absorption of ionizing radiation (energies typically $> 10\,\mathrm{eV}$). There are many examples in which luminescence is used as the signal transduction scheme, due to the fact that often aromatic molecules with conjugated π systems are used as the linker molecules in MOFs, and many of these systems show photoluminescence[156–163] (typically upon excitation with UV or blue light) or radioluminescence[164]. An example of how photoluminescence, host–guest interactions, the unique feature of coordinative bonds that connect the linker molecules to the metal ions, and a turn-on fluorescence signal transduction scheme are used for highly sensitive and selective fluoride detection in water is given in Chapter 6 of this thesis. Another luminescence type that has great potential as a read-out concept, namely chemiluminescence in a metal–organic

framework, is discussed in Chapter 5.

Solvatochromism[165] and vaporchromism[166] refer to a color change of a material when it is subjected to different solvents or vapors, often correlating with the polarity of the solvent or vapor. Typically, the effect is caused when the electronic transition that is responsible for the color of the material is accompanied by a charge transfer, which also causes a change of the dipole moment of the molecule when transitioning from the ground state to the excited state. This change in dipole moment means that the stabilizing effects of a polar solvent differ for the ground state and the excited state, resulting in a relative shift of the respective energy levels and hence a shift of the absorption spectrum of the material. Interferometry – in contrast to solvatochromism or luminescence – is not based on the absorption or emission of light, but rather on a change in the refractive index of a material. When a highly porous MOF is subjected to an analyte, the initially empty pores are filled with the analyte molecules, which causes a change of the refractive index of the material that can be monitored with interferometry or ellipsometry.[167] We demonstrated this concept for a one-dimensional metal–organic framework/titania photonic crystal (see also Sections 10.1 and 10.2).[168] Localized surface plasmon resonance can also be used to detect shifts of the refractive index by monitoring plasmon resonance frequency shifts of small copper, silver or gold nanoparticles upon changing their surrounding medium. When coating such nanoparticles with MOFs, the absorption of analyte molecules leads to a shift of the refractive index, which can then be detected as shifts in the visible extinction spectrum by localized surface plasmon resonance spectroscopy.[169]

Electromechanical sensors are based on a mass change upon adsorption of analytes inside the porous framework of a MOF host material. In the case of a quartz crystal microbalance[170,171], small changes in the resonance frequency of a vibration propagating perpendicular to the quartz surface is monitored, while in surface acoustic wave devices, changes in the frequency of acoustic waves traveling parallel to the sensor surface are used to detect mass changes after absorption of an analyte by a MOF coated on top of a sensor chip. Microcantilevers detect mass changes upon analyte absorption either *via* a change in the resonance frequency of a cantilevered beam or *via* a strain-induced deflection of the latter.[172]

Besides sensitivity, chemical selectivity plays an important role for analyte detection and sensing. Considering the porous nature of MOFs and their flexible pore and aperture sizes (see also Figure 1.15), "sieving" or size exclusion are probably the most straightforward tools that can be used to implement selectivity for certain analyte

species. Another approach is based on tailoring host–guest interactions by carefully choosing suitably modified linker molecules or by a post-synthetic modification of the framework structure. Lastly, a preferable interaction of analyte molecules with unsaturated metal sites can be used to implement chemical selectivity. In Chapter 6, a new approach based on competitive coordination chemistry to achieve very high selectivities is introduced. This example also demonstrates that another crucial point, namely the (in)stability of the porous material, can also be used to implement new ways of analyte detection, and that an apparent disadvantage of the material can be turned into an advantage and can be used to achieve high selectivities. Another factor that has to be considered besides the chemical stability is the thermal stability, which is typically lower for MOF materials (often below 350 – 400 °C)[116] than for other porous frameworks such as micro or mesoporous silica systems. When it comes to fast response times, diffusion processes within the porous systems often play an important role. Diffusion rates depend not only on particle size or film thickness of the sensor device, but also on host–guest interactions.

Even beyond sensor applications, diffusion is an important property of porous materials (see also Section 1.1), and Chapters 3 and 4 are dedicated to an in-depth diffusion study of single molecules within porous silica host structures.

Chapter 2

. . . . . .

Characterization and Patterning Techniques

2.1 Fluorescence Microscopy

Fluorescence microscopy is a special kind of conventional light microscopy (see Figure 2.1.a) which uses the principle of fluorescence to image the observed specimen.[173–175] For fluorescence to occur, a fluorophore is required that can be brought into an excited state through the absorption of light. This excitation results in electrons being promoted to short lived ($\approx 10^{-8}$ s) high energy states. Among other possible pathways, the energy set free by a relaxation back to the ground state can be dissipated by emission of a photon of the corresponding wavelength (see also Section 2.2). In standard down-conversion fluorescence, the wavelength of this photon is larger than that of the light that caused the excitation ("Stokes-Shift"), so filters can be used to separate the excitation light from the emission light (see Figure 2.1.b). Most typically, these filters are assembled in so-called filter cubes, consisting of an excitation filter, a dichroic mirror, and an emission or barrier filter. The excitation filter is usually a band-pass filter used to filter light with a wavelength suitable for excitation of the fluorophore from a white light source. If a monochromatic light source such as a laser is used instead, the filter can in principle be omitted. The excitation light that passed the excitation filter is then cast on a dichroic mirror at a 45° angle. A dichroic mirror changes its transmission and reflection properties depending on the wavelength of the incident light and can therefore be used to separate the excitation from the emission light. Ideally, the dichroic mirror in the filter cube is nearly 100 % reflective at the wavelength

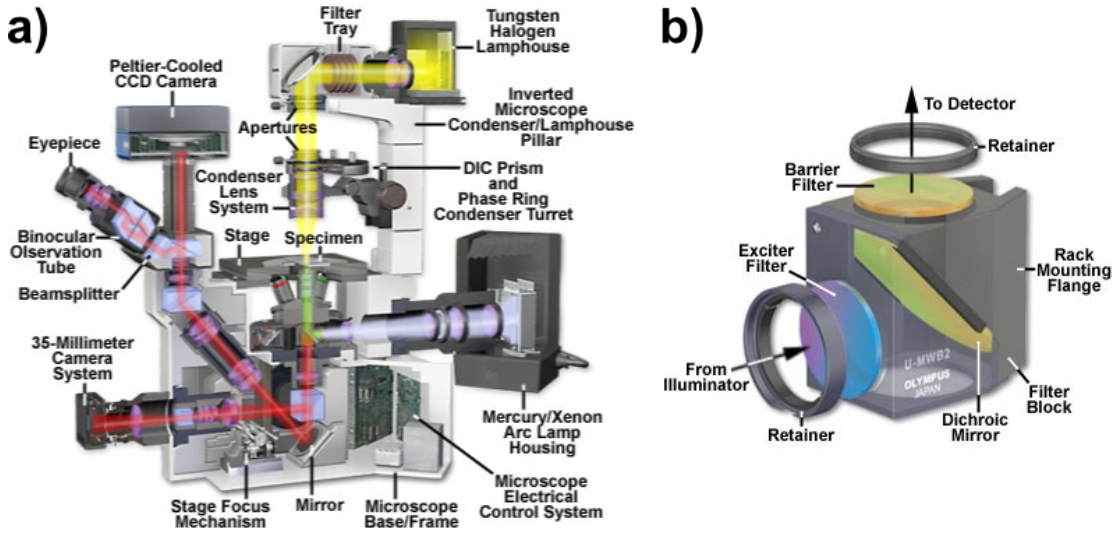

Figure 2.1: Basics of fluorescence microscopy. (a) Setup of an inverted fluorescence microscope[176]. (b) Filter cube[177].

range that can pass through the excitation band-pass filter and its transmission is close to 100 % for the light emitted from the fluorophore. After the excitation light is reflected off the dichroic mirror onto the sample, it causes emission of photons that have a different wavelength as the excitation light. The emitted photons can pass through the dichroic mirror (while scattered excitation light is reflected back to the light source) and through another band-pass filter (the emission or barrier filter) and reach the detector. Careful separation of the emitted light from the excitation light is crucial since the intensity of the excitation light is typically much higher than that of the emitted light. However, with a matching filter set, the technique can be very sensitive and even be suitable to detect single molecules (see below), since the light emitted from the sample is visualized against a virtually dark background.

For the research described in Chapters 3 and 4, single molecule fluorescence microscopy was extensively used for sample characterization. Highly sensitive detectors, very bright and stable fluorescent dyes, and highly clean samples make the observation of light emitted from one single dye molecule possible. Observation of single molecules can potentially give very detailed information on a specific measurement parameter, since it avoids the averaging usually done in conventional ensemble measurements. Although the light that is observed in these experiments is originating from one single dye molecule, the spot on the detector is much larger than the molecule itself. This is due to diffraction, resulting in an airy disk pattern observed on the detector with its broadening depending on the point spread function of the optical system. This intrin-

sic resolution limit is also known as the Abbe limit and can be written mathematically in the following form (for two objects in the focal plane):

$$d = \frac{0.61\lambda}{NA} \,. \tag{2.1}$$

where λ is the wavelength of the emitted light, NA is the numerical aperture of the objective, and d is the minimum distance of two objects that are to be resolved according to the Rayleigh criterion. The Rayleigh criterion states that two objects can be distinguished if the maximum of the airy disk of one object coincides with the minimum of the airy disk of the other object, which also gives rise to the constant factor of 0.61 in Equation (2.1). However, the positioning accuracy of the fluorophore in single molecule fluorescence microscopy can be much higher than that, in favorable cases only a few nanometers. Since the Abbe limit still holds, it is crucial to ensure that the distance between the single fluorophores that are detected satisfies Equation (2.1). In that case, one can be sure that the observed light is really originating from one single molecule, and hence the intensities observed on the detector are determined by the point spread function of the optical system. If there is little background and many photons are collected, the maximum of this function and hence the most likely position of the fluorophore can be determined very accurately by fitting an appropriate function to the data (see Figure 2.2). Theoretically, the angular intensity distribution of an airy disk resulting from a circular aperture can be described as

$$I(\theta) = I_0 \frac{2J_1(ka\sin\theta)}{ka\sin\theta} \,, \tag{2.2}$$

where I_0 is the maximum intensity of the airy disk, J_1 is the Bessel function of first kind of order one, k is the angular wave number, a is the radius of the aperture, and θ is the angle of observation, measured from the optical axis through the center of the aperture to the observation point. However, for the sake of simplicity, the data is usually modeled by a two-dimensional Gaussian function of the form

$$f(x, y, A, \sigma, x_0, y_0) = Ae^{-\left(\frac{x-x_0}{\sigma}\right)^2} e^{-\left(\frac{y-y_0}{\sigma}\right)^2} \,, \tag{2.3}$$

where x and y specify the position on the detector in pixels, and the fitting parameters A, σ, x_0 and y_0 represent the amplitude, a measure for the width of the point spread function, the center of the Gaussian in x direction, and the center of the Gaussian in y-direction, respectively. While the minimum width of the Gaussian is still determined

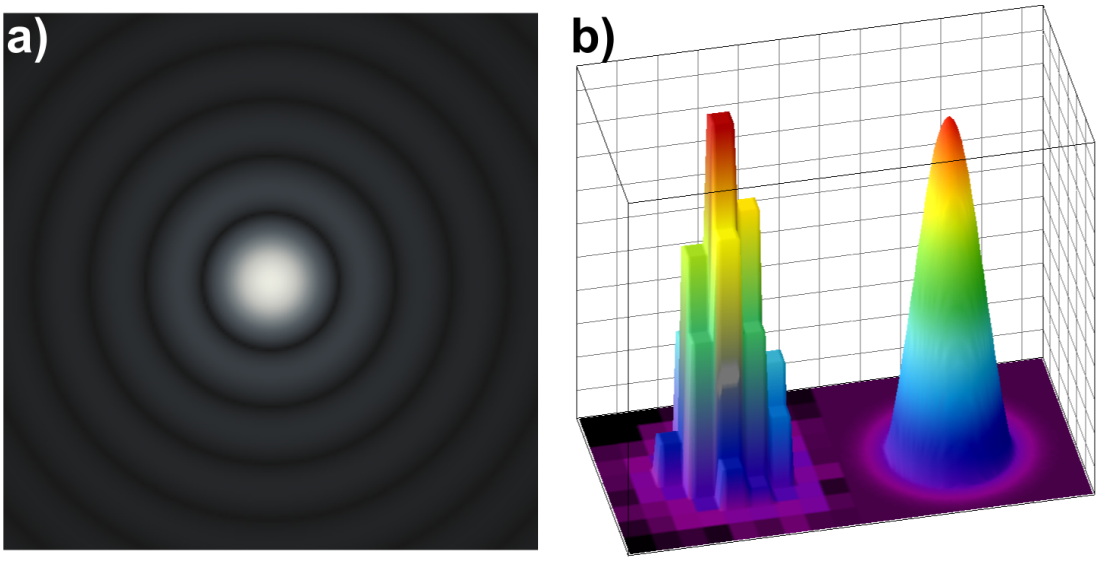

Figure 2.2: (a) Simulation of an airy disk pattern (the contrast was adjusted with a gamma value of 0.4 to emphasize the higher order maxima). (b) Representation of the raw pixel values of a fluorescence signal originating from a single molecule (left) and the plot of a two-dimensional Gaussian fit to the data (right).

by the limits imposed by the Abbe law, the standard error of the fitting parameters x_0 and y_0 and hence the positioning error can be very low, especially in the case of little background and a high number of collected photons, resulting in the above mentioned high positioning accuracy of a few nanometers. The standard error of the fitting parameters σ_i can be calculated from the χ^2 value of the fit and the covariance matrix $\boldsymbol{C}$ respectively the Jacobian $\boldsymbol{J}$ as follows:

$$\sigma_i = \sqrt{\chi^2 \cdot C_{ii}} \qquad \text{where} \qquad \boldsymbol{C} = \left(\boldsymbol{J}^T \boldsymbol{J}\right)^{-1} . \tag{2.4}$$

Once the positions of the dye molecules are determined, dynamic information such as trajectories or diffusion coefficients can be extracted from an image sequence by single molecule tracking. In order to do so, the positions of individual dye molecules are determined in every image of the sequence and then linked together forming trajectories. The linking can be difficult, especially if molecules blink, bleach, or the paths of two or more molecules intersect in one frame. However, once the tracking is done, detailed information about the structural and dynamical properties of the host–guest system can be obtained, as demonstrated in Chapters 3 and 4.

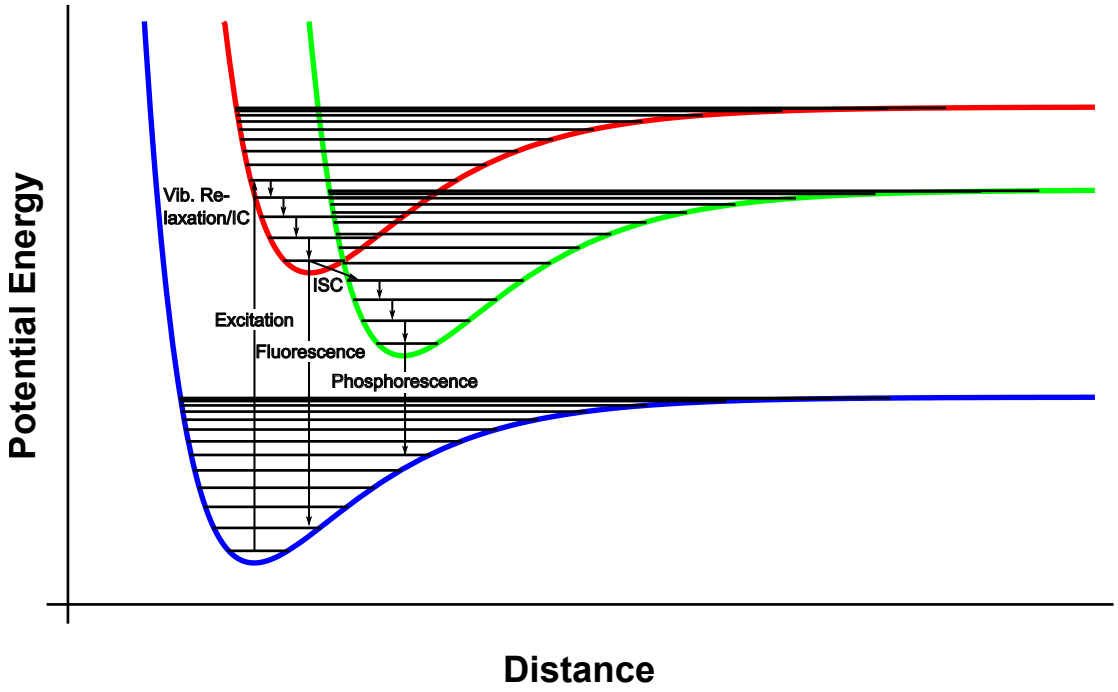

Figure 2.3: Schematic overview of different transitions between potential energy surfaces in a luminescent system.

2.2 Luminescence Spectroscopy

In luminescence spectroscopy, the light emitted from a luminescent system is recorded in a temporally and spectrally resolved way.[178,179] One of the most well-known luminescence processes is photoluminescence (PL), in which the absorption of a photon excites a luminescent system into higher energy states. If the excitation is caused by a chemical reaction rather than by the absorption of light, the process is called chemiluminescence (CL). In both cases, the energy for returning to the ground state is dissipated at some point through the emission of a photon.

Photoluminescence can be divided into fluorescence (see also Section 2.1) and phosphorescence, depending on the internal mechanism and the lifetime of the excited states before the emission of the photon. A schematic overview of different internal processes can be found in Figure 2.3.

Fluorescence is a fast process, with a lifetime of the excited state of typically $\leq 10^{-8}$ s. On the other hand, phosphorescence is a phenomenon that usually appears at time scales $\gg 10^{-8}$ s, sometimes up to minutes or even hours. The difference in kinetics of the two processes is due to different internal transitions between potential energy surfaces (PESs) preceding the light emission. Both processes are initiated by

the absorption of a photon that causes the excitation of the system from the ground state to an electronically excited state. From there on, the energy can be dissipated by different mechanisms. Nonradiative transitions usually involve energy dissipation from the excited system to its surroundings or "internal conversion" (IC) in which a vibrational state of the electronically excited PES couples to a vibrational state of a lower-energy PES (typically the ground state). A third possible mechanism is "inter-system crossing" (ISC), in which the system passes from an excited PES to another one with a different spin multiplicity. In order to make such a process possible without violating selection rules, spin-orbit coupling is usually required, so that these processes often play a more important role in systems involving heavy atoms. After the system reaches the vibrational ground state of the excited PES by the radiationless processes described above, further relaxation back to the ground state PES is accompanied by a radiative transition, i.e., the emission of a photon. In the case of fluorescence, this transition occurs between two PESs with the same spin multiplicity, while in the case of phosphorescence, the spin multiplicity has to change once again, resulting in the different kinetics of the two processes. Chemiluminescence often also involves ISC processes. Under certain conditions (e.g., the presence of particular substances or surroundings) a non radiative de-excitation of the luminescent system from an excited PES to the ground state PES can be favored. This process is known as quenching.

Within the scope of this work, fluorescence not only played an important role in fluorescence microscopy experiments (see Section 2.1 and Chapters 3 and 4), but also for the investigations described in Chapter 6. Chemiluminescent properties were investigated in the project described in Chapter 5.

2.3 Scanning Electron Microscopy

As already described in Section 2.1, the Abbe limit imposes a restriction to the maximum resolution that can be obtained with an optical microscope. In order to image very small features (smaller than about half the wavelength of visible light), an electron microscope can be used.[179,180] Since the resolution in microscopy is proportional to the wavelength of the electromagnetic wave used to image a specimen (see Equation (2.1)), waves of short wavelengths are needed. Using the de Broglie relation describing the quantum mechanical effect of particle-wave duality, the wavelength of an electron

beam can be estimated by:

$$\lambda = \frac{h}{p}\,, \tag{2.5}$$

where λ is the wavelength, h is Planck's constant and p is the momentum. Assuming an acceleration voltage of $U = 5000\,\mathrm{V}$, which leads to a kinetic energy of $5000\,\mathrm{eV} = 8.01 \times 10^{-16}\,\mathrm{J}$, the momentum can be estimated to be $p \approx 3.82 \times 10^{-23}\,\mathrm{kg\,m\,s^{-1}}$, which gives a wavelength of

$$\lambda \approx 17.3\,\mathrm{pm}\,.$$

Compared to optical microscopy which uses visible light with a wavelength of roughly 400 nm to 800 nm, the resolution that can theoretically be achieved with an electron microscope is at least four orders of magnitude higher.

In a scanning electron microscope primary electrons are accelerated by an anode and then focused by several coils on the specimen, scanning the latter line by line.[180] In general, the electrons are generated from a tungsten filament inside the electron gun by thermionic emission or field emission. Then they are accelerated by an anode to a kinetic energy which is typically between several hundred and a few ten thousand electron volts and focused by condenser lenses to a diameter typically between 0.5 nm and 5 nm. The collimated beam then passes through deflector plates or scanning coils, which scan it in a raster pattern over the specimen surface. Depending on the nature of the substrate and the energy of the primary electrons, different processes can occur when the electron beam hits the surface of the specimen. Primary electrons hitting the surface can be reflected by elastic scattering or they can cause ionization of atoms in the surface resulting in low energetic secondary electrons (inelastic scattering, when interaction with outer shell electrons occurred) or the emission of electromagnetic radiation (in particular X-rays when interaction with inner shell electrons occurred). An overview of the different processes that can occur when the primary electron beam hits the sample is given in Figure 2.4.

Unlike in optical microscopy, the magnification of an SEM does not depend on the power of a magnification lens. Here, the objective and condenser lenses inside the electron column are rather used to focus the beam to a small diameter. In an SEM, the primary electron beam rastering the surface is synchronized with a display and the resulting image is obtained by mapping the intensity of the detected signal while scanning to the screen. The magnification can therefore be controlled by altering the

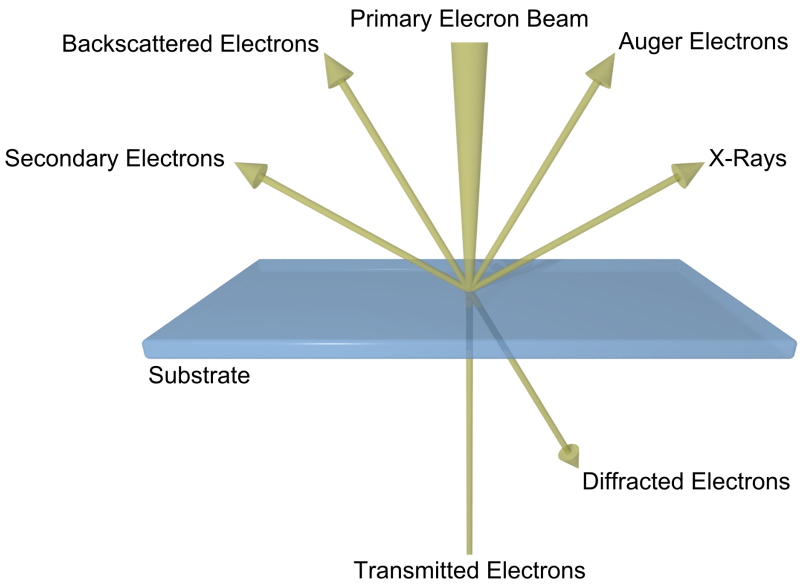

Figure 2.4: Overview of the different processes that can occur when the primary electron beam hits a sample.

size of the region scanned by the primary electron beam. Decreasing the x- and y-dimensions of this area results in a higher magnification. A schematic picture of the setup of an SEM is given in Figure 2.5.

In this work, SEM was used for structural characterization of the samples presented in Chapters 3 – 8.

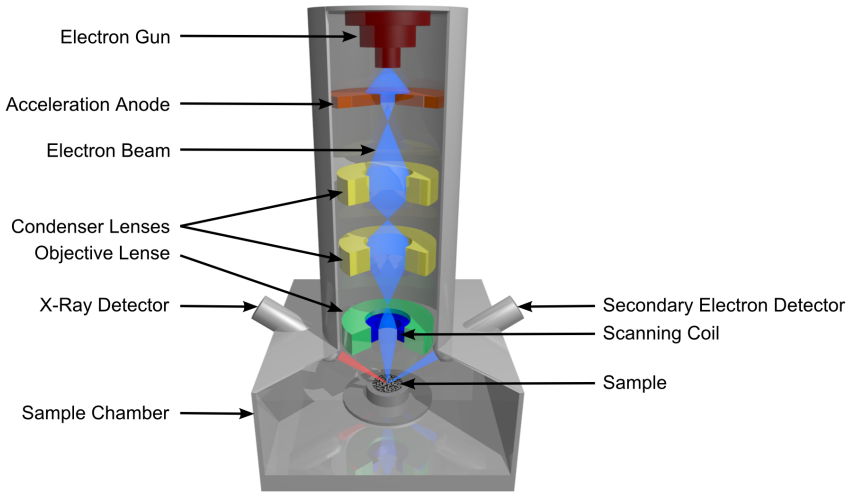

Figure 2.5: Schematic setup of a scanning electron microscope.

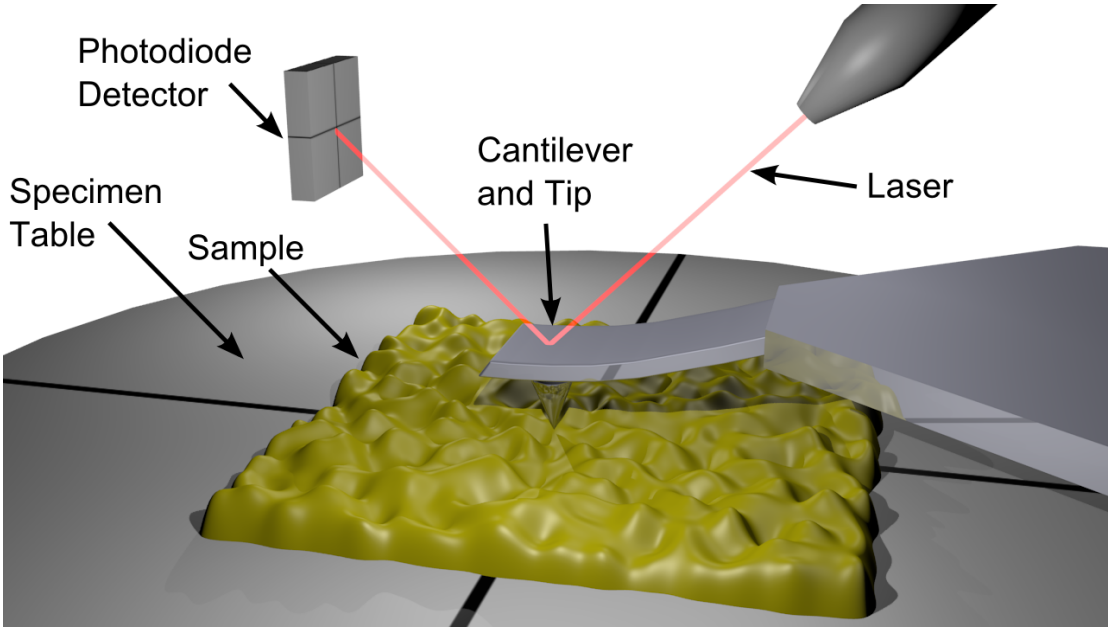

Figure 2.6: Schematic setup of an Atomic Force Microscope.

2.4 Atomic Force Microscopy

Atomic Force Microscopy (AFM) is another imaging method that allows for high resolution imaging at the nanoscale level.[181,182] Unlike SEM, it does not require conductive samples, there are no beam damages and no ultra-high vacuum (UHV) conditions, and the topographic information that is obtained resembles the three-dimensional surface topology rather than just giving a two-dimensional projection. However, the scan size is considerably smaller than in SEM, image acquisition typically takes much longer, and imaging artifacts can make data interpretation more difficult.

For AFM imaging, a sharp tip at the end of a cantilever is scanned over the surface of the sample. Forces (mainly Coulomb and Van-der-Waals forces) between the tip and the sample cause a deflection of the cantilever, which is measured by monitoring a laser that is reflected off the backside of the cantilever onto a photodiode detector (see Figure 2.6 for a schematic representation).

There are different measurement modes available for an AFM. The first one is the contact mode. Here, the tip of the cantilever is in close contact with the sample at all times while scanning the surface. In constant height mode, the height of the cantilever is left unchanged and the topographic information is gained from the deflection of the cantilever. In modern AFMs, usually a constant force mode is used in which the position of the laser on the photodiode is fed into a feedback loop that controls piezo

crystals to adjust the distance between the sample and the tip such that the deflection of the cantilever stays constant. In non-contact mode, the cantilever is kept a few 10 to 100 nm above the sample surface while it is excited to oscillate at a frequency close to its resonance frequency. Topography changes are reflected in a change of the oscillation amplitude, which is again fed into a feedback loop controlling the sample-tip distance. A third operation mode is the tapping mode, which can be considered an intermediate between contact mode and non-contact mode. In tapping mode, the cantilever is also oscillating while scanning the surface, however, in this mode the tip-sample distance is much smaller so that the tip touches the surface during oscillations.

Apart from gaining three-dimensional topographical information of the sample surface, an AFM can also be used to gather information about material contrast on the sample surface. In contact mode, lateral force microscopy (LFM) can be used for this purpose, while phase imaging is available in non-contact mode. In LFM, the tilting of the cantilever along its long axis is monitored additionally to its deflection. This tilting gives information about changes in friction on the sample surface and can hence help to distinguish different materials. In phase imaging, the phase shift of the cantilever response relative to its driving oscillation is observed, which also gives feedback about different materials on the sample surface.

Within the scope of this thesis, AFM imaging was used for characterization of the structures shown in Chapters 3, 4 and for the characterization of (patterned) self-assembled monolayers (SAMs) in Chapter 8.

2.5 X-Ray Diffraction

X-ray diffraction (XRD) can be used to obtain information about the structural parameters and the symmetry in periodically arranged matter.[179] It relies on the interaction of X-rays with periodic variations of electron densities defining lattice planes. Since the lattice constants are in the same order of magnitude as the wavelength of the X-rays that are used for the XRD experiment (typically Cu-K_α radiation with a wavelength of $\lambda = 1.540\,562$ Å), diffraction can occur. The Bragg equation defines the condition that has to be satisfied in order to obtain constructive interference (see also Figure 2.7):

$$2d \sin\theta = n\lambda\,. \tag{2.6}$$

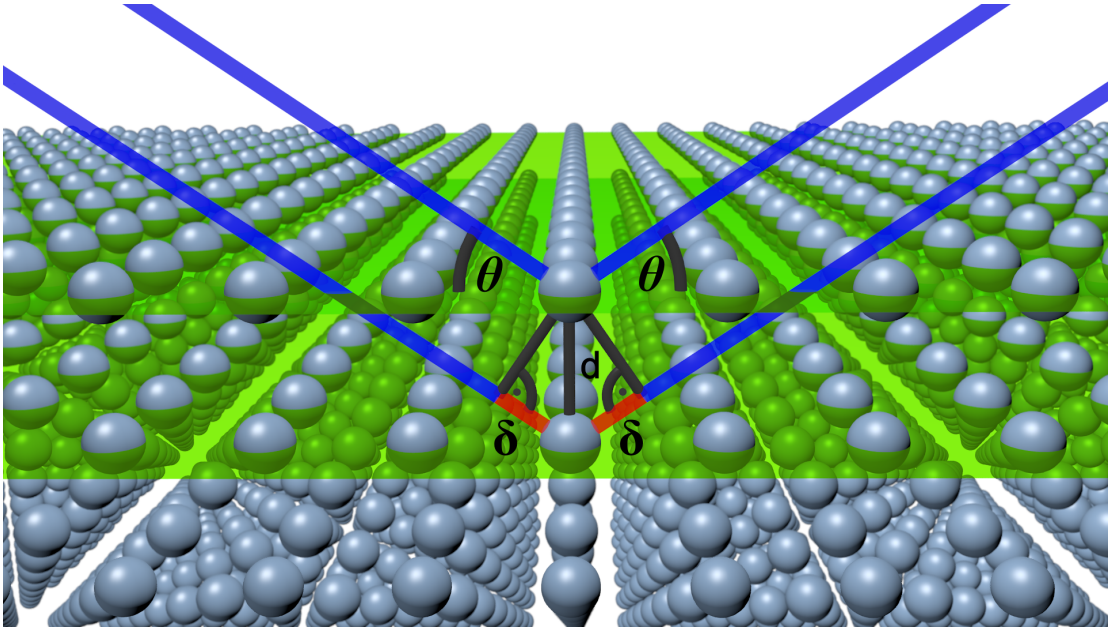

Figure 2.7: Schematic illustration of the Bragg condition.

Here, d denotes the distance of the lattice planes, θ is the angle of incidence of the X-rays, n is an integer number, λ corresponds to the wavelength of the X-rays that are used, and $2d \sin\theta = 2\delta$ is the path difference of two beams. The Bragg equation reflects the fact that constructive interference can only occur if the path difference is an integral multiple of the wavelength.

The width of the reflexes depends on the size of the crystalline domains, as described by the Scherrer equation:[183]

$$d = \frac{K\lambda}{\beta \cos\theta} \,. \tag{2.7}$$

Here, d denotes the size of the crystalline domains, K is a dimensionless shape factor (its exact value depends on the shape of the crystalline domains, but typical values are approximately 0.9), λ corresponds to the wavelength of the employed X-rays, β represents the line broadening (full width at half maximum in terms of degrees 2θ), and θ is the Bragg angle. The reflex intensity depends on the scattering volume, which is usually small for small domains. In thin film measurements, the domain sizes and the scattering volume are limited by the thickness of the film, which also limits the sharpness and intensity of the observed reflections.

The XRD patterns in this work were measured in Bragg-Brentano- or $\theta-\theta$-geometry. In this setup, the (flat) sample is kept stationary, and the detector and the X-ray tube

are moved around the sample on two arms of a goniometer at the same angle. When this geometry is used, only reflections caused by lattice planes parallel to the substrate plane can be observed. Since the thin films examined in this work usually show a specific alignment of the pores with respect to the substrate plane (e.g., the [0,1]-direction in 2D-hexagonal mesoporous silica), often only one reflex (and its higher orders) can be observed. In powder samples, the orientation of the lattice planes with respect to the substrate plane is random, and so typically all reflections can be observed.

If the distance between the lattice planes is rather large, the diffraction pattern will feature reflexes at small angles (because of the reciprocal relationship between d and $\sin\theta$, see Equation (2.6)). This can often be observed in mesoporous materials in which the material itself does not feature a crystalline order (for example silica), but the pores are arranged in a periodic manner. On the other hand, the lattice constants of a crystalline material in which the crystallinity results from a periodic arrangement of atoms or molecules are typically smaller and hence give rise to reflections at higher angles. Typically, measurements in the range of 0.5 to 10° 2θ are referred to as small angle X-ray scattering (SAXS), while measurements at angles $>$ 10° 2θ up to 100° 2θ or more are called wide angle X-ray scattering (WAXS).

SAXS was used within the scope of this work for characterization of the thin silica films presented in Chapters 3 and 4, while WAXS was used to confirm the crystallinity and the correct phase of the materials discussed in Chapters 5 and 6.

2.6 Infrared and Raman Spectroscopy

Infrared (IR) and Raman spectroscopy can both be used to obtain information about functional groups that are present in a sample by exciting vibrational transitions of chemical bonds.[178,179,184] The energetic difference between two vibrational states is often characteristic for a specific bond or functional group. Typically, vibrational transitions with an energy ranging from 400 to 4000 cm^{-1} are recorded. In the near infrared (NIR) region (0.8 µm to 2.5 µm, 12 800 cm^{-1} to 4000 cm^{-1}), usually higher harmonics of vibrations can be found, while in the mid infrared (MIR) region (2.5 µm to 50 µm, 4000 cm^{-1} to 200 cm^{-1}) fundamental vibrations occur, and the far infrared (FIR) region (50 µm to 1000 µm, 200 cm^{-1} to 10 cm^{-1}) usually features phonon modes or rotations.

In older, dispersive IR instruments, light from a polychromatic IR light source was

passed through a monochromator and then through the sample, and the absorbance was measured by comparing the light intensity to a reference beam. However, today usually Fourier transform infrared spectroscopy (FTIR spectroscopy) is used, in which polychromatic IR light is passed through a Michelson interferometer and then through the sample, followed by a background subtraction and a Fourier transform to calculate the spectrum from the recorded interferogram. This procedure has the advantage of a better signal-to-noise ratio (SNR), higher accuracy, and faster measurements.

In order for a vibration to be IR active (i.e., the IR vibrational transition is allowed through absorption of light), the dipole moment of the molecule has to change during the vibration. This can be explained in analogy to a Hertzian dipole in which the dipole interacts with electromagnetic radiation. In terms of quantum mechanics this condition is satisfied if the expectation value of the dipole moment operator $\hat{\boldsymbol{\mu}}$ is different from zero,

$$\langle \hat{\boldsymbol{\mu}} \rangle = \int \psi_1 \hat{\boldsymbol{\mu}} \psi_2 d\mathbf{r} \neq 0 \,, \tag{2.8}$$

where ψ_1 and ψ_2 represent the wave functions of the vibrational states between which the transition occurs. In terms of group theory, this condition states that the direct product of a representation of the symmetry of the ground state, the dipole moment operator, and the excited state has to contain the totally symmetric representation of the corresponding point group. In the case of a harmonic oscillator, there is also the quantum mechanical selection rule that the vibrational quantum number v has to change by $\Delta v = \pm 1$. This can be seen from Equation (2.8), the orthonormality of the eigenfunctions of the harmonic oscillator, and the following recursion formula for the Hermite polynomials:

$$x H_v(x) = v H_{v-1}(x) + \frac{1}{2} H_{v+1}(x) \,. \tag{2.9}$$

The fact that (weak) overtones can be observed in IR spectroscopy is due to anharmonicities in the oscillator's potential.

In Raman spectroscopy, there are different selection rules, so that data from Raman spectra often complement data from IR spectra (and vice versa). Namely, the polarizability rather than the dipole moment of the molecule has to change during Raman scattering in order for a vibration to be Raman active. The difference in the selection rules is based on the fact that the Raman process is a scattering process rather than a direct transition between two vibrational states. It occurs when a molecule absorbs

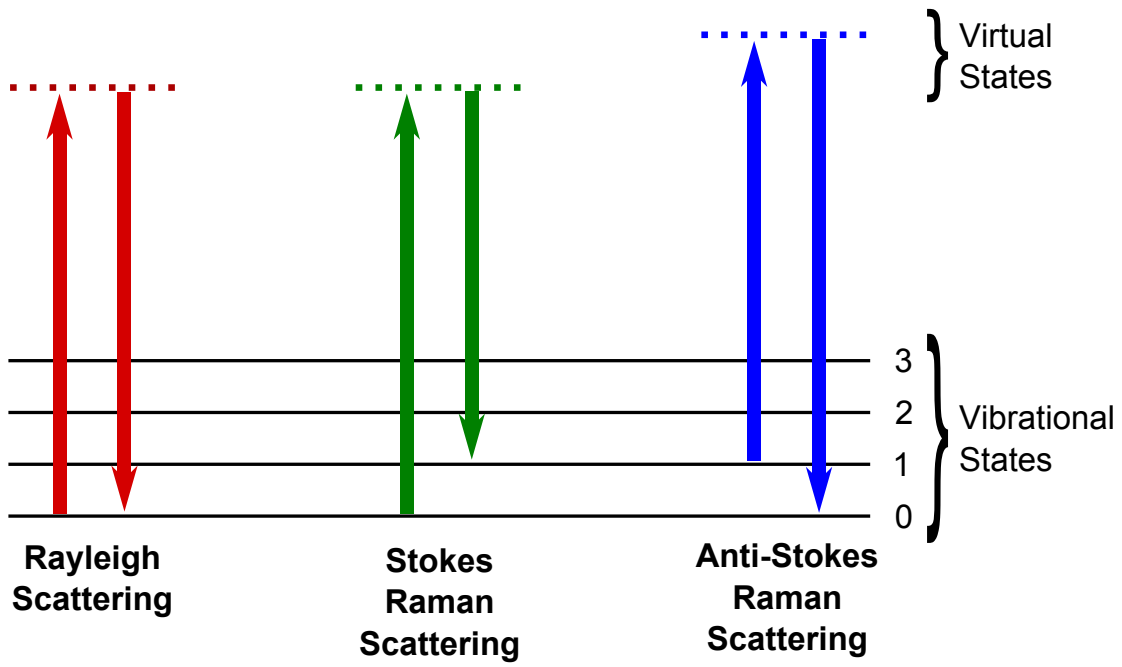

Figure 2.8: Schematic illustration of the different transitions and the resulting types of scattering.

light and is thereby excited to a virtual state, which relaxes immediately back to a (real) lower energy state. If the relaxation takes the system back to its initial state, the emitted photon has the same energy as the absorbed photon. This elastic scattering process is called Rayleigh scattering. If however the relaxation takes the system to a state that is higher or lower in energy than the initial state, an inelastic scattering process called Stokes respectively Anti-Stokes Raman scattering takes place, and a photon of lower respectively higher energy than the absorbed photon is emitted. Due to the relatively low population of vibrationally excited states, the intensity of the Stokes Raman scattering is typically much higher than that of the Anti-Stokes Raman scattering, and that is why these photons are usually used in Raman spectroscopy. The different transitions and the resulting types of scattering are summarized in Figure 2.8.

IR and Raman spectroscopy were used to investigate the samples discussed in Chapters 5 and 6 of this work.

2.7 Thermogravimetric Analysis and Differential Scanning Calorimetry

Thermogravimetric analysis (TGA) measures the weight loss of a sample subjected to a defined heating ramp over time.[185] During the heating, different processes can occur that are reflected in a weight loss of the sample. Most important for porous materials are desorption, decomposition, and combustion processes. Due to their high porosity and high specific surface area, porous materials can often accommodate a considerable amount of adsorbed volatile compounds that can be desorbed at elevated temperatures. This process is accompanied by a weight loss of the sample. At even higher temperatures, the framework of the material can decompose, or organic groups can be combusted (if the TGA measurement is carried out in synthetic air). To avoid a combustion of organic moieties, the measurements can also be carried out in an inert atmosphere (e.g., under nitrogen gas).

In order to distinguish combustion processes from desorption processes, differential scanning calorimetry (DSC) can be carried out simultaneously with the TGA measurement.[185] In DSC, the amount of heat that is required to increase the temperature of the sample is compared to that of an inert reference material as a function of temperature, giving information about whether a weight loss step observed in TGA is related to an endothermic or an exothermic process. While weight losses caused by desorption processes are endothermic, weight losses connected to combustions are exothermic.

In this work, TGA and DSC were used to determine the thermal stability of the compounds discussed in Chapters 5 and 6.

2.8 Nitrogen Sorption Analysis

As already briefly mentioned above, sorption processes play an important role for porous materials due to the high porosity and high surface area of the latter. Nitrogen sorption analysis can be used to obtain information about the pore volume, the specific surface area, and the pore size distribution (PSD) of a sample.[186,187] During a nitrogen sorption experiment, the volume of adsorbed nitrogen is recorded at different relative pressures p/p_0 (with p being the absolute pressure and p_0 being the saturation vapor pressure) at constant temperature (usually at the boiling point of liquid nitrogen), giving adsorption and desorption isotherms. These isotherms can be classified

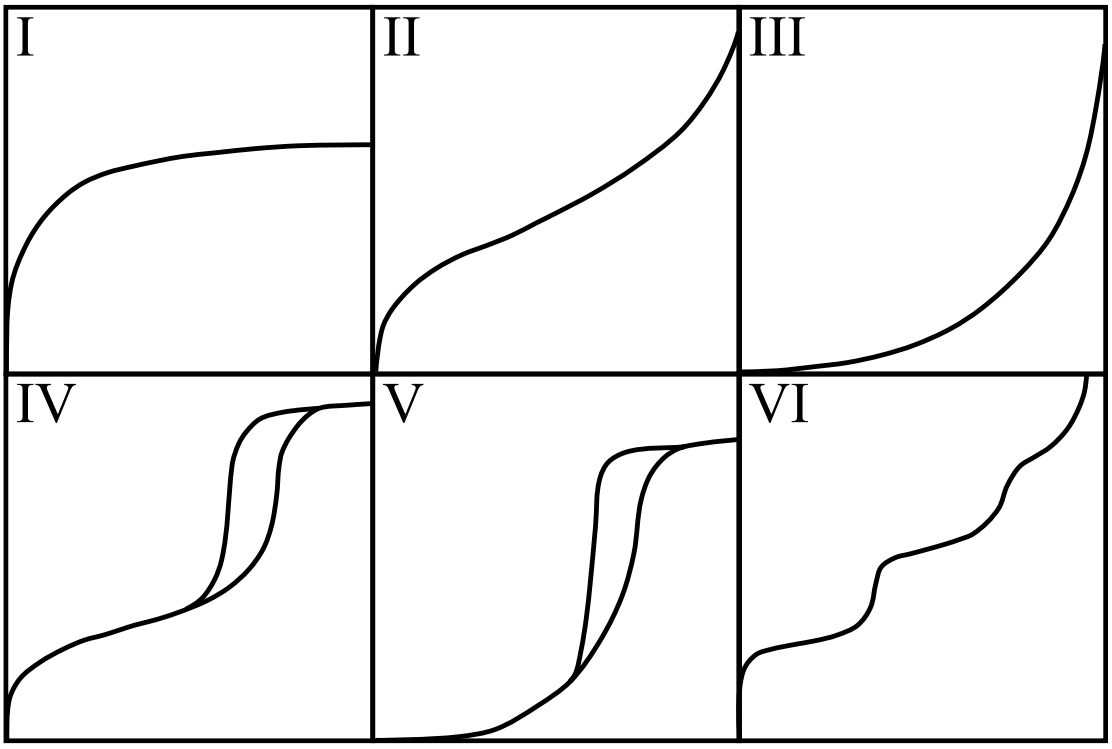

Figure 2.9: The six major types of sorption isotherms according to IUPAC. Reproduced after Reference 186.

according to IUPAC as six major types, each typical for a certain class of materials (see Figure 2.9 and Table 2.1).

Isotherm Type	Corresponding Material
Type I	Microporous material/chemisorption
Type II	Non- or macroporous material, high adsorption enthalpy
Type III	Non- or macroporous material, low adsorption enthalpy
Type IV	Mesoporous material, high adsorption enthalpy
Type V	Mesoporous material, low adsorption enthalpy
Type VI	Nonporous, uniform material, layer-by-layer adsorption

Table 2.1: The six major types of sorption isotherms according to IUPAC and typical examples of materials that give rise to these isotherms.

The classification into micropores, mesopores and macropores depends on the pore diameter. According to IUPAC,[186] pores with a diameter $\leq 2\,\text{nm}$ are called micropores. If the pore width is between 2 and 50 nm, the corresponding pores are called mesopores, and pores with a width $\geq 50\,\text{nm}$ are called macropores.

The pore size can be obtained from the recorded isotherms by different methods.

One standard method was developed by Barrett, Joyner, and Halenda (BJH method). This method is based on a modified form of the Kelvin equation[187]

$$RT \ln\left(\frac{p}{p_0}\right) = 2\sigma V_m r_k \,, \tag{2.10}$$

and hence also suffers from its applicability issues and limitations. The Kelvin equation describes the relative vapor pressure p/p_0 over a curved surface, with R being the universal gas constant, T the absolute temperature, σ the surface tension, V_m the molar volume, and r_k the radius of the hemispherical meniscus. Assuming a certain pore geometry, the BJH method can be used to describe the capillary condensation in the pores. However, it usually fails to describe the pore widths of small pores such as micropores or small mesopores accurately, since the thermodynamic model of a smooth liquid-solid interface and a bulk-like pore fluid no longer holds for these kinds of pores.

More recent methods to calculate pore size distributions from the recorded isotherms are based on microscopic methods such as non-local density functional theory (NLDFT) or grand canonical monte carlo simulations (GCMC simulations). These methods use a microscopic model to accurately describe the local fluid structure in the proximity of curved interfaces. The resulting pore widths are accurate for micropores up to large mesopores, and hence this method was used to calculate PSDs from the sorption isotherms presented in this thesis.

In addition to calculations of the PSD, the isotherms also allow for the determination of the substrate's specific surface area. The most commonly used method is based on a model described by Brunnauer, Emmett, and Teller (BET). This model is an extension of the Langmuir equation that describes monolayer adsorption:[188]

$$\frac{n^a}{n_m^a} = \frac{Bp}{1+Bp} \,. \tag{2.11}$$

Here, n^a is the adsorbed amount, n_m^a corresponds to the monolayer capacity, p describes the pressure, and B is a constant depending on the equilibrium constant K of the sorption process. In this model, the following assumptions are made:

- There is only monolayer adsorption.
- All sorptive sites are equal and the surface is uniform.
- There are no interactions between neighboring adsorption sites or particles.

The BET model extends this model to include multilayer adsorption:[187]

$$\frac{p}{n^a\,(p_0 - p)} = \frac{1}{n_m^a C} + \frac{(C-1)}{n_m^a C} \cdot \frac{p}{p_0}\,. \tag{2.12}$$

The newly introduced constant C is related exponentially to the enthalpy (heat) of adsorption in the first adsorbed layer,[186] the meaning of the other parameters is the same as above. The BET model makes the following additional assumptions:

- The adsorption enthalpy of all multilayer adsorption processes is the same, i.e., only the first layer has a distinct adsorption enthalpy due to its interaction with the substrate, while the adsorption enthalpy of all the following layers only depends on the interaction with the monolayer directly underneath it.

- There is no limit to the number of layers that can be adsorbed.

Although these assumptions do not always hold in real systems, the BET method is the standard method for calculating surface areas, and it was also used for surface area calculations in this work.

2.9 Nuclear Magnetic Resonance Spectroscopy

Nuclear magnetic resonance (NMR) spectroscopy gives information about the electronic environment of individual atoms and the interactions with their neighboring atoms.[179,184] It relies on the interaction of the magnetic moment of a nucleus with an electromagnetic field in the presence of strong magnetic fields. Since the magnetic moment of a nucleus results from its spin I, only isotopes possessing a non-zero nuclear spin can be examined.

In the presence of external magnetic fields, a preferential axis is introduced, and according to quantum mechanics, the magnetic moment resulting from the spin of the nucleus can only assume certain orientations relative to this axis, as described by the magnetic quantum number m_I. If the preferential axis is the z axis, the values $m_I\hbar$ describe the eigenvalues of the z component of the angular momentum. m_I can only take values ranging from $-I$ to $+I$, resulting in a total of $2I + 1$ angular momentum states. In the absence of an external magnetic field, all these states are degenerate. However, if an external magnetic field is present, the energies corresponding to these states split up in a process called Zeeman splitting, and the energetic difference ΔE

between two states becomes

$$\Delta E = \hbar\gamma B_0 = \hbar\omega_0 \,, \tag{2.13}$$

where γ denotes the gyromagnetic ratio (i.e., the proportionality factor of the angular momentum or spin of a nucleus and the resulting magnetic moment) and B_0 corresponds to the (local) magnetic field at the nucleus. The product of both, ω_0, is called the Lamor frequency, which is in the range of radiofrequencies of the electromagnetic spectrum. NMR spectroscopy uses the fact that the Lamor frequency and hence also the resonance frequency to trigger transitions between two angular momentum states depends on the local magnetic field B_0 at a given nucleus, which can differ from the external magnetic field depending on the electronic surrounding or magnetic interactions with neighboring nuclei and is therefore characteristic for the environment of that nucleus.

In old NMR devices, resonance was achieved by either keeping the externally applied magnetic field constant while varying the frequency of an alternating high-frequency electromagnetic field (continuous field method), or by keeping the frequency of the alternating electromagnetic field constant while varying the strength of the externally applied magnetic field (continuous wave method). In modern NMR devices, (short) radiofrequency pulses are used to excite the NMR transitions of all the nuclei at once. The bandwidth that can be excited with the short radiofrequency pulse is inversely proportional to the pulse duration. By tuning the power and the duration of the pulse, the net magnetization vector is tilted away from its equilibrium position to the plane perpendicular to the externally applied magnetic field. When the pulse ends, each nucleus precesses about the externally applied magnetic field vector at its own Lamor frequency. The vector sum of these oscillations, known as FID (free induction decay) is picked up via electromagnetic induction by the same coil that sent out the radiofrequency pulse. Fourier transform of the FID converts the spectrum from the time domain to the frequency domain, extracting the individual Lamor frequencies from the sum recorded in the FID and yielding the NMR spectrum.

There are two main relaxation mechanisms in NMR spectroscopy, namely the spin-lattice or longitudinal relaxation T_1 and the spin-spin or transversal relaxation T_2. The T_1 relaxation describes the relaxation of the spin from its excited state back to the ground state by dissipation of energy as heat. The T_2 relaxation describes the dephasing of the transversal magnetization due to entropic effects, triggered by

random fluctuations of the local magnetic field (if there are further inhomogeneities in the magnetic field because of differences in susceptibility within the sample or inhomogeneities in the externally applied magnetic field, the process is sometimes called T_2^* relaxation). This form of relaxation does not dissipate any energy, but causes the decay of the transversal magnetization observed in the FID.

NMR spectroscopy was used in this thesis to characterize the aluminum and fluoride complexes that were investigated in Chapter 6.

2.10 Dynamic Light Scattering

Dynamic light scattering (DLS) can be used to gain information about the hydrodynamic radius of particles in a colloidal suspension.[189,190] This is done by measuring the Brownian motion of the particles and correlating it to the particle size.

When the particle size is small compared to the wavelength of the incident light, Rayleigh scattering can occur (see also Section 2.6), and when a coherent light source such as a laser is used, interference of the scattered light leads to intensity variations that are recorded by a detector. Since the particles in solution are constantly moving due to Brownian motion, the interparticle distance changes constantly, and with it the conditions for constructive and destructive interference, resulting in time dependent intensity fluctuations of the scattered light. Since the diffusion of small particles is faster than that of larger ones, the intensity of the scattered light will change more rapidly for small particles than for large particles.

In a DLS experiment, these intensity changes are recorded over time, and a second-order auto-correlation function is generated from the resulting intensity traces:

$$g^{\mathrm{II}}(q,\tau) = \frac{\langle I(t)I(t+\tau)\rangle}{\langle I(t)\rangle^2} \,. \tag{2.14}$$

Here, q corresponds to the wave vector, I denotes the intensity, and τ is the time delay. This auto-correlation function can be used to obtain single-exponential decays related to the translational diffusion coefficients of differently sized particles in a polydisperse sample (in a perfectly monodisperse sample, only one single-exponential decay would be obtained). The diffusion coefficients D themselves depend on the hydrodynamic

particle size d, as described by the Stokes-Einstein equation for spherical particles:

$$D = \frac{k_B T}{3\pi\eta d} \,. \tag{2.15}$$

Here, k_B is the Boltzmann constant, T corresponds to the temperature, and η is the viscosity of the solvent.

2.11 Photolithography

In general, photolithography is used to write patterns on a substrate using selective exposure of a photosensitive component (photoresist) to light, typically by shining UV light through a shadow mask or by using a laser in a direct writing process.[191] Photolithography is commonly used in semiconductor manufacturing and for the production of micro-electro-mechanical-systems (MEMS). In this project, the technique was used for the production of masters needed for PDMS replica molding (see Section 2.12) and for the direct patterning of substrates themselves (see Chapter 7). An overview of the exact processing conditions of the different photoresists used in the framework of this thesis is given in Table 10.7 in the appendix.

2.11.1 "Standard" Photolithography

In "standard" photolithography, a mask aligner is used to gently press the substrate against the shadow mask (typically chromium on quartz glass) and then expose the resist through this mask with uniform, high-intensity UV light. Further processing and development steps finally yield the pattern of the mask transferred into the resist. There are three main types of photoresists: positive resists, negative resists and image reversal (IR) resists, which will be discussed in more detail in the following sections. The patterning in all these resists results from changing the solubility of the resist in a developer due to light exposure and heating steps.

Positive Resist

In a positive resist, regions that were exposed to light are rendered soluble in the developer, resulting in a positive image of the mask pattern (i.e., features visible on the mask will result in photoresist features on the substrate, while transparent parts of the mask will not produce any photoresist features).[191,192]

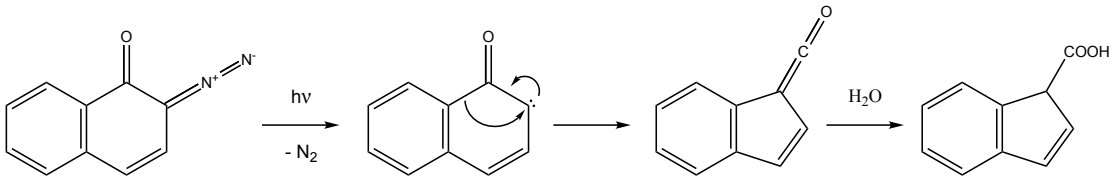

Figure 2.10: Reaction of diazonaphthoquinone upon exposure to UV light, yielding indene carboxylic acid.

In a typical procedure, the resist is spin-coated onto the substrate at a certain speed, determining the thickness of the resist layer. It is then heated on a hot plate ("pre-bake") which causes the evaporation of the solvent and the formation of a loosely cross-linked phenol formaldehyde resin. After that, the resist is exposed to UV light, which causes the decay of the photoactive component (PAC) and renders the exposed regions soluble in the subsequent development step.

Typically, a positive photoresist consists of three components: the phenol formaldehyde resin, which forms upon heating in the pre-bake step, a hydrophobic photoactive component, typically diazonaphthoquinone, and a solvent. While the phenol formaldehyde resin itself is hydrophilic and readily dissolvable in aqueous alkaline solutions, addition of the hydrophobic diazonaphthoquinone disturbs wetting and penetration of the developer, rendering the photoresist insoluble. Upon illumination with UV light, the diazonaphthoquinone undergoes a Wolff rearrangement, yielding indene carboxylic acid (see Figure 2.10) which is readily dissolvable and very hydrophilic, allowing the developer to wet and penetrate exposed regions and thereby dissolve the phenol formaldehyde resin.

Negative Resist

In a negative resist, the regions that were exposed to light become insoluble in the developer, resulting in a negative image of the mask pattern after development (i.e., transparent features on the mask will give rise to photoresist features).[191–193] In a typical procedure, the resist is spin-coated onto the substrate. If a very viscous resist (i.e., a resist for thick layers) is used, it can be beneficial to first spin-coat at a low speed to spread the photoresist evenly ("spread cycle") and subsequently at a higher speed to control the thickness of the layer ("spin cycle"). After spinning, the substrate is heated on a hot plate in order to evaporate the solvent and thereby densify the polymer film ("pre-bake"). However, unlike in the case of positive photoresists, this does not cause curing of the resist. The polymerization of the resin is rather initiated upon exposure

to UV light, which causes the decay of a polymerization initiator. Subsequently, the substrate is heated on a hot plate in order to perform the actual cross-linking reaction and cure the resist ("post-exposure bake"). For thick resist layers, the heating can be divided into two steps, due to the different expansion coefficients of the wafer and the resist. Then, the substrate is put into a developer solution. After development, only the regions which were exposed to UV light and hence cross-linked in the post-exposure bake remain on the substrate.

Typically, negative resists consist of an epoxy resin, a solvent and up to 10 % of a triarylsulfonium salt as the photoactive component. Exposure to UV light causes the decay of the latter yielding superacidic $HSbF_6$ which catalyses the cationic ring opening polymerization of the epoxy resin upon heating (see Figure 2.11).

Polymerization renders the resin insoluble in the developer whereas the unpolymerized monomers are washed away in the subsequent development process. After development, the substrates are rinsed with ultra pure water and blown dry with nitrogen. For further hardening of the resist, a "hard bake" can be performed in which the developed resist is further cured at elevated temperature for a longer time.

Image Reversal Resist

An image reversal resist can act as a positive tone resist or a negative tone resist, depending on the processing conditions. Like a positive resist, an IR resist usually consists of a phenol formaldehyde resin and diazonaphthoquinone as the PAC. However, there is another PAC that becomes active and causes cross-linking of the resin after exposure to UV light and heating at elevated temperatures. This makes the image reversal possible and causes the resist to behave like a negative tone resist if there is an additional heating step after exposure or like a normal positive tone resist if this heating step is omitted.

If the resist is used in positive mode, it is spin-coated onto the substrate at the desired thickness, pre-baked to loosely cross-link the resin, exposed to UV light, and then put directly into the developer bath. Although UV light exposure activated both PACs in the exposed regions at once, only the (decomposed) diazonaphthoquinone will have an effect during development, since the other PAC also requires a heat treatment to be effective. Hence, if image reversal is intended, the substrate is heated again after the exposure ("IR bake"), causing further cross-linking of the exposed regions and rendering them insoluble in the developer and insensitive to further light exposure. The unexposed regions however still behave like a normal, unexposed positive resist.

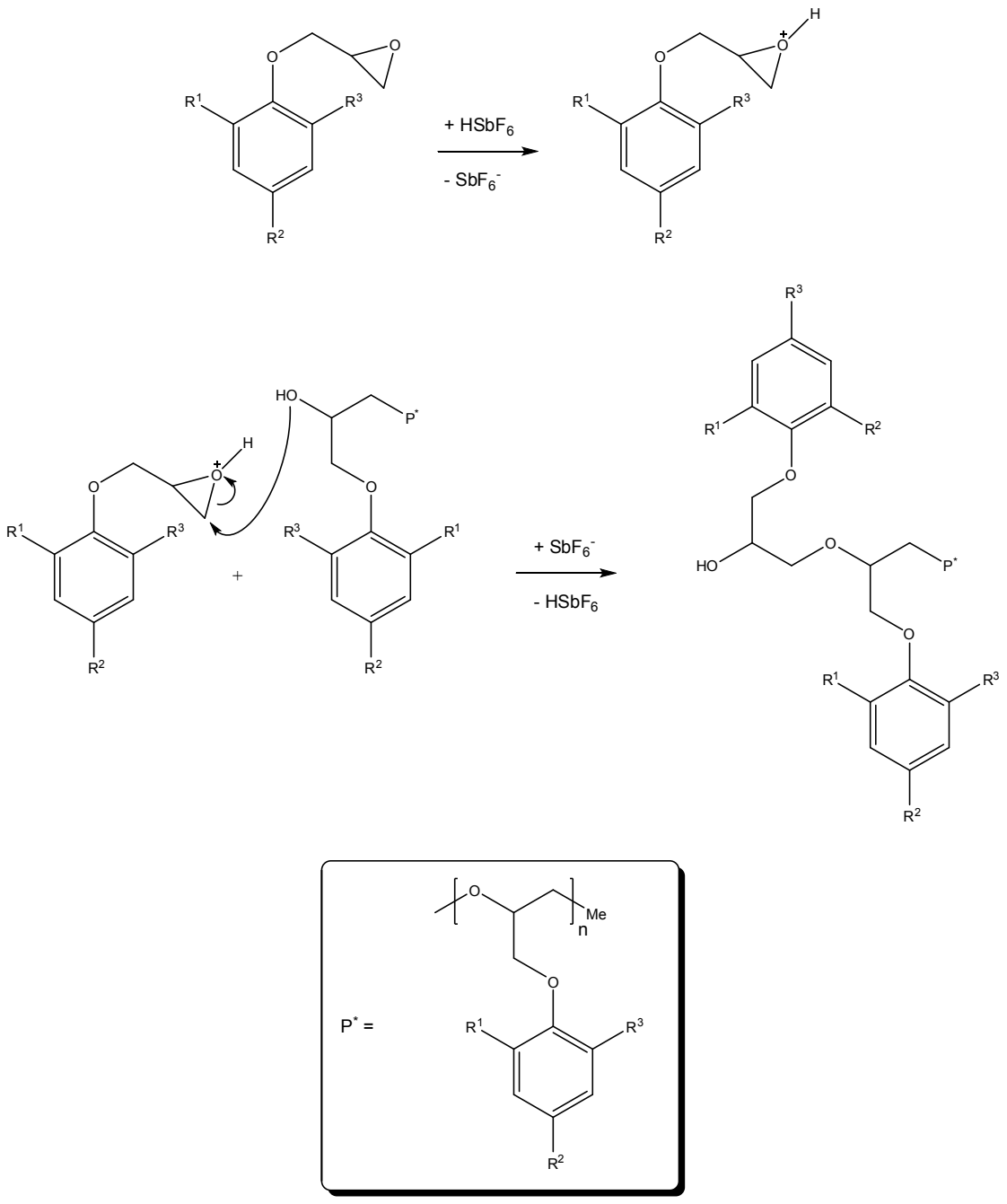

Figure 2.11: Mechanisms leading to the hardening of a negative photoresist in regions exposed to UV light.

After a flood exposure (without a mask) at high UV doses, these regions will be dissolved in the following development step. Overall, the exposed regions remain on the substrate, hence the resist behaves like a negative tone resist after image reversal.

2.11.2 Microscope Projection Lithography

Microscope projection lithography is a technique which employs a standard commercial microscope with a photomask in the light path to project a pattern onto a photosensitive substrate on the specimen stage of the microscope.[194] The mask is inserted into the field stop position of the microscope so that it is in an optical plane conjugate to the focal plane of the substrate. Then a built-in UV fluorescence lamp is used to project the pattern of the mask onto the substrate causing activation of the PAC. This is an elegant way to produce microstructures without the need for elaborate clean room equipment.

The masks used for this technique can either be "standard" chromium/quartz glass masks or, even simpler, high resolution prints of the patterns on transparent foils. In this work, high-resolution (25 400 dpi) prints were used.[1] When designing the masks, the reduction of the pattern size due to the optics of the microscope has to be taken into account. If there is no further change in magnification due to additional lenses in the internal light path, the reduction corresponds to the magnification power of the objective (i.e., a 100 µm sized feature on the mask will produce a 10 µm sized feature on the substrate when a 10x objective is used and a 1 µm sized feature when a 100x objective is used).

Another point that has to be considered (especially when high-resolution patterns are desired) is the chromatic aberration of the objective.[195] Especially low magnification objectives are often not corrected for chromatic aberration, resulting in a shift of the focal planes when using yellow light for focusing prior to writing (typically yellow light is used for adjusting the focus since the PAC is not sensitive in this spectral region) as opposed to using UV light in the actual writing step. This shift can be determined experimentally (see Section 10.4). Table 10.6 in the appendix gives an overview of the corrections of the focal shift due to chromatic aberration for the setup used in this work.

[1] The masks were obtained from KOENEN GmbH HighTech Screens, Otto-Hahn-Str. 40, 85521 Ottobrunn, Germany. Due to the simplicity and the periodicity of the mask patterns used in this project, a Java program was written that created the patterns in the "gerber" file format (for the source code, see Supplementary CD).

2.12 Soft Lithography using PDMS Molds

Poly(dimethylsiloxane) is a silicone polymer widely used in soft lithography that features a number of beneficial properties for such processes.[196] It is appreciated for its non-toxicity, transparency with respect to visible light (down to approximately 300 nm), non-biofouling properties and commercial availability. Moreover, PDMS is deformable enough that it can establish a conformal contact even on nonplanar substrates. Its elastic properties also help releasing the stamp from complex and fragile structures. Additionally, the surface of PDMS itself has a relatively low interfacial free energy and is chemically rather inert, but it can be functionalized by exposure to an oxygen plasma followed by the formation of self-assembled monolayers (SAMs), hence providing means to tailor the surface properties. These characteristics make it an important material for microcontact printing, microfluidics, and lab-on-a-chip devices. In the framework of this project it was used to produce stamps for micromolding (see Chapters 3, 4, and 7) and microcontact printing (see Chapter 8).

In order to obtain a PDMS mold, the prepolymer solution is prepared by mixing the monomer and a polymerization catalyst in a 1:10 (w/w) ratio. The mixture is degassed *in vacuo* in a desiccator for 30 min and then cast on a photolithographically patterned master (see Section 2.11.1), silanized with 1H,1H,2H,2H-perfluorooctyltrichlorsilane. Then it is cured in a convection oven at 60 °C overnight. The heat triggers the polymerization of the monomers yielding solid PDMS, which can be peeled off carefully from the master.

The prepolymer mixture contains siloxane oligomers terminated with vinyl groups and with silicon hydride bonds and a platinum based catalyst. During the curing process the platinum complex catalyses the addition of SiH bonds to the vinyl groups resulting in Si–CH_2–CH_2–Si linkages[197]. The catalytic cycle is depicted in Figure 2.12.

Depending on the chemical nature of the prepolymer and the processing conditions, the degree of cross-linking and hence the elasticity and deformability of the resulting PDMS elastomer can be controlled to a certain degree. While the elastic properties of PDMS are important for soft lithography techniques (see discussion above), they can also introduce artifacts and patterning defects, as shown in Figure 2.13. When the aspect ratio of the relief features on the stamp is too large (typically >2), the PDMS microstructures might fall under their own weight or collapse due to forces exerted during the inking or printing process. When the aspect ratio is too low (typically <0.2), or the features are too far apart (typically when the distance between two

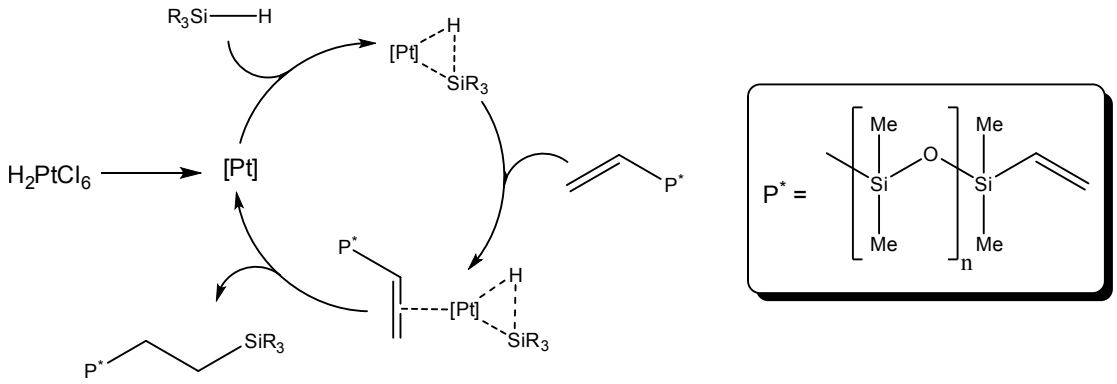

Figure 2.12: Polymerization reaction yielding cured PDMS.

features is >20 times the height of the features), the relief structures might not be able to withstand pressure during the stamping process, resulting in "sagging". Moreover, the pattern might get distorted due to shrinking (during PDMS curing) or swelling (due to solvent exposure) of the elastomeric stamps.

2.12.1 Microcontact Printing

In microcontact printing, the relief structure of a PDMS stamp is used to transfer a pattern to a substrate by coating the stamp with a suitable compound and bringing it into conformal contact with an appropriate substrate (see Figure 2.14).[198,199] Typically, molecules that can form SAMs are used as the "ink" and printed on a substrate that exhibits reactivity towards a functional group of the ink. One of the best characterized systems of SAMs are those formed by alkanethiolates ($CH_3(CH_2)_nS^-$) on gold.[196] Alkanethiols chemisorb spontaneously onto gold substrates, and the sulfur–gold bond brings the alkyl chains into close proximity. Van-der-Waals interactions between the alkyl chains freeze out configurational entropy and lead to an ordered structure. Usually, alkanethiolates with n>6 are necessary to form such highly ordered monolayers.[200] Typically, the formation of alkanethiolate SAMs on gold is a fast process, occurring within minutes (when deposited from solution) or even a few seconds (when deposited *via* microcontact printing). Since microcontact printing is a parallel technique (i.e., the pattern is transferred to the whole contact area at once), and since there is in principle no size limit to the stamp, even large areas can be patterned rapidly.

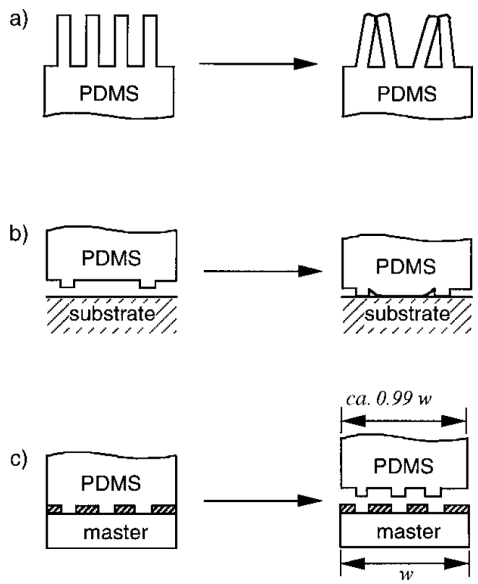

Figure 2.13: Schematic illustration of possible deformations and distortions of microstructures in the surfaces of elastomers such as PDMS. (a) Pairing, (b) sagging, and (c) shrinking. Taken from Reference 196.

2.12.2 Micromolding

Micromolding is another soft lithography technique that allows for pattern transfer using PDMS stamps.[196]. Micromolding is a generic term that includes various related methods, such as "standard" replica molding (REM), microtransfer molding (µTM), micromolding in capillaries (MIMIC) and solvent-assisted micromolding (SAMIM) (see also Figure 2.15)

In REM, a precursor that can be cross-linked or polymerized (such as polyurethane, epoxy-resins, *etc.*) is cast onto a PDMS stamp. After solidification, the stamp can be separated from the polymerized film, yielding a negative copy of the stamp's relief pattern. A similar process is used for creating PDMS stamps from photolithography masters. In µTM, the precursor that is cast onto the stamp is transferred to a solid substrate prior to polymerization, yielding the negative replica of the stamp on a solid support. MIMIC is in a way similar to µTM, and the resulting pattern looks identical. However, in MIMIC the stamp is brought into contact with the substrate first, then a droplet of the precursor solution is added to one side of the stamp, and the channels are filled by capillary action. In MIMIC, all features have to have a hydraulic connection, hence it cannot be used to form isolated features (unlike µTM). Also, the filling due to capillary action might be slow or incomplete at larger scales or problematic if a very viscous liquid is used for infiltration. In SAMIM, a thin polymer film is deposited on

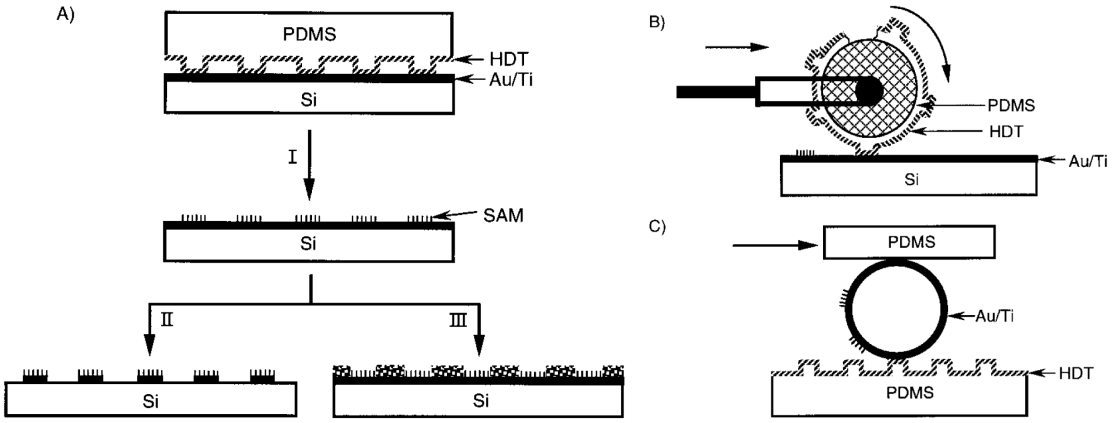

Figure 2.14: Schematic illustration of procedures for microcontact printing of hexadecanethiol (HDT) on a gold surface: (A) Printing on a planar surface with a planar stamp (I: printing of the SAM, II: etching, III: deposition). (B) Large-area printing on a planar surface with a rolling stamp. (C) Printing on a nonplanar surface with a planar stamp. Taken from Reference 196.

a substrate, and then a PDMS stamp is "inked" with a solvent that swells or dissolves the polymer (e.g., acetone, ethanol, *etc.*) and brought into contact with the polymer film. The swelling or dissolution of the polymer film causes an "embossing" of the PDMS relief structure into the polymer, and after solvent evaporation, the polymer film stays in its newly imposed structure. This approach is limited to rather volatile solvents, and the solvents need to be compatible with PDMS (i.e., they should not swell PDMS extensively since this leads to pattern distortions).

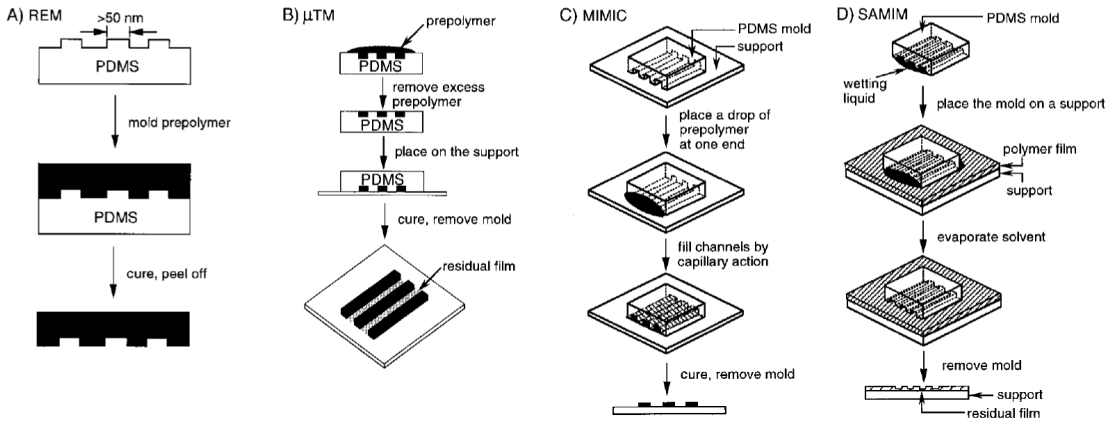

Figure 2.15: Schematic illustration of procedures for (A) replica molding, (B) microtransfer molding, (C) micromolding in capillaries, and (D) solvent-assisted micromolding. Taken from Reference 196.

Chapter 3

. . . . . .

Highly Oriented Mesoporous Silica Channels Synthesized in Microgrooves and Visualized with Single Molecule Diffusion

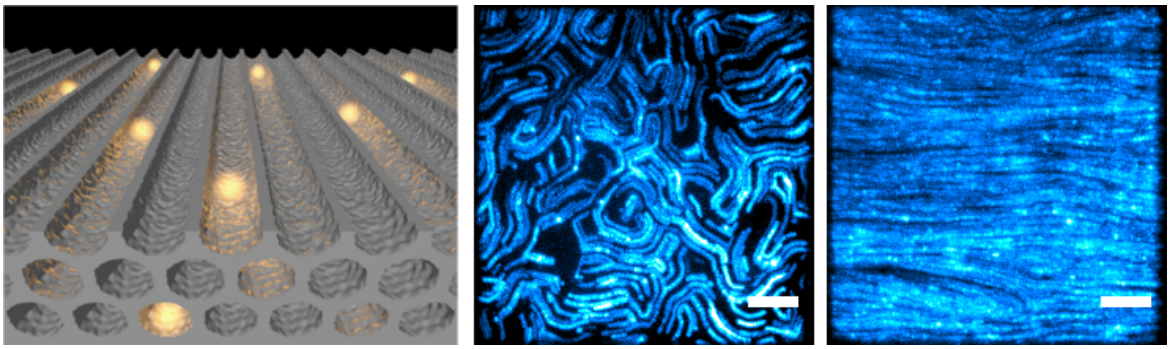

This chapter is based on the article "Highly Oriented Mesoporous Silica Channels Synthesized in Microgrooves and Visualized with Single-Molecule Diffusion" by B. Rühle, M. Davies, T. Lebold, C. Bräuchle, and T. Bein, published in *ACS Nano*, **2012**, 6 (3), 1948-1960.

3.1 Abstract

A novel synthesis method for large-pore, well-aligned 2D-hexagonal mesoporous silica thin films is reported. The alignment was achieved by confinement in poly(dimethyl-

siloxane) (PDMS) microgrooves without the necessity of additional forces (such as electric fields). We describe the influence of various experimental conditions including the way the grooves are filled, surface modification at the solid/liquid interfaces, and the height-to-width ratio of the microgrooves on mesopore alignment. With this technique, highly oriented mesoporous silica channels can be obtained at a length scale of several millimeters. For a nondestructive, detailed, and wide-ranging structural and dynamic characterization of the as-synthesized mesochannel silica network, dye molecules were incorporated into the channels at concentrations suitable for single-molecule microscopy. A "maximum projection" of individual frames recorded with a fluorescence microscope immediately gives a global overview ("map") of the pore structure, thus providing direct feedback for tuning synthesis conditions. In addition, deeper insights into the real nanoscale structure of the mesoporous silica framework were obtained through high-accuracy single-molecule tracking experiments. The high spatial accuracy of the experiments allowed for the direct observation of jumps of single dye molecules between individual channels in the mesoporous silica host. Nevertheless, due to the low concentration of defects, the diffusion could be described as a one-dimensional random walk where the molecules diffuse along the highly oriented, parallel channels and sometimes switch from channel to channel through small defects in the pore walls. Furthermore, it could be shown with single-molecule microscopy that template removal and calcination of the aligned films results in an increased defect concentration; however, the overall order of the structures remained intact.

3.2 Introduction

Two-dimensional hexagonal (*p6mm*) mesoporous silica materials have attracted much attention as a host for versatile applications including nanofluidics and nanoreactors,[31] oriented growth of nanowires,[32] and optoelectronic devices.[33] For these applications, control over pore alignment can be crucial. However, the evaporation-induced self-assembly (EISA) approach,[12] which is one of the most common ways to prepare these structures, usually results in small domains with randomly oriented mesoporous channels. This can be attributed to the lack of a preferential direction on the substrate, and a variety of ways that have been reported aimed at introducing a preferential direction of the mesopores on a macroscopic scale, including microtrenches,[34] external electric[36,37] and magnetic fields,[38] substrate surface modification,[39] and shear flow control.[41] However, these approaches often require specialized equipment or impose

constraints on the applicable substrates or surfactants. In the case of employing microtrenches, a clean room and a photolithography or even an electron-beam lithography setup is needed, rendering these approaches costly and time-consuming. The use of external fields requires charged templates such as CTAB, hence limiting this approach to mesoporous silica with small pores. The other approaches require crystalline substrates with a certain crystallographic orientation or result in channel lengths typically $< 1\,\mu m$. In this contribution, we describe a general approach for the design of oriented mesoporous silica films with large pores and large channel length (typically around $10\,\mu m$) that serve as model systems for the investigation of single-molecule diffusion. This approach is not limited by the need for specific substrates (e.g., non-conductive substrates or substrates with crystalline order), specific templates (e.g., ionic surfactants), or the application of strong electric or magnetic fields that may be difficult to implement. Moreover, to the best of our knowledge, this is the first report of an in-depth investigation of the structural features (such as correlation length and domain sizes) and dynamical properties (such as guest diffusion) of large-pore silica materials with macroscopically aligned mesochannels.

Our approach was inspired by a technique initially introduced by Whitesides *et al.* as micromolding in capillaries (MIMIC),[36,37] where an EISA precursor solution is filled into microgrooves defined by a poly(dimethylsiloxane) (PDMS) stamp. This technique is, in principle, compatible with any flat substrate and any surfactant, and no specialized equipment is needed once the masters for the PDMS stamps are obtained. Moreover, the PDMS stamps can be reused, rendering this approach very simple, fast, and cost-effective. We extended the MIMIC approach and investigated mesopore alignment inside PDMS microgrooves using the well-known, uncharged Pluronic F127 triblock copolymer as a template. We found that the reaction conditions and the surface modification at the solid-liquid interfaces inside the microgrooves can drastically influence the direction of the mesopore alignment. We also introduce single-molecule fluorescence microscopy as a very efficient and powerful tool to gain direct insights into the mesochannel structure, correlation length, and pore directionality in the mesoporous silica films. This method provides unique nanoscale structural information about the pore system and about the interactions of guest molecules with the porous host that cannot be obtained with any other analytical technique (see also Section 3.3 for a more detailed description of this concept).[52–54,73]

3.3 Results and Discussion

Before the detailed description of the synthetic strategies and how different parameters can affect mesopore alignment, we present some general remarks about the 2D-hexagonal (*p6mm*) silica structure itself and the way single-molecule fluorescence microscopy is used as a fast and efficient tool to investigate mesopore alignment and correlation length. It is known from the literature that an EISA precursor solution of the composition described below (see Section 3.5) can give a 2D-hexagonal phase of mesoporous silica with cylindrical (or elliptical) mesopores lying preferentially in a plane parallel to the substrate.[42] These structures are commonly characterized using X-ray diffraction (XRD) or (cross-sectional) electron microscopy techniques. However, a simple 1D XRD pattern can only give information about the phase (hexagonal or cubic) of a mesoporous silica thin film but says little about its in-plane ordering or the domain sizes. More elaborate X-ray diffraction techniques can also give information about the pore directionality of the mesopores, but these techniques also do not provide much information about the domain size and correlation length of the cylindrical mesopores, and they give only averaged data for a certain area without spatial resolution. On the other hand, electron microscopy top view images of the structure can give information about the phase, the alignment and – to some extent – the correlation lengths of the individual mesopores. However, this only works for the topmost layer in scanning electron microscopy (SEM) (or thin layers in transmission electron microscopy (TEM)), but as will be shown in this work, the alignment of the mesopores can differ drastically between top and bottom layers. In contrast, cross sections can provide information about the orientation at different heights, but they do not directly provide information about domain sizes of the mesopore channels and they usually require destruction of the sample.

Single-molecule fluorescence microscopy can complement XRD and electron microscopy data[52] and directly provide spatially resolved information about alignment and correlation lengths of mesoporous channels in a fast, direct, and nondestructive way. Moreover, several additional parameters such as the diffusion coefficient of the fluorescent dyes inside the mesopores or even information about defects in the mesoporous structure can be obtained, as will be shown later. In order to gain information about pore directionality and correlation length, we mixed a fluorescent dye (N-(2,6-diisopropylphenyl)-N'-octylterrylene-3,4,11,12-tetracarboxdiimide (As-TDI)) at a very low concentration (typically 10^{-10} – 10^{-11} M) into the EISA precursor solution. During

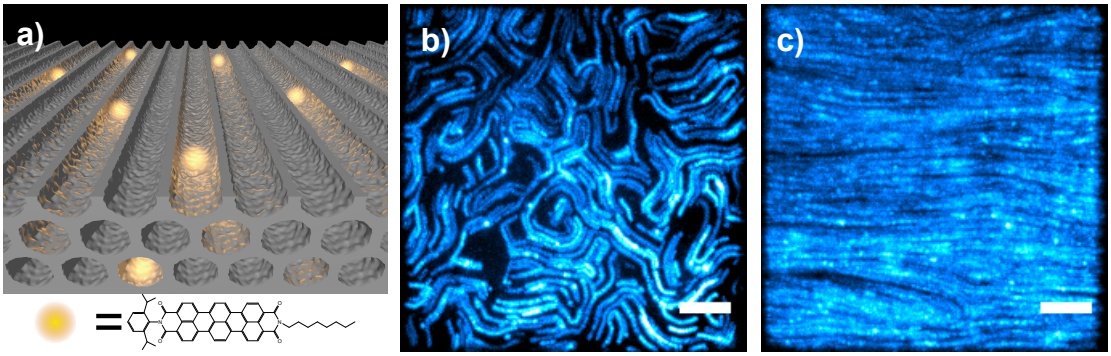

Figure 3.1: Representation of schematic structure and different domain patterns in the mesoporous thin films. (a, top) Schematic representation of fluorescent dye molecules diffusing inside 2D-hexagonally arranged mesopores of a porous silica host (the template is omitted for clarity) and (a, bottom) the chemical structure of N-(2,6-diisopropylphenyl)-N'-octylterrylene-3,4,11,12-tetracarboxdiimide (As-TDI). (b,c) Maximum projection of the individual frames of a movie recorded with a fluorescence microscope at a frame rate of 2.5 fps taken from sample 1, revealing the ordering of the mesoporous structure (false-colored in blue; scale bars are 5 µm; see also movies M1 and M2 on the Supplementary CD). (b) The cylindrical mesopores lie in a plane parallel to the substrate, but they do not show macroscopic in-plane alignment. (c) The mesopores lie in a plane parallel to the substrate and show a preferential alignment (left-right) on a macroscopic length scale (c).

self-assembly of the mesoporous silica structure, the hydrophobic dye is incorporated into the hydrophobic core of the micelles inside the cylindrical mesopores. After solidification of the silica network, the dye remains mobile inside the mesopores, presumably due to the presence of the template acting as a lubricant phase. However, the diffusional movement of the dye molecules is now confined by the silica side walls, so each of the "trapped" dye molecules moves inside a mesoporous channel network, exploring and mapping out the possible pathways. The positions of the dye molecules at different points in time hence create a "map" of the mesoporous structure inside the silica host (Figure 3.1).

This map can be obtained by recording a movie at the desired position of the sample with a fluorescence microscope (in this work, typically 200-1000 images at a frame rate of 2.5 frames per second (fps) were used) and subsequently overlaying the individual frames of the movie in an appropriate way (see next paragraph). This overlay shows directly that the dye molecules do not perform a random walk movement as it would be expected for dye molecules that are merely adsorbed on a surface or, to some extent, dye molecules inside a cubic ($Im\bar{3}m$) structure, but they rather show a confined movement along certain pathways. Moreover, pore directionality and

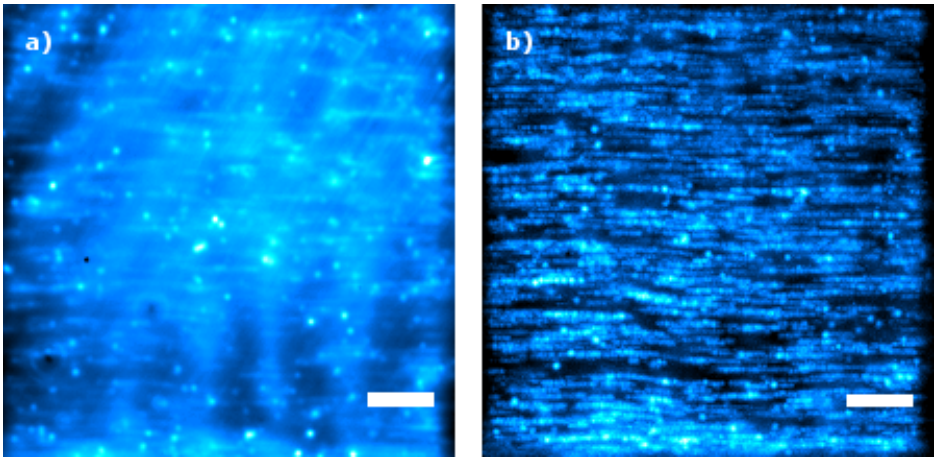

Figure 3.2: Two different ways of obtaining the overlay: (a) by averaging over the individual frames and (b) by using a maximum projection. Both images are reconstructed from the same movie taken from sample 2, false-colored in blue, and contrast and brightness were optimized. Both scale bars are 5 µm. The corresponding movie M3 can be found on the Supplementary CD.

correlation length can also be directly obtained by analyzing the overlays. The fact that the dye molecules do not diffuse in and out of focus during the recording period of the movies shows that they are inside the 2D-hexagonal mesoporous network with the pores aligned preferentially in a plane parallel to the substrate.

The most direct way of creating these overlays would be a summation of (or averaging over) the individual frames of the movie. While this technique works in principle, it has some drawbacks. Most importantly, it overemphasizes stationary fluorescent objects (e.g., constant background, contaminations, immobile dye molecules, defects, etc.) compared to (fast) moving objects because a moving object only contributes intensity to a certain pixel of the overlay when it passes exactly this point in one of the frames of the movie (which might only be the case for a small fraction of the total frames), while a stationary object contributes the same intensity in each frame. For this reason, we used a "maximum projection" in this work, where each pixel in the overlay assumes the maximum value of the corresponding pixels in the individual frames that was reached during the recording time. Hence, the final overlay consists only of the brightest pixels of the movie. This technique treats moving and stationary fluorescent objects more equal and usually provides information-rich images. It is, however, more prone to overemphasizing noise than the averaging method described above since a bright spot in the background that occurs in only one of the frames of the movie is likely to end up in the final overlay. However, with bright fluorophores

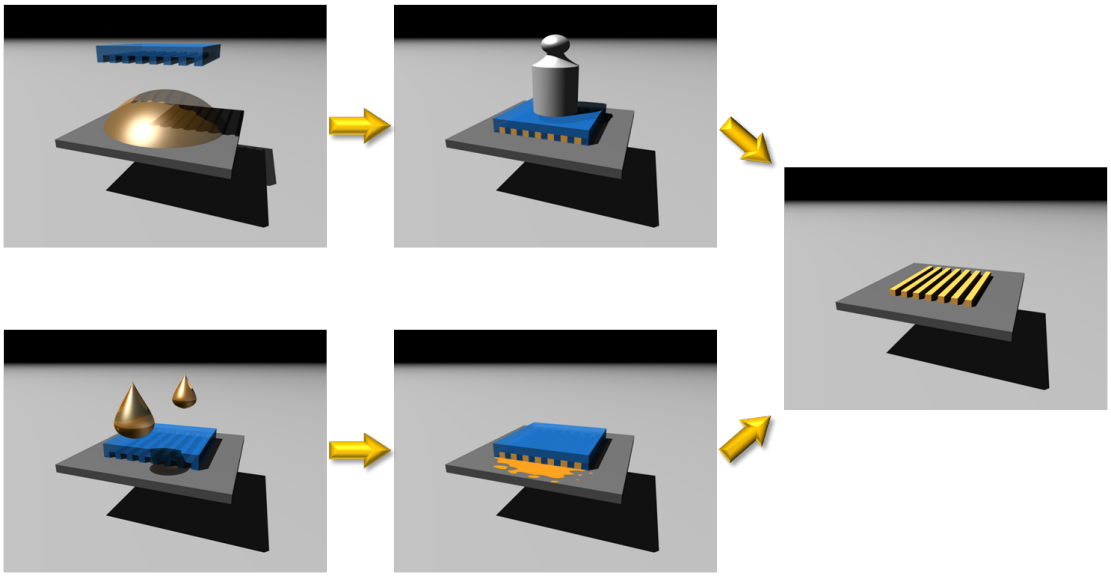

Figure 3.3: Schematic representation of the two approaches used to trigger mesopore alignment by confinement in PDMS microgrooves.

and a high signal-to-noise ratio, this is usually not a problem (Figure 3.2).

In order to trigger mesopore alignment during the EISA process, the condensation of the precursor solution was performed in confined spaces defined by a PDMS stamp with a stripe pattern. Two different approaches were pursued that are depicted schematically in Figure 3.3. In the first approach ("stamping approach"), a droplet of the precursor solution was deposited on the substrate, the stamp was placed on the latter, and pressure was applied on the stamp in order to achieve dewetting of the surface and to transfer the pattern of the stamp. In the other case ("capillary flow approach"), the stamp was placed on the substrate first, and then a droplet of the precursor solution was applied to both ends of the stamp. The solution gets sucked into the microgrooves defined by the stamp and the substrate by capillary flow. After solidification of the solution, the stamps can be carefully peeled off to obtain the final structure.

In the course of this work, we varied different parameters to investigate their influence on mesopore alignment. In addition to the two approaches described above, we also varied the height-to-width ratio of the microgrooves, the surface modification of the stamp and the substrate, and the synthetic conditions during solidification of the silica framework.

When stamps with microgrooves of a height-to-width ratio of approximately 1:2 (ca. 1.5 µm high and 3.0 µm wide) were used in the stamping approach without further

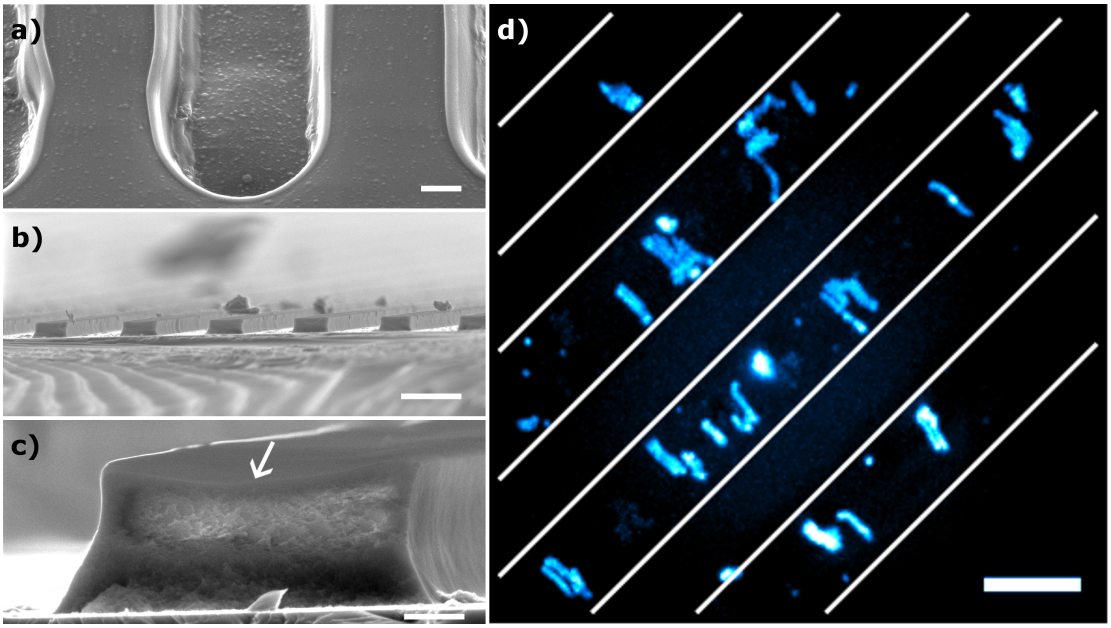

Figure 3.4: Microgrooves and silica mesopore patterns. (a) Microgrooves in the PDMS stamp (scale bar is 1 µm). (b,c) Mesoporous silica pattern, produced by the "stamping approach" (scale bars are 5 µm and 500 nm, respectively). In (c), the top surface of the silica bar is indicated by the arrow. (d) Maximum projection through 500 individual frames of a movie recorded with a single-molecule fluorescence microscopy setup at 2.5 fps taken from sample 3, indicating the orientation of the mesochannels (false-colored in blue; white lines indicate the direction of the microgrooves; scale bar is 5 µm; see also movie M4 on the Supplementary CD).

modification of the stamp or the substrate, we found that the mesopores inside the structure tend to align perpendicular to the long axis of the channel (Figure 3.4). This finding is somewhat surprising since according to Aksay *et al.* the formation of end-caps in self-assembled micelle cylinders is unfavored due to their high free energy of formation.[37]

As the original goal was to obtain long, well-aligned mesochannels (preferably longer than the microgroove width), we investigated the influence of different synthesis parameters in order to favor mesopore alignment along the long axis of the microgrooves. Endo *et al.* showed that in silicon trenches with hydrophobic side walls the mesochannels of SBA-15 films tend to align perpendicular to the long axis of the trenches,[35] while in trenches with hydrophilic side walls a parallel alignment was favored. Additionally, it was known from dip-coating experiments conducted by Okubo *et al.*[42] that shear forces can also influence the alignment of the mesochannels favoring pore directionality parallel to the direction of flow (i.e., the dipping direction in their experiments).

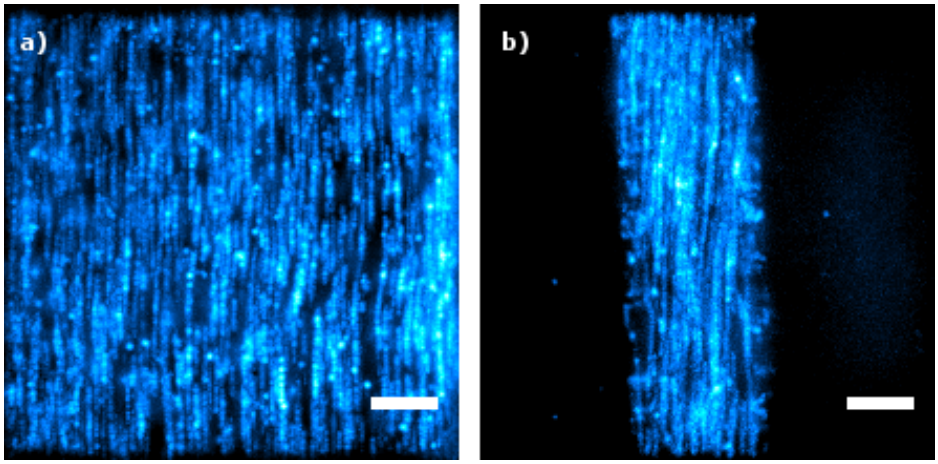

Figure 3.5: Maximum projection indicating the orientation of the mesochannels in (a) a low height-to-width ratio channel (approximately 1:20; sample 2; rotated by 90° for clarity) and (b) a higher height-to-width ratio channel (approximately 1:6; sample 4) (false-colored in blue; both scale bars are 5 µm; see also movies M3 and M5 on the Supplementary CD).

With this in mind, we investigated the capillary flow approach, which can provide shear forces during filling of the microgrooves in the stamp, in combination with different modifications of the surface properties of stamp and substrate regarding their hydrophilicity and hydrophobicity. The surface properties of the stamp and the substrate can be varied independently. Modification of the stamp influences the solid/liquid interface at three side walls of the resulting microgrooves, while modification of the substrate influences one solid/liquid interface. Modification of the interfacial properties can indeed strongly influence the alignment of the mesoporous channels. Of the four possible combinations for surface functionalization of the stamp/substrate pair (i.e., hydrophilic/hydrophilic, hydrophilic/hydrophobic, hydrophobic/hydrophilic, and hydrophobic/hydrophobic), best results (meaning preferential alignment of mesochannels parallel to the microgrooves) were achieved by using substrates rendered hydrophobic with PFOTS and stamps rendered hydrophilic by exposure to oxygen plasma and subsequent incubation in an acidic aqueous solution of TEOS. Using this combination, very well aligned mesopores could be obtained in narrow microgrooves (typically with a height of 1.5 µm and a width of 10 – 15 µm, i.e., a height-to-width ratio smaller than 1:7 to 1:10) in 60 – 80 % of the cases. In some cases, parallel alignment could also be observed in extremely low height-to-width ratio grooves with a height of approximately 1.5 µm and a width of ca. 30 µm, that is, a ratio of 1:20 (Figure 3.5).

The parallel alignment usually extends over several millimeters from the ends into

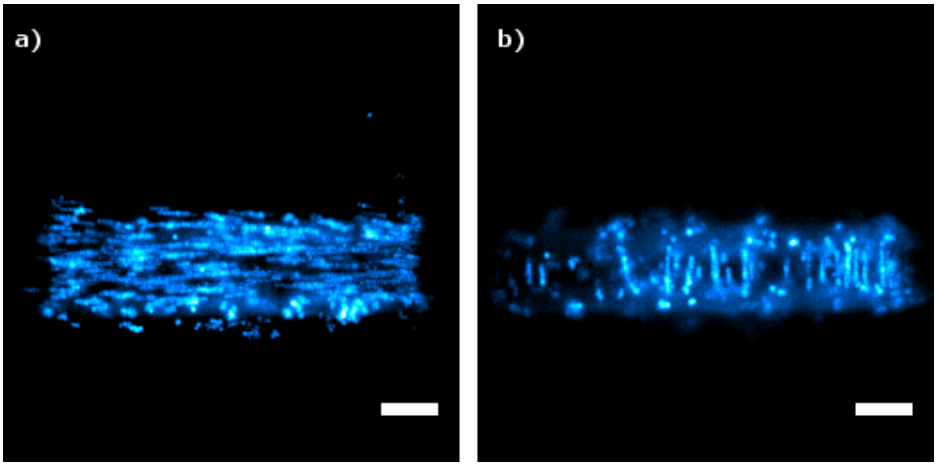

Figure 3.6: Maximum projection taken from sample 2, indicating the orientation of the mesochannels in a focal plane (a) close to the substrate and (b) higher above the substrate (false-colored in blue; both scale bars are 5 µm; see also movie M6 on the Supplementary CD).

the interior of the microgroove, and under favorable circumstances, the entire resulting silica bar of 1 – 2 cm length showed alignment of the mesopores. The end regions differ from the middle region mainly in the following aspects. First, the capillary flow in these regions is stronger, indicated by the fact that the movement of the meniscus and hence the filling of the microgrooves occurs quite fast in the beginning (right after the droplet of the precursor solution was added to the open end of the stamp) but then rapidly slows down. Second, the supply with fresh reactants from excess solution that has not filled the microgrooves is better in these regions. Third, the evaporation rate of the solvent in these regions is different from the middle region since evaporation can occur easier through the open ends of the PDMS stamps.

Interestingly, in some cases, the pore directionality changed abruptly within one channel depending on the height above the substrate (i.e., it changed within different focal planes of the microscope). While close to the substrate, an alignment parallel to the microgrooves could be observed, the orientation changed to a perpendicular alignment at higher positions (Figure 3.6).

We believe that this might be due to the fact that the silica patterns show a concave rather than a flat surface (see Figure 3.4.c and Figure 3.7), and the alignment could follow this concave curvature. Similar observations were made by Endo *et al.* for dip-coated films in silicon microtrenches, and the authors attributed the effect to shear flow during solvent evaporation.[35]

We also observed that mesopore alignment parallel to the microgrooves can be

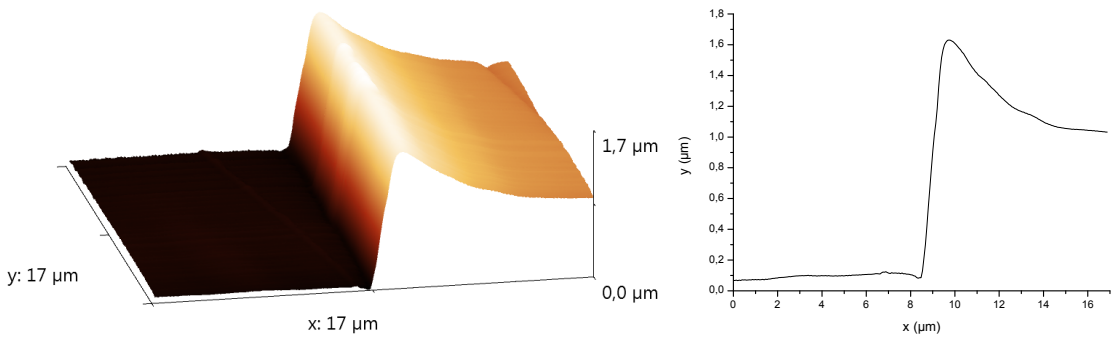

Figure 3.7: AFM Image and line profile from a silica bar showing its concave surface (sample 5); shown is one-half of the bar's cross section.

achieved in higher microgrooves (4 – 8 µm height) by employing the "capillary flow approach" in combination with a hydrophobic (i.e., untreated) PDMS stamp and a hydrophilic substrate. This is interesting for the possible removal of the stamp by controlling the adhesion with the silica bar. In these experiments, we obtained results comparable to the ones shown above regarding mesopore orientation and correlation length when the samples are first incubated in a saturated atmosphere of ethanol at about 22 °C for 21 h and then additionally 24 h at ambient conditions (Figure 3.8). The saturated ethanol atmosphere slows down the evaporation rate of the solvent and hence the solidification of the silica matrix. However, after these aging times, the structures were found to be sufficiently stable to withstand mechanical stress (such as the stamp removal or SEM preparation) and further treatment such as extraction, and hence the solidification process, was considered to be complete after these times.

To determine the structure of the mesoporous silica in the microgrooves, small-angle X-ray scattering (SAXS) experiments and cross-sectional high-resolution scanning electron microscopy (HR-SEM) were performed (Figure 3.9). Both provide evidence for hexagonally arranged mesopores lying in a plane parallel to the substrate. The cross-sectional HR-SEM images (cleaved perpendicular to the microgroove direction) also indicate the well-ordered state of the mesopores along the long axis of a microgroove. The elliptical shape of the mesopores is typical because of the anisotropic shrinkage in mesoporous silica films during drying. Image analysis of the HR-SEM data gives a mean mesopore width of 6 – 8 nm and a height of 5 – 7 nm and a pore-to-pore distance of 12 – 16 nm horizontally and 9 – 13 nm diagonally, which is in line with the d spacing of the XRD (100) peak of ca. 7.5 nm.

Samples prepared in the way explained above (i.e., samples 6 – 9) were also subjected to a more detailed analysis using single-molecule fluorescence microscopy. We

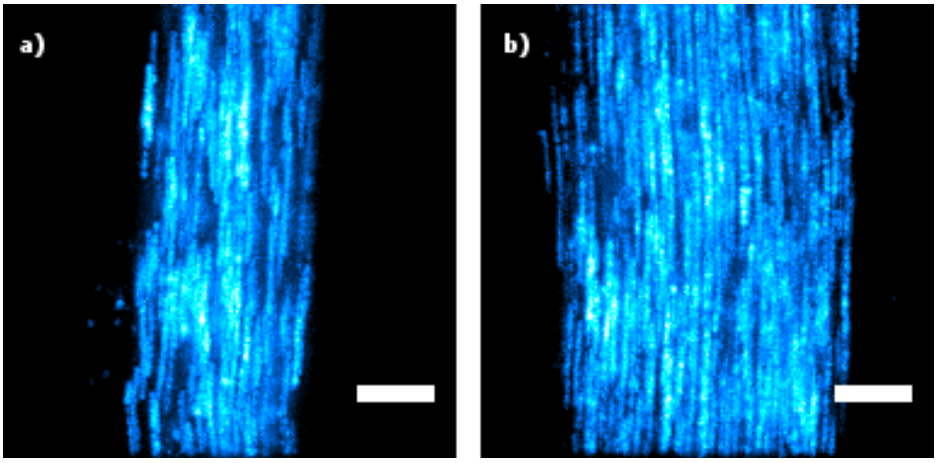

Figure 3.8: Maximum projection taken from sample 6, indicating the orientation of the mesochannels in silica bars of different widths prepared as described above (false-colored in blue; both scale bars are 5 µm; see also movies M7 and M8 on the Supplementary CD).

obtained high spatial resolution for the pathways of single molecules inside the mesopores and thus could analyze the individual channel structures in much more detail. Furthermore, we could gain dynamic information about the diffusion of the molecules in such structures. The main driving force for molecular movement in these channel systems is Brownian motion, while biased motion due to concentration or structural gradients cannot be fully excluded.

In order to follow the pathway of single molecules with much higher accuracy, the dye concentrations were reduced even further than in the experiments performed before. A direct consequence of such low dye concentrations is the much better separation of the pathways of the single molecules from each other, as shown in Figure 3.10.a.

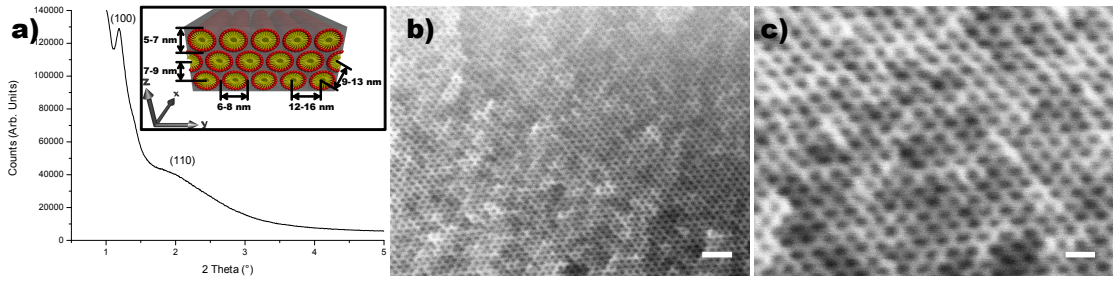

Figure 3.9: Structural analysis of the mesopore system of sample 7. (a) XRD pattern and (b,c) cross-sectional HR-SEM images (cleaved perpendicular to the long axis of a silicon bar) of mesoporous silica produced as described above. Scale bars are (b) 50 nm and (c) 20 nm. The inset in (a) schematically illustrates the dimensions mentioned in the text.

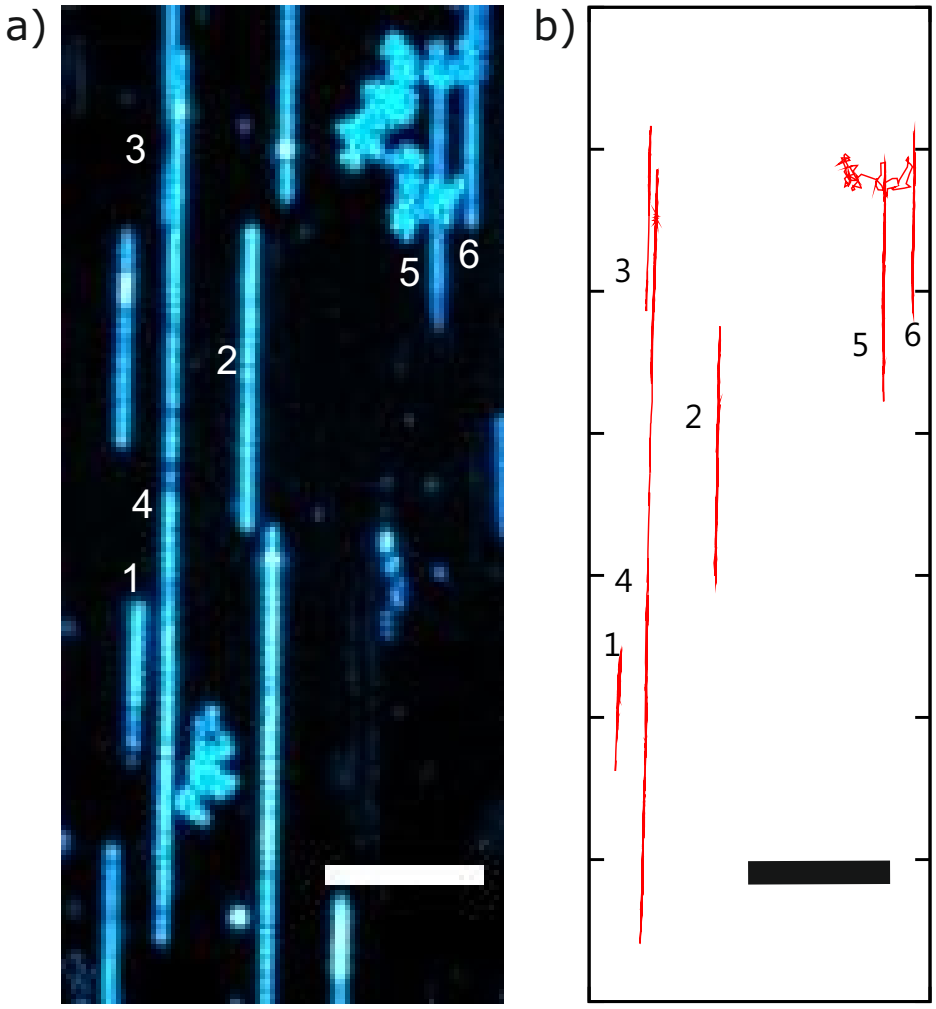

Figure 3.10: Maximum projection and trajectories of single molecules taken from sample 8. (a) Maximum projection of the individual frames of a movie recorded with a fluorescence microscope at a frame rate of 2.5 fps, revealing the pathways of single molecules in the mesoporous structure. The mesopores lie in a plane parallel to the substrate and show a preferential alignment on a macroscopic length scale (scale bar is 5 µm; see also movie M9 on the Supplementary CD). (b) Trajectories of all tracked single molecules in (a) in the mesoporous silica structure. Scale bar is 5 µm.

Furthermore, such low concentrations increase the signal-to-noise ratio because of less background. Figure 3.10.a shows the high contrast for the traces of 10 single molecules that can be obtained under such experimental conditions. The traces of 6 of these molecules were analyzed in greater detail and show a striking parallel alignment, thus indicating the high order of the silica channels at a large scale. Furthermore, the traces show different lengths whereby the trajectory of molecule no. 4 with 27 µm is one of the longest observed in our experiments. However, besides these well-ordered traces,

some molecules diffuse in a random manner. These molecules are presumably at the surface of the sample where no guidance by the channel structure exists. Such behavior has been observed in previous studies[53] and is of no further interest here (movie M9 on the Supplementary CD shows the movement of the molecules in Figure 3.10.a in time lapse (10x)).

The pathway of a single molecule in Figure 3.10.a was obtained by single-particle tracking, that is, the position of the molecule was determined in each of the 1000 frames of the movie. In each frame, the position can be analyzed by simulating the point spread function of the fluorescent spot with a two-dimensional Gaussian. The positioning accuracy depends on the signal-to-noise ratio and is typically in the range of 6 – 8 nm in our experiments (see also Figure 3.11.b). The resulting trajectories are shown in Figure 3.10.b for the corresponding pathways of the molecules in Figure 3.10.a. These trajectories permit a detailed analysis of the movement of the molecules in the channels and give further information about the structure of these channels. As an example, we concentrated on the trajectory no. 1 in Figure 3.10. This trajectory is enlarged in Figure 3.11.a and extends about 4 µm in the channel direction, which is chosen as the x-direction. In y-direction, however, it varies its width, being broad in the top region and thinning out toward the bottom region. This suggests that the molecule may not only travel up and down in a single channel but, in addition, may switch between neighboring channels through defects in the channel walls.

In order to analyze this in more detail, we determined the distribution of the positioning accuracy for this trajectory, which is depicted in Figure 3.11.b. The histogram shows that the most likely positioning accuracy is 6 – 8 nm. This value is clearly smaller than the horizontal pore-to-pore distance (12 – 16 nm; see also Figure 3.9) and hence allows us to localize the dye molecule and distinguish its position from the position in a neighboring channel.

To analyze a possible switching of molecule no. 1 between adjacent channels, the y-axis was enlarged into the nanometer range while keeping the x-axis in the µm range. The plot of the trajectory in this axis system is shown in Figure 3.11.c. It clearly indicates four different distinguishable regions in the y direction marked with four different colors. From this x-y plot of the trajectory, the two separate graphs x(t) and y(t) can be obtained, shown in Figure 3.11.d,e. They provide the movement of the molecule as a function of time separated in x and y direction.[73] From the graph y(t) in Figure 3.11.e, it is obvious that the molecule jumps in the y direction in four

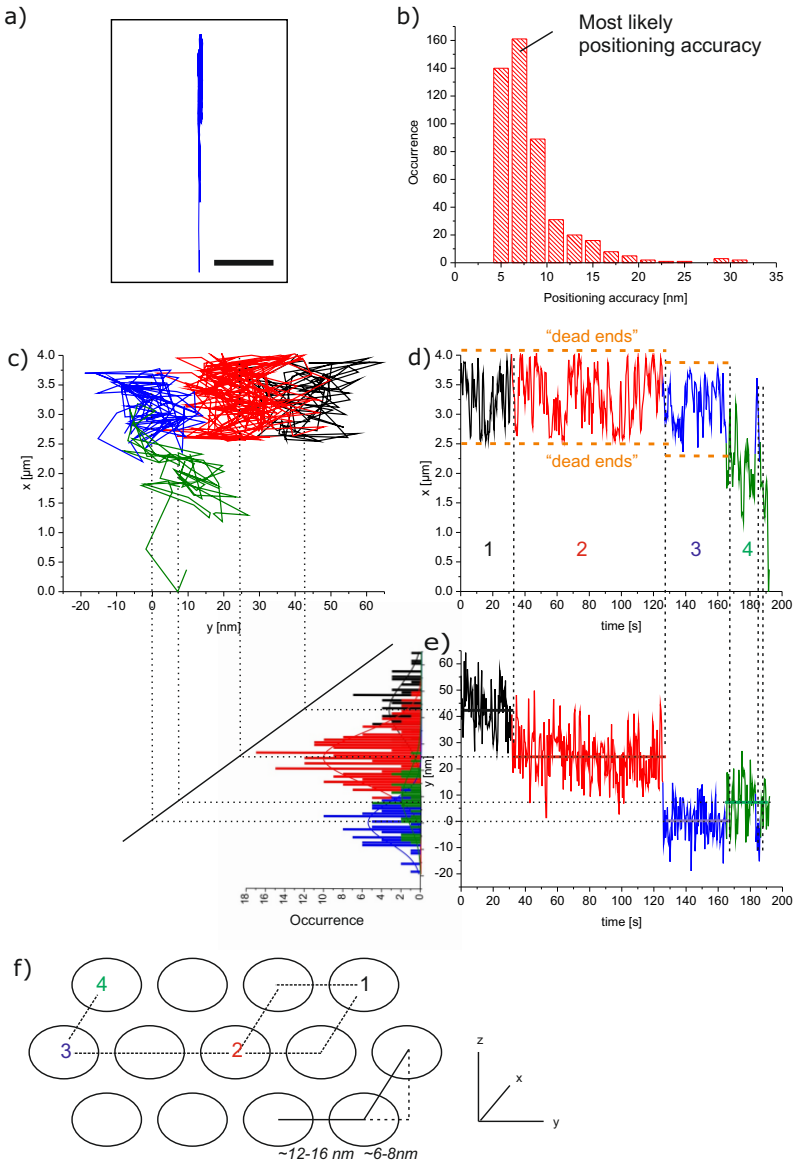

Figure 3.11: Detailed analysis of a trajectory in space and time. (a) Trajectory of molecule no. 1 of the sample depicted in Figure 3.10 (sample 8) with its x-axis parallel to the pore direction, scale bar is 5 µm. (b) Histogram of the positioning accuracy for this trajectory; the most likely positioning accuracy is 6 – 8 nm. (c) Trajectory of molecule no. 1 with the y-axis in the nanometer range and the x-axis in the um range for better clarity. (d,e) Projection of x and y coordinates as a function of time for the single As-TDI molecule no. 1 shows diffusion of the molecule in at least four distinct neighboring pores (marked with black, red, blue, and green), while the molecule moves back and forth in each pore. Histograms of the y lateral coordinate (bottom left) for the four different time intervals with their Gaussian fits (black, 42.8 ± 1.0 nm; red, 24.6 ± 0.7 nm; blue, 0.0 ± 0.7 nm; green, 7.5 ± 0.2 nm). (f) A possible pathway of the single molecule, switching between neighboring channels.

consecutive steps. These distributions can be fitted by four Gaussian curves with a maximum at 42.8 nm (black), 24.6 nm (red), 0.0 nm (blue), and 7.5 nm (green). The distances of these jumps can be correlated to jumps between adjacent channels. The corresponding channel structure in the z-y plane is shown in Figure 3.11.f. With this figure, the jumps of the molecule from region 1 (black) to region 4 (green) can be clearly interpreted as switches between adjacent channels. So the molecule starts in channel 1 and then jumps after 31.6 s through an adjacent channel to channel 2 where it then moves for further 93.9 s. Then it jumps again through an adjacent channel into channel 3 and stays there for an additional 39.2 s to finally jump into channel 4. For this pathway in y the jump widths correlate quite well with a horizontal mesochannel spacing of approximately 13 nm, which is in line with HR-SEM images shown in Figure 3.9. However, we cannot distinguish the ± direction of the jumps in z. Therefore, the jumps in the -z direction could also occur in +z or vice versa. From Figure 3.11.f, it is obvious that the jumps from 1 to 2 and 2 to 3 have to occur in larger defects since they include at least two adjacent channels.

Additional information can be obtained from the graph x(t) in Figure 3.11.d. This plot shows that the molecule diffuses up and down within a range of approximately 1.5 µm in the first 165 s. The most striking pattern of this part of the trajectory is that the molecule frequently hits the same point at the upper and lower part in the x direction, indicating that there exist two blockades. Thus, the molecule is limited in its pathway along the channel direction by two dead ends. Interestingly, these dead ends seem to be nearly at the same position in x for the first two channels and may change somewhat for the third channel. When the molecule finally switches into channel 4 after 165 s, it finds a pathway that extends further in the x direction for more than 2.5 µm. So the molecule reaches the full extension of the trajectory in the x direction not in one channel but by switching into neighboring channels. A similar picture is obtained by the analysis of the other trajectories shown in Figure 3.10 (data not shown).

In summary, a molecule in such a mesoporous system mainly moves up and down along a single channel that may be blocked by imperfections. However, the molecule eventually finds a defect in the side wall which allows it to switch into a neighboring channel. There it can find its way further along the channel. The impact of imperfections that may block the pathway of molecules may be balanced by the defects in the side walls, allowing the molecule to circumvent dead ends. Thus, the molecule seems to move in a maze with channels oriented along one direction including some small

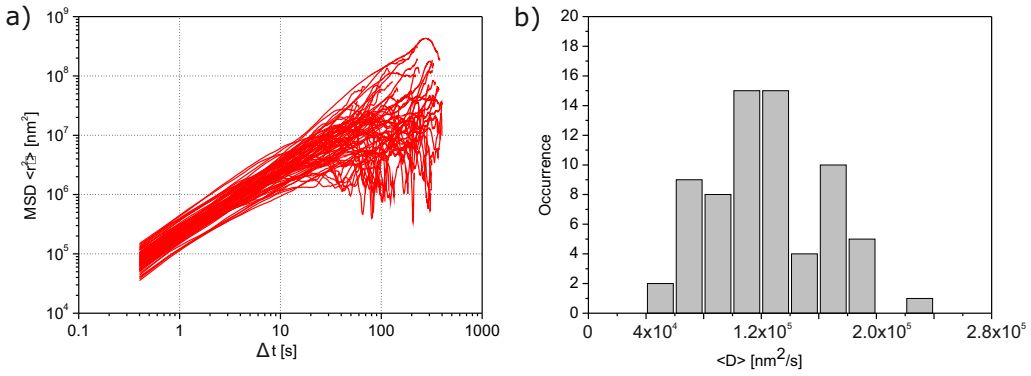

Figure 3.12: Statistical analysis of 70 molecular trajectories. (a) Mean square displacements (MSD) versus time of 70 single-molecule trajectories (As-TDI). (b) Histogram of the mean diffusion coefficient $\langle D \rangle = 1.21 \times 10^5\,\mathrm{nm^2\,s^{-1}}$ extracted from the linear part of the individual MSD plots for 70 As-TDI molecules.

openings to the side and blockades within the channels. This shows the real structure of the mesoporous system including its most relevant defects.

In addition to the structural details discussed above, our experiments reveal the dynamic properties of single molecules in such guest–host systems.[54] For this purpose, a statistical analysis based on the mean-square displacements (MSDs) as a function of time was performed for about 70 single-molecule trajectories for As-TDI. The resulting MSDs are plotted versus time Δt in Figure 3.12.a.

The MSD graphs are approximately linear for at least the first 10 points (2 orders of magnitude in time) as expected for normal diffusion (Brownian motion). Therefore, it is possible to extract a diffusion coefficient using the relationship between MSD and time for a random walk in one dimension, as the molecules diffuse inside the highly oriented, parallel channels:

$$MSD = \langle D(t) \rangle = 2Dt\,, \tag{3.1}$$

where D is the diffusion coefficient. Most of the MSD plots are not perfectly linear for higher values of "Δt" but are slightly curved in the upper regime. This is a further indication of the presence of a confined diffusion, which is consistent with the presence of "dead ends" in the structure as discussed above.

The distribution of the diffusion coefficients for the 70 trajectories is shown in Figure 3.12.b. It resembles a Gaussian curve with a mean diffusion coefficient of $1.21 \times 10^5\,\mathrm{nm^2\,s^{-1}}$, where the linear parts of the MSDs were fitted with a minor de-

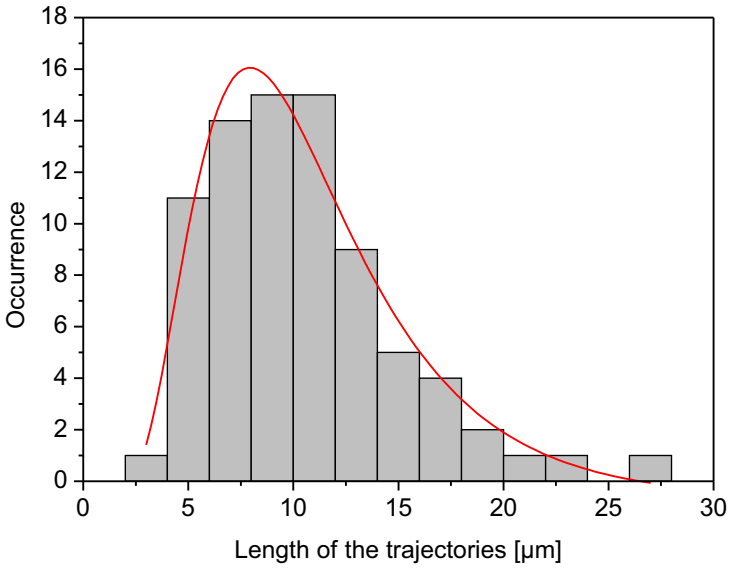

Figure 3.13: Histogram showing the length of the trajectories of 70 molecules within 400 s. The geometric mean and the multiplicative standard deviation of the fitted log-normal distribution (red line) are 9.0 ˣ/ 1.6 µm.[201]

viation of $\pm 2 \times 10^3\,\mathrm{nm^2\,s^{-1}}$. The diffusion coefficient of our samples is about 6 times higher for As-TDI than in other comparable known systems, such as Brij-56.[54] This can be mainly explained by the larger diameter of the pores used in this work (obtained with Pluronic F127 (Ø 6 – 8 nm) compared to Brij-56 (Ø 4 – 5 nm)). In addition, the different interactions between TDI/Brij-56 and TDI/F127 may influence the diffusion coefficient. Furthermore, the width of the distribution shows the heterogeneity of the mesoporous material; that is, it describes the large variation of the interactions between the molecules and their surroundings inside the channels.

The length of the accessible pores can be related to the resulting trajectories as discussed above.[52,53] Seventy molecules were observed, each for 1000 frames, which corresponds to an observation time of 400 s. In this time, the molecules can move up and down in the channels and switch between them. In order to characterize the possibility of a molecule to diffuse along the channel direction in such a time, a statistical plot of the lengths of the trajectories is given in Figure 3.13. The broad distribution of the histogram in Figure 3.13 shows again the large heterogeneity of the system and was fitted with a log-normal function. The geometric mean and the multiplicative standard deviation of this log-normal distribution are 9.0 ˣ/ 1.6 µm.[201]

The results discussed so far demonstrate how the quality of the mesoporous struc-

ture can be assessed directly from as-synthesized samples (i.e., the dye molecules are diffusing inside the template-filled mesopores, and the PDMS stamp is not (necessarily) removed from the structures). For many applications, however, freely accessible mesopores that are not filled with a template are desired. The most common way to remove the template inside the pores is to calcine the material, typically at 400 – 500 °C. However, if the quality of the template-free structures is to be investigated by single-molecule fluorescence microscopy similar to the procedure shown above, calcination of the silica material is not an option since it usually results in a high background fluorescence that makes it impossible to identify single fluorophores. We found that this can be avoided by first extracting the template by refluxing in ethanol for 90 min before calcination. The resulting template-free mesoporous silica films can then again be loaded with various guest molecules. In order to examine the nature of the structure after this treatment, we loaded a fluorophore into the channels by submerging the films in an ethanolic solution of the dye at a concentration of approximately $10^{-10} - 10^{-11}$ M for a few hours under mild agitation, followed by rinsing in ethanol. During the incubation in the ethanolic dye solution, the fluorophores can enter the mesoporous network through open mesopores or defects in the structure. However, without a lubricant phase (like the template), the single dye molecules inside the mesoporous channels appear immobile because of strong interactions with active silanol groups at the walls of the channels (at least at the time scales we typically use for observation, i.e., a few minutes). In order to enable dye movement inside the pores, an atmosphere of an organic solvent such as ethanol or chloroform (good solvents for As-TDI) is required, which results in the formation of a lubricant-like phase inside the pores. In the presence of such a solvent atmosphere, dye molecules inside the pores usually move much faster and also tend to photobleach more rapidly than in unextracted samples. However, it is still possible to follow the movement of single dye molecules and thus obtain the corresponding trajectories indicating the pathways in the mesoporous silica network, as explained above (Figure 3.14). These trajectories indicate that there still is a preferential direction of diffusion; however, by comparing the trajectories to those shown in Figure 3.10, it is obvious that there are more defects in the silica network after this treatment.

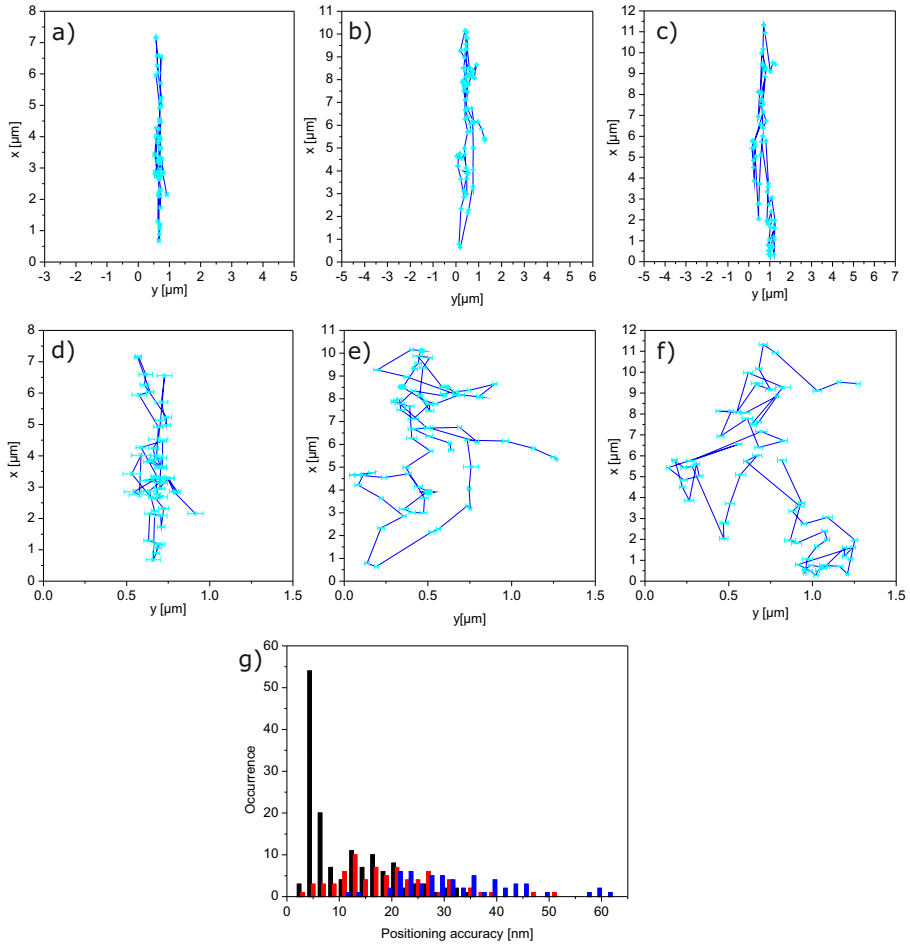

Figure 3.14: Trajectories of single fluorescent dye molecules reloaded into extracted mesoporous silica thin films and exposed to ethanol vapor. Trajectories in sample 9 (a,d) and sample 10 (b,c,e,f) are shown with an axis aspect ratio of 1 in (a-c) and a magnification of the y-axes for the same trajectories in (d-f). All axes are in µm. See also movie M10 (a,d) and M11 (b,c,e,f) on the Supplementary CD. The positioning accuracy in these samples (blue (a,d), black (b,e), and red (c,f)) is plotted in the histogram below (g).

3.4 Conclusion

In this study, we have demonstrated that well-defined macroscopic alignment of Pluronic F127-templated, large-pore mesochannels in mesoporous silica can be achieved by confinement in PDMS microgrooves. The influence of various experimental conditions including the way the channels are filled, the surface modification at the solid/liquid interfaces, and the aspect ratio of the microgrooves were investigated. Furthermore,

we found that the alignment of the mesochannels can change abruptly from parallel to perpendicular depending on the height within the microgrooves.

We also show how single-molecule fluorescence microscopy can be used to directly assess the mesopore structure of the as-synthesized silica thin films, how a maximum projection can give a global overview on the pore structure, how it can give deeper insights into the real microscopic structure of the mesoporous silica framework, and how it can help us to gain dynamic information about the diffusion of guest molecules inside these compounds. The spatial accuracy in these experiments is high enough to observe movements of the dye molecules between individual channels in the mesoporous silica. This high resolution allows us to observe details of long-distance movement of the molecules: in order to travel the very large distances in these highly ordered structures, the molecules circumvent defects by moving to neighboring channels. Finally, we illustrate how solvent-extracted samples can be investigated by this technique and how the defect concentration increases as a result of template removal.

3.5 Experimental Part

If not stated otherwise, all chemicals were used as received. Absolute ethanol, tetraethylorthosilicate (TEOS), and Pluronic F127 were purchased from Sigma-Aldrich Co. HCl (1 M) was purchased from AppliChem GmbH. Standard glass coverslips (#1, 22 x 22 mm) were purchased from Gerhard Menzel, Glasbearbeitungswerk GmbH & Co. KG. Hellmanex cleaning solution was purchased from Hellma GmbH & Co. KG. PDMS and PDMS curing agent were purchased from Dow Corning Co. 1H,1H,2H,2H-perfluorooctyltriethoxysilane (PFOTS) was purchased from abcr GmbH & Co. KG. Aqueous ammonium hydroxide solution (25 %) was purchased from VWR International GmbH.

Exposure to oxygen plasma was carried out with a Femto Plasma System from Diener Electronic typically operated at a power of 50 W and an oxygen flow of 4 – 5 sccm. Atomic force microscopy (AFM) images were recorded with a Nanoink NScriptor DPN System in close contact mode. One-dimensional X-ray diffraction (XRD) patterns were obtained with a Bruker D8 Discover X-ray diffractometer using Cu K_α radiation. Scanning electron microscopy (SEM) and high-resolution scanning electron microscopy (HR-SEM) images were obtained with a JEOL JSM6500F scanning electron microscope equipped with a field-emission gun, typically operated at an acceleration voltage of 4 kV and 10 kV and a working distance of 10 mm and 7 mm for SEM and HR-SEM,

respectively. Single-molecule fluorescence images of the as-synthesized samples with the PDMS stamp still in place were recorded with a wide-field setup, using an Eclipse TE200 (Nikon) epi-fluorescence microscope with a high numerical aperture (NA) oil-immersion objective (Nikon Plan Apo, 100x, NA = 1.40). The fluorescent dye N-(2,6-diisopropylphenyl)-N'-octylterrylene-3,4,11,12-tetracarboxdiimide (called As-TDI in this work; for the chemical structure, see Figure 3.10 and Reference 202) with a high photostability and excellent quantum yield were incorporated into the material in single-molecule concentrations (10^{-10} – 10^{-11} mol L^{-1}). The dye was kindly provided by the research group of Prof. Klaus Müllen (Max-Planck-Institute for Polymer Research, Mainz, Germany).

The molecules were excited at 633 nm with a He-Ne gas laser (Coherent, 75 mW maximum at 632.8 nm) with an intensity of 0.3 kW cm^{-2}. Their fluorescence was detected with a back-illuminated electron multiplying charge-coupled device (EM-CCD) camera in frame transfer mode (Andor iXon DV897). Incident laser light was blocked by a dichroic mirror (640 nm cutoff, AHF) and a band-pass filter (730/140 AHF). One pixel on the camera chip corresponds to 154 nm on the sample. The individual molecule patterns were fitted by a Gaussian function

$$f(x, y, A, w) = A \cdot e^{-\left(\frac{x-x_0}{w}\right)} \cdot e^{-\left(\frac{y-y_0}{w}\right)},$$

where A and w are the amplitude and the width of the Gaussian curve, respectively. The method was described in detail in previous studies.[53,70,71] The resulting positions can be combined frame by frame to form molecular trajectories as described in the text.

The EISA precursor solution was prepared following a procedure from Okubo *et al.*[42] with slight modifications. First, 700 µL of Millipore water and 100 µL of HCl (1 M) were mixed with 4.4 g of ethanol (abs.) and 1.0 g of tetraethylorthosilicate (TEOS) and stirred at 65 °C for 1 h in a sealed polypropylene beaker. At the same time, 475 mg of Pluronic F127 was mixed with 4.4 g of ethanol and stirred at room temperature for 1 h. Then, the surfactant solution was added to the silica solution, and the resulting clear liquid of molar composition $1.00 : 7.37 \times 10^{-3} : 39.8 : 2.19 \times 10^{-2} : 9.27$ (TEOS/F127/ethanol/HCl/water) was stirred for another 2 – 4 h at room temperature. PDMS stamps were fabricated by replica molding from photolithographically patterned masters using standard techniques. The final thickness of the stamps was typically about 1.0 – 1.5 mm. The substrates were cleaned by submerging them

in a water/Hellmanex solution at 60 °C for 1 h, followed by ultrasonic agitation for 3 min and rinsing with DI water. For further surface modification, the cleaned substrates were treated by submersion in piranha solution for 1 h or by exposing them to oxygen plasma for 15 min. When hydrophilic substrates were desired, the substrates were directly used after this treatment. For hydrophobic substrates, the activated glass coverslips were placed in a desiccator alongside a Petri dish with 1H,1H,2H,2H-perfluorooctyltriethoxysilane (PFOTS), the pressure was reduced until the boiling pressure of the silane was reached at ambient temperature (approximately 7×10^{-2} mbar), and the substrates were incubated in the resulting silane atmosphere for 3 – 4 h. When hydrophobic stamps were desired, the PDMS replica molds were used without further modifications because PDMS is intrinsically hydrophobic. To render the PDMS hydrophilic, it was exposed to oxygen plasma for 90 s and then submerged in an aqueous solution of TEOS (3 mM) and HCl (96 mM) for 2 h. It is well-known that functionalized trialkoxy- and trichlorosilanes can be grafted to reactive surface hydroxyl groups from the liquid or the gas phase.[203,204]

In some cases, extraction of the template was achieved by refluxing the samples in ethanol (abs.) for 90 min after they had been subjected to an NH_3 atmosphere obtained by incubating the samples in a closed container next to a Petri dish containing an ammonium hydroxide solution (25 % in water) at room temperature for 10 – 15 min (to promote silica condensation). Subsequently, the samples were calcined in air by first heating at 60 °C for 90 min (ramp: 1 °C min^{-1}), then at 160 °C for 90 min (ramp: 1 °C min^{-1}), and finally at 400 °C for 4 h (ramp: 1 °C min^{-1}).

An overview of the different samples discussed in this work including precise treatment and synthesis conditions can be found in Table 3.1.

Table 3.1: Overview of the samples discussed in the text[1]

Sample Code	Microgroove heigt [µm]	Surface Properties of PDMS Stamp	Surface Properties of Glass Substrate	Microgroove Filling Method	Ageing Conditions	Post Treatment
1	2	Hydrophilic	Hydrophobic	Capillary Flow	48 h at RT and amb. hum.	None
2	2	Hydrophilic	Hydrophobic	Capillary Flow	48 h at RT and amb. hum.	None
3	2	Hydrophobic	Neutral (untreated)	Stamping	48 h at RT and amb. hum.	None
4	2	Hydrophilic	Hydrophobic	Capillary Flow	48 h at RT and amb. hum.	None
5	2	Hydrophilic	Hydrophobic	Capillary Flow	48 h at RT and amb. hum.	Removal of PDMS Stamp
6	4-8	Hydrophobic	Hydrophilic	Capillary Flow	21 h at RT and sat. EtOH atm. and 24 h at RT and amb. hum.	None
7	4-8	Hydrophobic	Hydrophilic	Capillary Flow	21 h at RT and sat. EtOH atm. and 24 h at RT and amb. hum.	Removal of PDMS Stamp and standard SEM cross-section preparation
8	4-8	Hydrophobic	Hydrophilic	Capillary Flow	21 h at RT and sat. EtOH atm. and 24 h at RT and amb. hum.	None
9	4-8	Hydrophobic	Hydrophilic	Capillary Flow	21 h at RT and sat. EtOH atm. and 24 h at RT and amb. hum.	Removal of PDMS Stamp, incubation in NH_3-atm., Extraction in EtOH (reflux), calcination in air
10	4-8	Hydrophobic	Hydrophilic	Capillary Flow	21 h at RT and sat. EtOH atm. and 24 h at RT and amb. hum.	Removal of PDMS Stamp, incubation in NH_3-atm., Extraction in EtOH (reflux), calcination in air

[1]See the experimental part for further details on the entries of the table; rt = room temperature (typically 22 – 25 °C); amb. hum. = ambient humidity (typically 30 – 60 %); atm. = atmosphere

Chapter 4

. . . . . .

Electrophoresis of Single Dye Molecules in Highly Oriented Mesoporous Silica Channels

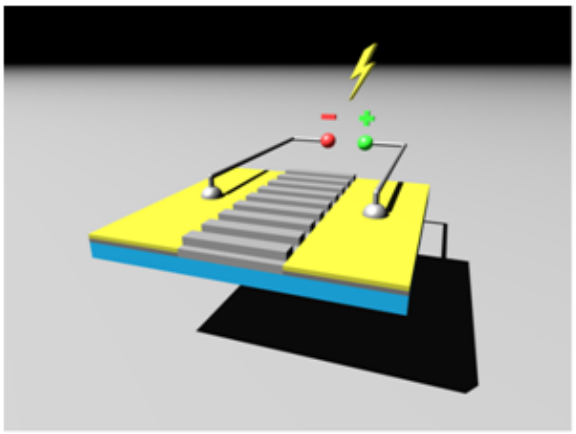

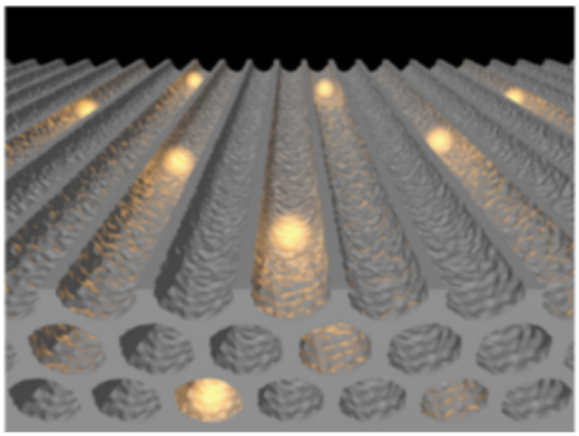

This chapter is based on a manuscript of an article by B. Rühle, M. Davies, K. Müllen, T. Bein, and C. Bräuchle, which is currently in preparation.

4.1 Abstract

In this paper we show for the first time the controlled movement of single molecules in highly oriented, template-filled mesoporous silica thin films under the influence of an electric field. Moreover, we propose a model for the structure of the host and for single molecule diffusion of charged and uncharged species. The velocity of the

charged molecules increases with increasing electric field strength and could therefore be directly influenced by an external stimulus. By applying an electric field diagonally to the aligned pores, we could observe that the molecules which were located in the mesopores showed a directed movement along the mesoporous silica channels, whereas molecules next to, but outside of the structure followed the electric field lines. In addition, we show the application of the mesoporous host material for separation of differently charged molecules.

4.2 Introduction

Electrophoresis and electrochemical sensing are important tools in biochemistry and biology and are commonly used for separation and detection of various biomolecules. The separation and detection result from the different mobility of these molecules depending on their size, charge and conformation as well as their interaction with the host material. Extending these concepts to mesoporous silica host systems could be very beneficial due to the enormous structural and functional versatility of these systems. Although there are several examples in which modified mesoporous silica is used for separation and as an electrode coating material for electrochemical sensing,[205–208] little is known about the detailed behavior and interactions of the guest species inside the mesoporous silica host channels on a single molecule basis.

In this work, we investigated mesoporous silica thin films with a highly ordered mesoporous structure in order to gain deeper insights into the triggered movement under the influence of an electric field, pure diffusional behavior and the interactions of charged guests inside the porous silica host. This is, to the best of our knowledge, the first time a direct observation of the movement of charged guest species in mesoporous silica hosts is described and analyzed. This analysis was carried out using single molecule microscopy, which allows for a detailed investigation of the diffusional pathways and the triggered movement of uncharged and charged dye molecules under the influence of an electric field and gives deeper insights into the interaction of the guest molecules with their porous host and with the electric field. Moreover, a separation of differently charged molecules inside the host structure could be directly observed on a single molecule basis.

We have recently demonstrated that well-defined macroscopic alignment of large-pore mesochannels (diameter about 9 nm) in mesoporous silica can be achieved by confinement in poly(dimethylsiloxane) microgrooves. The detailed synthesis and anal-

ysis of these systems was published elsewhere[43] and is therefore described only briefly here (see Section 4.5). In this work we demonstrate the feasibility of electrophoresis experiments in such highly oriented silica channels. For our investigations, differently charged fluorescent dye molecules were incorporated into mesoporous silica channels in single molecule concentrations ($10^{-10} - 10^{-11}$ M) and directly influenced by an externally applied electric field. We also carried out investigations with uncharged terrylenediimide (TDI) dyes to ensure the integrity of the mesoporous structure under the experimental conditions, i.e., the presence of strong electric fields.

By determining the position of the molecules in each frame of a movie recorded with a wide-field fluorescence microscope and overlaying the individual frames of the movie, the pathway of the molecules can be depicted. Specifically, each pixel in the overlay assumes the maximum value of the corresponding pixels in the individual frames that was reached during the recording time. The final overlay consists only of the brightest pixels of the movie. We call this procedure a "maximum projection" (see also Rühle *et al.*[43]). This method gives a global overview of the pore alignment. In addition, single molecule tracking allowed for a more detailed structural and dynamic analysis of the guest molecule movement.

4.3 Results and Discussion

In order to verify the mesopore alignment of the porous host material, we used uncharged guest molecules (Dip-TDI, As-TDI and Sw-TDI, chemical structures see Figure 4.1) in a preliminary experiment. The movies recorded with our wide-field microscope (see movie M1, movie M2 and movie M3 on the Supplementary CD) clearly show a structured movement of the molecules parallel to the pore direction of the silica channels. The maximum projections of the individual frames of the movies directly depict the pathways of the molecules and thus the macroscopic alignment of the mesoporous channels (Figure 4.1.a,b,c). Single molecule trajectories reveal the structure of the channels in even more detail, showing defects and dead ends present in the porous system (Figure 4.1.d,e,f). By analyzing the trajectories of the molecules in space and time one can even observe the switching of guest molecules from one channel to another channel through defects in the silica walls, as also discussed in our previous report.[43]

By incorporating charged dye molecules into the same samples we observed that uncharged molecules show structured movement along the well aligned mesochannels,

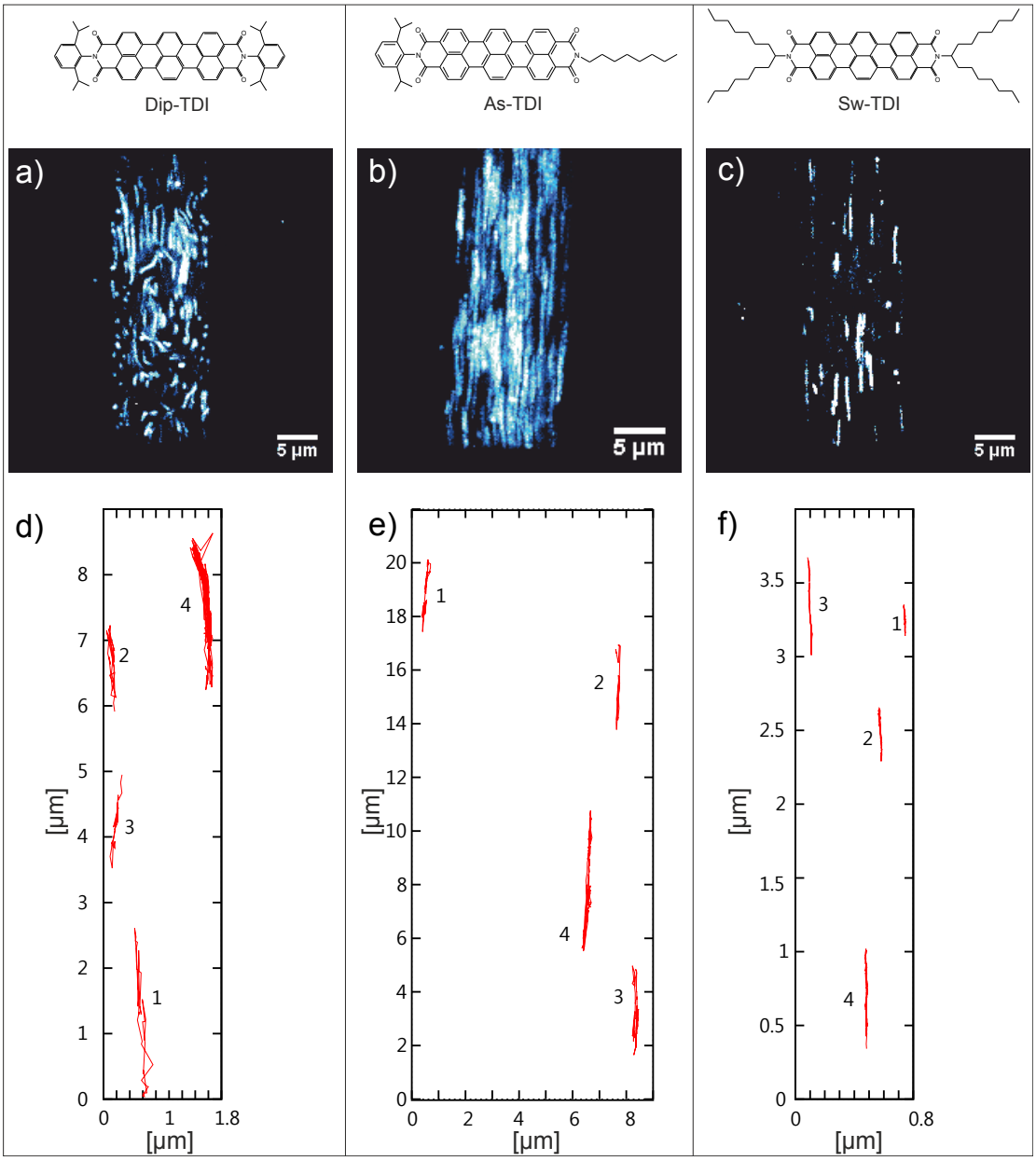

Figure 4.1: Maximum projection of several consecutive wide-field images indicating the alignment of the mesoporous silica channels. (a) Dip-TDI (N,N'-bis(2,6-diisopropylphenyl)terrylene-3,4,11,12-tetracarboxdiimide), (b) As-TDI (N-(2,6-diisopropylphenyl)-N'-octylterrylene-3,4,11,12-tetracarboxdiimide) and (c) Sw-TDI (N,N'-(pentadecan-8-yl)terrylene-3,4,11,12-tetracarboxdiimide) molecules were incorporated as fluorescent guest dyes into the mesopores during the synthesis in order to gain information about pore directionality. Exemplary single molecule trajectories of (d) DIP-TDI, (e) As-TDI and (f) Sw-TDI reveal the structure and alignment of the mesopores.

while charged molecules took totally different, more random diffusional pathways. We mixed uncharged As-TDI molecules with charged Qu81 molecules (chemical structure

shown in Figure 4.2.a) and incorporated them into the same sample. Qu81 was excited with a 532 nm diode Laser in order to be able to spectrally separate its fluorescence signal from the signal of As-TDI molecules which were excited with a He-Ne-Laser (633 nm), and we detected both fluorescence signals simultaneously in different channels. Channel 1 shows the fluorescence signal of Qu81 molecules and Channel 2 shows the signal of As-TDI molecules. The uncharged molecules (As-TDI) showed structured movement up and down (see movie M4 on the Supplementary CD and also maximum projection in Figure 4.2.b) while the charged molecules (Qu81) moved more randomly (see movie M5 on the Supplementary CD and also maximum projection in Figure 4.2.a). By switching on the electric field (1200 $V\,cm^{-1}$) we could observe a directed movement of the charged Qu81 molecules before photobleaching (movie M6 on the Supplementary CD). As expected, the diffusional movement of the uncharged As-TDI molecules was not affected by the electric field. They continued moving in a structured way exactly as they did without the electric field. We consider this a strong indication that the highly ordered sample structure is maintained under the influence of a (strong) electric field and that the rather unstructured movement of the charged dyes is due to other effects than the destruction of the ordered mesoporous structure (see also discussion below).

In a further experiment, we introduced charged Atto633 molecules and uncharged As-TDI molecules into the same sample. Both dyes were excited with a 633 nm He-Ne Laser and detected in the same channel. We detected two different species. Both could be clearly distinguished due to their physical properties. The species that moved randomly was bleaching faster and since it is known that Atto dyes are not as photostable as TDI dyes,[209] we assigned these signals to Atto633 molecules. The molecules which moved in a structured way showed good photostability and could therefore be identified as As-TDI molecules (see movie M7 on the Supplementary CD). Figure 4.3.a shows the maximum projection of all frames of the movie M7 (Supplementary CD) recorded with our fluorescence microscope, revealing the pathways of both species of single molecules in the mesoporous structure. A maximum projection of the last 100 frames of the same movie M7 reveals the pathway of only one species (As-TDI) which shows structured movement (Figure 4.3.b), while all unstructured Atto633 molecules have already been photo-bleached.

In order to compare the patterns of movement of both dyes, exemplary trajectories of each dye are plotted in Figure 4.3.c. As-TDI molecules (red trajectories in Figure 4.3.c) move up and down in y-direction (which is the direction of the mesoporous

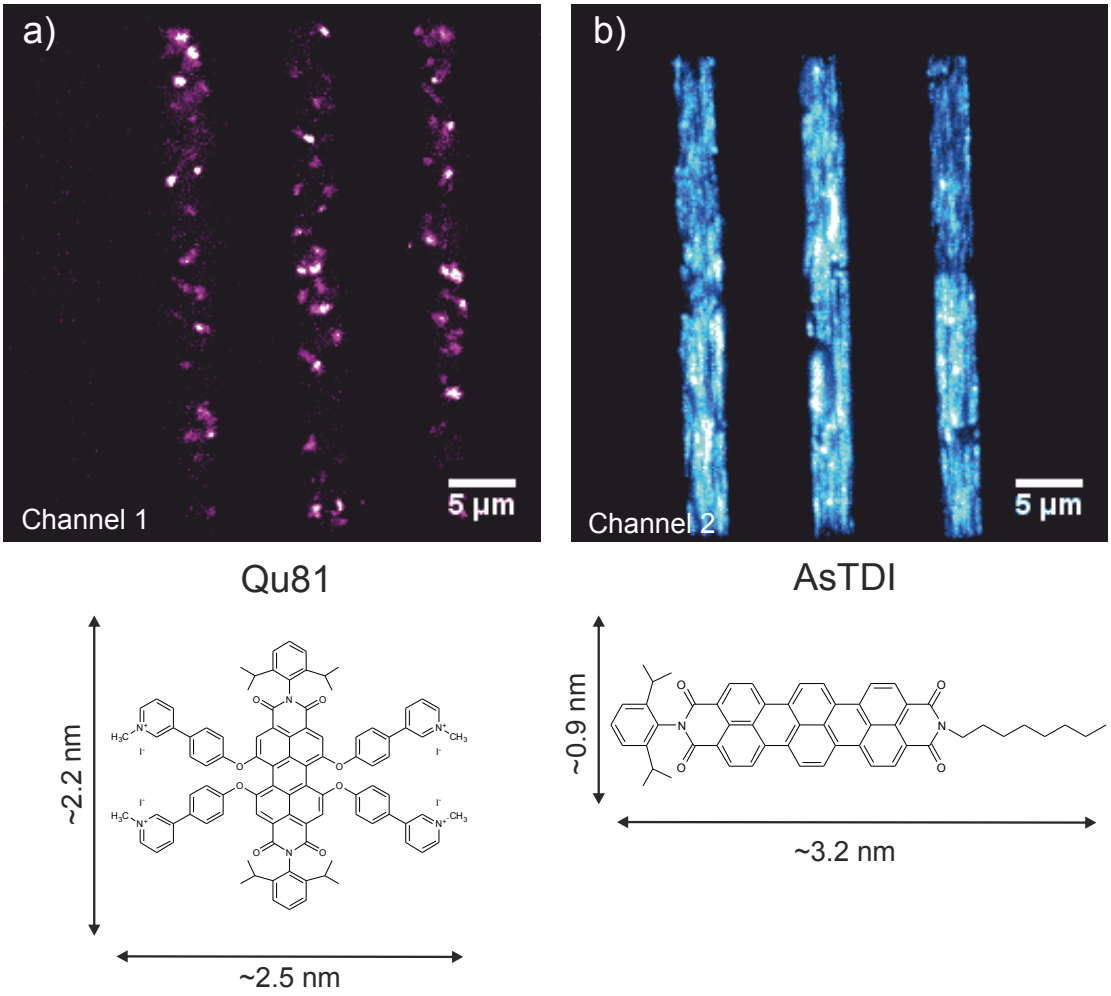

Figure 4.2: Maximum projection of the individual frames of a movie recorded with a fluorescence microscope at a frame rate of 2.5 frames per second (fps), revealing the pathways of (a) Qu81 and (b) As-TDI molecules.

silica channels) in a structured way, while Atto633 molecules (green trajectories in Figure 4.3.c) move rather randomly, having a greater propagation in x-direction and lacking the preferential movement in y-direction.

In order to address the question why charged dye molecules showed a different pattern of movement than uncharged dyes, we tested various charged dyes (Qu81, Atto633, Atto532, Ws-TDI, KP160) to rule out that the random movement inside the porous host was due to the chemical nature of the respective dye. However, all of the charged dyes that were investigated showed the same behavior in the material. We believe that this phenomenon can be explained by assuming the following model of the host–guest system (see Figure 4.4). For the synthesis of the mesoporous silica channels we used the triblock-copolymer Pluronic F127 in an evaporation-induced

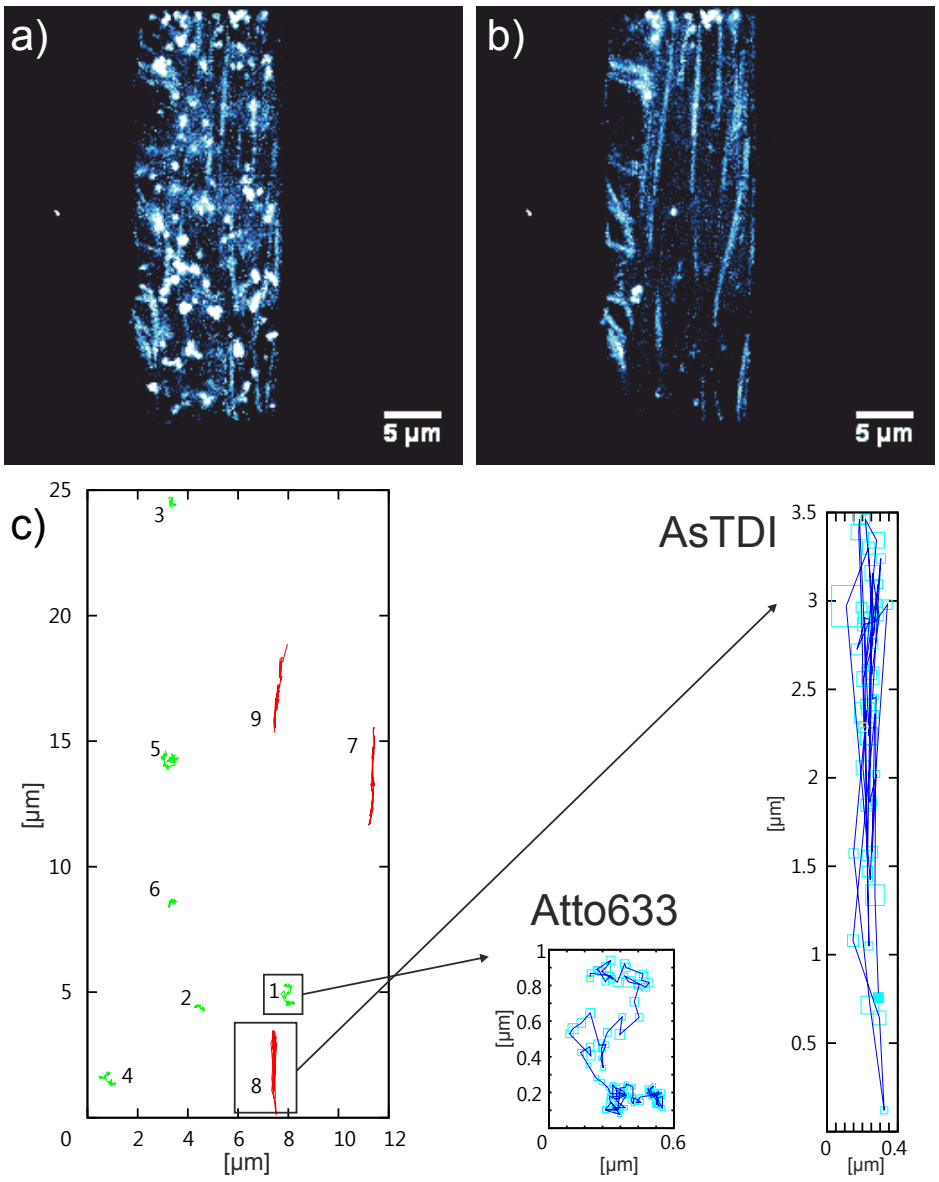

Figure 4.3: Maximum projection and trajectories of As-TDI and Atto633. (a) Maximum projection of the individual frames of a movie recorded with a fluorescence microscope at a frame rate of 2.5 fps, revealing the pathways of two different species of single molecules (Atto633 and As-TDI) in the mesoporous structure. (b) Maximum projection after photobleaching revealing only one species (As-TDI), which shows structured movement. (c) Direct comparison of exemplary trajectories of As-TDI (red) and Atto633 (green). As-TDI molecules show structured, aligned pathways while Atto633 molecules feature an unstructured, random movement.

self-assembly (EISA) approach. This template creates mesopores by forming cylindrical micelles in the polar solvent mixture with a diameter of about 9 nm, with the micelles featuring a hydrophobic interior and a hydrophilic exterior. The hydrophilic

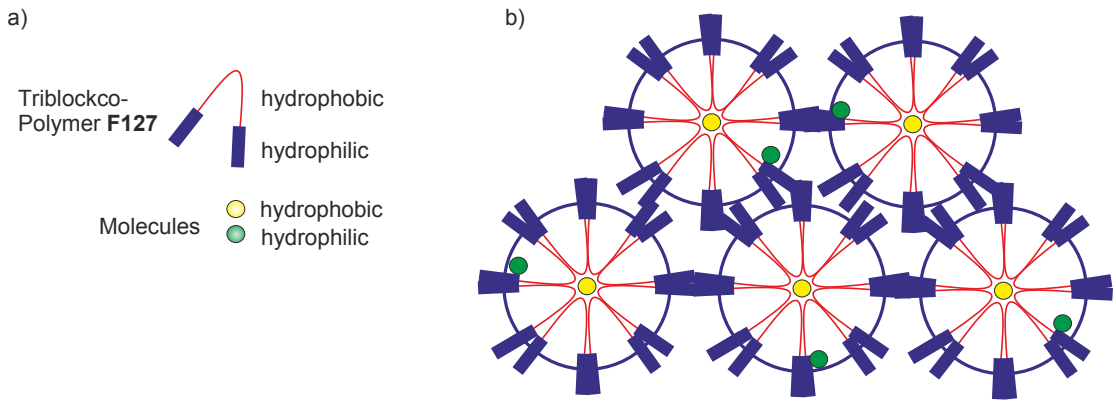

Figure 4.4: Model of the guest–host system.

ends of the template protrude into the silica walls and can cause intrawall porosity.[210–212] The existence of such intrawall pores was already described in the literature for Pluronic-templated mesoporous silica and has been studied by sorption measurements and electron microscopy of nanomolded platinum replicas.[213–218] In unextracted (i.e. template-filled) mesoporous silica films, we assume that these outer parts of the micellar template structure are preferred by hydrophilic, charged molecules whereas hydrophobic, uncharged molecules prefer the hydrophobic core of the micelles from where they cannot access the defects in the pore wall. This could be a possible explanation why uncharged molecules move in a structured way inside the channels, while charged molecules moving in close proximity to the pore wall can access defects and switch to other channels.

As a further proof of this model and in order to further assure that the charged molecules are moving inside the pores of the mesoporous silica structure despite their rather random movement patterns, we prepared a sample containing only Atto633 in a single dye molecule concentration and applied an electric field diagonally to the aligned pores (movie M8 on the Supplementary CD). We could observe that the molecules which were located in the mesopores showed a directed movement along the mesoporous silica channels whereas molecules next to, but outside of the structure followed the electric field lines. The maximum projection of the individual frames of movie M8 is depicted in Figure 4.5.a. We also observed molecules next to the silica structure changing their direction abruptly when slipping into the mesoporous structure (see exemplary trajectory 3 in Figure 4.5.b) and also slipping out of it (see exemplary trajectory 1 in Figure 4.5.b). This is possible because of numerous defects in the silica walls as explained above. Moreover, the experiment demonstrates that the molecules are guided by the mesoporous silica channels (see exemplary trajectory 2 in

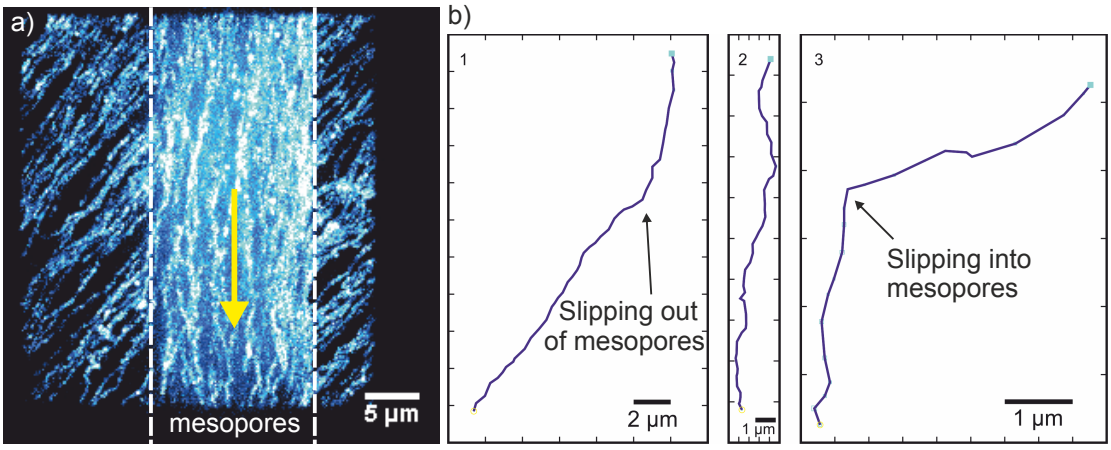

Figure 4.5: Electrophoresis of Atto633 molecules in a diagonal electric field. (a) Maximum projection of the individual frames of a movie recorded with a fluorescence microscope revealing the pathway of Atto633 molecules influenced by a diagonal electric field. Molecules inside the mesoporous structure are guided by the aligned mesopore channels, whereas molecules next to the microgroove follow the electric field lines. The yellow arrow indicates the direction of movement of the molecules inside the mesopores. (b) Exemplary trajectories of Atto633.

Figure 4.5.b) aligned in y-direction. The trajectories of the charged dye molecules are again not as straight as in the case of uncharged dye molecules, as explained above in the guest–host model (Figure 4.4).

We then investigated the influence of the electric field strength on the average velocity of single Atto633 dye molecules. For this purpose the electric field was applied along the channel direction. At the beginning, the electric field was adjusted to 1800 $\mathrm{V\,cm^{-1}}$ and then reduced stepwise to 100 $\mathrm{V\,cm^{-1}}$. The velocity of the molecules decreases with decreasing electric field strength and could therefore be directly influenced by the electric field acting as an external stimulus. Figure 4.6 shows the maximum projection of the individual frames of movie M9 (see Supplementary CD) revealing the pathway of Atto633 molecules pulled along the silica channels. By averaging the positions (pixels converted to distance) *versus* time of at least five individual molecules for each electric field strength, the dependence of the average velocity on the electric field strength could be calculated (Figure 4.6.b). The error bars show the standard deviations of the averages. A linear trend can be seen for the increase of the average velocities with the electric field strength. From the slope we can calculate the mobility ($b = 5 \times 10^{-8}\,\mathrm{cm^2\,V^{-1}\,s^{-1}}$) of the Atto633 molecules in the silica host.

To demonstrate the possibility of electrophoretic separation, we incorporated WS-TDI (negatively charged, molecular structure see Figure 4.7) and KP160 (positively

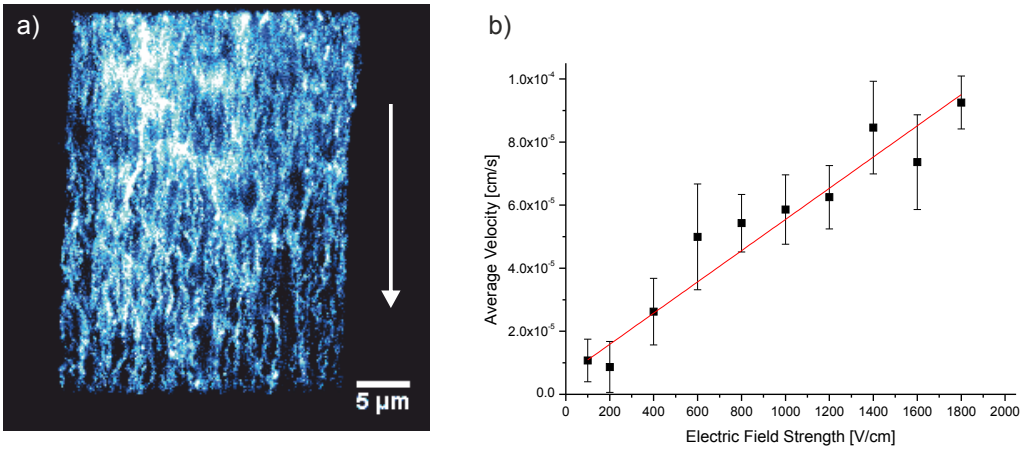

Figure 4.6: Maximum projection and average velocity. (a) Maximum projection of the individual frames of a movie recorded with a fluorescence microscope revealing the pathway of Atto633 molecules pulled along the silica channels by an electric field. The white arrow indicates the direction of movement of the molecules inside the mesopores. (b) Plot of the average velocity of Atto633 molecules versus electric field strength increasing from 100 to 1800 $\mathrm{V\,cm^{-1}}$. A linear fit ($y = a + bx$) with $a = 6 \times 10^{-6}\,\mathrm{cm\,s^{-1}}$ and $b = 5 \times 10^{-8}\,\mathrm{cm^2\,V^{-1}\,s^{-1}}$ is shown in red.

charged, molecular structure see Figure 4.7) into the same sample. Again, we detect both fluorescence signals simultaneously in different channels. Channel 1 shows the fluorescence signal of KP160 molecules (see maximum projection in Figure 4.7.a and movie M10 on the Supplementary CD) moving in the opposite direction as WS-TDI molecules in Channel 2 (see maximum projection in Figure 4.7.b and movie M10 on the Supplementary CD). By switching the electric field on and off, the directed movement of the molecules could be controlled. Thus we demonstrated the feasibility of separating differently charged molecules in a porous silica host.

4.4 Conclusion

In this study we have demonstrated the controlled movement of single molecules in highly oriented, template-filled mesoporous silica thin films under the influence of an electric field. Single molecule trajectories directly reveal the mesoporous structure of the silica thin films with their defects and dead ends. By incorporating various uncharged dyes into the mesochannels we observed structured movement along the well-defined large-pore mesochannels in y-direction, while charged molecules took totally different, more random diffusional pathways and showed a greater propagation

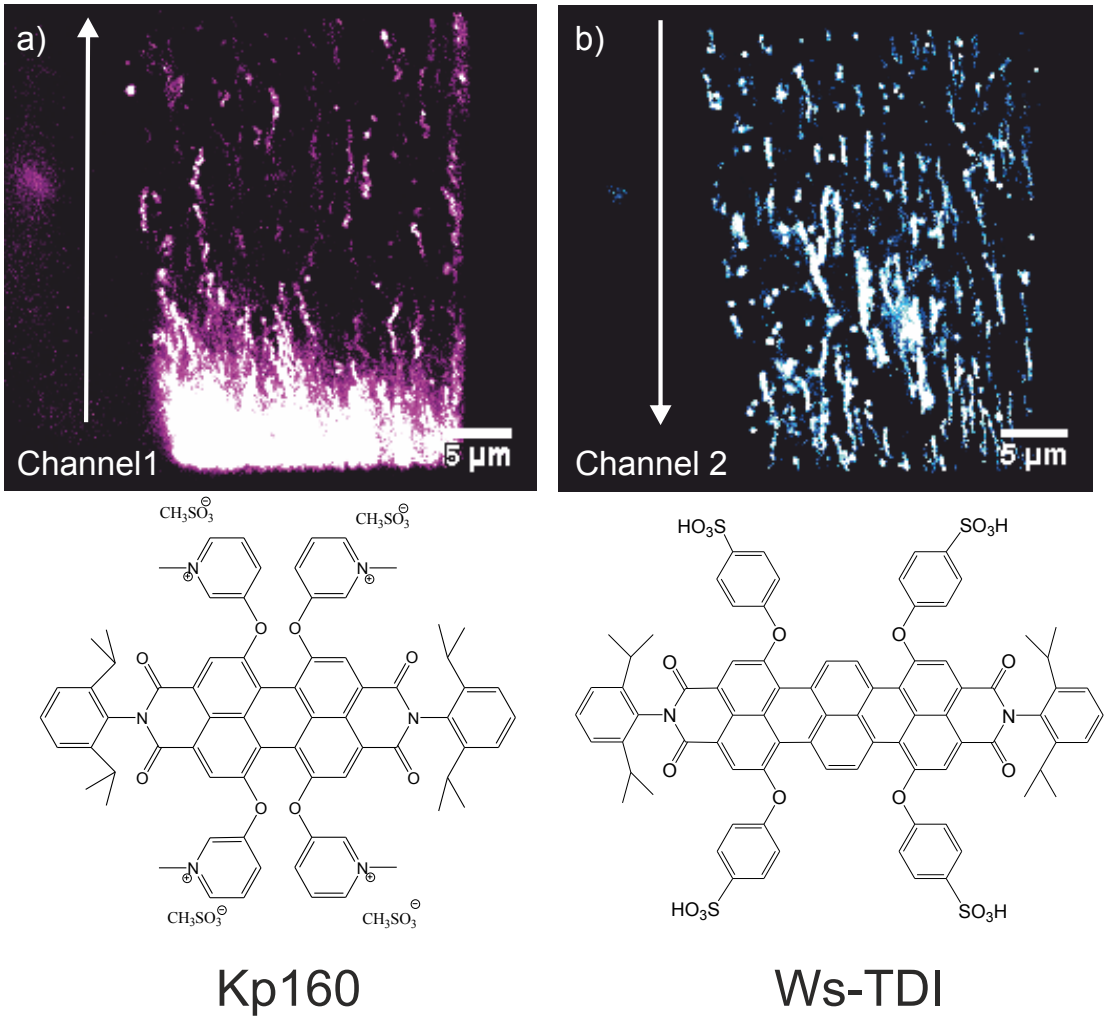

Figure 4.7: Separation of differently charged dyes. The maximum projections of the individual frames of a movie recorded with a fluorescence microscope at a frame rate of 2.5 fps reveal the pathways of (a) KP160 and (b) Ws-TDI molecules. The white arrows indicate the direction of movement of the molecules inside the mesopores under the influence of an electric field (1000 V cm^{-1}).

in x-direction. Based on these observations we presented a host–guest model which explains the different pathways of the molecules in such mesoporous materials.

Furthermore, the influence of the electric field strength on charged molecules was investigated. The velocity of the charged molecules increased monotonically with increasing electric field strength, were the slope of the plot is the mobility of the guest molecule inside the host. By applying a diagonal electric field we could even observe molecules switching into the mesoporous structure, guided by the well aligned pores and also switching out of the mesoporous material through defects in the silica walls. Finally, we illustrate the controlled separation of differently charged molecules in the

template-filled mesoporous silica thin films which can be directly observed with our single molecule fluorescence wide-field microscope.

4.5 Experimental Part

Single molecule fluorescence images were recorded with a wide-field setup, using an Eclipse TE200 (Nikon) epi-fluorescence microscope with a high numerical aperture (NA) oil-immersion objective (Nikon Plan Apo x100, NA = 1.40). The fluorescent uncharged dyes N-(2,6-diisopropylphenyl)-N'-octylterrylene-3,4:11,12-tetracarboxdiimide (called As-TDI in this work and Reference 202), N,N'-bis(2,6-diisopropylphenyl)-terrylene-3,4:11,12-tetracarboxdiimide (called Dip-TDI in this work) and N,N'-bis(pentadecan-8-yl)-terrylene-3,4:11,12-tetracarboxdiimide (called Sw-TDI in this work) (for their chemical structures see Figure 4.1) with a high photostability and excellent quantum yield and the charged fluorescent dyes N,N'-bis(2,6-diisopropylphenyl)-1,6,7,12-tetra-(1-methyl-3-(4-phenoxy)-pyridinium)-perylene-3,4:9,10-tetracarboxdiimide tetraiodide (called Qu81 in this work; chemical structure in Figure 4.2 and synthesized as described in Reference 219), N,N'-bis(2,6-diisopropylphenyl)-1,6,7,12-tetra-(1-methylpyridinium-3-oxy)-perylene-3,4:9,10-tetracarboxdiimide tetramethanesulfonate (called KP160 in this work and synthesized as described in Reference 220) and N,N'-bis(2,6-diisopropylphenyl)-1,6,9,14-tetra-(4-sulfonylphenoxy)-terrylene-3,4:11,12-tetracarboxdiimide (called Ws-TDI in this work and synthesized as described in Reference 221) (chemical structures in Figure 4.4) were incorporated into the material in single molecule concentrations (10^{-10} – 10^{-11} M).

The molecules were either excited at 633 nm with a He-Ne gas laser (Coherent, 75 mW maximum at 632.8 nm) with an intensity of 0.3 kW cm^{-2} or at 532 nm with a diode pumped solid-state laser (Cobolt Samba TM Laser) with an intensity of 0.05 kW cm^{-2}. Their fluorescence was detected with a back-illuminated electron multiplying charge-coupled device (EM-CCD) camera in frame transfer mode (Andor iXon DV897, 512x512 pixels). Incident laser light was blocked by a dichroic mirror (dual line beam splitter 532/633, AHF Analysentechnik) and by band-pass filters (675/250 and 560/40 for Channel 1 and 730/140 for Channel 2, AHF Analysentechnik). One pixel on the camera chip corresponds to 154 nm on the sample. The movement of the single molecules was detected in dependence of an electric field. In this study, electric field strengths up to 1800 V/cm were used. Single molecule tracking was done by

fitting the fluorescence spot by a 2D-Gaussian function:

$$f(x, y, A, w) = Ae^{-\left(\frac{x-x_0}{w}\right)^2} e^{-\left(\frac{y-y_0}{w}\right)^2} ,$$

where A and w are the amplitude and the width of the Gaussian curve, to the point-spread function of the signals recorded with a back-illuminated EM-CCD camera. The method was described in detail in previous studies.[53,70,71] The resulting positions can be combined frame by frame to form molecular trajectories.

The mesoporous silica thin films were prepared as described in our previous work.[43] Briefly, 700 µL of Milli-Q water and 100 µL of aqueous HCl (1 M) were diluted in 4.40 mL of absolute ethanol. Then, 1.00 mL of tetraethylorthosilicate (TEOS) were added and the solution was stirred (≈ 400 rpm) at 65 °C for 1 h. Simultaneously, a mixture of 475 mg of Pluronic F127 in 4.40 mL of Ethanol was stirred at room temperature for 1 h. Then, this solution was poured slowly into the ethanolic TEOS solution, and the resulting clear solution was stirred at room temperature for 2 h. Afterwards, the solution was used to infiltrate the voids of a PDMS-stamp that was brought into close contact with a plasma-treated standard glass cover slip and aged at room temperature for 21 h in a saturated ethanolic atmosphere and for 24 – 48 h under ambient conditions.

Electrodes for applying the electric field were either obtained by depositing a thin silver film (typically 100 nm) with a gap of the desired width (typically 1 – 5 mm) on the glass coverslips by a sputter-coating process using a shadow mask, or they were made by cutting the structure to the desired width after the ageing process (typically 1 – 5 mm) with a razor blade and applying a conductive silver paste to both sides of the remaining structure forming two pads for connection to the high voltage generator.

Chapter 5

. . . . . .

A Chemiluminescent Metal–Organic Framework

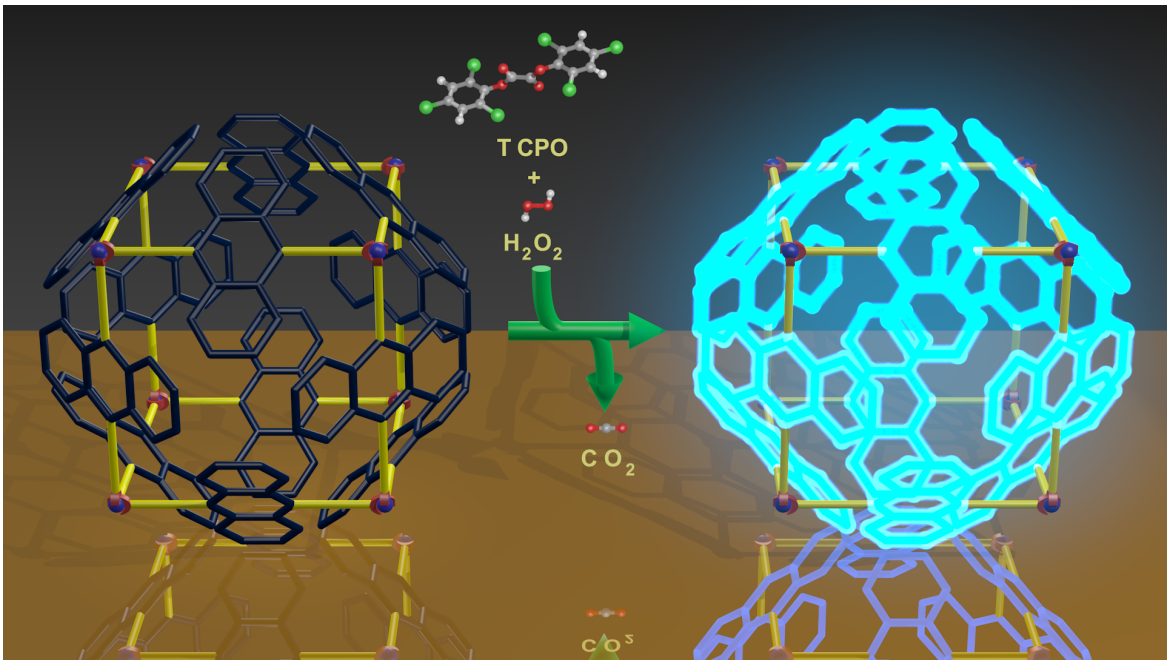

This chapter is based on a manuscript of an article by B. Rühle, S. Wuttke, F. M. Hinterholzinger, P. Roy, A. Godt, and T. Bein, which is currently in preparation.

5.1 Introduction

The great interest in metal–organic frameworks (MOFs) is a consequence of the simultaneous occurrence of important characteristics in a single material. MOFs are crystalline solids that are connected by strong metal-ligand interactions, which can confer permanent porosity to the material, i.e., it is possible to remove the solvent and impurity molecules completely without structural collapse. The pore size, shape, and dimensionality of the MOF pore system as well as its local chemical environment can be easily controlled by the judicious selection of the building blocks (metal and organic linkers) and their connection.[116,222] This ability of tailoring the pore functionality and with it the scaffold has been used to integrate different functionalities for different purposes such as incorporation of catalysts for various catalytic reactions,[151,152] tuning the pore radii and surface area for gas storage or separation,[148,223] synthesis of MOFs with contrast agents for magnetic resonance imaging diagnostics,[153] or the synthesis of luminescent MOFs for applications as fluorescent sensors.[154,155]

Luminescence as a transduction mechanism has many advantages that can be summarized in the following way: measurements are usually very sensitive, easily performed, and they can offer high spatial resolution with even single molecule visualization as well as high temporal resolution. Therefore, luminescence is frequently used as a reporter mode for the design of a chemosensor. In this context, fluorescence is by far the most widely investigated type of luminescence. However, to the best of the author's knowledge, no MOF featuring chemiluminescence has been reported so far. Luminescence is defined as the emission of electromagnetic radiation when an electron in an excited state of an atom or molecule returns to its ground state energy level. In chemiluminescence the excitation of the electron is induced by a chemical reaction rather than by absorption of photons, as it is the case for fluorescence. A distinct advantage in comparison to fluorescence spectroscopy is the absence of external light sources, which means that the analytically relevant emission can be measured against a completely dark background, resulting in a potentially higher sensitivity with this transducer concept.

To implement chemiluminescence into a MOF structure, we chose 9,10-diphenylanthracene for the incorporation into a MOF scaffold because it exhibits intense chemiluminescence elicited by the reaction between oxalic acid esters and hydrogen peroxide in the presence of a base.[224] It is important that the MOF remains stable under the conditions of chemiluminescence, in this case stable against a mixture of hydrogen peroxide

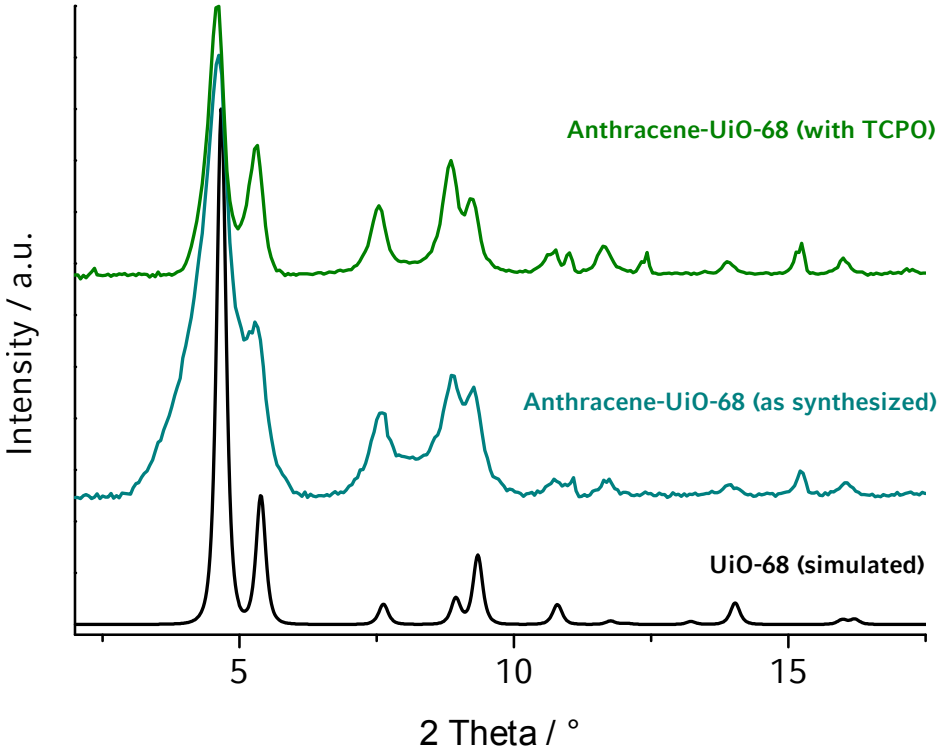

Figure 5.1: PXRD patterns of the UiO-68(anthracene) before (blue) and after (green) exposure to the conditions of the chemiluminescence reaction, and the simulated PXRD pattern of UiO-68 (black)

and sodium salicylate as well as the compounds formed *in situ* to bring about chemiluminescence. Several studies have demonstrated that Zr-based MOF structures are chemically quite robust.[225–228] In order to design a MOF with diphenylanthracene moieties being part of the linker, we chose the UiO-66 topology. The framework of UiO-66 consists of $Zr_6O_4(OH)_4(CO_2)_{12}$ clusters, where each one connected with twelve other clusters by a dicarboxylate liniker.[225,226]

5.2 Results and Discussion

The UiO-68(anthracene) was synthesized under solvothermal synthesis conditions from 4,4'-(anthracene-9,10-diyl)dibenzoic acid and $ZrCl_4$ in DMF and H_2O at 120 °C for 24 h. The reaction conditions were found *via* high-throughput screening of the effects of various molar ratios of starting materials, various concentrations, different solvent ratios, and of the addition of benzoic acid. It turned out in this case that the addition of benzoic acid, the modulator used for the syntheses of UiO-66, UiO-67, UiO-68(NH_2)[226] and the structurally closely related PIZOFs[229] was not needed, which simplifies the

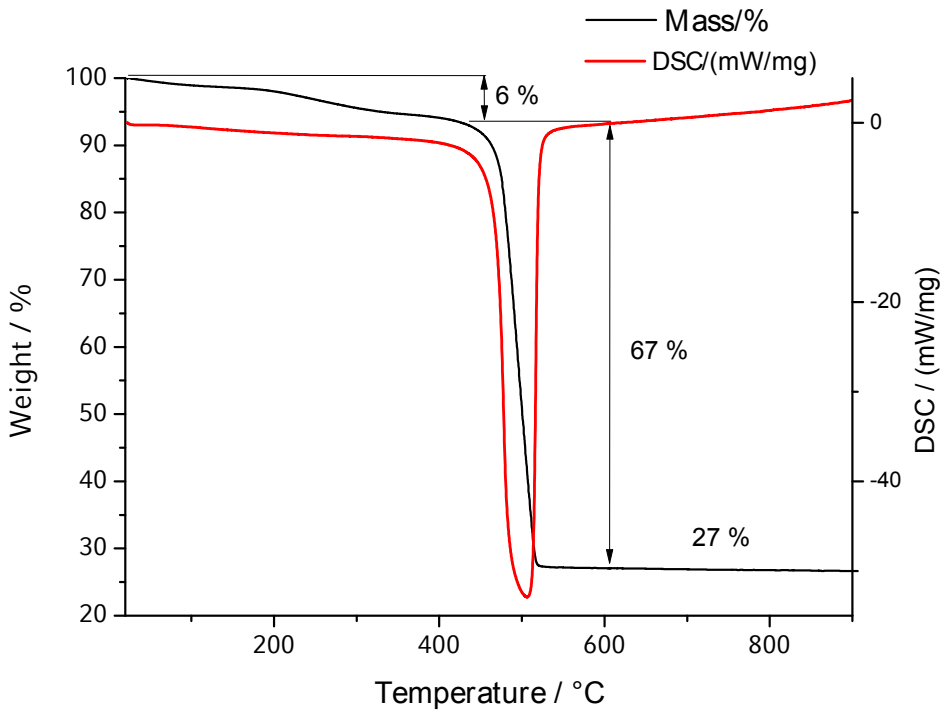

Figure 5.2: Thermogravimetric analysis of UiO-68(anthracene) in flowing air with a heating rate of 1 K min^{-1} and a flow rate 25 mL min^{-1}

.

purification of the MOF.

X-ray diffraction analysis confirmed that the solid is isostructural (isoreticular) to UiO-68 and that UiO-68(anthracene) was obtained in a purely crystalline form (Figure 5.1). Thermogravimetric analysis (TGA) showed two significant weight loss steps (Figure 5.2). The first endothermic step with a mass loss of 6 % in the range between 25 °C and 420 °C is attributed to the evaporation of solvent. The second weight loss of 67 % between 420 °C and 530 °C is due to the decomposition of the organic linkers. Thus, this MOF exhibits an exceptional thermal stability in comparison to other MOFs, especially when considering the mesoporous nature of this MOF (the UiO-68 structure features mesopores of 2.7 nm with large windows of 1.0 nm, as described in Reference 226). Often a mesoporous MOF structure leads to poor thermal stability. Moreover, the measured BET surface area of about 1349 m^2 g^{-1} is so far the highest reported surface area of a UiO-68 structure (Figure 5.2).

One of the most common and efficient ways to excite chemiluminescence of diphenylanthracene is an energy transfer to the diphenylanthracene moiety,[230–233] resulting from the reaction of oxalic acid esters, such as bis(2,4,6-trichlorophenyl)oxalate (TCPO), with hydrogen peroxide as depicted in a simplified manner in Figure 5.4. In

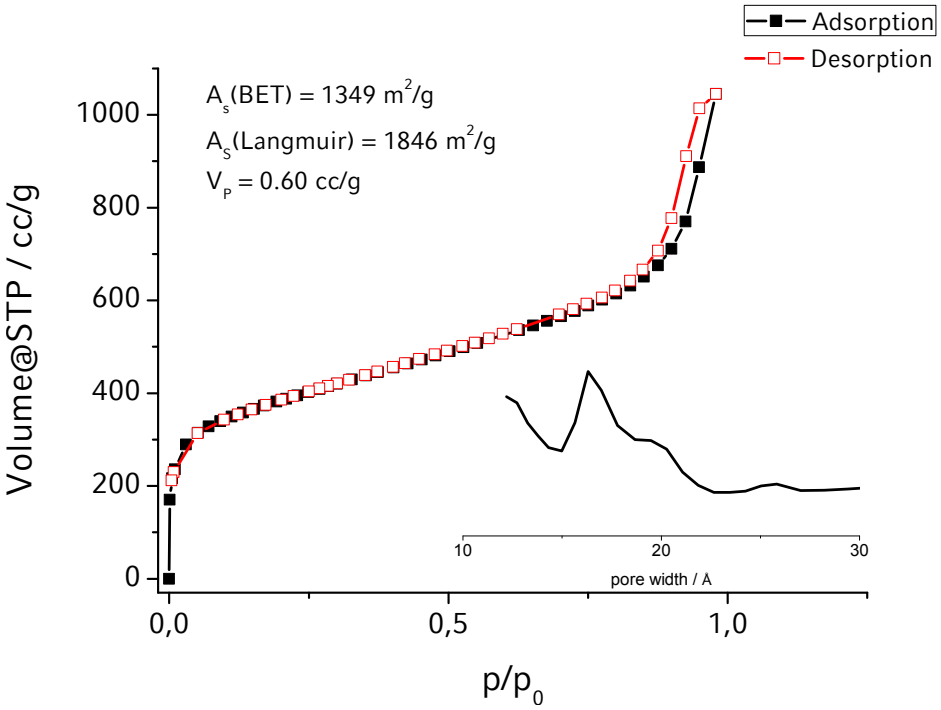

Figure 5.3: Results of the physisorption measurement performed with nitrogen at 77 K on bulk UiO-68(anthracene) showing the characteristic shape of the isotherm, the specific surface area (BET/Langmuir), the pore volume and the calculated pore-size distribution (NLDFT).

fact, the detailed mechanism of the energy transfer might be more involved, including the formation of an encounter complex between an intermediate (e.g., dioxetandione) and the diphenylanthracene moiety, followed by radical formation *via* single electron transfers, thus rendering the whole process a chemically initiated electron exchange luminescence.[230–232]

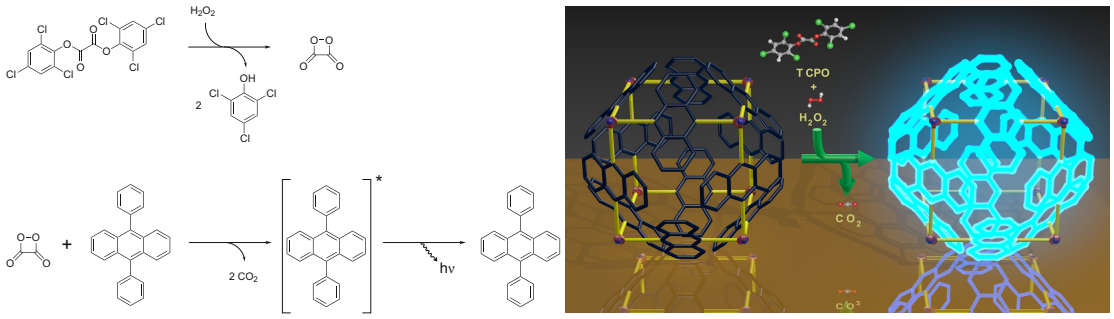

Figure 5.4: Simplified representation of the assumed mechanism leading to the electronic excitation and subsequent chemiluminescence of 9,10-diphenylanthracene through reaction with 1,2-dioxetan-3,4-dione formed *in situ*.[232] The asterisk indicates an electronically excited state.

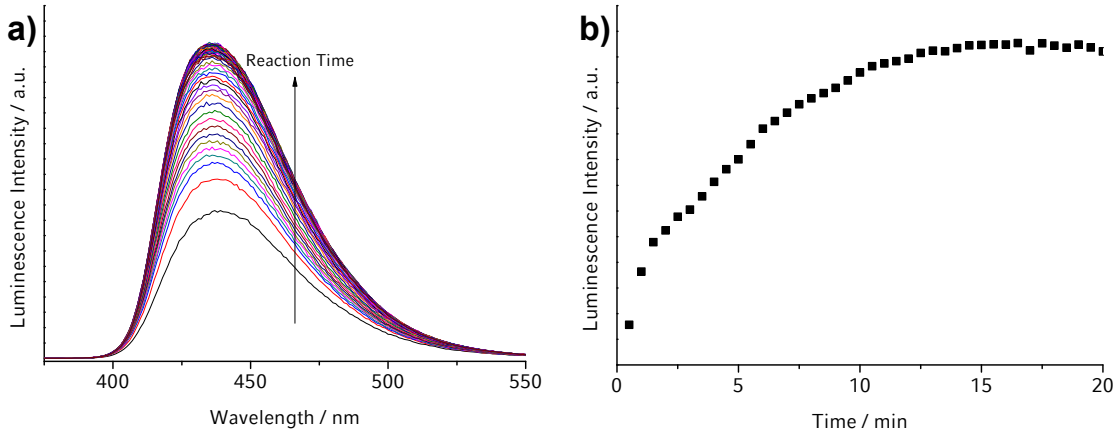

Figure 5.5: (a) Chemiluminescence spectra of UiO-68(anthracene) in a mixture of dimethyl and dibutylphthalate at different points in time. (b) Development of the fluorescence intensity at $\lambda_{max} = 436\,\text{nm}$ over time.

When performing the chemiluminescence reaction we followed a published procedure[234] with slight modifications (see Section 5.4 for details). The reaction was carried out in a mixture of dimethyl and dibutylphthalate in the presence of a small amount of a weak base such as sodium salicylate. Presumably, the base assists in the formation of the proposed 1,2-dioxetan-3,4-dione through deprotonation of the intermediate oxalic peroxyacid.[233] Figure 5.5 shows the strong chemiluminescence observed when mixing the MOF with the components mentioned above. The chemiluminescence was monitored over time with a photoluminescence setup. It reached its emission maximum after approximately 10 min (Figure 5.5).

To ensure that the observed luminescence is indeed emitted from the metal–organic framework and does not result from linker molecules in the solution as a result of framework decomposition, we carried out the following experiments. We subjected the UiO-68(anthracene) to the reagents and conditions of the chemiluminescence reaction, isolated the solid material from the dispersion, and characterized the material by X-ray diffraction. The PXRD pattern (Figure 5.1) clearly indicates that the crystalline structure of the framework was maintained even after exposing the MOF to the conditions during the chemiluminescence reaction. Furthermore, we used optical microscopy in order to identify the source of luminescence. When observing MOF particles sitting at the bottom of a container with a fluorescence microscope (without using excitation light) upon addition of a solution of bis(2,4,6-trichlorophenyl)oxalat (TCPO) and a solution of hydrogen peroxide and sodium salicylate, strong luminescence originating from the MOF crystallites was seen, whereas the background

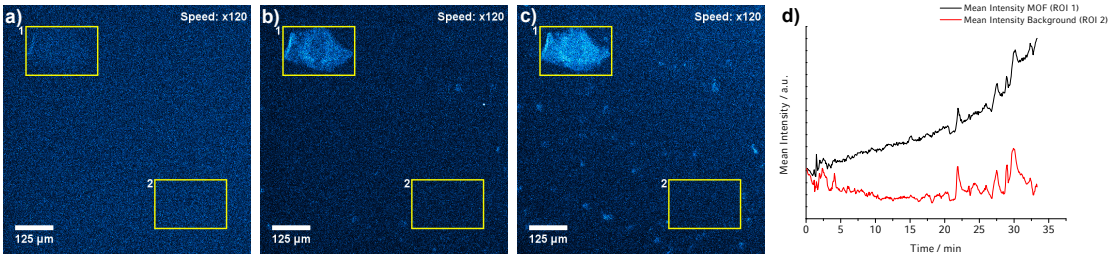

Figure 5.6: (a-c) Images taken from movie M1, showing the luminescence 0 min (a), 14 min (b), and 28 min (c) following addition of a solution of bis(2,4,6-trichlorophenyl)oxalate (TCPO) in dibutylphthalate and a solution of hydrogen peroxide and sodium salicylate in dimethylphthalate and *tert*-butanol to particles of UiO-68(anthracene) sitting at the bottom of a vessel. (d) Graph showing the mean integrated intensities of the two regions of interest (ROIs) highlighted in (a-c) and in movie M1 (see Supplementary CD). ROI 1 contains the MOF crystallite, ROI 2 contains only background.

luminescence did not show a significant increase. This is shown by the development of the mean integrated intensities within two equally sized rectangular regions of interest (ROIs) over time, one containing a MOF crystallite (ROI 1) and one containing only background (ROI 2) (Figure 5.6 and movie M1 on the Supplementary CD). If the framework had decomposed, free linker molecules should have diffused into the surrounding solution and would have caused an increase in background luminescence.

5.3 Conclusion

In conclusion, the synthesis of the novel MOF UiO-68(anthracene) was developed *via* a high-throughput approach. In contrast to the structurally related UiO-68(NH_2) and PIZOFs, no modulation agent is necessary to obtain a highly crystalline material. Nitrogen sorption analysis demonstrates the high porosity of this MOF, and thermogravimetry points to exceptional thermal stability. Strikingly, UiO-68(anthracene), a Zr-based MOF with 4,4'-(anthracene-9,10-diyl)dibenzoate as the linker and the topology of UiO-66, shows strong chemiluminescence once exposed to a solution of bis(2,4,6-trichlorophenyl)oxalate, hydrogen peroxide and sodium salicylate. During the chemiluminescence reaction the structure of UiO-68(anthracene) persists. To the best of our knowledge, this is the first ever MOF structure showing the phenomenon of chemiluminescence.

5.4 Experimental Part

5.4.1 Methods and characterization

Powder X-ray diffraction (PXRD) measurements were performed using a Bruker D8 diffractometer (Cu-$K_{\alpha 1}$ = 1.5406 Å; Cu-$K_{\alpha 2}$ = 1.5444 Å) in theta-theta geometry equipped with a Lynx-Eye detector. The powder samples were measured between 2° and 45° two theta, with a step size of 0.05° two theta.

Chemiluminescence was monitored using a PTI fluorescence spectrometer featuring a PTI 814 photomultiplier detector, a PTI MD5020 motor driver, and a Quantum Northwest TC 125 sample holder. No excitation light was used since the samples emit light. The band-pass of the detector was set to 2 nm, and each 30 s an emission spectrum was recorded from 350 nm to 550 nm at a step width of 1 nm and an integration time of 0.1 s per step.

Microscopy images were recorded using a Nikon Eclipse Ti-U inverted microscope equipped with a Nikon Plan Fluor 10x/0.30 objective and an Andor iXon+ DU897-BV back-illuminated electron multiplying charge-coupled device (EM-CCD) camera in kinetic mode with an exposure time of 2 s and a kinetic cycle time of 5 s. 1 pixel on the detector corresponds to 1.57 µm. The detector was cooled to −80 °C during measurements. No excitation light was used.

FTIR measurements were performed in transmission mode on a Bruker Equinox 55s between 4000 and 400 cm^{-1} at a resolution of 4 cm^{-1}.

Nitrogen sorption measurements were performed on a Quantachrome Instruments Autosorb at 77 K. The sample was heated to 393 K for 12 h prior to sorption studies. Pore sizes and pore volumes were calculated using a NLDFT equilibrium model of N_2 on silica, based on the adsorption isotherm. The BET surface area was calculated over the range of 0.05 – 0.20 p/p_0. The pore volume was calculated based on the uptake (cm^3/g) at a relative pressure of 0.30 p/p_0.

Thermogravimetric analyses of the bulk samples were performed on a Netzsch STA 440 C TG/DSC with a heating rate of 1 K min^{-1} in a stream of synthetic air at about 25 mL min^{-1}.

5.4.2 Chemicals

Zirconiumtetrachloride (99.9 %, Aldrich), N,N-dimethylformamide (DMF; 99.8 %, Aldrich), bis(2,4,6-trichlorophenyl)oxalate (TCPO; 98 %, TCI), dimethyl phthalate (99 %, Aldrich),

dibutyl phthalate (99 %, Aldrich), hydrogen peroxide (30 %; Merck), *tert*-butanol (99.7 %, Aldrich), and sodium salicylate (99.5 %, Aldrich) were used as received.

5.4.3 Synthesis of 4,4'-(Anthracene-9,10-diyl)dibenzoic acid

The synthesis of 4,4'-(Anthracene-9,10-diyl)dibenzoic acid was performed in the group of Prof. Adelheid Godt at the University of Bielefeld.

5.4.4 Synthesis of UiO-68(anthracene)

The synthesis was performed in a high throughput (HT) parallel reactor with 24 wells, each containing the same reaction mixture. 4,4'-(Anthracene-9,10-diyl)dibenzoic acid (16.9 mg, 40 µmol), zirconium tetrachloride (9.3 mg, 40 µmol), water (1.1 µL, 61.1 µmol) and DMF (1 mL) were added to each well. The HT parallel reactor containing the reaction mixture was heated to 200 °C for 21 h. After cooling to room temperature the precipitate was isolated. It was washed three times with DMF and then three times with dichloromethane and was finally dried at reduced pressure.

5.4.5 Chemiluminescence experiments

For carrying out the chemiluminescence experiments, we followed a published procedure with slight modifications.[234] UiO-68(anthracene) (1 mg) was suspended in a solution of bis(2,4,6-trichlorophenyl)oxalate (TCPO) (30 mg, 66.8 µmol) in dibutyl phthalate (1 mL) using vortex shaking and brief sonification. In another vessel, a solution of *tert*-butanol (3.55 mL, 37.8 mmol), aqueous H_2O_2 (30 %; 3.00 mL, 38.1 mmol), and sodium salicylate (1.80 mg, 11.25 µmol) in dimethyl phthalate (13.45 mL) was prepared and stirred at room temperature for 5 min at 500 rpm. Then, more sodium salicylate (1.80 mg, 11.25 µmol) was added and the solution was stirred at room temperature for another 5 min at 500 rpm. To start the chemiluminescence reaction, equal volumes (1 mL each) of both solutions were combined.

For testing the stability of UiO-68(anthracene) during the chemiluminescence experiment the two solutions were prepared as described above, however 5 mg of UiO-68(anthracene) were used. The two solutions were combined and the resulting mixture was stirred for 10 min at room temperature. The solid was isolated by centrifugation (5 min at 14 000 rpm (16 873 rcf)), washed three times with dichloromethane (15 mL), dried with a stream of nitrogen, and finally subjected to X-ray diffraction analysis.

For the chemiluminescence experiment monitored with optical microscopy the two solutions were prepared as described above, however without adding the UiO-68(anthracene). Both solutions were centrifuged at 14 000 rpm (16 873 rcf) for 4 min in an Eppendorf tabletop centrifuge (Model No. 5418) to remove any particulate matter from the solutions. MOF crystallites were spread out at the bottom of one microwell of an 8-well Lab-Tek II Chambered #1.5 German Coverglass System (NUNC, 155409 - 8 Chamber). The two solutions were mixed at a volume ratio of 1:1, and this mixture (400 µL) was added to the MOF crystallites in the microwell.

Chapter 6

. . . . . .

Highly Sensitive and Selective Fluoride Detection in Water through Fluorophore Release from a Metal–Organic Framework

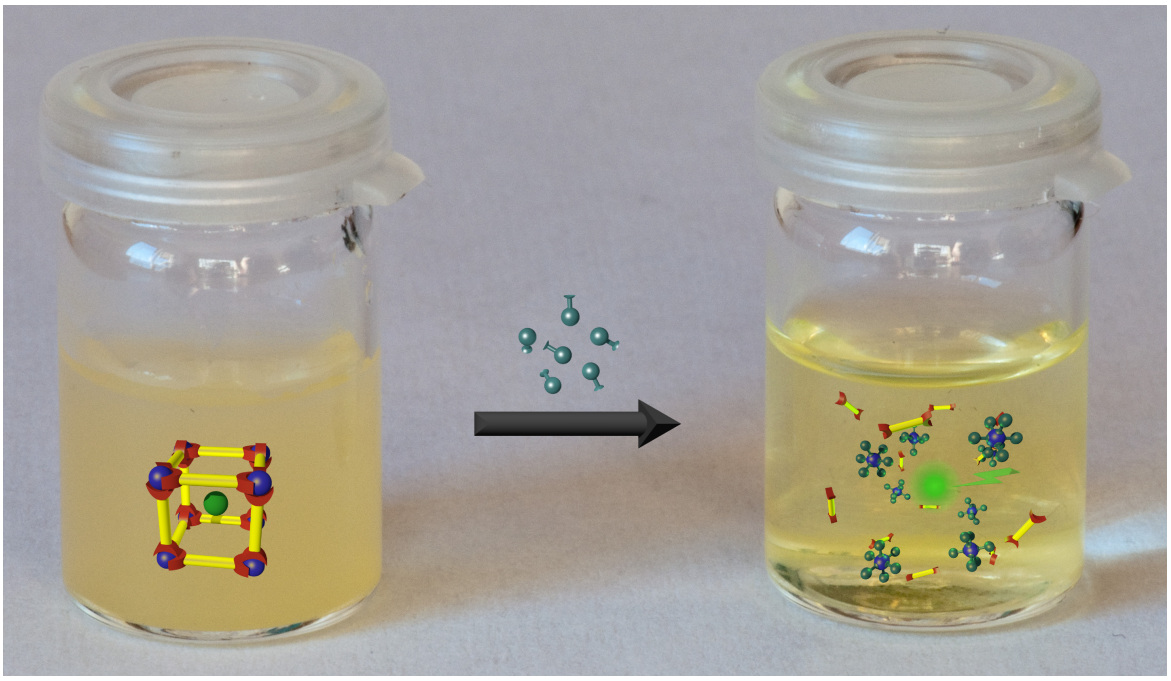

This chapter is based on the article "Highly sensitive and selective fluoride detection in water through fluorophore release from a metal–organic framework" by B. Rühle, F. M. Hinterholzinger, S. Wuttke, K. Karaghiosoff, and T. Bein, which has been

submitted and is currently being reviewed.

6.1 Abstract

The detection, differentiation and visualization of compounds such as gases, liquids or ions are key challenges for the design of selective optical chemosensors. Optical chemical sensors employ a transduction mechanism that converts a specific analyte recognition event into an optical signal. Here we report a novel concept for fluoride ion sensing where a porous crystalline framework serves as a host for a fluorescent reporter molecule. The detection is based on the decomposition of the host scaffold which induces the release of the fluorescent dye molecule. Specifically, the hybrid composite of the metal–organic framework NH_2-MIL-101(Al) and fluorescein acting as reporter shows an exceptional turn-on fluorescence in aqueous fluoride-containing solutions. Using this novel strategy, the optical detection of fluoride is extremely sensitive and highly selective in the presence of many other anions.

6.2 Introduction

Over the past decades a great deal of attention has been devoted to the discovery of new analytical methods for the reliable detection of target species.[235–238] The real-time monitoring of fluoride ion concentration in aqueous and physiological media as well as its quantitative determination across a large concentration range is of vital importance for various environmental and health-care issues as well as in industrial and scientific applications.[239–242] Several strategies have been reported on fluoride detection using recognition-transduction schemes based on the optical read-out of a luminescent or colorimetric signal. Examples include molecular recognition protocols using boron-based anion receptors[239,240,243–245], or mesoporous silica host materials[246] that are equipped with a reporter molecule to monitor either luminescence quenching or turn-on processes, whereas recently a sensitive colorimetric fluoride sensor based on supramolecular interactions such as charge or electron transfer, respectively, was described.[247] However, most of the molecule-based analytical methods suffer from interference with other anions or are incompatible with aqueous media, which greatly limits the scope of their use.[248,249] Here we demonstrate how the analyte-induced degradation of a hybrid host material with embedded reporter molecules can be efficiently used as an extremely sensitive signal transduction mode (Figure 6.1). It is thus

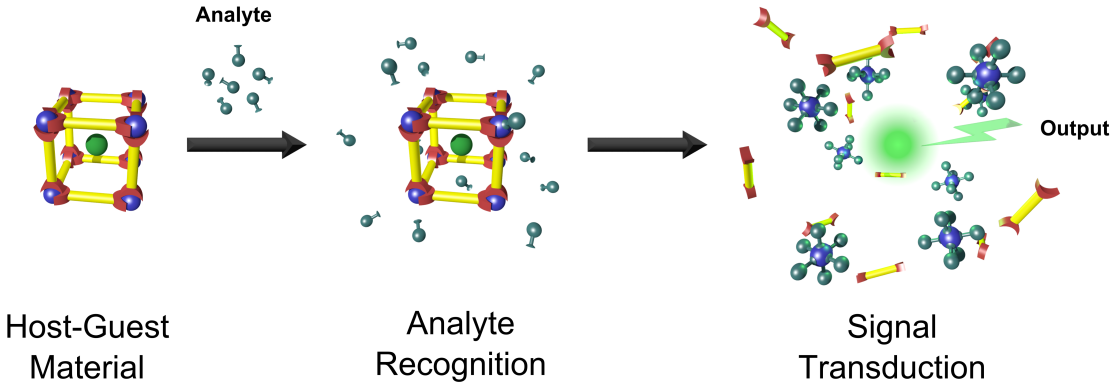

Figure 6.1: Schematic illustration of the recognition-transduction scheme by metal-anion complexation-induced decomposition of a MOF framework. The MOF scaffold with covalently entrapped reporter molecules serves as a non-emissive host–guest material for the detection of analyte species. The recognition is realized as a competitive metal-anion complexation in an aqueous analyte-containing environment. The degradation process leads directly to the turn-on of the fluorescence of the reporter molecules, which is correlated with the fluoride ion concentration.

anticipated that our new recognition-transduction mechanism contributes to the development of optically encoded chemosensors and hence for the sensitive visualization of specific host–guest interactions.

Metal–organic frameworks (MOFs), also known as porous coordination polymers (PCPs),[116,222,250] have attracted great interest in the last decade as a new class of highly porous materials ideally suited for applications in gas adsorption, separation processes[147,251,252] and chemical sensing.[155,253,254] The underlying modular concept of combining inorganic metal-clusters and organic linker molecules allows for the targeted design of three-dimensional crystalline molecular skeletons with defined pore dimensions, uniform pore shapes and versatile functionalities.

Our strategy for visualizing the recognition of a target ion requires the implementation of a fluorescent reporter molecule into the confined crystalline environment of a hybrid host material. As a consequence of the confinement of the reporter molecules within the three-dimensional host, almost complete fluorescence quenching is observed. However, the selective trapping of fluoride ions from aqueous analytes directly correlates with an intense turn-on fluorescence signal that can easily be monitored by fluorescence spectroscopy. More specifically, the turn-on of fluorescence that is triggered by the controlled decomposition of the host material exhibits great advantages over luminescence quenching methods reported for luminescent MOFs.[253,255] The turn-on

fluorescence is an extremely sensitive technique, having the capability to detect even single molecules in solution and has great potential for the highly sensitive monitoring of the fluoride ion concentration in different media. Although there are several reports dealing with the intrinsic luminescence of MOFs and its use in chemical sensing[163,253,256], none of these optical detection schemes tolerates aqueous environments and simultaneously shows turn-on fluorescence response triggered by the highly selective capture of fluoride ions.

Here we report on highly selective and extremely sensitive fluoride sensors based on an amino-functionalized metal–organic framework designated NH_2-MIL-101(Al)[257] that covalently binds fluorescein 5(6)-isothiocyanate (FITC) as fluorescent reporter molecule. We demonstrate an unprecedented methodology for the detection of fluoride ions in aqueous solutions that is based on the decomposition of the MOF and provides an intense turn-on switching response induced by the release of the quenched reporter molecules. The intact crystalline MOF material with embedded fluorescein dyes itself is non-fluorescent and selectively binds fluoride ions from water. The capture of fluoride ions results in the formation of different aluminum complexes, which induces the structural decomposition of the MOF host. The detection mechanism after infiltrating the MOF with an aqueous fluoride-containing analyte solution is revealed by ^{19}F and ^{27}Al-NMR titration experiments. To the best of our knowledge, the fluorescein-labeled MOF composite material is the first example of a MOF-based fluoride sensor system which tolerates aqueous environments, exhibits high selectivity *versus* other anions and covers a broad range of anion concentrations. We anticipate that the general concept of creating a fluorescence output by the controlled release of quenched fluorescence dye molecules from a porous host can be extended to other analyte detection schemes, thus adding to the toolbox for the development of advanced optical chemosensors and the understanding of signal transduction schemes.

6.3 Results and Discussion

Recently, the group of F. Kapteijn reported on the amino-functionalized analogue of a large-pore metal–organic framework, designated NH_2-MIL-101(Al)[257]. The aluminum-based MOF scaffold with implemented amino-functionality represents an ideal candidate for the post-synthetic dye-labeling that was performed by exposing the porous host to FITC at room temperature. Powder X-ray diffraction (PXRD) measurements of the as-synthesized MOF material, as well as the post-synthetically fluorescein-

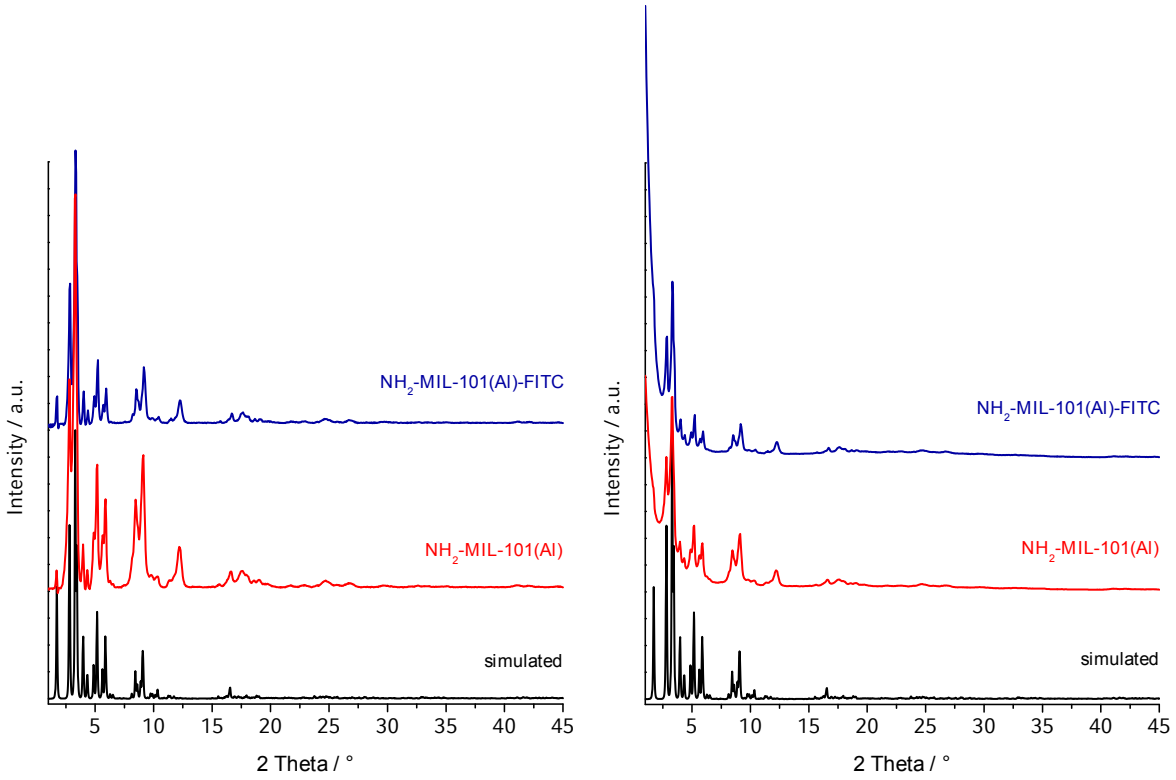

Figure 6.2: Background-corrected X-ray diffraction patterns (left) and raw data (right) of as-synthesized NH_2-MIL-101(Al) (red) as well as post-synthetically fluorescein labeled NH_2-MIL-101(Al) bulk material (blue) compared to simulated data (black).

labeled host are in good agreement with simulated data indicating that the crystalline structure remains intact upon dye-labeling (Figure 6.2).

Scanning electron microscope measurements (SEM) additionally confirm that the crystal morphology of the host MOF does not change significantly after being post-synthetically modified with fluorescein dye molecules (Figure 6.3).

After dye loading, a significant decrease of the specific surface area from 2315 $m^2\,g^{-1}$ to 698 $m^2\,g^{-1}$ as well as a reduction of the pore volume of the host material is revealed by physisorption experiments. This indicates a successful introduction of FITC into the porous structure of the host (Figure 6.4).

Thermogravimetric analysis and differential scanning calorimetry demonstrate the removal of residual molecules trapped within the pores as well as the decomposition of the framework at higher temperatures.

Infrared and Raman spectroscopy show the presence of a strong characteristic absorption band corresponding to the isothiocyanate group of free FITC, whereas no such absorption band is observed after fluorescein is incorporated into the host framework

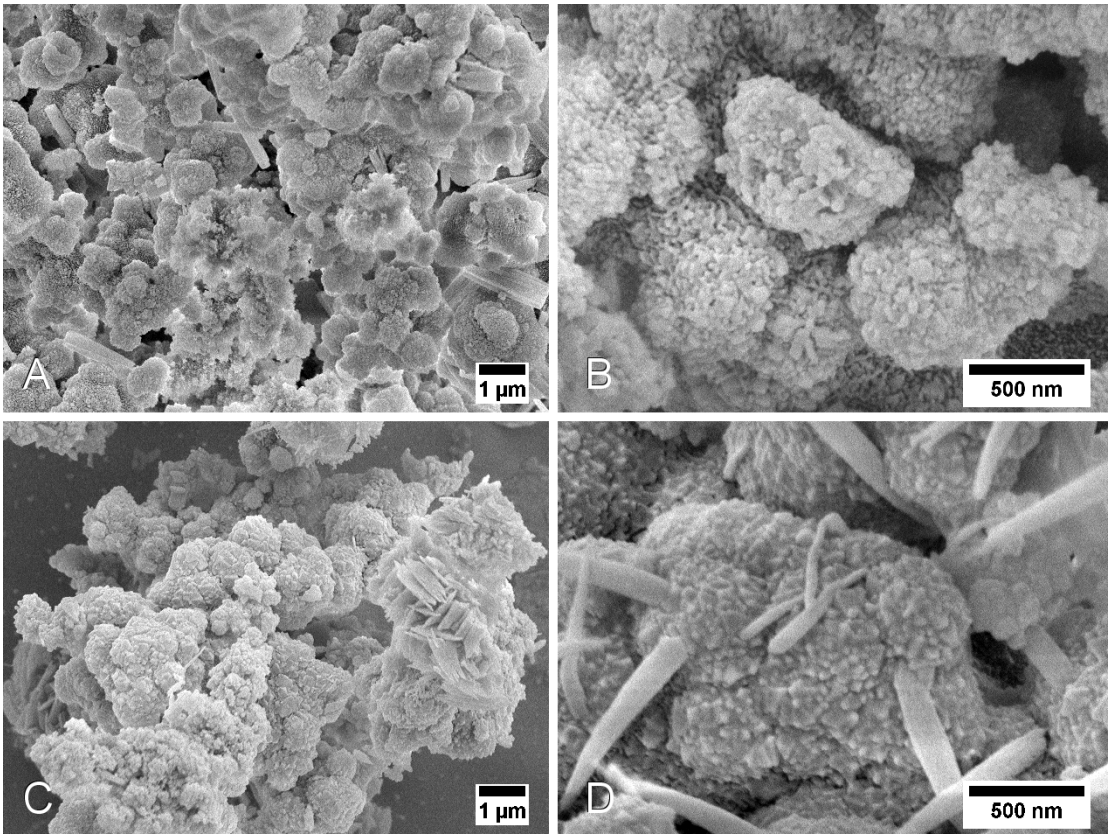

Figure 6.3: Scanning electron microscopy (SEM) images of a polycrystalline bulk NH_2-MIL-101(Al) powder sample. (A,B) after FITC labeling. (C,D) before FITC labeling.

(Figures 6.7 and 6.8).

Fluorescence spectroscopy shows that the fluorescence intensity of the fluorescein guests drops significantly (almost to the background level, see Figure 6.9) once they are incorporated into the framework. We believe that this is caused by the well-known concentration- or self-quenching-effect of fluorescent dyes like fluorescein[258,259], or by interactions of fluorescein either with aromatic groups of the linker molecules, the metal centers, or the amino groups inside the MOF. Inspired by this observation, we developed the novel MOF-based fluoride sensing concept using the selective release of the fluorescent dye: since the framework is not connected by strong covalent bonds, it can be broken up under mild conditions by other, more strongly coordinating ligands for the respective metal. While this "instability" can certainly be a disadvantage in certain applications, it is of key importance for the working principle of the fluoride sensor and the new sensing pathway presented in this work: upon replacing the MOF-linker molecules by other ligands, the fluorescent guest is released into the solution where its fluorescence is dequenched and a strong increase in the fluorescence signal can

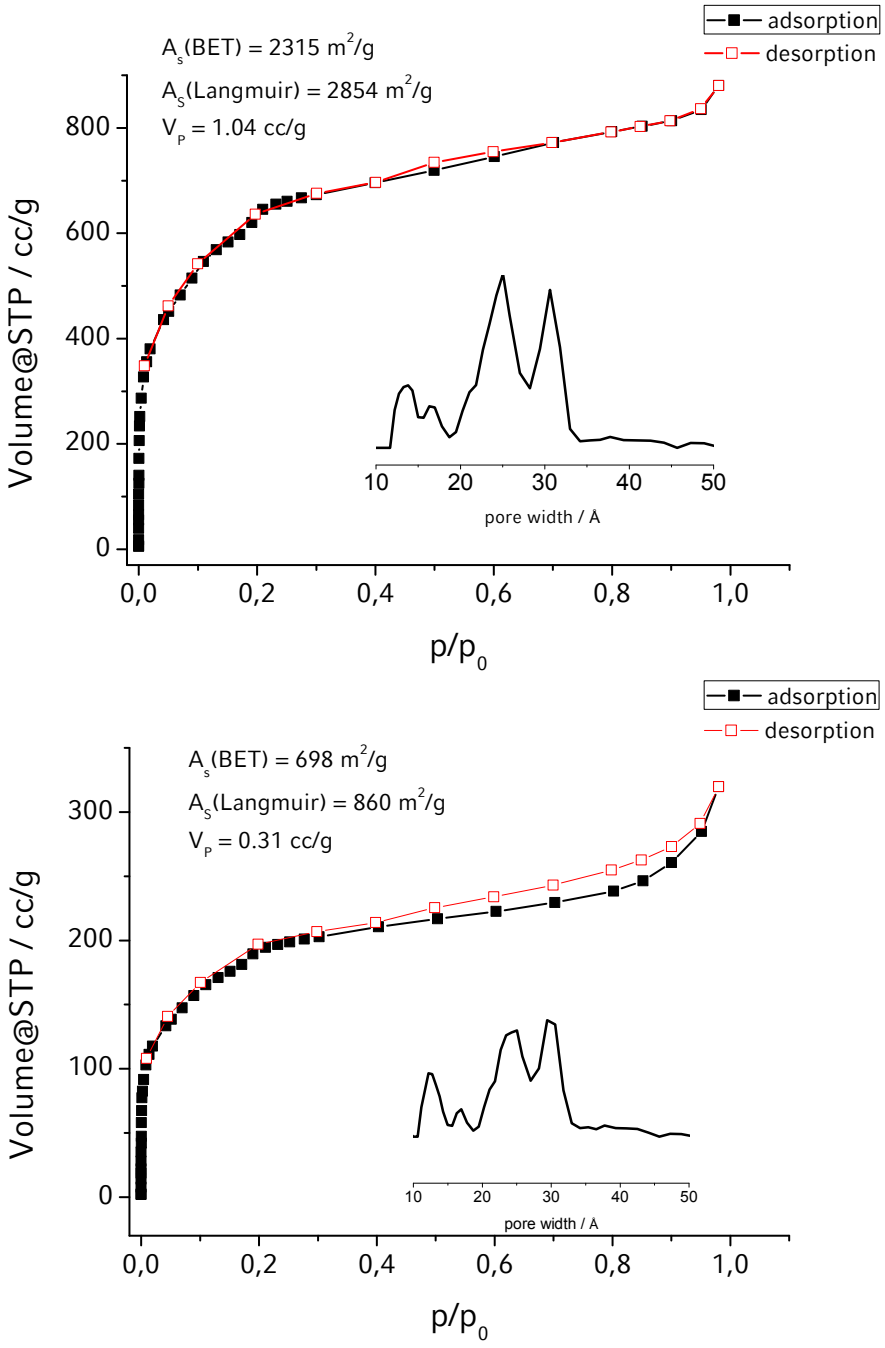

Figure 6.4: Physisorption measurement performed with nitrogen at 77 K for bulk NH_2-MIL-101(Al) (top) and for NH_2-MIL-101(Al)-FITC (bottom) showing the characteristic shape of the isotherm, the specific surface area (BET/Langmuir), the pore volume and the calculated pore-size distribution (NLDFT).

be detected. Due to the fact that the degradation of the framework is based on different affinities of the metal ions constituting the MOF towards linker and analyte molecules, this pathway has the potential of being highly selective and tailorable by choosing

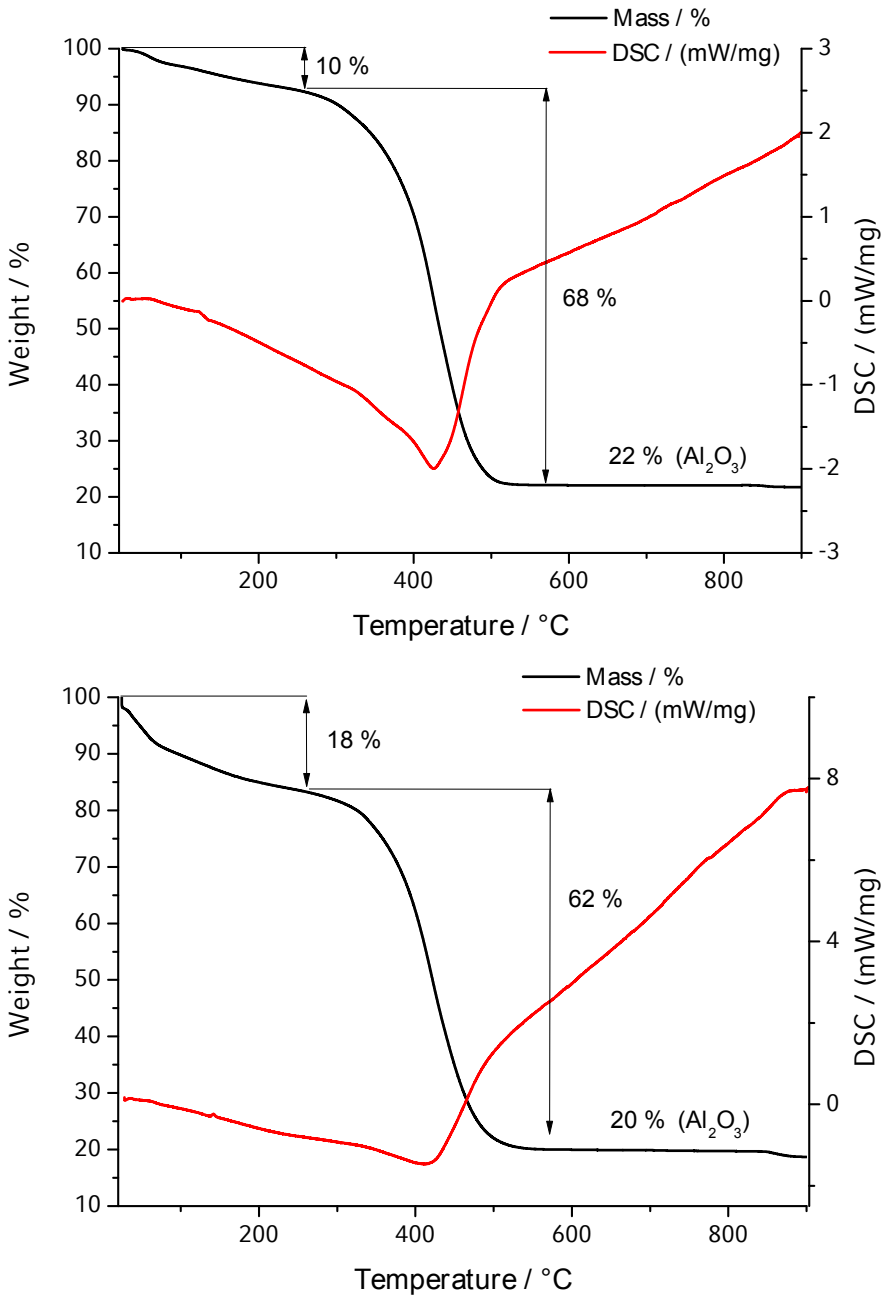

Figure 6.5: Thermogravimetric analysis (TGA) and differential scanning calorimetry (DSC) of bulk NH_2-MIL-101(Al) (top) and NH_2-MIL-101(Al)-FITC (bottom) illustrating the removal of residual molecules trapped within the pores as well as the decomposition of the framework.

suitable MOFs (i.e. metal/linker combinations) for the respective target analytes. The fact that the release of the fluorescent dye results in a fluorescence increase rather than a quenching or loss of color contributes to the high sensitivity of this approach. Both the high selectivity based on strong interactions of aluminum with fluoride ions [260] and

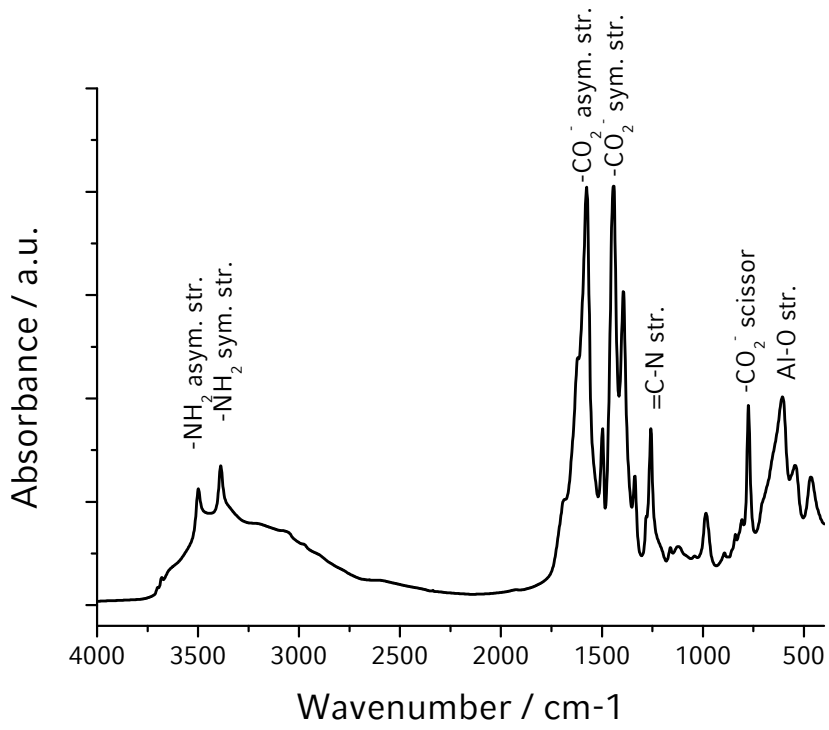

Figure 6.6: IR spectrum of bulk NH_2-MIL-101(Al).

the high sensitivity based on the fluorescence dequenching are demonstrated in the following for NH_2-MIL-101(Al)-FITC.

The remarkable selectivity of the sensor is demonstrated by fluorescence titrations of NH_2-MIL-101(Al)-FITC with sodium salt solutions of different anions, which show that there is virtually no interference by other halides (see Figure 6.10). The strongest interference among the anions tested in this work is caused by sodium bicarbonate, which can be expected to mimic the coordination chemistry of the linker molecules, i.e. coordination of aluminum via carboxylate groups. Interestingly, sodium acetate shows only very weak interference, although it also exhibits a carboxylate group. The absence of strong acetate interference also proves that the recorded fluorescence increase does not simply depend on an increase of the pH, since the basicity of acetate is higher than that of fluoride ($pKA(CH_3COOH) \approx 4.75$ vs. $pKA(HF) \approx 3.45$)[188]. However, the fluorescence signal is much stronger after fluoride addition than after acetate addition, indicating that the fluorescence increase is triggered by coordination of fluoride to aluminum metal centers rather than by a rise of the pH.

Additionally, more detailed information about the different fluoride species in solution as well as mechanistic insights into the dissolution process were gained by performing NMR titration experiments, which prove that the framework is indeed dissolved

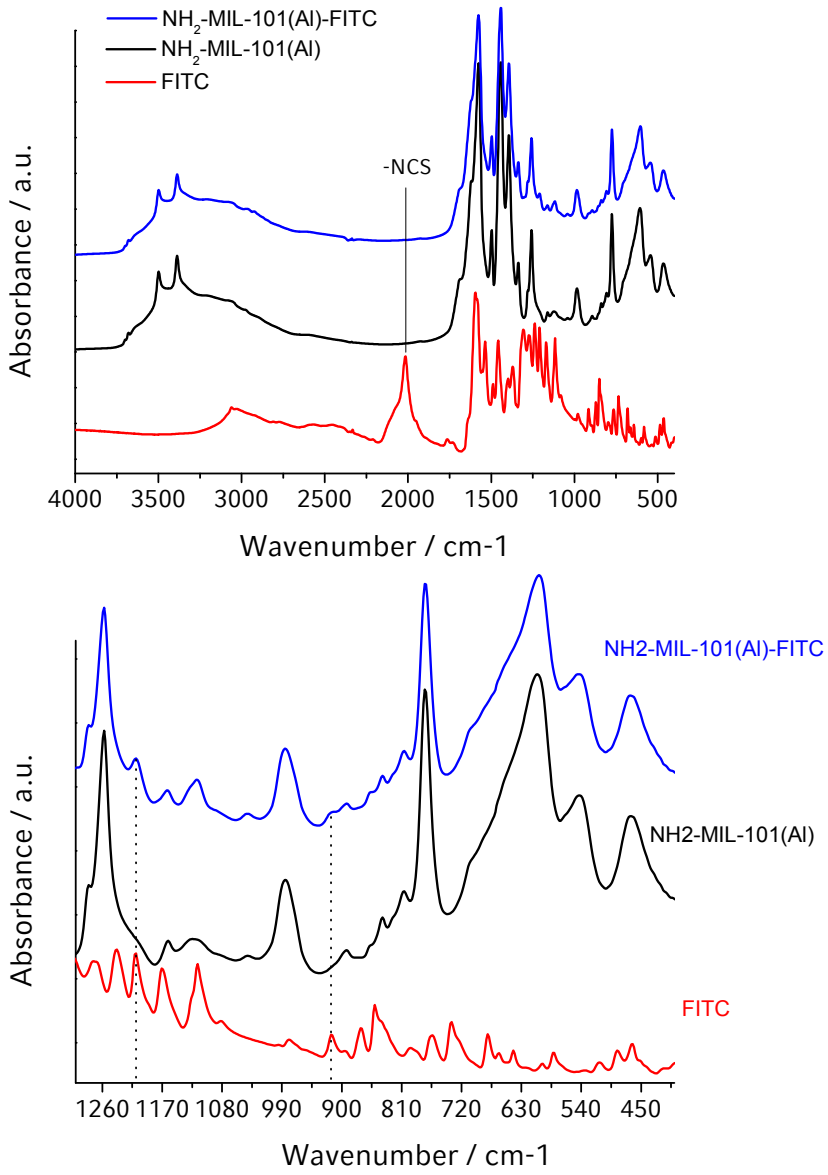

Figure 6.7: IR spectra (top: full spectrum, bottom: zoom-in) of bulk fluorescein-5(6) isothiocyanate (red), NH_2-MIL-101(Al) (black) as well as of NH_2-MIL-101(Al)-FITC (blue) illustrating the absence of the isothiocyanate absorption band after the post-synthetic dye modification of the MOF structure.

by coordination of fluoride to aluminum ions from the framework.

Figure 6.11.a shows the ^{19}F NMR spectra after sequential additions of NaF to NH_2-MIL-101(Al)-FITC in water. The data demonstrate how the number of fluoride ions binding to aluminum increases with increasing fluoride concentration. The peaks of the aluminum complexes with high fluoride content (i.e. more than four fluoride atoms) cannot be observed here, most probably because they are too broad. Similar

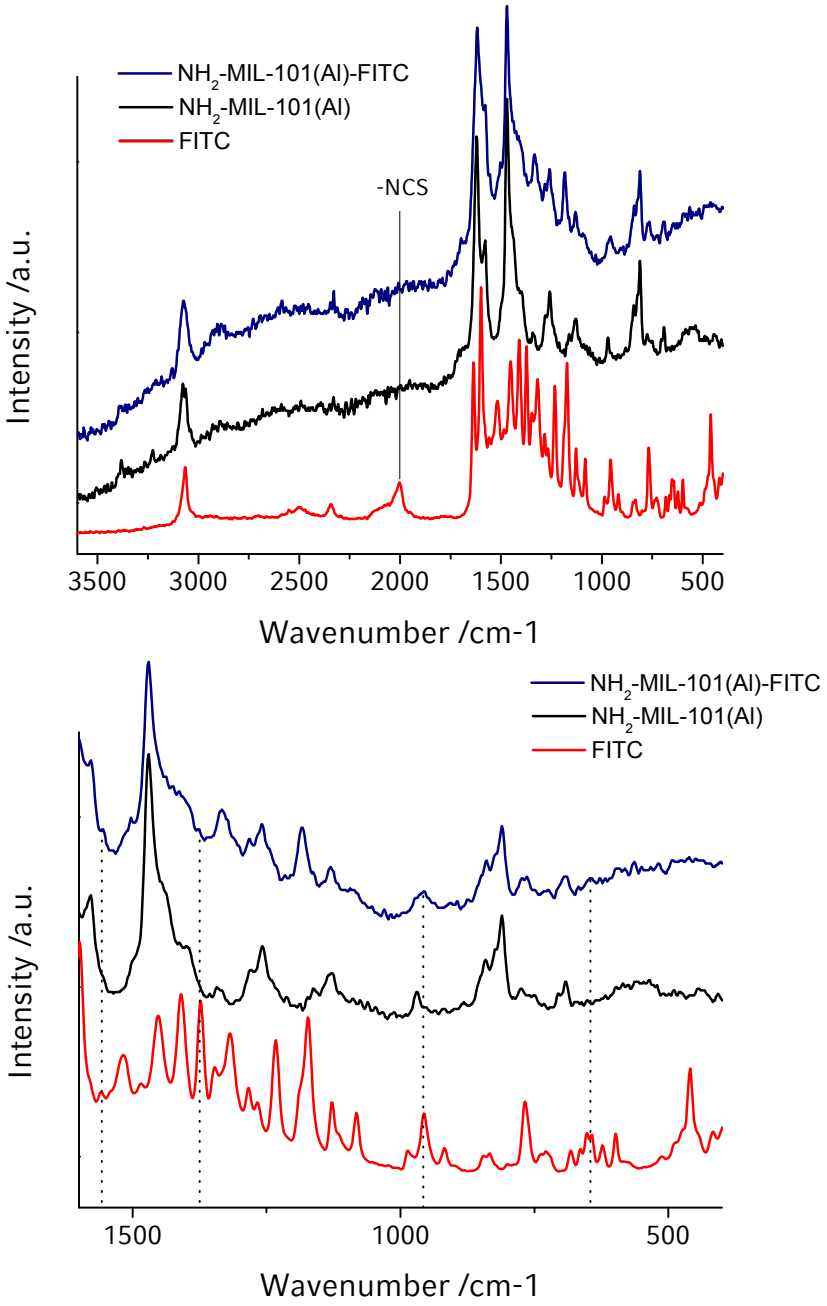

Figure 6.8: Raman spectra (top: full spectrum, bottom: zoom-in) of bulk fluorescein-5(6) isothiocyanate (red), NH_2-MIL-101(Al) (black) as well as of NH_2-MIL-101(Al)-FITC (blue) illustrating the absence of the isothiocyanate absorption band after the post-synthetic dye modification of the MOF structure.

observations were made by Sur *et al.*[261] and by Bodor *et al.*[262]. Sur *et al.* attribute the line broadening mainly to a two-site exchange between free fluoride ions and fluoroaluminum complexes, although scalar relaxation mechanisms are also discussed. Bodor

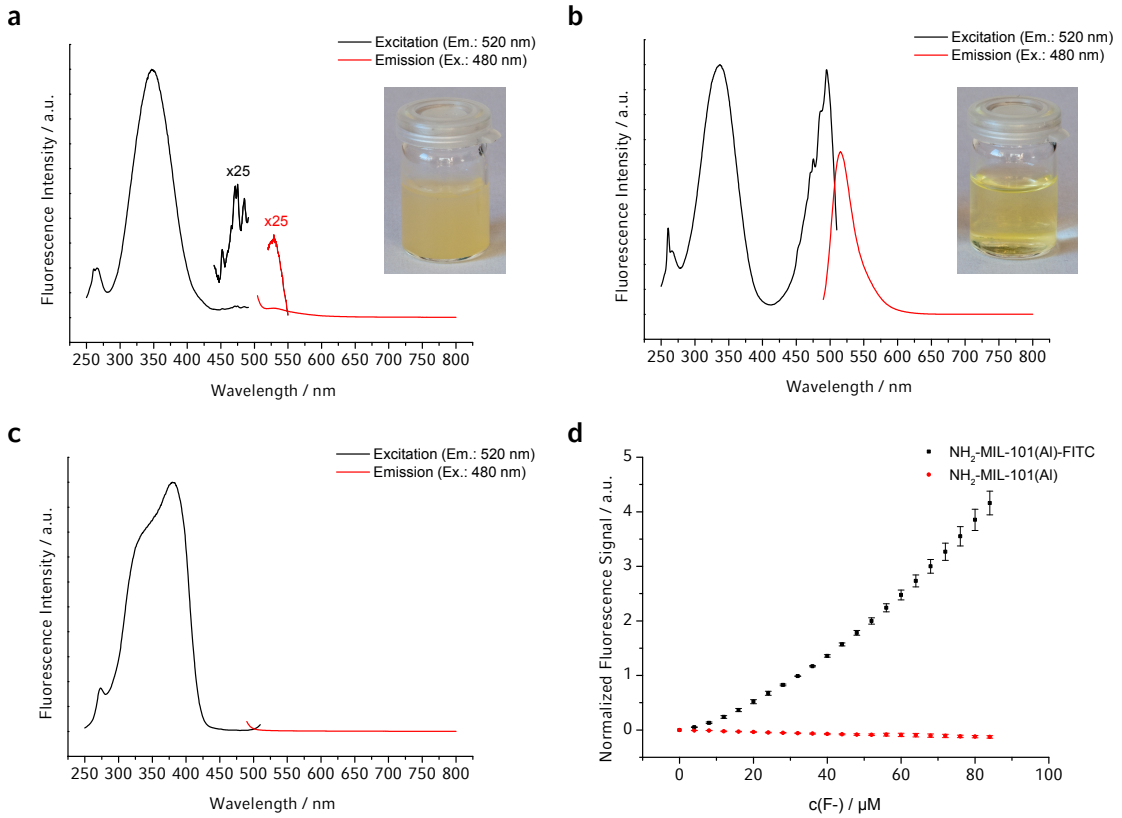

Figure 6.9: Fluorescence spectroscopy data. (a) Excitation and emission spectra of NH_2-MIL-101(Al)-FITC before fluoride addition. (b) Excitation and emission spectra of NH_2-MIL-101(Al)-FITC after fluoride addition. (c) Excitation and emission spectra of 2-amino terephthalic acid, representing the linker molecule in NH_2-MIL-101(Al). (d) Comparison of fluorescence titrations of NH_2-MIL-101(Al)-FITC and unlabeled NH_2-MIL-101(Al) (error bars indicate the deviation of two individual measurements with different MOF and titration stock solutions; for a more detailed description of experimental details, data analysis, and raw spectral data see section 6.5). Insets in (a) and (b), Photographs of the MOF stock solution before (a) and after (b) fluoride addition.

et al. also attribute the broadening to fluoride exchange; however, the authors also briefly mention precipitation and the formation of mixed aluminum hydroxo species as possible causes.

Going deeper into the exact nature of the aluminum fluoride species that are formed is beyond the scope of this work, but our NMR titration experiments clearly show that differently coordinated molecular aluminum fluoride species are formed upon fluoride addition to a dispersion of the MOF in water. In agreement with the literature, we found complexes with one and two fluoride atoms bound to aluminum at low fluoride concentrations. With increasing fluoride concentration, aluminum species that are coordinated by more and more fluoride ions are formed, while the amount

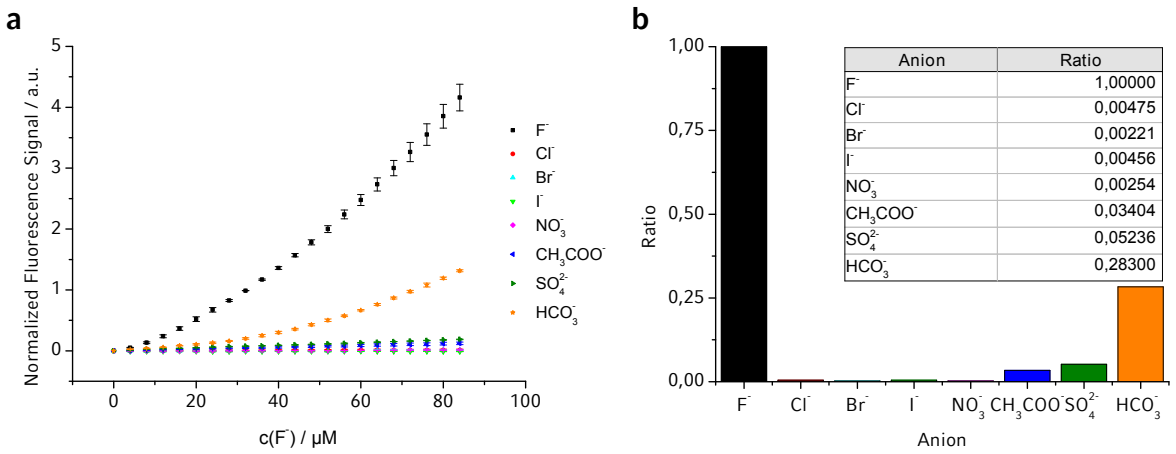

Figure 6.10: Sensor selectivity data obtained from fluorescence titrations with different salt solutions. (a) Data obtained from fluorescence titrations of NH_2-MIL-101(Al)-FITC with sodium salts of different anions. Error bars indicate the deviation of two individual measurements with different MOF and titration stock solutions. (b) Ratio of slopes obtained by fitting a line through the origin to the data in (a). For a more detailed description of experimental details, data analysis, and raw spectral data see Section 6.5.

of aluminum species with lower fluoride amounts decreases. Interestingly, the amount of "free" fluoride (i.e. fluoride ions that are not coordinating a metal ion) observed at $\delta \approx -119.2$ ppm is very low at the beginning, and after the corresponding peak

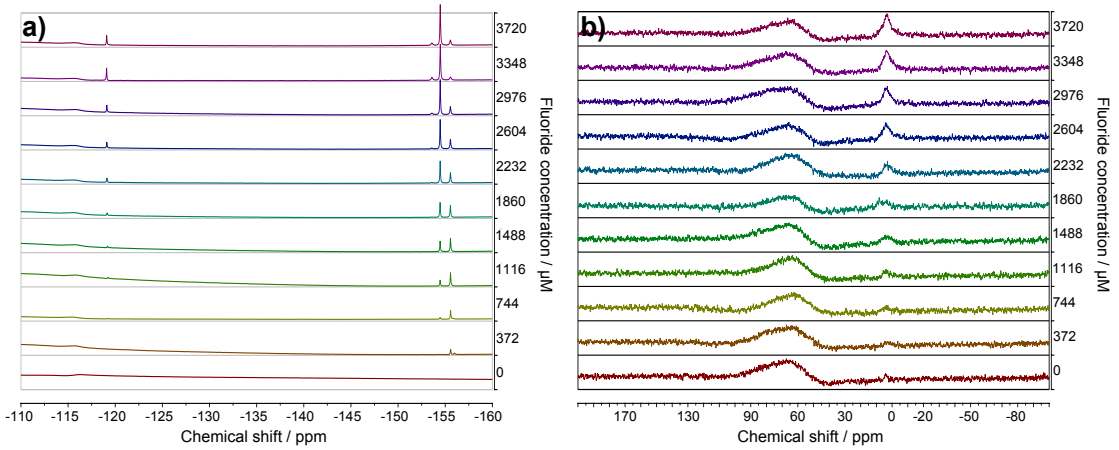

Figure 6.11: ^{19}F and ^{27}Al NMR titration of NH_2-MIL-101(Al)-FITC. a, ^{19}F NMR. b, ^{27}Al NMR. The broad signal in the ^{27}Al NMR between $\delta \approx 50$ ppm and $\delta \approx 110$ ppm arises from aluminum atoms from the NMR probe head or the NMR glass tube (see Figure 6.14). The concentration of fluoride was adjusted to the values given in the figure. The peak assignments are based on references.[261,262] For a detailed description of experimental parameters, FID processing and raw spectral data see Section 6.5 and Figure 6.14.

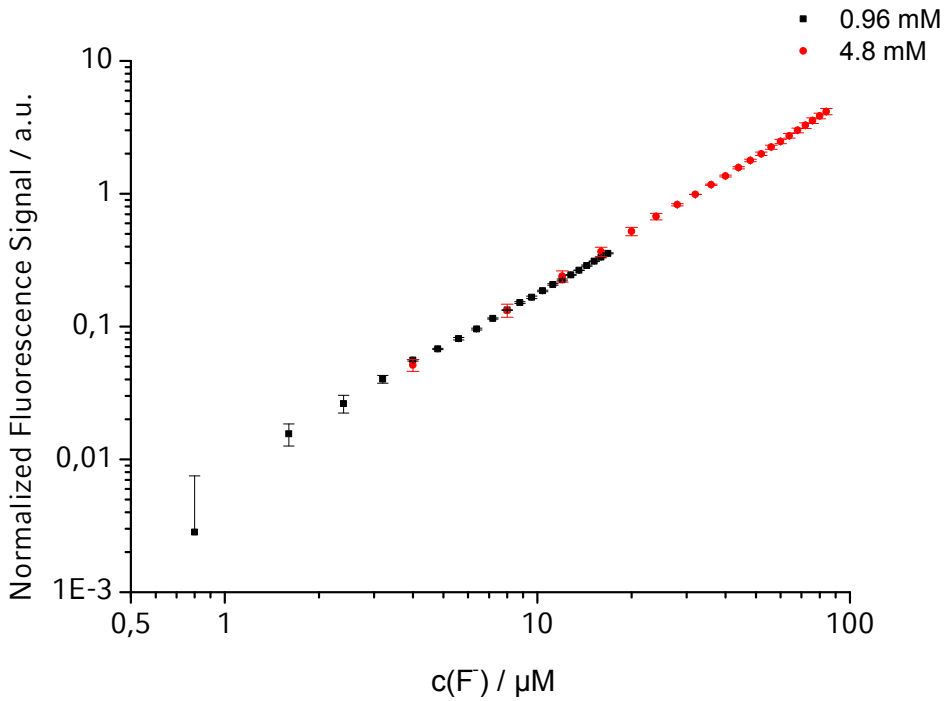

Figure 6.12: Fluorescence titration curves. The data show fluorescence titrations of NH_2-MIL-101(Al)-FITC with two titration solutions of different concentration. Error bars indicate the deviation of two individual measurements with different MOF and titration stock solutions. For a more detailed description of experimental details, data analysis, and raw spectral data see section 6.5 and Figure 10.4.

starts to develop at about 1000 µM, it stays at a low level. We propose the following detection mechanism: aluminum fluoride complexes and linker molecules (together with the fluorescent dye) are liberated from the framework into the solution via a displacement of linker molecules by fluoride ions. This is also backed up by the ^{27}Al NMR spectra (see Figure 6.11.b), which feature a broad peak at $\delta \approx 4$ ppm that can be assigned to $[AlF_x(H_2O)_{(6-x)}]^{(3-x)}$.[257] Before fluoride addition, no signals can be observed in the ^{27}Al NMR, indicating that there is no appreciable amount of aluminum present in the solution at the beginning. Only after addition of fluoride, aluminum fluoride complexes can be found in solution. This indicates that the aluminum source is really the MOF and that the fluoride complexes that can be observed by NMR are indeed formed by a degradation of the metal–organic framework.

In addition to the remarkable selectivity of NH_2-MIL-101(Al)-FITC towards fluoride, we could also demonstrate a very high sensitivity covering a broad range of fluoride ion concentrations from approximately 15 µg up to at least 1600 µg of fluoride per 1 L of water, or 15 to 1600 ppb. (see Figure 6.12).

We believe that the main reason for the high sensitivity is the efficient quenching and dequenching of fluorescein fluorescence upon incorporation into and liberation from the host framework, respectively. The slight deviation from linear behavior at low fluoride concentration (which can be better seen in a non-double-logarithmic plot, as for example in Figure 6.1.d) is attributed to the initial coordination of fluoride ions to trace amounts of free aluminum precursor still present in the porous framework or from coordination to unsaturated metal centers inside the MOF. Both effects do not lead to a replacement of linker molecules by fluoride and hence the amount of fluorescein that is released into the solution is lower than expected. Once all these metal ions are coordinated by fluoride, further addition of fluoride results in linker displacement and liberation of fluorescein into the solution and the concomitant fluorescence dequenching discussed above. Assuming a homogeneous distribution of fluorescein throughout the framework, the fluorescence signal should hence increase linearly with fluoride concentration, until the framework is more or less completely dissolved, at which point the fluorescence signal should level off. However, that point was not reached in the titrations shown here.

6.4 Conclusion

In this study we have introduced a new signal transduction scheme in the field of MOFs, which is based on the efficient quenching of fluorescent guests upon incorporation into the porous framework and the subsequent dequenching upon analyte-specific degradation of the host material. This new sensing concept was illustrated with the dye-loaded MOF NH_2-MIL-101(Al), thus introducing a highly sensitive and selective fluoride sensor that is compatible with aqueous analyte solutions. Deeper insights into the transduction mechanism were gained by ^{19}F and ^{27}Al NMR titration studies, revealing that the porous host framework is indeed dissolved upon fluoride ion addition due to competing coordination of fluoride to metal centers inside the metal organic framework. We believe that the high sensitivity of the system is controlled by the coordination chemistry and the different affinities of the metal ions inside the framework towards linker molecules, fluoride ions, and other interfering ions. Fluorescence titration experiments were used to quantitatively show the remarkable selectivity and sensitivity of our fluoride sensor. We attribute the high sensitivity to the fact that a turn-on fluorescence signal rather than a color- or fluorescence-quenching based signal transduction scheme is used. All in all, the sensitivity of the sensor presented

in this work is far better than that of the commonly used optical fluoride detection methods in aqueous solution according to data presented by the World Health Organization (WHO) and the American Public Health Association,[263,264] namely the sodium-2-(parasulfophenylazo)-dihydroxy-3,6-napthalene disulfonate (SPADNS) method and the complexone method. These references give a fluoride detection range of 0.1 to 1.4 mg L^{-1} for the SPADNS method and a range of 0.05 to 2.0 mg L^{-1} for the complexone method, at comparable anion selectivity. In our work, we have demonstrated a detection range from 0.015 mg L^{-1} up to at least 1.6 mg L^{-1}.

We believe that the general concept of releasing fluorescent guest molecules from MOFs can be extended to other combinations of analytes and metal coordination environments, thus adding to the growing toolbox of optical chemosensors.

6.5 Experimental Part

6.5.1 Methods and Characterization

Powder X-ray diffraction (PXRD) measurements were performed using a Bruker D8 diffractometer (Cu-$K_{\alpha 1}$ = 1.5406 Å; Cu-$K_{\alpha 2}$ = 1.5444 Å) in theta-theta geometry equipped with a Lynx-Eye detector. The powder samples were measured between 2° and 45° two theta, with a step-size of 0.05° two theta.

Scanning electron microscopy (SEM) images were recorded with a JEOL JSM-6500F microscope equipped with a field emission gun, operated at an acceleration voltage of 5 kV and a working distance of 10 mm. Prior to measurements a thin gold layer (purity: 99.95 %) was deposited on the samples using an Oerlikon Leybold Vacuum UNIVEX 350 sputter coater system operated at a base pressure of 1×10^{-6} mbar, an Argon pressure of 1×10^{-2} mbar, a power of 25 W and a sputtering time of 5 min.

Fluorescence titrations were carried out using a Hamilton Microlab 500 semiautomatic precision liquid processor with a Hamilton 1705TLLX 50 µL syringe connected to a PTI fluorescence spectrometer featuring a PTI 814 photomultiplier detector, a PTI MD5020 motor driver, a Quantum Northwest TC 125 sample holder, and an Ushio UXL-75XE Xenon short arc lamp in a PTI A-1010B arc lamp housing driven by a PTI LPS-220B lamp power supply.

FTIR measurements were performed in transmission mode on a Bruker Equinox 55s between 4000 cm^{-1} and 400 cm^{-1} and a resolution of 4 cm^{-1}.

Raman spectra were recorded using a Bruker FRA106/S FT Raman module at-

tached to a Bruker Equinox 55s FTIR spectrometer and a Coherent Compass 1064-500N Nd:YAG laser. Measurements were performed with a laser power of 100 mW at a wavelength of 1064 nm.

Nitrogen sorption measurements were performed on a Quantachrome Instruments Autosorb at 77 K. Sample outgassing was performed for 12 h at 393 K. Pore size and pore volume were calculated by a NLDFT equilibrium model of N_2 on silica, based on the adsorption branch of the isotherms. BET surface area was calculated over the range of partial pressure between 0.05 – 0.20 p/p0. The pore volume was calculated based on the uptake ($cm^3\,g^{-1}$) at a relative pressure of 0.30 p/p0.

Thermogravimetric analyses of the bulk samples were performed on a Netzsch STA 440 C TG/DSC with a heating rate of $1\,K\,min^{-1}$ in a stream of synthetic air at about $25\,mL\,min^{-1}$.

Dynamic light scattering (DLS) was performed on a Malvern Zetasizer-Nano instrument equipped with a 4 mW He-Ne laser (633 nm) and an avalanche photodiode detector.

NMR spectra were recorded on a Jeol EX 400 or a Jeol Eclipse 400 instrument at room temperature and at a frequency of 376.17 MHz with 2048 scans for ^{19}F NMR and 104.17 MHz with 4096 scans for ^{27}Al NMR.

6.5.2 Chemicals

Aluminum(III) chloride hexahydrate (99.9 %, Aldrich), 2-amino terephthalic acid (99 %, Aldrich), N,N-dimethylformamide (99.8 %, Aldrich), fluorescein 5(6)-isothiocyanate (90 %, Aldrich, FITC), sodium fluoride (99 %, Grüssing), sodium chloride (99.8 %, Aldrich), sodium bromide (99 %, Fluka), sodium iodide (99 %, VWR), sodium bicarbonate (99.5 %, Fluka), disodium sulfate (99 %, Grüssing), sodium acetate trihydrate (99.5 %, Merck), sodium nitrate (98 %, Applichem) as well as all solvents are commercially available and were used as received without further purification. Millipore water ($> 18\,M\Omega\,cm^{-1}$) was used for ^{19}F and ^{27}Al NMR, for fluorescence titrations and for the preparation of stock solutions.

6.5.3 Synthesis of NH_2-MIL-101(Al)

The solvothermal synthesis of NH_2-MIL-101(Al) was carried out according to a slightly modified literature synthesis.[257] In a 50 mL glass reactor, aluminum(III) chloride hexahydrate (0.51 g, 2.11 mmol, 1.0 eq.) and 2-amino terephthalic acid (0.56 g, 3.09 mmol,

1.5 eq.) were dissolved in 30 mL N,N-dimethylformamide (DMF) in an ultrasonic bath. The sealed glass reactor was kept for 72 h in a preheated oven at 403 K. The resulting yellow powder was filtered under vacuum and washed with acetone. To remove organic species trapped within the pores, the samples were extracted in boiling methanol for 8 h and stored at 373 K.

6.5.4 Synthesis of NH_2-MIL-101(Al)-FITC

For dye labeling experiments, fluorescein 5(6)-isothiocyanate (FITC; 15.0 mg, 0.0385 mmol) was dissolved in absolute ethanol (50 mL). NH_2-MIL-101(Al) (100 mg, 0.157 mmol) was added to the ethanolic dye solution and left for 48 h on an orbital shaker. NH_2-MIL-101(Al)-FITC was filtered and repeatedly washed with ethanol and deionized water.

6.5.5 Fluorescence titrations of NH_2-MIL-101(Al)-FITC

For fluorescence titration measurements, a stock solution of NH_2-MIL-101(Al)-FITC in water with a mass concentration of 1 mg mL^{-1} was freshly prepared and sonicated very briefly (a few seconds) in an ultrasonic bath to obtain a homogeneous suspension of the MOF in water with a hydrodynamic particle size of approximately 300 nm as determined by dynamic light scattering (see Figure 6.13). Then, 100 µL of this stock solution was diluted in 2900 µL of water (resulting in a total volume of 3 mL and a final mass concentration of 33 µg mL^{-1}) in a quartz glass cuvette and stirred magnetically at room temperature. While stirring, the fluorescence emission was monitored continuously at 520 nm every second, using an excitation wavelength of 485 nm and an integration time of 1 s. The band-pass for excitation and emission was 4 nm. When the solution was equilibrated and the fluorescence signal did not change any more over time (typically after 20 – 40 min), a sodium fluoride solution (freshly prepared by dissolving an appropriate amount of NaF in water) was dispensed stepwise in portions of 2.5 µL from a 50 µL syringe into the fluorescence cuvette. After each step, the fluorescence was monitored for 4 min using the same parameters as above (see Figure 6.14).

Titrations with other salt solutions and with the unlabeled MOF were performed accordingly, using 4.8 mM stock solutions of the corresponding salts and a MOF mass concentration of 33 µg mL^{-1}.

For data analysis, the mean fluorescence signal was calculated for each salt addition

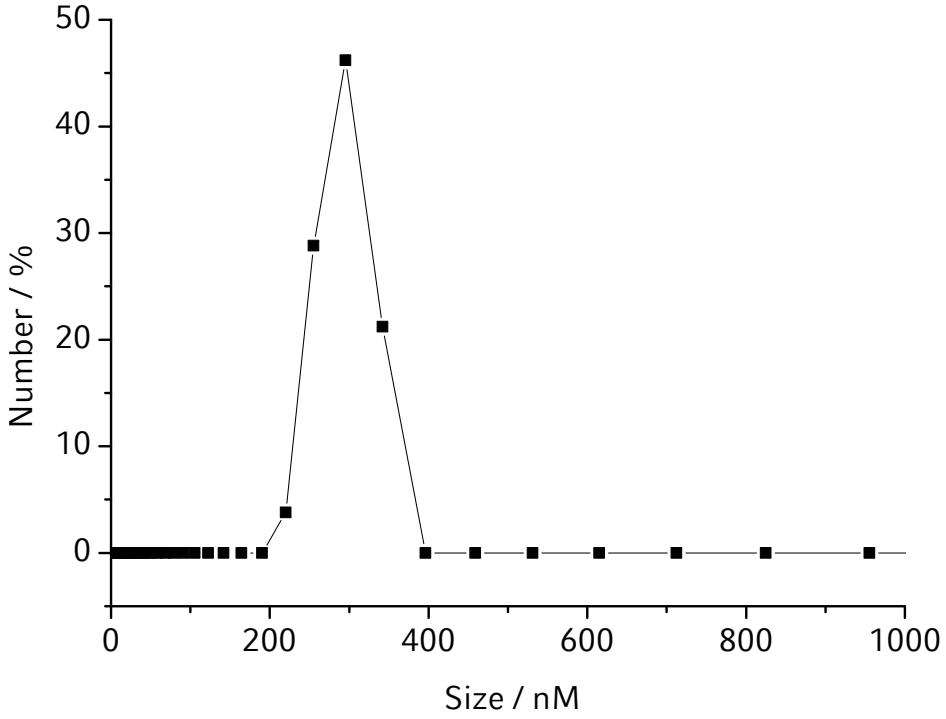

Figure 6.13: Dynamic light scattering (DLS) measurement of a suspension of the labeled MOF in water (33 µg mL^{-1}), indicating a mean hydrodynamic size of the particles of approximately 300 nm.

step from the last 60 seconds of the 4 minutes measurement interval (typically, the change in fluorescence signal was negligible 10 to 180 seconds after salt addition), the background fluorescence (i.e. the fluorescence signal before fluoride addition) was subtracted, the values were normalized to the starting intensity, and then plotted against the anion concentration in the cuvette. Dilution of the solution due to volume changes caused by the addition of the salt solutions was neglected (the total volume change was 2 % max.). Errors were calculated from the deviation of two individual measurements made with different MOF and salt stock solutions. Lines through the origin were fitted using a standard linear regression model.

6.5.6 NMR titrations of NH_2-MIL-101(Al)-FITC

For ^{19}F and ^{27}Al NMR titrations, a stock solution of NH_2-MIL-101(Al)-FITC in H_2O with a mass concentration of 1.2 mg mL^{-1} was prepared. Then, 0, 40, 80, 120, 160, 200, 240, 280, 320, 360 and 400 µL of freshly prepared aqueous NaF stock solutions (7.43 mM) was added to 400 µL of the MOF stock solution in an 1.5 mL Eppendorf cup, and the total volume was adjusted to 800 µL with H_2O. The resulting solutions

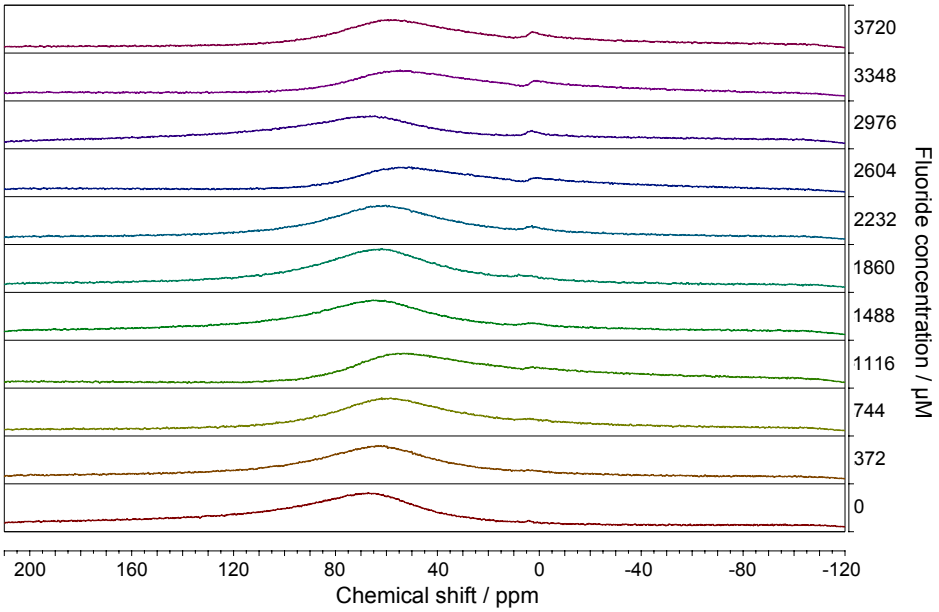

Figure 6.14: ^{27}Al NMR spectra before background correction.

were mixed by shaking on a vortexer and by sonication in an ultrasonic bath and subsequently transferred to an NMR tube.

^{19}F and ^{27}Al NMR spectra were recorded at room temperature at 376.17 MHz and 104.17 MHz and with 2048 and 4096 scans, respectively. The FIDs were processed using zero filling, phase correction and Gauss- and exponential window functions prior to FFT. In the case of ^{27}Al NMR spectra, the background was subtracted for each spectrum individually by using the Whittaker smoother algorithm as implemented in MestReNova v5.2.5. For uncorrected spectra, see Figure 6.14.

Chapter 7

. . . . . .

Hierarchically Patterned Thin Silica Films

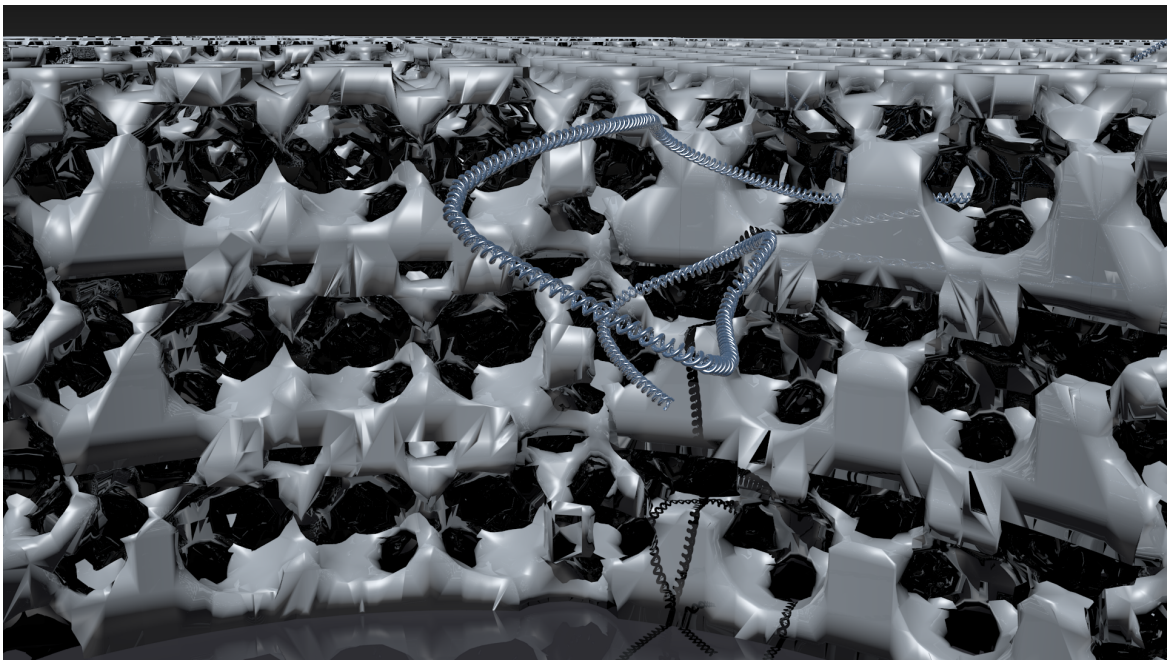

7.1 Abstract

Different methods for producing hierarchically structured thin silica films are presented. Such films could provide a platform for investigation of different movement modes of macromolecules inside constrained geometries and could also prove benefi-

cial for miniaturization of macromolecule separation *via* the entropic barrier transport mechanism. In order to produce the patterned films, a combination of various top-down and bottom-up strategies was combined, including soft templating, hard templating, soft lithography and photolithography. The properties of the resulting structures are compared and their advantages and disadvantages are discussed.

7.2 Introduction

The motion of macromolecules in confined spaces plays an important role in many processes, ranging from chromatographic separation techniques to molecular pore complexes inside cells. There are three main mechanisms that describe the mode of motion of a macromolecule in a constraining medium, namely sieving, reptation, and entropic barrier transport. In sieving, the macromolecule is treated as a rigid sphere and is assigned a fixed radius. Pores or constrictions within the medium that are smaller than this radius exclude the macromolecules from taking certain pathways, hence limiting the amount of transversable paths for larger molecules and leading to a slower diffusion rate.[265] In the reptation model, a (linear) macromolecule is described as being enveloped by a virtual tube, undergoing snake-like movement in the confining medium.[266,267] The third mechanism, entropic barrier transport,[268,269] takes into account that a flexible macromolecule has to adopt a certain conformation in order to be able to fit through constrictions inside the medium. This limitation of the amount of accessible conformations of the macromolecule leads to a loss in entropy.[270] Hence, the entropic barriers that arise from spatial constraints within the medium cause macromolecules to stay preferably in less constricting environments, where their entropy is higher.[271–273]

In this ongoing research project, hierarchically structured silica thin films featuring well-defined structures that introduce porosity at different length scales were investigated. These could provide means to study the different modes of macromolecular motion, especially the entropic barrier transport, on a single molecule basis. Such a model system could not only greatly enhance our understanding of these complex processes, but could provide a platform for efficient macromolecule separation on the nanoscale. In order to achieve the hierarchical structuring, various top-down and bottom-up strategies were combined, including soft templating, hard templating, soft lithography and photolithography.

7.3 Results and Discussion

In order to be able to implement a platform for studying the entropic barrier transport of macromolecules in thin silica films, a hierarchical structure was designed that features periodically arranged large voids imposing little conformational constraints, interconnected by a network of pores with smaller windows imposing large conformational constraints. The large voids were introduced into the thin silica film through posts or pillars (approximately 1 µm in diameter and separated by approximately 1 µm) with a soft lithography or a photolithography process. The porosity within the porous silica thin films providing areas with large conformational constraints was introduced either by soft templating using the triblock copolymer Pluronic F127 or through hard templating using poly(methylmethacrylate) (PMMA) spheres.

7.3.1 Photolithography combined with soft templating

In this first example, a hexagonal pillar pattern was produced photolithographically on a substrate (see Figure 7.1.a,b), and the pillars defined the areas of the large voids. The pillars were produced using microscope projection lithography.[194] In this technique, a shadow mask is inserted into the field stop position of a standard inverted microscope and the microscope objective is used to reproduce the pattern of the mask in a photoresist layer on the sample (see also Section 2.11.2). Next, a mesoporous silica precursor solution was spin-coated onto the substrate, yielding mesoporous silica thin films *via* the evaporation-induced self-assembly (EISA) process[19] (see Figure 7.1.c,d). The triblock copolymer Pluronic F127 was used as the structure directing agent to introduce mesoporosity, resulting in a cubic structure with mesopores of about 10 nm in diameter.[274] Lift-off of the photoresist pillars in dimethyl sulfoxide (DMSO) or N-methyl-2-pyrrolidone (NMP) at 60 °C, followed by extraction of the Pluronic template *via* refluxing in an acidified solution of ethanol and subsequent tempering at elevated temperatures yields the desired hierarchically structured thin silica films (see Figure 7.1.e,f). Further functionalization of the films can be achieved by post-synthetic grafting through refluxing the films in toluene in the presence of a functionalized alkyltrialkoxysilane.

An image reversal photoresist was used in negative mode for producing the photoresist pillar patterns, and the processing conditions (exposure time, IR-bake, development time, hard-bake) were optimized to make the resist durable enough to withstand the ethanolic solvent during spin coating of the mesoporous silica precursor solution,

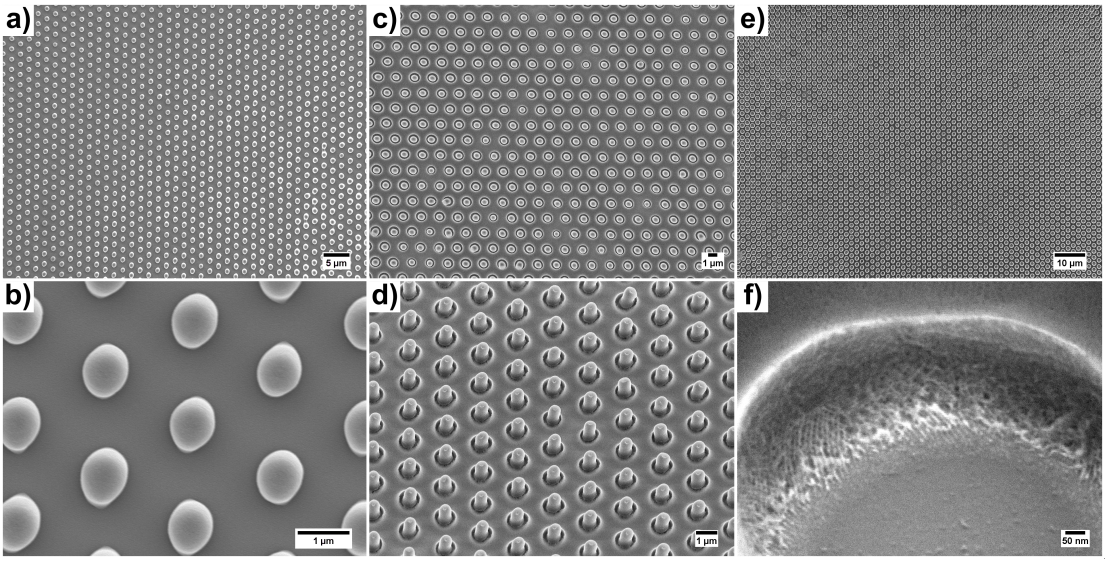

Figure 7.1: Scanning electron microscopy images of the three stages for creating hierarchically patterned thin silica films using photolithography and soft templating. The images show photoresist pillars (a,b) before and (c,d) after deposition of the thin silica film, and (e,f) the final structure after resist lift-off. In (f), the mesoporous structure of the silica can be seen.

while still being removable at later points in time. However, even very small amounts of photoresist residues that remain on the substrate after resist lift-off impede single molecule microscopy measurements due to highly fluorescent compounds in the resist. Hence, a different approach was investigated in which the large voids are introduced by a soft lithography process, avoiding the use of fluorescent components for structuring the thin silica films.

7.3.2 Soft lithography combined with soft templating

For using soft lithography, a master was prepared by MPL using the same hexagonal pattern as above. However, since the pattern is inverted in the PDMS replica molding step, this time cylindrical "holes" rather than pillars were desired. This was achieved by using the same photolithography process as above, but without the image reversal step (i.e., the resist was used in positive mode). After development, a photoresist layer with cylindrical holes is obtained, which will result in PDMS pillars after the replica molding process. The IR photoresist remains photoactive after development, and exposing it to a high dose of UV light and subsequently subjecting it to a hard-bake step causes further cross-linking of the resist and makes it more durable. Poly(dimethylsiloxane) (PDMS) stamps were produced from this master in a standard PDMS replica molding

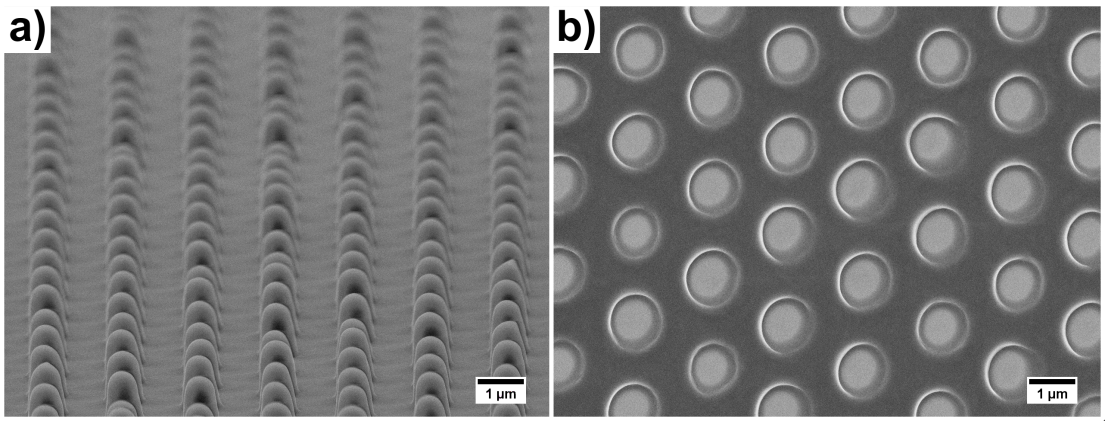

Figure 7.2: (a) Scanning electron microscopy images of the PDMS stamp used for soft lithography and (b) the resulting hierarchically structured thin silica film.

process. Note that the PDMS stamps feature pillars now, due to the inversion of the structure (see Figure 7.2.a). Subsequently, the same EISA precursor solution that was used in the previous approach was drop-casted on a substrate and the PDMS stamp was carefully applied on top, resulting in the pattern transfer (see Figure 7.2.b).

7.3.3 Soft lithography combined with hard templating

Since the maximum pore size and also the window size between the pores in a cubic mesoporous silica thin film obtained from soft templating is somewhat limited, a hard templating approach with PMMA spheres was also pursued. In this approach, PMMA beads of a defined size are mixed into the EISA precursor solution prior to drop-casting on the substrate and applying the PDMS stamp. After solidification, the PMMA spheres can be extracted by refluxing in tetrahydrofuran (THF) and acetone to give the final structures (see Figure 7.3).

7.3.4 Comparison of structures obtained from soft lithography and from photolithography

One important aspect that favors soft lithography over photolithography in this project is the fact that strongly fluorescent compounds in the resist that remain on the substrate after resist lift-off can impede single molecule fluorescence microscopy measurements, as already briefly mentioned above. The soft lithography process is also easier, cheaper, and faster, since it does not involve so many individual steps. Moreover, thin films that were prepared *via* photolithographic patterning show a rim around the

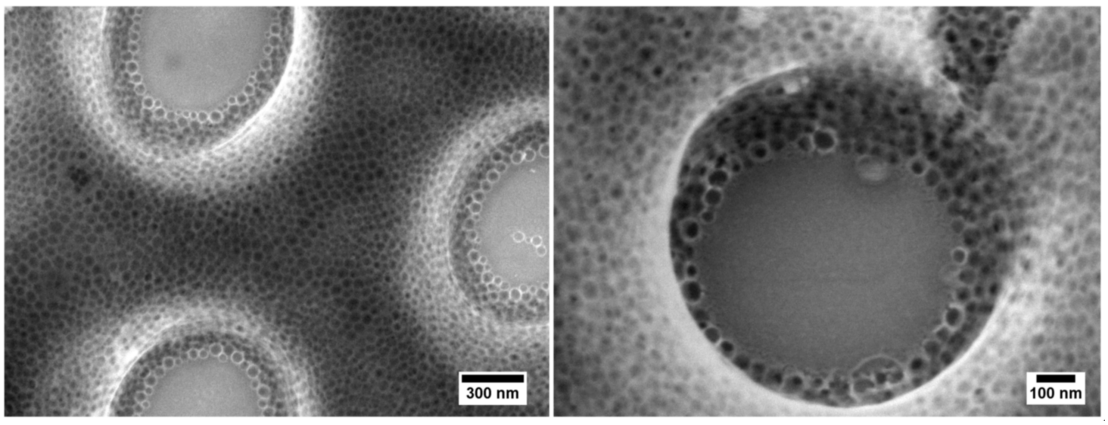

Figure 7.3: Scanning electron microscopy images of a hierarchically structured thin silica film obtained by soft lithography and hard templating.

cylindrical voids (see Figure 7.4 (top)), presumably due to wetting of the photoresist pillars by the EISA precursor solution, whereas the PDMS pillars are not well wetted and hence no rim appears in samples obtained *via* soft lithography (see Figure 7.4 (bottom)). However, on larger scales the photolithographically patterned films are more uniform, while films patterned by soft lithography occasionally show defects due to a deformation or collapse of the PDMS pillars caused by forces during the patterning process.

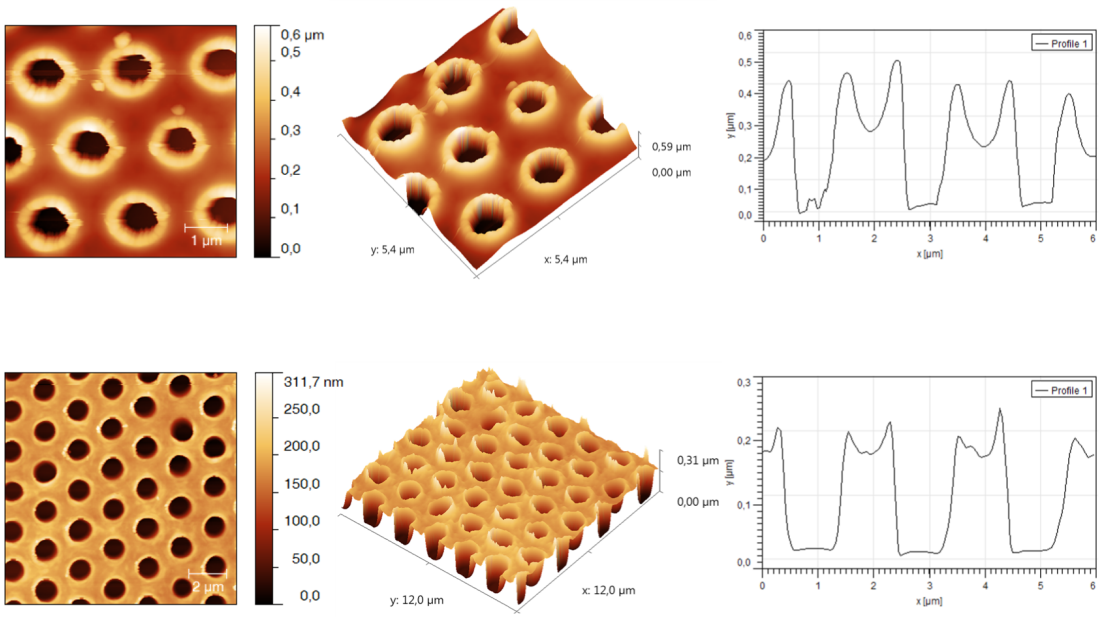

Figure 7.4: AFM images and line profiles of thin films patterned by photolithography (top) and soft lithography (bottom).

7.4 Conclusion and Outlook

We introduced different methods for producing hierarchically structured thin silica films featuring structures at different length scales (from the nanometer to the micrometer range) and compared the properties of the resulting patterns. While photolithography has the advantage of yielding more uniform patterns, soft lithography using PDMS stamps is in general quicker, easier, and more cost-efficient. Moreover, soft lithography circumvents the problem of highly fluorescent residues that remain on the substrate after lift-off of a photoresist, hence making the process compatible with single molecule fluorescent microscopy studies. Using a colloidal hard templating approach with PMMA spheres instead of a soft templating with block copolymers allows for an extension of the pore sizes beyond 20 nm.

In future projects, the pore sizes and window openings of the mesopores can be systematically varied and tailored to the macromolecules of interest by using PMMA spheres of different sizes. Depending on the studied macromolecules, different functionalizations of the silica walls could be necessary, such as a functionalization with amino, cyano or phenyl groups in order to ensure DNA mobility inside the pores.[47,48] In the end, macromolecules of various sizes can be included into the structure, and their movement modes can be analyzed by single molecule fluorescence microscopy. Moreover, a separation of macromolecules of different sizes due to the entropic barrier transport mechanism could be envisioned.

7.5 Experimental Part

7.5.1 Methods and characterization

Exposure to oxygen plasma was carried out with a Femto Plasma System from Diener Electronic typically operated at a power of 50 W and an oxygen flow of 4 – 5 sccm. Atomic force microscopy (AFM) images were recorded with a Nanoink NScriptor DPN System in close contact mode. Scanning electron microscopy (SEM) images were obtained with a JEOL JSM6500F scanning electron microscope equipped with a field-emission gun, typically operated at an acceleration voltage of 4 kV and a working distance of 5 – 10 mm. Microscope projection lithography (MPL) was carried out using a Nikon Eclipse Ti-U inverted microscope with a Nikon Intensilight C-HGFI fluorescence lamp and a Nikon Plan APO 60x/1.20 water immersion objective. Yel-

low light for avoiding exposure during focusing was obtained by switching a 500 nm LWP edge barrier filter into the light path. For exposure, this filter was replaced by a Brightline HC 370/36 band-pass excitation filter, and the light was reflected onto the sample with a 80R/20T UV/Vis (300 – 700 nm) beam splitter. Exposure times were controlled manually *via* a shutter on the Intensilight C-HGFI light source. High-resolution prints (25 400 dpi) of transparency masks were obtained from KOENEN GmbH HighTech Screens and inserted into the field stop position of the microscope during MPL. The aperture was adjusted to maximize the contrast of the projected image (approximately 90 % closed). PDMS stamps were fabricated by replica molding from photolithographically patterned masters using standard techniques. The synthesis of the PMMA spheres was carried out by B. Mandlmeier and is described elsewhere.[275,276]

7.5.2 Chemicals

If not stated otherwise, all chemicals were used as received. Acetone, absolute ethanol, dry toluene, dimethyl sulfoxide (DMSO), N-methyl-2-pyrrolidone (NMP), hexamethyldisilazane (HMDS), tetraethylorthosilicate (TEOS), and Pluronic F127 were purchased from Sigma-Aldrich Co. HCl (1 M) was purchased from AppliChem GmbH. Standard glass coverslips (#1, 22 x 22 mm^2) were purchased from Gerhard Menzel, Glasbearbeitungswerk GmbH & Co. KG. Hellmanex cleaning solution was purchased from Hellma GmbH & Co. KG. PDMS and PDMS curing agent were purchased from Dow Corning Co. 1H,1H,2H,2H-perfluorooctyltriethoxysilane (PFOTS) was purchased from abcr GmbH & Co. KG. Aqueous ammonium hydroxide solution (25 %) was purchased from VWR International GmbH. AZ5214E image reversal photoresist and MIF726 developer were purchased from MicroChemicals GmbH.

7.5.3 Lithographic patterning

In a typical MPL process, glass coverslips were cleaned with isopropanol in an ultrasonic bath for 15 min, rinsed with DI water, submerged in a water/Hellmanex solution (100:1 v/v) at 60 °C for 1 h, followed by ultrasonic agitation for 3 min, rinsing with DI water and blowing dry with compressed air. The dried substrates were heated on a hot plate at 200 °C for 15 min to desorb water from the hydrophilic glass surface that can cause adhesion problems of the photoresist. In some cases, an adhesion-promoter (HMDS) was spin-coated onto the substrates prior to resist deposition. Then, 250 µL

of AZ5214E was spin-coated onto the substrates at 6000 rpm for 33 s, using a ramp of 2000 rpm s^{-1}. This resulted in a final photoresist thickness of approximately 1.1 µm. Subsequently, the resist was soft-baked on a hot plate at 110 – 115 °C for 50 s. Exposure times with a 60x objective were about 6 – 8 s, using a ND16 filter to attenuate the light intensity. When the resist was used in negative mode, an image reversal bake was carried out after the exposure by heating the substrate at 110 – 115 °C for 120 s on a hot plate, followed by a 5 min flood exposure (2.5 min from each side of the transparent substrate) with a 2x4 W Herolab UV lamp at a distance of approximately 1 – 2 cm. The resist was subsequently developed for 90 s in a MIF726 developer bath under static conditions, rinsed with DI water, and blown dry with compressed air. When the resist was used in positive mode (i.e., for the production of PDMS masters), it was subjected to a 5 min flood exposure with a 2x4 W Herolab UV lamp after the development step. The samples were then hard-baked in an oven for 30 min at 155 °C. When HMDS was applied as adhesion promoter before resist deposition, it was removed after the hard-bake step by exposure to an oxygen plasma for 3 min. The processing parameters are also summarized in Tables 10.6 and 10.7.

7.5.4 Thin film deposition

The EISA precursor solution was prepared by dissolving 0.6 g of Pluronic F127 in 10.0 g of ethanol and adding 500 µL of DI water and 100 µL of HCl (1 M). The resulting solution was stirred for 1 min at 500 rpm at room temperature, and then 1.0 g of TEOS was added and the solution was aged under constant stirring (500 rpm) at room temperature for 1.5 h. For the experiments involving PMMA spheres, 400 µL of the aged solution was mixed with 600 µL of a suspension of PMMA spheres in water (6.7 wt. %). In the experiments involving photolithography, the precursor solution was spin coated onto the patterned, hard-baked samples (30 s at 2000 rpm), while in the experiments involving soft lithography, the solution was drop-casted on a substrate treated with oxygen plasma for 15 min, followed by careful application of the PDMS stamps using only gravity and without any further external pressure. The deposited solution was left to solidify under ambient conditions for 1 – 2 days, followed by incubation in a saturated NH_3 atmosphere, obtained by incubating the samples in a closed container next to a Petri dish containing an ammonium hydroxide solution (25 % in water). For photolithographically patterned substrates, the photoresist was subsequently removed by heating the substrates to 60 °C in dimethyl sulfoxide (DMSO) or N-methyl-2-pyrrolidone (NMP) for 15 min, followed by an ultrasonic treatment for

5 min. The substrates were then rinsed immediately with acetone, isopropanol, and water, and blown dry with compressed air. For substrates produced by soft lithography, the PDMS stamps were carefully removed before incubation in the NH_3 atmosphere.

7.5.5 Extraction and further treatment

Solvent extraction of Pluronic F127 was achieved by refluxing the substrates in an acidified ethanolic solution (ethanol/HCl(conc.) = 90:10 v/v) for 1.5 h. For samples including PMMA spheres, the PMMA was dissolved by refluxing in tetrahydrofurane (THF) or acetone for 8 h, followed by rinsing with acetone, isopropanol, and water and drying in a stream of compressed air. The samples were then heated in an oven for 1.5 h at 60 °C (ramp: 1 °C min^{-1}), 1.5 h at 160 °C (ramp: 1 °C min^{-1}), and 4.0 h at 200 °C (ramp: 1 °C min^{-1}).

For grafting functional groups onto the silica, the samples were heated for 1 h at 115 °C *in vacuo* (approximately 1 mbar), flushed with nitrogen, refluxed for 3 h in an 8 mM solution of the respective alkyltriethoxysilane in dry toluene under an inert atmosphere of dry nitrogen, rinsed with ethanol, and blown dry with compressed air.

Chapter 8

. . . . . .

Creating Patterns of Multifunctional Mesoporous Silica Nanoparticles

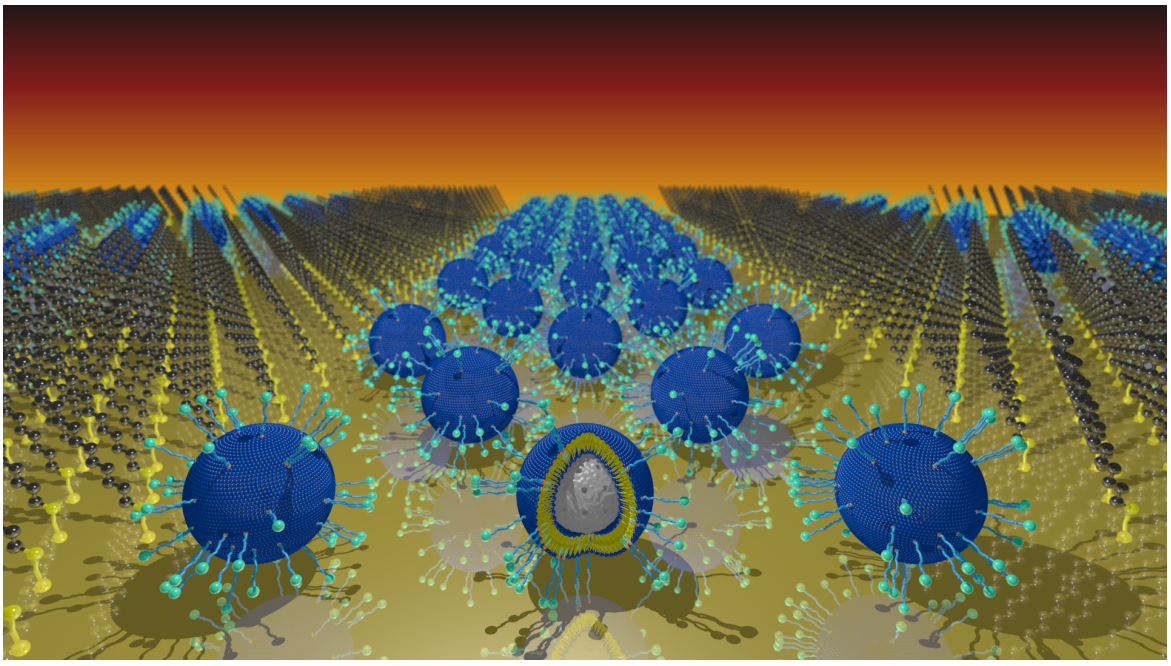

8.1 Abstract

We describe different methods for creating patterns of lipid bilayer-coated multifunctional mesoporous silica nanoparticles on gold and glass substrates. Providing the possibility to anchor different ligands or peptides to the membrane, such patterns are

of interest for studying cell–receptor interactions or for specific, spatial control of cell behavior. The patterning is achieved by endowing the nanoparticles with functional groups through anchoring of functionalized lipids to the supported lipid bilayer membrane and binding them to patterned substrates of complementary functionality. In this context, biocompatible reactions that can be carried out under mild conditions are investigated for the attachment of the nanoparticles to the surface, namely an EDC/NHS mediated amide bond formation, a Michael addition of thiols to maleimide groups, and the binding of thiols to gold.

8.2 Introduction

Mesoporous silica nanoparticles are promising candidates for controlling cell functions *via* the delivery of bioactive components due to their well-defined nanoscale porosity and their efficient uptake into cells. Moreover, site-selective surface modification can introduce a large variety of functionalities to the inner core and the outer shell of the nanoparticles, thereby specifically affecting host–guest-interactions, diffusion and release of guest molecules, and cell-surface interaction and recognition. Endowing nanoparticles with specific binding elements and creating patterns of these multifunctional nanoparticles could provide deeper insights into cell–receptor interactions and enable us to control cell behavior in a spatially controlled way. One very interesting aspect in this context would be the incorporation of signaling molecules that can influence cell adhesion, migration and differentiation into a supported lipid bilayer (SLB) membrane that is created around the multifunctional mesoporous nanoparticles.

In this ongoing research project, we discuss different ways to create patterns of mesoporous silica nanoparticles carrying a supported lipid bilayer (SLB@MSN) on glass or gold substrates. In order to do so, different functional groups are incorporated into the SLB that allow for specific binding to patterns of complementary chemical functionality created on the substrates. Since the particles still carry the SLB after the patterning, integration of various membrane bound or transmembrane proteins prior to or after the pattern creation could be envisioned, providing a platform for studying the interaction of these highly complex systems with cells or using them to specifically influence cell behavior.

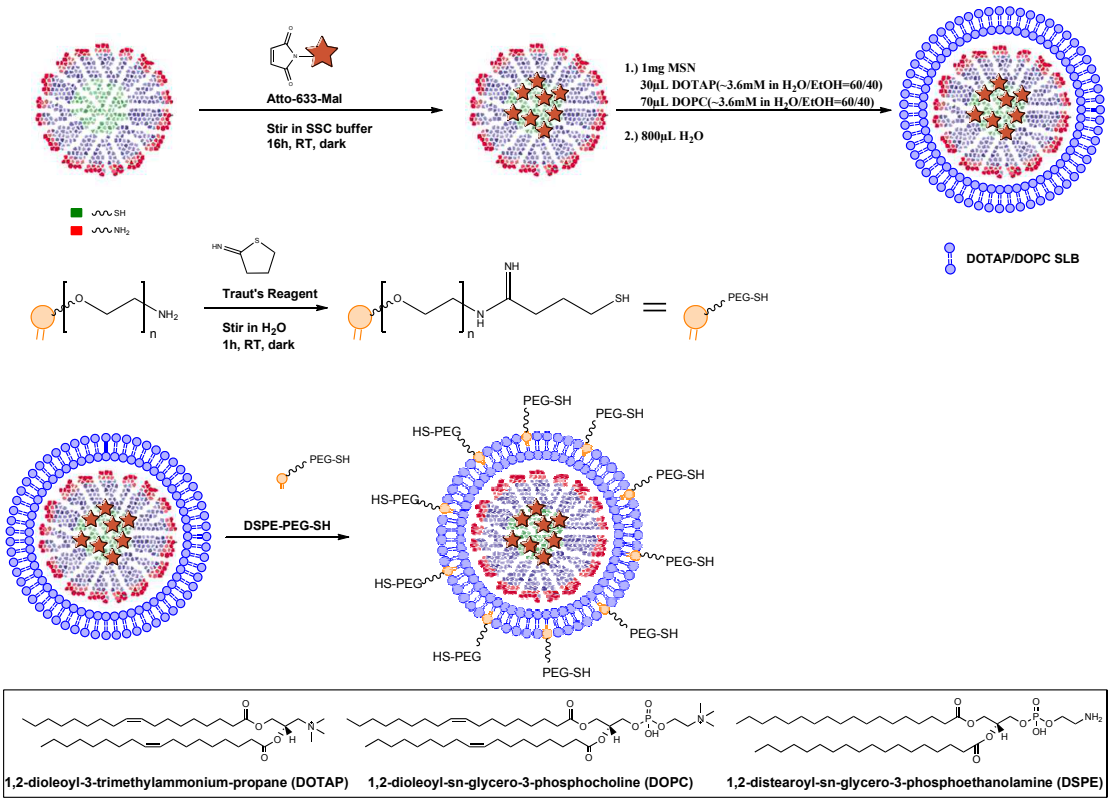

Figure 8.1: Schematic representation of the synthesis steps for creating fluorescently labeled SLB@MSN core–shell silica nanoparticles carrying functional groups in the SLB.

8.3 Results and Discussion

8.3.1 Preparation of mesoporous silica nanoparticles carrying a supported lipid bilayer membrane

Core–shell mesoporous silica nanoparticles carrying thiol groups in the core and amino groups in the outer shell (denoted MSN-SH_{core}-$NH_{2\,shell}$) were used throughout this work. Such particles can be synthesized *via* a delayed co-condensation approach, as described in literature.[112,113,277] The site-selective, "orthogonal" functionalization of the MSN allows for the specific binding of different compounds either to the inside or the outside of the particles. We attached a fluorescent label (Atto633) carrying a maleimide group specifically to the inside of the particles *via* a Michael addition of the maleimide group to the thiol groups in the core. Next, we constructed a supported lipid bilayer consisting of DOTAP (1,2-dioleyl-3-trimethylammoniumpropane) and DOPC (1,2-dioleyl-sn-glycero-phosphocholine) around the particles through a one-

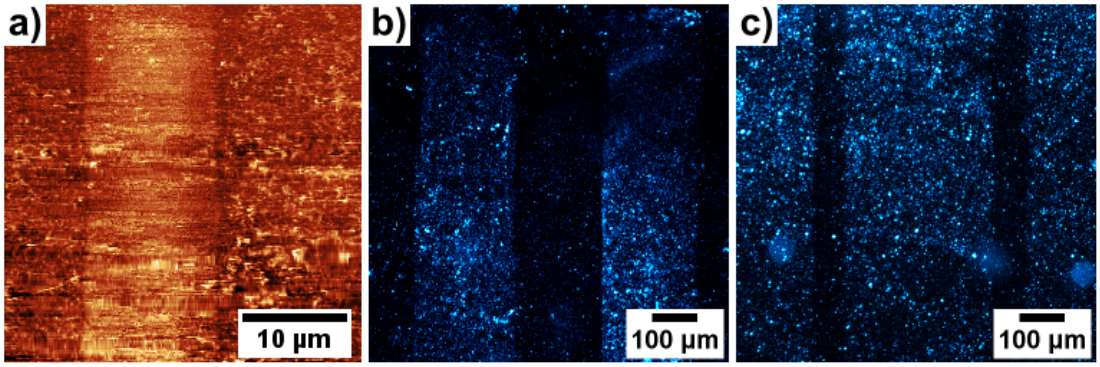

Figure 8.2: (a) Lateral force microscopy (LFM) image of a glass surface patterned with a stripe pattern of methyl and carboxyl terminated alkyl chains. (b,c) Fluorescence microscopy image of the pattern after covalently binding fluorescently labeled, amino-functionalized SLB@MSN to the carboxyl functionalized areas *via* EDC/NHS mediated amide bond formation.

step solvent exchange route.[114] Functional groups for specific binding to patterned substrates were incorporated into the supported lipid bilayer by letting DSPE lipids (1,2-distearoyl-sn-glycero-phosphoethanolamine) that carry different functional groups (denoted DSPE-PEG-X, where PEG denotes a poly(ethylene glycol) spacer to provide flexibility during the binding to the substrates and X indicates the functional group) diffuse into the membrane . The binding modes for creating nanoparticle patterns on substrates investigated in this work include bond formation between amino and carboxylic acid groups, between thiol and maleimide groups, and between thiol groups and gold. DSPE-PEG-SH was synthesized from DSPE-PEG-NH_2 using Traut's reagent (2-Iminothiolane). The whole process that gives functionalized, fluorescently labeled SLB@MSN core–shell silica nanoparticles carrying different functional groups anchored to the SLB is summarized schematically for the synthesis of DSPE-PEG-SH@SLB@MSN-SH_{core}-$NH_{2\,shell}$ in Figure 8.1.

8.3.2 Creating patterns through amide bond formation

In this approach, a glass coverslip was patterned with a stripe pattern of silanes carrying carboxyl groups, which can react with amino groups incorporated into the SLB of nanoparticles through an EDC/NHS (1-Ethyl-3-(3-dimethylaminopropyl)carbodiimide/N-Hydroxysuccinimide) mediated amide bond formation under mild conditions. The stripe pattern was prepared through microcontact printing (µCP) of hexadecyltrichlorosilane (HDTCS) or perfluoroctyltrichlorosilane (PFOTS) on plasma-treated

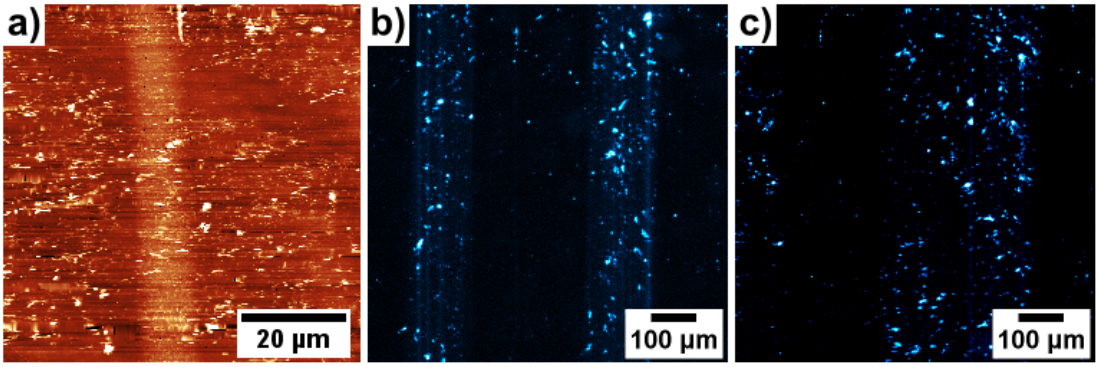

Figure 8.3: (a) Lateral force microscopy (LFM) image of a glass surface patterned with a stripe pattern of methyl and thiol terminated alkyl chains. (b,c) Fluorescence microscopy image of the pattern after covalently binding fluorescently labeled, maleimide-functionalized SLB@MSN to the thiol functionalized areas *via* a Michael addition.

glass coverslips. This resulted in passivated areas on the glass that prevent unspecific particle adsorption and binding during the EDC/NHS coupling step. Next, the unpassivated regions on the glass were reacted with 10-undecenyltrichlorosilane (UDTCS) to introduce a terminal C=C double bond to the glass surface, that can then be oxidatively cleaved to a carboxyl group through reaction with a mixture of sodium permanganate and sodium periodate.[278] The whole process results in a pattern of alternating stripes that are either passivated by hexadecyl or perfluoroctyl groups or that feature reactive carboxyl groups (Figure 8.2.a). The patterned substrates are then incubated in a dispersion of SLB@MSN with amino groups anchored to the SLB in the presence of EDC and NHS, which catalyze the amide bond formation between the carboxylic acid groups on the substrate and the amino groups on the nanoparticles. The passivated areas do not exhibit reactivity towards the amino groups even in the presence of EDC/NHS. After rinsing with water, the majority of unspecifically adsorbed particles is washed away, and only covalently attached particles remain on the substrate, revealing the stripe pattern (Figure 8.2.b,c).

8.3.3 Creating patterns through thiol–maleimide binding

Another binding mode that is often used in combination with biological samples due to the mild reaction conditions is a bond formation *via* a Michael addition between thiol groups and maleimide groups. The procedure for obtaining the pattern is similar to the one described in the previous section. First, some areas on a glass substrate are passivated by µCP with HDTCS or PFOTCS, followed by grafting of (3-

mercaptopropyl)triethoxysilane (MPTES) to the unpassivated regions of the substrate (Figure 8.3.a). Subsequent incubation in a dispersion of maleimide functionalized SLB@MSN results in a covalent binding of the maleimide group to the thiol groups on the surface, while no reaction occurs between the maleimide group and the passivated areas. The stripe pattern is again visualized by fluorescence microscopy, showing the position of fluorescently labeled SLB@MSN after rinsing off unbound nanoparticles (Figure 8.3.b,c).

8.3.4 Creating patterns through thiol–gold binding

A well-established method for creating patterns of self-assembled monolayers is the selective deposition of thiols on gold.[196] Here, two approaches were pursued. In the first approach, some areas on a gold substrate were again passivated through µCP of HDT, followed by the selective binding of thiol-functionalized SLB@MSN to the bare gold regions. In another approach, an alkanethiol SAM was used to create a pattern on the gold substrate that subsequently acts as an etch resist to a ferro-/ferricyanide etchant that selectively removes the unpatterned gold regions,[279] exposing the underlying glass substrate or titanium adhesion layer. Since the interaction of thiols with gold should be much stronger than the interaction of thiols with glass or titanium, this approach could in principle also provide means for a selective deposition of thiol-functionalized particles to the remaining gold regions.

Passivation with alkanethiols

In this approach, µCP with hexadecanethiol (HDT) was used to selectively passivate certain areas on a gold substrate, leaving a bare gold surface in the unpatterned regions. Subsequent incubation in a dispersion of thiol-functionalized SLB@MSN leads to a selective deposition of the particles on the bare gold regions, due to the strong thiol–gold interaction. Figure 8.4 shows electron microscopy and fluorescence microscopy images of the resulting patterns.

Selective etching

The last approach described here does not rely on a passivation of certain areas on the substrate to prevent particle adsorption, but rather introduces areas of different affinities towards the functional group anchored to the SLB of the nanoparticles by exposing different materials on the substrate. This is done by selective etching of

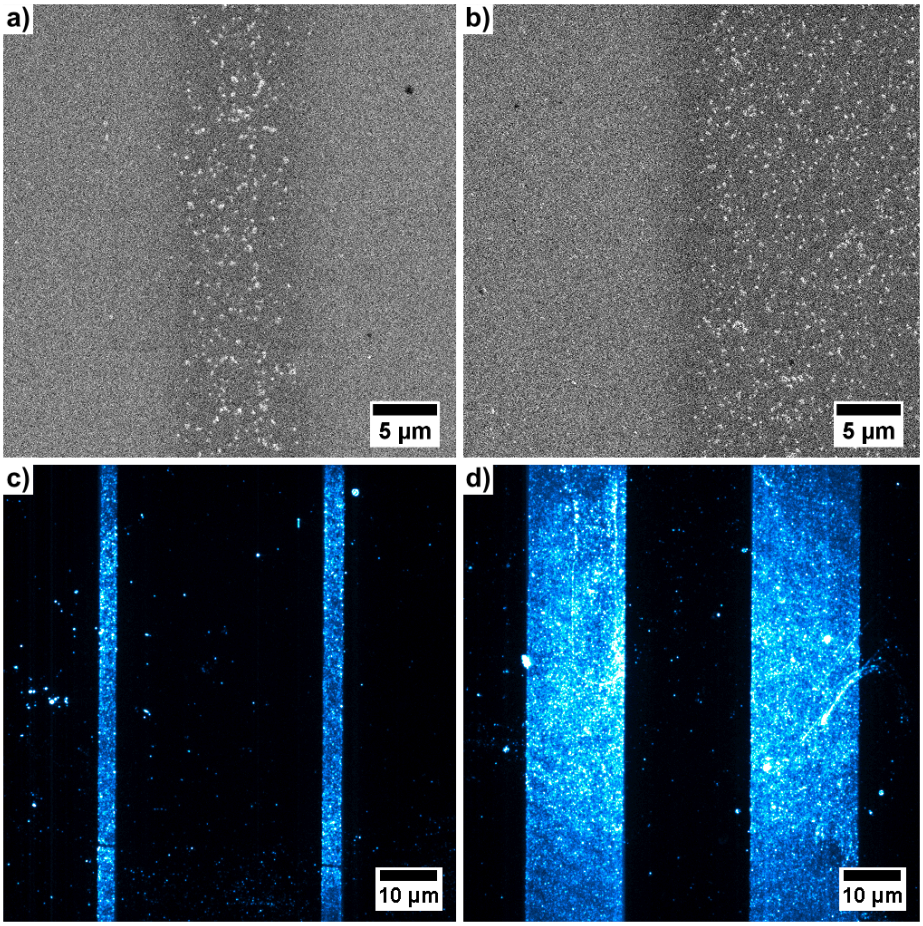

Figure 8.4: Scanning electron microscopy images (a,b) and fluorescence microscopy images (c,d) of a pattern of fluorescently labeled, thiol-functionalized SLB@MSN binding selectively to unpassivated areas of a gold substrate.

certain areas of a thin gold layer deposited on a glass substrate, resulting in either gold or glass (respectively titanium from a thin adhesion layer required for the deposition of gold on glass) being exposed to thiol-functionalized SLB@MSN.

It is known from literature that alkanethiol SAMs can act as etch resists for a ferro-/ferricyanide etchant.[279] Two different possibilities for creating SAM etch resist patterns on gold were investigated, either by using µCP to deposit hexadecanethiol (HDT) on the gold substrate (Figure 8.5.a,b), or by using dip-pen nanolithography (DPN) to create patterns of 16-mercaptohexadecanoic acid (MHDA; Figure 8.5.c,d). In DPN, an AFM tip is inked with a solution of the molecule to be deposited on the substrate (here MHDA), and brought into contact with the substrate surface for a defined time. This results in a transfer of the molecules from the tip to the surface and a spontaneous SAM formation in the contact region. Subsequent exposure of the

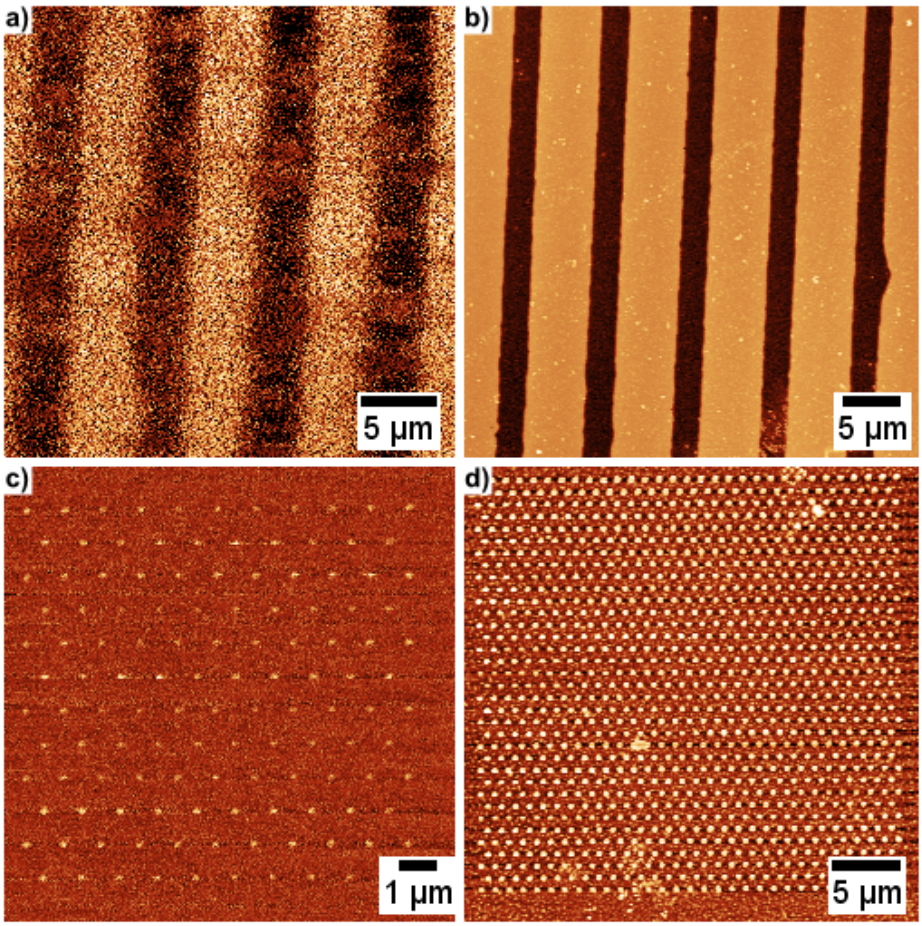

Figure 8.5: (a) Atomic force microscopy (AFM) phase image of a patterned SAM prepared by µCP of hexadecanethiol on gold. (b) AFM topography image after etching with a ferro-/ferricyanide etchant. (c) Lateral force microscopy (LFM) image of a patterned SAM prepared by dip-pen nanolithography(DPN) of 16-mercaptohexadecanoic acid on gold. (d) AFM topography image after etching with a ferro-/ferricyanide etchant.

substrates to a ferro-/ferricyanide etchant results in selective etching of the regions that are not protected by the SAM. Subsequently, the SAM can be removed by exposure to an oxygen plasma, resulting in a pattern of bare gold surfaces on a glass substrate. Note however that this approach also introduces a topographic contrast.

8.4 Conclusion and Outlook

Various ways to produce patterns of multifunctional mesoporous silica nanoparticles carrying a supported lipid bilayer on different substrates were discussed. For linking the particles to the surface, we focused on binding modes that are compatible with

biomolecules such as lipids and proteins, namely an EDC/NHS mediated amide bond formation, a Michael addition of thiols to maleimide groups, or binding of thiols to gold. All these reactions can be carried out in aqueous solutions at room temperature and neutral pH. In order to achieve binding, patterns exhibiting different functionality (carboxyl groups, thiol groups, bare gold atoms) were created on the substrates and reacted with complementary functional groups (amine groups, maleimide groups, thiol groups) that are anchored to the SLB of the nanoparticles *via* a PEG linker that is attached to a DSPE lipid.

In future projects, membrane-bound or transmembrane proteins such as ephrin could be reconstituted into the supported lipid bilayer of multifunctional mesoporous silica nanoparticles, e.g., *via* cell-free expression. The patterns of the multifunctional mesoporous silica nanoparticles carrying different ligands in their lipid membranes could serve as a platform for studying cell–receptor interactions or for a spatially controlled, specific influence of cell behavior.

8.5 Experimental Part

8.5.1 Methods and characterization

Atomic force microscopy (AFM) and dip pen nanolithography (DPN) were carried out with a Nanoink NScriptor DPN System. Before each DPN process, the dependence of the spot size on the dwell time was determined experimentally. DPN was carried out by dipping DPN single pens into a 2.5 – 5.0 mM solution of 16-mercaptohexadecanoic acid (MHDA) in acetonitrile and blowing them dry with a stream of dry nitrogen. Then, hexagonal dot patterns designed with the InkCAD software were written on the gold substrates. Typically, dot spacings were 1 µm and dot diameters were between 100 and 500 nm. Scanning electron microscopy (SEM) images were obtained with a JEOL JSM6500F scanning electron microscope equipped with a field-emission gun, typically operated at an acceleration voltage of 4 kV and a working distance of 5 – 10 mm. Exposure to oxygen plasma was carried out with a Femto Plasma System from Diener Electronic typically operated at a power of 50 W and an oxygen flow of 4 – 5 sccm. Thin metal film deposition was done with an Oerlikon Leybold Vacuum UNIVEX 350 sputter coater/evaporation system. Fluorescence microscopy images were recorded with a Nikon Eclipse Ti-U inverted microscope equipped with a Melles-Griot 10 mW He-Ne laser, using a Nikon Plan Fluor 10x/0.30 objective, a Nikon Cy-5 filter cube,

and an AndoriXon+ DU897-BV back-illuminated electron multiplying charge-coupled device (EM-CCD) camera, cooled to −80 °C during measurements. PDMS stamps were fabricated by replica molding from photolithographically patterned masters using standard techniques.

8.5.2 Chemicals

If not stated otherwise, all chemicals were used as received. Octadecyltrichlorosilane (ODTCS), tetraethyl orthosilicate (TEOS), triethanolamine (TEA), cetyltrimethylammonium chloride (CTAC), 16-mercaptohexadecanoic acid (MHDA), 1-hexadecanethiol (HDT), (3-mercaptopropyl)-triethoxysilane (MPTES), (3-aminopropyl)-triethoxysilane (APTES), 2-iminothiolane hydrochloride (Traut's reagent), N-(3-Dimethylaminopropyl)-N-ethylcarbodiimide (EDC), N-Hydroxysulfosuccinimide sodium salt (NHS), hexane, ethanol, acetone, acetonitrile, dimethyl formamide (DMF), and dry toluene were purchased from Sigma-Aldrich Co. Standard glass coverslips (#1, 22 x 22 mm^2) were purchased from Gerhard Menzel, Glasbearbeitungswerk GmbH & Co. KG. Hellmanex cleaning solution was purchased from Hellma GmbH & Co. KG. PDMS and PDMS curing agent were purchased from Dow Corning Co. 1H,1H,2H,2H-perfluorooctyltrichlorosilane (PFOTS) and 10-undecenyltrichlorosilane (UDTCS) were purchased from abcr GmbH & Co. KG. DOTAP (1,2-dioleyl-3-trimethylammoniumpropane), DOPC (1,2-dioleyl-sn-glycero-phosphocholine), DSPE-PEG(2000)-Maleimide (DSPE = 1,2-distearoyl-sn-glycero-phosphoethanolamine), and DSPE-PEG(2000)-NH_2 were purchased from Avanti Polar Lipids, Inc.

8.5.3 Preparation of fluorescently labeled core-shell mesoporous silica nanoparticles

MSN-SH_{core}-$NH_{2\,shell}$ were provided by Christian Argyo. The nanoparticles were synthesized *via* the delayed co-condensation approach as described elsewhere.[112,113,277] In brief, 14.3 g of triethanolamine (TEA; 95 mmol), 1.75 mL of tetraethyl orthosilicate (TEOS; 1.63 g, 7.82 mmol), and 20.0 µL of (3-mercaptopropyl)-triethoxysilane (MPTES; 19.7 mg, 82.8 µmol) were heated to 90 °C without stirring in a 100 mL polypropylene reactor. After 20 min a solution of 2.14 mL of cetyltrimethylammonium chloride (CTAC; 25 %, 1.83 mmol) in 21.7 mL bi-distilled water (21.7 g, 1.21 mol), preheated to 60 °C, was added to the polypropylene beaker and the resulting mixture was stirred at 600 rpm for 30 min. Then, 20.4 µL of (3-aminopropyl)-triethoxysilane

(APTES; 21.5 mg, 92.2 µmol) mixed with 20.5 µL of TEOS (19.2 mg, 92.2 µmol) were added and the resulting solution was stirred at 600 rpm over night. After addition of 100 mL of ethanol, the nanoparticles were separated by centrifugation at 19 000 rpm (43 146 rcf) for 20 min and redispersed in ethanol. The CTAC template was extracted from the nanoparticles by heating the latter in 100 mL of an ethanolic solution containing 2 g of ammonium nitrate under reflux at 90 °C for 45 minutes, followed by 45 min under reflux in 100 mL of a mixture of ethanol and concentrated hydrochloric acid (90:10 v/v). The nanoparticles were purified by centrifugation and washed with ethanol after each extraction step.

The labeling with the Atto-633 fluorescent dye was done by stirring 500 µL of an ethanolic MSN solution (containing approximately 10 mg mL^{-1} of MSN-SH_{core}-$NH_{2\,shell}$) with 15 µL of a solution of Atto-633-Maleimide in DMF (2 mg mL^{-1}) over night, followed by five washing steps in ethanol *via* centrifugation (14 000 rpm, 16 873 rcf, 4 min). After washing, no fluorescence could be observed in the supernatant solution. The fluorescently labeled particles were then redispersed in 500 µL of ethanol and this stock solution was stored in the dark.

8.5.4 Preparation of the functionalized supported lipid bilayers

The SLB was constructed around fluorescently labeled MSN-SH_{core}-$NH_{2\,shell}$ via a solvent exchange route, as previously reported.[114] In brief, nanoparticles were separated from 100 µL of the ethanolic stock solution (containing approximately 10 mg mL^{-1} of nanoparticles) by centrifugation (14 000 rpm, 16 873 rcf, 4 min), and immediately redispersed in a mixture of 30 µL of DOTAP (3.6 mM in H_2O/EtOH = 60:40 v/v) and 70 µL of DOPC (3.6 mM in H_2O/EtOH = 60:40 v/v) by brief ultrasonic agitation. Then, 800 µL of bi-distilled water was added to form the supported lipid bilayer. Functional groups were anchored to the lipid membrane by letting functionalized DSPE lipids diffuse into the SLB. To do so, 3.5 µL of DSPE-PEG-NH_2 (3.6 mM in H_2O/EtOH = 60:40 v/v) or DSPE-PEG-Maleimide (3.6 mM in EtOH), or 103.5 µL of DSPE-PEG-SH (122 µM in H_2O/EtOH = 100:3.5 v/v) were added to the solution, and the resulting mixture was kept under static conditions for 1 h in the dark.

DSPE-PEG-SH was synthesized from DSPE-PEG-NH_2 using Traut's reagent (2-iminothiolane hydrochloride). 1 mg of 2-iminothiolane hydrochloride was added to a solution of 3.5 µL of DSPE-PEG-NH_2 (3.6 mM in EtOH) in 100 µL bi-distilled water and stirred for 1 h at room temperature in the dark at 500 rpm.

8.5.5 Preparation of gold-coated glass substrates

Prior to metal deposition, the substrates were cleaned for 15 min in acetone, 15 min in isopropanol, and 15 min in an aqueous Hellmanex solution (1:100 v/v) under ultrasonic agitation, followed by rinsing with bi-distilled water and plasma-cleaning in an oxygen plasma for 15 min. Then, a titanium adhesion layer and a thin film of gold (purity: 99.95 %) were deposited on the substrates either by sputter coating or by thermal evaporation. For sputter coating, a base pressure of 1×10^{-6} mbar, an Argon pressure of 5×10^{-3} mbar, a power of 70 W and a sputtering time of 15 min was used for the titanium layer and an Argon pressure of 1×10^{-2} mbar, a power of 25 W and a sputtering time of 20 min for the gold layer, resulting in an approximately 100 nm thick layer of gold on a 10 nm layer of titanium. For thermal evaporation, titanium was deposited at a rate of $0.5\,\mathrm{nm\,s^{-1}}$ to a final thickness of 10 nm, and gold was deposited at a rate of $1\,\mathrm{nm\,s^{-1}}$ to a final thickness of 100 nm. Rates and thicknesses were monitored using a quartz crystal microbalance (QCM) chip.

8.5.6 Creating patterns through amide bond formation

First, glass substrates were subjected to an oxygen plasma treatment for 15 min to enhance the surface reactivity through the creation of hydroxyl groups. Then, patterns of ODTCS or PFOTS were created on the substrate through microcontact printing by applying a 5 mM hexanic solution of the respective alkyltrichlorosilane to a PDMS stamp with a cotton swab, followed by drying in a stream of dry nitrogen for 45 s and bringing the stamp into conformal contact with the substrate for 30 min. Next, the unpatterned regions of the glass substrate were functionalized with UDTCS by incubation in a 10 mM hexanic solution of the silane for 1 h at room temperature. Then, the substrates were rinsed with toluene and ethanol, and the double bonds of the UDTCS were cleaved oxidatively to carboxyl groups by incubation in a solution containing 2 mg of $KMnO_4$ and 84 mg of $NaIO_4$ in 20 mL of H_2O.[278]

For the EDC/NHS mediated coupling of SLB@MSN-SH_{core}-$NH_{2\,shell}$ functionalized with DSPE-PEG-NH_2 to the surface, the oxidized substrates were incubated in a solution of 1 µL of EDC in 700 µL of bi-distilled water under constant shaking for 5 min. Then, 0.5 – 1 mg of NHS was added, again followed by a shaking period of 5 min. Lastly, 70 µL of the particle solution was added and the substrates were incubated in this solution for 4 – 48 h.

8.5.7 Creating patterns through thiol–maleimide binding

First, glass substrates were subjected to an oxygen plasma treatment for 15 min to enhance the surface reactivity through the creation of hydroxyl groups. Then, patterns of ODTCS or PFOTS were created on the substrate through microcontact printing by applying a 5 mM hexanic solution of the respective alkyltrichlorosilane to a PDMS stamp with a cotton swab, followed by drying in a stream of dry nitrogen for 45 s and bringing the stamp into conformal contact with the substrate for 30 min. Next, the unpatterned regions of the glass substrate were functionalized with MPTES by refluxing in an 8 mM solution of MPTES in toluene for 4 – 8 h under an inert atmosphere of dry nitrogen, followed by rinsing in toluene and ethanol and blowing dry with compressed air.

For coupling of SLB@MSN-SH_{core}-$NH_{2\,shell}$ functionalized with DSPE-PEG-Mal to the surface, the substrates were incubated in a solution of 70 µL of the particles in 700 µL of bi-distilled water for 4 – 48 h.

8.5.8 Creating patterns through thiol–gold binding

First, gold substrates were selectively passivated through microcontact printing by applying a 2.5 – 10 mM ethanolic solution of HDT to a PDMS stamp with a cotton swab, followed by drying in a stream of dry nitrogen for 45 s and bringing the stamp into conformal contact with the substrate for 10 s. Then, the substrates were rinsed with ethanol, blown dry with compressed air and incubated in a solution of 70 µL of SLB@MSN-SH_{core}-$NH_{2\,shell}$ functionalized with DSPE-PEG-SH in 700 µL of H_2O for 4 – 48 h.

8.5.9 Selective gold etching

Prior to etching, patterns were created on a gold surface either through microcontact printing with HDT or through DPN with MHDA, as described above. Then, the patterned substrates were incubated in the etching solution containing 1.12 g of KOH, 316.2 mg of $Na_2S_2O_3$, 65.9 mg of $K_3[Fe(CN)_6]$, and 8.4 mg of $K_4[Fe(CN)_6]\cdot 3H_2O$ in 20 ml of bi-distilled H_2O for 20 – 50 min,[279] followed by rinsing with water and blowing dry with compressed air.

Chapter 9

. . . . . .

Conclusion and Outlook

In this work, porous host systems and their interactions with various guests were investigated. In Chapters 3, 4, 7, and 8, mesoporous silica was used as the host system, and patterning played an important role. In Chapters 5 and 6, metal–organic frameworks served as the porous hosts.

In Chapter 3, we showed how micromolding in capillaries (MIMIC) could be used to introduce a preferential direction on a substrate that can trigger in-plane mesopore alignment in mesoporous silica thin films on a macroscopic length scale. In this approach, an EISA precursor solution was filled into channels defined by a PDMS polymeric stamp. We investigated the influence of various experimental conditions on the mesopore alignment, including the way the channels were filled, the surface modification at the solid/liquid interfaces, and the aspect ratio of the microgrooves. We also found that the mesopore directionality can change abruptly from an alignment parallel to the microgrooves to a perpendicular alignment, depending on the height within the silica film. Furthermore, it was demonstrated how single-molecule fluorescence microscopy studies can be used to directly assess the mesopore structure of the as-synthesized samples. We used a "maximum projection" to gain a quick overview of the pore structure, while an in-depth evaluation of single molecule trajectories was used to obtain deeper insights into the real nanoscale structure of the porous system as well as to extract dynamical information about the diffusion of guest molecules inside the host structure. In future projects, it might be interesting to extend this approach and use it for achieving pore alignment with other templates or even other materials than silica, such as periodic mesoporous organosilica or ordered mesoporous carbon.

In Chapter 4, the approach was further extended and charged species were incor-

porated into the host structure. We could demonstrate that the movement of single molecules inside a highly-oriented, template-filled mesoporous silica host could be directly controlled under the influence of externally applied electric fields. While uncharged dyes showed very structured diffusional movement inside the aligned mesopores, charged guests took different, more random diffusional pathways. Based on these observations we presented a host–guest model which explained the different pathways of the molecules in such mesoporous materials. We also investigated the influence of the strength of the electric field on the charged molecules and found that their velocity increased monotonically with increasing field strength. Finally, we demonstrated the controlled separation of oppositely charged molecules inside the thin silica films on a single-molecule level. In the future, it could be interesting to introduce macromolecules or biomolecules such as oligonucleotides or small proteins into these structures and analyze the effects of spatially confined electrophoresis on these species.

In Chapter 5, we demonstrated the synthesis of UiO-68(anthracene), a Zr-based MOF with a diphenylanthracene-based linker, that exhibited strong chemiluminescence upon subjecting the compound to a solution of bis(2,4,6-trichlorophenyl)oxalate, hydrogen peroxide and sodium salicylate. No modulation agent had to be added during synthesis to obtain a highly crystalline material, as opposed to other related Zr-based structures. A high BET surface area indicated an open porous system. The MOF was shown to be stable in air up to 400 °C. We also investigated the stability of the MOF during the chemiluminescence reaction by means of XRD and luminescence microscopy and could demonstrate that the structure of the MOF persisted under these conditions. Further research could aim at implementing chemiluminescence as a read-out transducer concept for the detection of specific analytes.

In Chapter 6, a new signal transduction scheme in the field of metal–organic frameworks was introduced, which was based on the efficient quenching of fluorescent guests upon incorporation into a MOF and the subsequent dequenching upon analyte-specific degradation of the host material. This new signal transduction concept was used to implement a novel fluoride detection system in aqueous solution. We used fluorescence titrations to demonstrate that the sensitivity towards fluoride exceeded the ones of commonly used optical fluoride detection methods in aqueous solution with comparable anion selectivity. We believe that the high sensitivity of the system is due to the fact that a turn-on fluorescence signal rather than a color- or fluorescence-quenching based signal transduction scheme was used, while the high selectivity of the system was attributed to a competitive coordination and different affinities of linker molecules,

fluoride ions, and other interfering ions to the aluminum metal ions in the framework. This was also backed up by ^{19}F and ^{27}Al NMR titration studies that revealed that the porous host framework is indeed degraded upon fluoride ion addition due to competing coordination of fluoride to metal centers inside the metal organic framework. It can be imagined that in future applications this new sensing concept could be extended and other specific metal-analyte interactions besides aluminum and fluoride could be used for selective and sensitive analyte detection.

In Chapter 7, different ways to obtain hierarchically patterned thin silica films having periodic structural features at different length scales were investigated and their properties were compared. While photolithography had the advantage of yielding more uniform patterns, soft lithography using PDMS stamps was in general quicker, easier, and more cost-efficient. Moreover, soft lithography circumvented the problem of highly fluorescent residues that remained on the substrate after lift-off of a photoresist, hence making the process compatible with single molecule fluorescence microscopy studies. Using a colloidal hard templating approach with PMMA spheres instead of a soft templating with block copolymers allowed for an extension of the pore sizes beyond 20 nm. In the future, differently sized PMMA spheres could be used to vary pore widths and aperture sizes. Then, macromolecules of different sizes could be included into these structures, their movement modes could be analyzed, and a size dependent separation due to the entropic barrier transport mechanism could be investigated.

In Chapter 8, we discussed various ways to produce patterns of multifunctional mesoporous silica nanoparticles carrying a supported lipid bilayer on different substrates. In this context, biocompatible binding modes (i.e., reactions that can be carried out at room temperature and at a neutral pH) were investigated, such as an EDC/NHS mediated amide bond formation, a Michael addition of thiols to maleimide groups, or the binding of thiols to gold. Particle functionalization was achieved by anchoring a DSPE lipid carrying a PEG spacer and a functional group (such as an amine group, a maleimide group, or a thiol group) to the supported lipid bilayer and subsequently binding them to patterned substrates exhibiting complementary functionality (i.e., carboxyl groups, thiol groups, or bare gold atoms). In future research projects, membrane-bound or transmembrane proteins such as ephrine could be reconstituted into the supported lipid bilayer of the multifunctional mesoporous silica nanoparticles, e.g., *via* cell-free expression. This system could then be used to study cell–receptor interactions or for a spatially controlled, specific influence of cell behavior.

In summary, porous host systems and their interaction with various guest molecules

are of great importance for a large variety of applications. A precise knowledge of the host structure, means to understand and control the host–guest interactions, and the ability to create patterns of the host systems are important to provide material scientists with the possibility to use these versatile materials in a variety of future applications, ranging from novel analyte detection methods to controlling molecular motion or even cell behavior.

Chapter 10

Appendix

10.1 Implementation of the Program "Flow Controller"

10.1.1 Description and Purpose

In order to automate the measurements that were performed for collecting the reflectance spectra data for the Bragg stacks investigated in Reference 168, two programs were written in Visual Basic .NET (using Microsoft Visual Basic 2010 Express) that control the flow controller setup (program "Flow Controller", see Supplementary CD) and the ellipsometer measurement software (program "Bot", see section 10.2 and Supplementary CD), respectively. Both programs communicate with each other over the network using the TCP/IP protocol, which enables the triggered change of flow parameters before the respective measurements and hence allows for synchronization of measurements and flow values. Moreover, a program was written for Wolfram Mathematica 7 that carries out a semi-automatic analysis and processing of the obtained data (see section 10.3 and Supplementary CD). The measurement automation greatly simplified data collection during time-consuming measurements (several hours) and made measurement routines with long equilibration times and small flow value increments easily possible. An overview of the individual components and their interactions used for automated data collection is given in Figure 10.1.

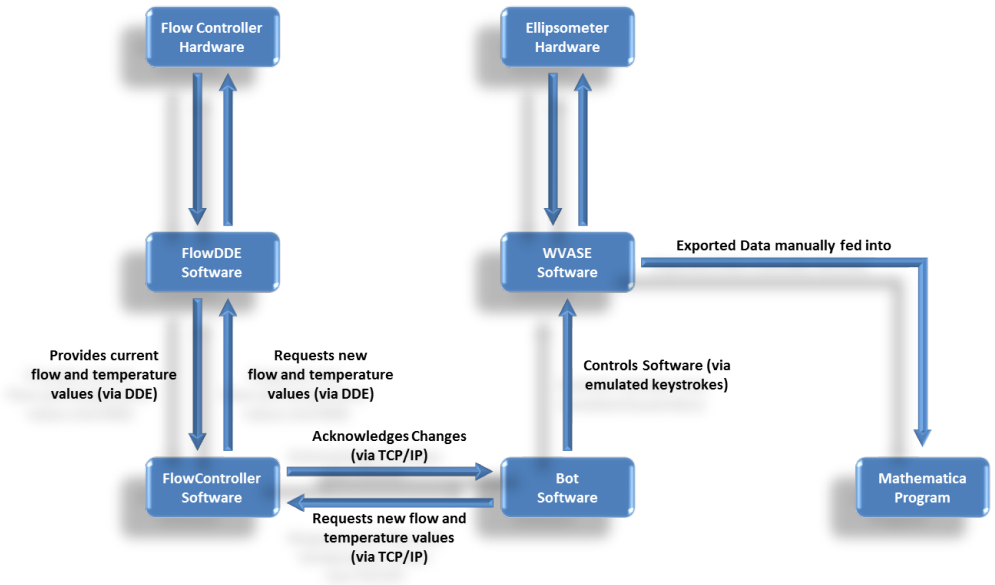

Figure 10.1: Individual components and their interactions used for automated data collection. The "bottom layer" was newly implemented for this project.

10.1.2 Graphical User Interface

The Graphical User Interface (GUI) of the program "Flow Controller" is shown in Figure 10.2. The GUI consists of four main parts. The top part is mainly for monitoring purposes and shows the flow values of the individual flow controllers and the temperature of the controlled evaporation mixer (CEM) in real time. The temperature for the CEM can be set with the control for the temperature setpoint, and the polling interval (time between updates of the flow and temperature values shown on the GUI) can be set with the control for the polling time.

The second part of the GUI contains a list box giving the channel, serial number and type of the individual flow controllers and of the CEM connected to the flow controller setup. The measurement type can be set by the radio buttons on the right. There are two different modes. In the first mode, the program acts as a server, accepting incoming client connections. Once a connection is established, the program awaits network messages containing the channel number and the new setpoint value for the device which uses this channel. For more details on the format of these messages, see section 10.1.3. The program also displays the current IP address assigned to the main network card which is used for network communication and allows for customization of the port number. In the second mode, the flow values are not set via network messages from another computer, but can rather be entered in the program itself. In

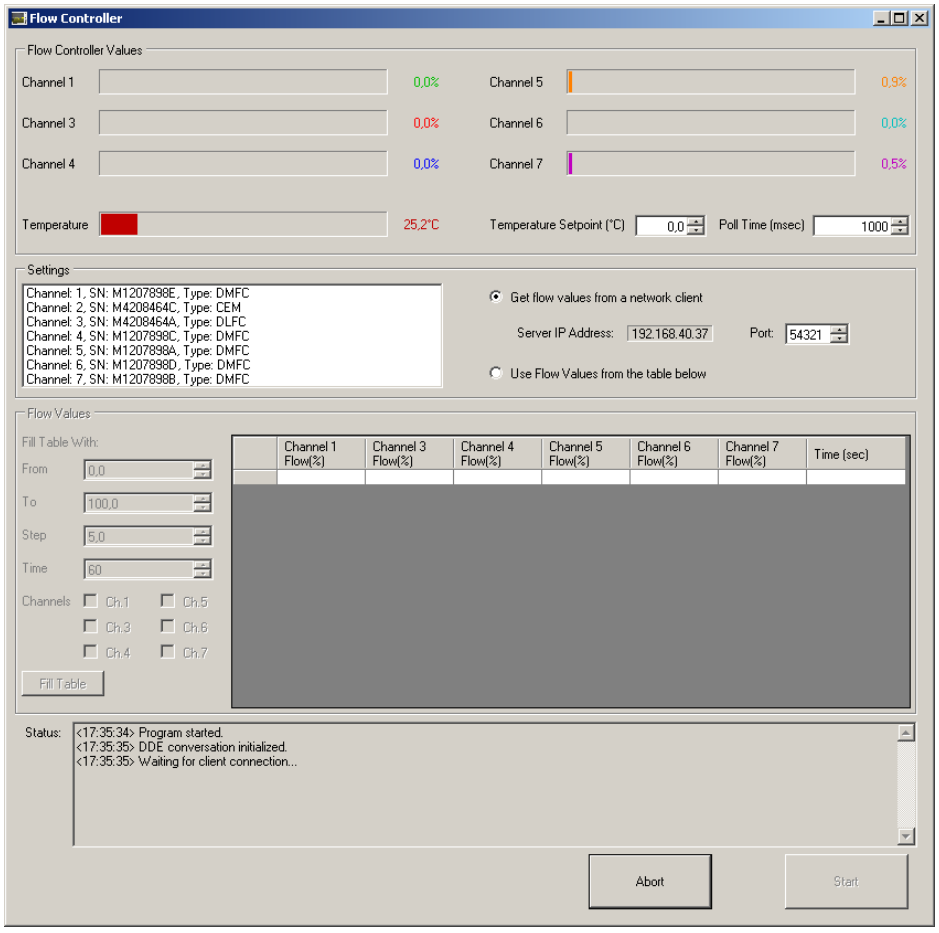

Figure 10.2: Screenshot of the Graphical User Interface (GUI) of the program “Flow Controller”.

this case, no synchronization with other devices is possible. If this mode is chosen, the flow values are taken from the table that can be found in the third part of the program.

The table contains one column for each flow controller with the desired flow value (in percent) for this device, and one column for the time that should pass until the flow values contained in the next row are processed. The controls to the left enable a quick and easy setup of simple flow routines by filling the table with incrementing flow values and a constant time value for the flow controllers that are chosen by the checkboxes. Empty flow value cells will be taken as zero. If a cell is left empty, but the cell above it contains a value, the same value will be used for this cell. Moreover, copy&paste functionality for copying to and pasting from Microsoft Excel was implemented for the table, allowing the user to write and save more complex flow routines in Microsoft Excel and reuse them with this program.

The bottom part contains status messages, e.g., about requests made over the network, but also about warnings and errors. Finally, there are two buttons that start or abort the execution of the program. In "Network Mode", the "Start" button is unavailable since the program constantly listens for flow and temperature values over the network socket and simply processes them as soon as they arrive. In the other mode, pressing the "Start" button will start processing the data given in the table.

10.1.3 Implementation

The program contains the two public classes `Form1` and `backgroundWorker`, with their methods mainly running in two individual threads. The class `Form1` handles all user interactions, the GUI, and the communication with the flow controllers in its thread, while the `backgroundWorker` class is used for receiving and sending network messages asynchronously. Separating the GUI thread from the network communication thread helps keeping the GUI responsive while waiting for incoming network messages. An overview of all the methods, types and parameters used by these two classes can be found in Tables 10.1 and 10.2 at the end of this section.

For communication with the flow controllers and the CEM, the program uses "Dynamic Data Exchange" (DDE), which is an interprocess communication technology used in Microsoft Windows. However, since DDE is no longer supported in VisualBasic .NET,[280] calls to unmanaged Windows Application Programming Interface (WinAPI) code were necessary for DDE conversation. A documentation of DDE and the WinAPI constants, parameters, and functions can be found online.[281] In brief, in order to use DDE communication, the client application first has to connect to a server application by using the WinAPI function `DdeInitialize`. In the present case, the DDE server functionality is implemented by the proprietary software "FlowDDE" provided by the manufacturer of the flow controller setup (the program "Flow Controller" was developed for "FlowDDE v4.58"). Once connected, the server can provide information contained in groups known as "topic", and each topic can have several pieces of data as "items". In order to address the topics and items, a string handle is needed that can be obtained by calling the WinAPI function `DdeCreateStringHandle`. To read or write data, conversation handles to the topics are required that can be obtained by calling the WinAPI function `DdeConnect`. Once these handles are not needed anymore, they should be freed by a call to the WinAPI function `DdeFreeStringHandle` (this is not done automatically by the .NET garbage collector since they were obtained from calls to unmanaged code). Similarly, at the end of the DDE conversation the

client should be disconnected by a call to the WinAPI function `DdeUninitialize`. The WinAPI function `DdeClientTransaction` is used to read or write data. For reading data, the conversation handle of the topic, the string handle of the item, and the `XTYP_REQUEST` flag (along with some other parameters) have to be passed to the `DdeClientTransaction` WinAPI function. In return, a data handle is obtained that can be used to retrieve a pointer to the data with the `DdeAccessData` WinAPI function. Once the data was processed, it should be unaccessed and the data handle should be freed by calling the WinAPI functions `DdeUnaccessData` and `DdeFreeDataHandle`, respectively (calling `DdeUnaccessData` alone will not destroy the data handle, while calling `DdeFreeDataHandle` alone will not unaccess the data). For writing data, the `XTYP_POKE` flag has to be used instead of the `XTYP_REQUEST` flag when making the call to the `DdeClientTransaction` function.

A documentation of the parameters for DDE communication can be obtained from the manufacturer.[282] The implementation of the "Flow Controller" program differs from the information given in the manual (Doc. no.: 9.17.027Q Date: 26-09-2011) in the following points: According to the documentation, the setpoint values are supposed to be of type `Unsigned Integer`. However, sending directly an `Unsigned Integer` value or a pointer to a variable of `Unsigned Integer` type holding the desired setpoint value via the WinAPI function `DdeClientTransaction` was not successful. On the other hand, when passing a pointer to the first element of an ASCII-encoded, zero-terminated `Byte Array` representation of the desired `Integer` value to the WinAPI function, the setpoint was changed as expected, hence this implementation was used. Similarly, according to the documentation, when reading the current flow or temperature values an `Unsigned Integer` value is given. However the data seems again rather to be in an ASCII-encoded, zero-terminated `Byte Array` representation, and the value that is obtained from a call to the `DdeClientTransaction` and the `DdeAccessData` methods appears to be a pointer to the first element of this array. Using this pointer to read successively from memory until the `Null Character` is encountered and parsing the obtained data to an `Integer` value gave the correct values.

The network messages that are received and processed by this application are expected to be of the following format:

```
ChannelNumber;Value[;DISCONNECT]$
```

A semicolon is used as the delimiter character for separating the individual parts of the message, while the Dollar sign is used to indicate the end of the message. No extra characters are allowed in the message. The last part of the message (`DISCONNECT`) is

optional, hence a valid message can consist of two or three parts. If only a channel number and a value are given, the program tries to process these values and – if successful – sends the string `OK$` back to the client application. If the changes were not successful, an error string is sent back to the client. If the optional argument `DISCONNECT` is given, the server application processes the data, but does not send an acknowledgment back to the client. Instead, it disconnects the client and awaits new client connections.

In combination with the "Bot" program used for automated ellipsometer measurements (see section 10.2), the `DISCONNECT` argument is not used, so that the client program knows exactly whether and when the flow values are changed and can then react accordingly. However, when using simpler ways to interact with the server application (e.g., *via* a vbscript written for the Bruker D8 measurement software to measure *in situ* XRD in a flow cell connected to the flow controller setup), it can be easier and less cumbersome to simply dispatch a message with the desired flow value over the network without worrying about receiving and processing further network messages, and in this case the optional `DISCONNECT` argument can be used. The individual actions of the server application can still be reconstructed from the logs contained in its status window, and in the case of errors or incoherent data, the measurement can be repeated manually.

The first argument of the network message (channel number) should be a single integer without leading zeros, while the second argument (value) should be a decimal number (also without leading zeros). For convenience, the values in the message can be given directly as % (in the case the indicated channel belongs to a flow controller) or in °C (in the case the indicated channel belongs to the CEM), and the program automatically converts them to the format expected from "FlowDDE", i.e., values between 0 and 32000 with 0 corresponding to a flow of 0 % and 32000 corresponding to 100 % if the addressed device is a flow controller, respectively 0 corresponding to 0 °C (the minimum temperature) and 32000 corresponding to 200 °C (the maximum temperature) if the addressed device is a CEM. For example, if channel 1 belongs to a flow controller and channel 2 belongs to the CEM, the network message `1;25$` would indicate that the flow setpoint of the flow controller on channel 1 should be changed to 25 % and a successful change should be acknowledged by the server application, while the message `2;90;DISCONNECT$` would indicate that the temperature of the CEM connected to channel 2 should be changed to 90 °C and that the client wishes to disconnect immediately without further network messages being sent back to it.

Table 10.1: Overview of the methods of class `Form1`. Parameters for the methods are given under the method name in italic, indented by · · · · · · .

Name	Modifier	Type[1]/Return Value	Description
DDECallbackDelegate	Private	UInt32	Delegate for the `DDECallback` function that processes DDE transactions sent by the system. The method is not really used in this project since the `CBF_SKIP_ALLNOTIFICATIONS` flag is set when initializing DDE communication (however, a pointer to this (empty) method is still required during initialization).
· · · · · · *wType*	Local	UInt32	Type of the current transaction. This parameter consists of a combination of transaction class flags and transaction type flags.
· · · · · · *wFmt*	Local	UInt32	Format in which data is sent or received.
· · · · · · *hConv*	Local	IntPtr	A handle to the conversation associated with the current transaction.
· · · · · · *hszTopic*	Local	IntPtr	A handle to a string. The meaning of this parameter depends on the type of the current transaction.
· · · · · · *hszItem*	Local	IntPtr	A handle to a string. The meaning of this parameter depends on the type of the current transaction.
· · · · · · *hData*	Local	IntPtr	A handle to DDE data. The meaning of this parameter depends on the type of the current transaction.
· · · · · · *lData1*	Local	UIntPtr	Transaction-specific data.
· · · · · · *lData2*	Local	UIntPtr	Transaction-specific data.
Form1_Load	Private	Void	Method executed when the program starts. In this method, the GUI controls and global variables are initialized, the DDE communication is set up, and the type and the serial- and channel-numbers of the connected flow controllers and CEM are queried.
· · · · · · *sender*	Local	System.Object	Object calling the method.
· · · · · · *e*	Local	System.EventArgs	Event arguments for the method call.
Form1_FormClosing	Private	Void	Method executed when the program exits. Some garbage disposal and uninitialization is done here.
· · · · · · *sender*	Local	System.Object	Object calling the method.
· · · · · · *e*	Local	System.EventArgs	Event arguments for the method call.
Button_Start_Click	Public	Void	Method executed when pressing the "Start" Button. Disables GUI controls, parses the values from the table and starts the timer for executing the flow changes.
· · · · · · *sender*	Local	System.Object	Object calling the method.

Continued on next page. . .

[1] `System.Windows.Forms` Namespace is included in Object Types.

Name	Modifier	Type/Return Value	Description
····· *e*	Local	System.EventArgs	Event arguments for the method call.
Button_Cancel_Click	Private	Void	Method executed when pressing the "Cancel" Button. Requests abort of the backgroundWorker thread, stops the timer, disconnects network connections, and re-enables GUI controls.
····· *sender*	Local	System.Object	Object calling the method.
····· *e*	Local	System.EventArgs	Event arguments for the method call.
Button_FillTable_Click	Private	Void	Method executed when pressing the "Fill Table" Button. Fills the table according to the data and options specified by the controls on the left.
····· *sender*	Local	System.Object	Object calling the method.
····· *e*	Local	System.EventArgs	Event arguments for the method call.
Timer_Writing_Tick	Private	Void	Method executed when the "Writing Timer" raises a "Tick" event. This occurs when the time specified in the last column of the table is expired. The method sets the new flow values or disables the timer if all rows of the table were processed.
····· *sender*	Local	System.Object	Object calling the method.
····· *e*	Local	System.EventArgs	Event arguments for the method call.
Timer_Polling_Tick	Private	Void	Method executed when the "Polling Timer" raises a "Tick" event. This occurs when the specified polling time is expired. The method retrieves the current values of the flow controllers and the CEM and displays them on the GUI.
····· *sender*	Local	System.Object	Object calling the method.
····· *e*	Local	System.EventArgs	Event arguments for the method call.
myEventHandler_ThreadAborted	Private	Void	Method executed when the backgroundWorker thread exited and raised the user-defined `threadAborted` event. This method disconnects network connections, and re-enables GUI controls.
myEventHandler_dataReceived	Private	Void	Method executed when the receiveData method of the backgroundWorker thread received data over the network and raised the user-defined `dataReceived` event. This method parses the incoming network message, performs a sanity check, determines the type of the request, and attempts to change the flow and temperature values accordingly. If successful and requested, the method sends an acknowledgment back to the sender over the network.
····· *msg*	Local	String	The network message that was received.
acceptTcpClientCallback	Public	Void	Callback function for receiving asynchronous calls after client-connection requests to the server socket. Handles and processes these requests and establishes a connection to the client.
····· *ar*	Local	IAsyncResult	Argument containing the results of the asynchronous call.

Continued on next page...

Name	Modifier	Type/Return Value	Description
DDECallback	Private	Long	Function that processes DDE transactions sent by the system. The method is not really used in this project since the `CBF_SKIP_ALLNOTIFICATIONS` flag is set when initializing DDE communication (however, a pointer to this (empty) method is still required during initialization). Returns 0 for all calls of this function.
····· *wType*	Local	UInt32	Type of the current transaction. This parameter consists of a combination of transaction class flags and transaction type flags. In this project, a combination of the flags `CBF_SKIP_ALLNOTIFICATIONS` and `APPCMD_CLIENTONLY` is used for initialization.
····· *wFmt*	Local	UInt32	Format in which data is sent or received.
····· *hConv*	Local	IntPtr	A handle to the conversation associated with the current transaction.
····· *hszTopic*	Local	IntPtr	A handle to a string. The meaning of this parameter depends on the type of the current transaction.
····· *hszItem*	Local	IntPtr	A handle to a string. The meaning of this parameter depends on the type of the current transaction.
····· *hData*	Local	IntPtr	A handle to DDE data. The meaning of this parameter depends on the type of the current transaction.
····· *lData1*	Local	UIntPtr	Transaction-specific data.
····· *lData2*	Local	UIntPtr	Transaction-specific data.
changeValue	Private	Boolean	Method for changing the value of the device connected to the given channel to a given setpoint. This method converts the given setpoints (% for flow controllers and °C for the CEM) to internally used values (0 to 32000) and sends the values to the respective flow controller or CEM channel via DDE. If the DDE call is successful, the method returns TRUE, otherwise, it returns FALSE.
····· *channelNumber*	Local	Integer	Channel number of the device whose value should be changed.
····· *value*	Local	Decimal	New setpoint value.
DDEStart	Private	Boolean	This method initializes DDE conversation, creates string handles for the DDE server and the DDE topics and uses these to connect the DDE topics to the DDE server, retrieving a conversation handle that is necessary to write to and read from the topics. If these operations are successful, the method returns TRUE, otherwise, it returns FALSE.
DDEEnd	Private	Boolean	Method executed when ending the DDE connection. If desired it switches off the flow controllers and the CEM, and does some garbage disposal for the unmanaged code, i.e., it frees the string handles, disconnects the DDE topics and uninitializes the DDE conversation.

Continued on next page...

Name	Modifier	Type/Return Value	Description
DDEWrite	Private	UInt32	Method executed when changing the setpoint of a flow controller or the CEM. This method converts the new setpoint values into an ASCII-encoded, zero-terminated byte array and uses the WinAPI function `DdeClientTransaction` to send an `XTYP_POKE` request to the device identified by its channel number, passing a pointer to the first element of the newly created byte array. If the transaction is successful, the return value is a variable that contains the result of the transaction, otherwise, the return value is 0.
····· *newValue*	Local	UInt32	New setpoint value.
····· *channelNumber*	Local	Integer	Channel number of the device whose value should be changed.
····· *timeout*	Local	UInt32	Optional timeout of the DDE transaction (default value is 1000 msec).
DDEReadValue	Private	Double	Method executed for reading the current value from a flow controller or the CEM. This method uses the WinAPI function `DdeClientTransaction` to send an `XTYP_REQUEST` request to the device identified by its channel number, receiving a data handle in return. By using the WinAPI function `DdeAccessData`, this data handle is used to retrieve a pointer to the first element of a zero-terminated byte array containing the requested data and the necessary buffer size. Starting from the address specified by the pointer, data is read successively from memory until the null character is read. The result is parsed to an integer and converted from internally used values (0 to 32000) to the appropriate units (% for flow controllers and °C for the CEM). If the execution is successful, the method returns this number, otherwise, it returns -32000.
····· *channelNumber*	Local	Integer	Channel number of the device whose value should be read.
····· *timeout*	Local	UInt32	Optional timeout of the DDE transaction (default value is 5000 msec).
DDEReadSerial	Private	String	Method executed for reading the serial numbers of the flow controllers and the CEM. This method uses the WinAPI function `DdeClientTransaction` to send an `XTYP_REQUEST` request to the device identified by its channel number, receiving a data handle in return. By using the WinAPI function `DdeAccessData`, this data handle is used to retrieve a pointer to the first element of a zero-terminated byte array containing the requested data and the necessary buffer size. Starting from the address specified by the pointer, data is read successively from memory until the null character is read. If the execution is successful, the method returns a string containing the serial number, otherwise, the string `ERR` is returned.
····· *channelNumber*	Local	Integer	Channel number of the device whose serial number should be read.
····· *timeout*	Local	UInt32	Optional timeout of the DDE transaction (default value is 1000 msec).

Continued on next page...

Name	Modifier	Type/Return Value	Description
incrementPtr	Private	IntPtr	Returns a pointer that is incremented by 4 (32-bit OS) or 8 (64-bit OS). If the method fails, it returns 0.
····· *ptr*	Local	IntPtr	Pointer that should be incremented.
fillEmptyCells	Private	Integer	Method that parses the table of flow values and attempts to fill cells that were left empty by the user. If the method succeeds, it returns an integer defining the index of the last row containing data in the table, otherwise it returns 0.
····· *checkForEmptyTimeColumn*	Local	Boolean	Optional Boolean Flag that determines whether the method should also check for empty cells in the "Time" column of the table (default value is TRUE).
DDEWrite_Del	Delegate	UInt32	Delegate for the `DDEWrite` method. This is necessary to execute the DDE conversations from the same thread that created them since DDE does not support cross-thread referencing.
····· *[newValue]*	Local	UInt32	The new setpoint value that is passed to the `DDEWrite` method
····· *[channelNumber]*	Local	Integer	The channel number that is passed to the `DDEWrite` method.
····· *[timeout]*	Local	UInt32	The timeout value that is passed to the `DDEWrite` method.
DDEWrite_Delegate	Private	UInt32	This method does the actual invocation of the delegate in the thread that created the DDE conversation handles. It returns the return value of the `DDEWrite` method.
····· *[newValue]*	Local	UInt32	The new setpoint value that is passed to the `DDEWrite` method
····· *[channelNumber]*	Local	Integer	The channel number that is passed to the `DDEWrite` method.
····· *[timeout]*	Local	UInt32	The timeout value that is passed to the `DDEWrite` method.
DDEReadValue_Del	Delegate	Double	Delegate for the "DDEReadValue" method. This is necessary to execute the DDE conversations from the same thread that created them since DDE does not support cross-thread referencing.
····· *[channelNumber]*	Local	Integer	The channel number that is passed to the `DDEReadValue` method.
····· *[timeout]*	Local	UInt32	The timeout value that is passed to the `DDEReadValue` method.
DDEReadValue_Delegate	Private	Double	This method does the actual invocation of the delegate in the thread that created the DDE conversation handles. It returns the return value of the `DDEReadValue` method.
····· *[channelNumber]*	Local	Integer	The channel number that is passed to the `DDEReadValue` method.
····· *[timeout]*	Local	UInt32	The timeout value that is passed to the `DDEReadValue` method.
DDEReadSerial_Del	Delegate	String	Delegate for the "DDEReadSerial" method. This is necessary to execute the DDE conversations from the same thread that created them since DDE does not support cross-thread referencing.
····· *[channelNumber]*	Local	Integer	The channel number that is passed to the `DDEReadSerial` method.
····· *[timeout]*	Local	UInt32	The timeout value that is passed to the `DDEReadSerial` method.

Continued on next page...

Name	Modifier	Type/Return Value	Description
DDEReadSerial_Delegate	Private	String	This method does the actual invocation of the delegate in the thread that created the DDE conversation handles. It returns the return value of the `DDEReadSerial` method.
..... *[channelNumber]*	Local	Integer	The channel number that is passed to the `DDEReadSerial` method.
..... *[timeout]*	Local	UInt32	The timeout value that is passed to the `DDEReadSerial` method.
SetButtonState_Delegate	Delegate	Void	Delegate to set the `enable` property of the Button control on the GUI. This is necessary for thread-safe enabling or disabling of the control from a thread other than the GUI thread that created the control.
..... *[Button]*	Local	Button	Button control on the GUI whose `enable` property should be changed.
..... *[value]*	Local	Boolean	Value the `enable` property should be changed to.
SetButtonState_ThreadSafe	Private	Void	This method does the actual invocation of the delegate in the thread that created the GUI controls.
..... *[Button]*	Local	Button	Button control on the GUI whose `enable` property should be changed.
..... *[value]*	Local	Boolean	Value the `enable` property should be changed to.
SetProgressBarValue_Delegate	Delegate	Void	Delegate to set the `value` property of the ProgressBar control on the GUI. This is necessary for thread-safe enabling or disabling of the control from a thread other than the GUI thread that created the control.
..... *[ProgressBar]*	Local	ProgressBar	ProgressBar control on the GUI whose `value` property should be changed.
..... *[value]*	Local	Decimal	Value the `value` property should be changed to.
SetProgressBarValue_ThreadSafe	Private	Void	This method does the actual invocation of the delegate in the thread that created the GUI controls.
..... *[ProgressBar]*	Local	ProgressBar	ProgressBar control on the GUI whose `enable` property should be changed.
..... *[value]*	Local	Decimal	Value the `value` property should be changed to.
SetNumericUpDownState_Delegate	Delegate	Void	Delegate to set the `enable` property of the NumericUpDown control on the GUI. This is necessary for changing the value displayed by the ProgressBar control in a thread-safe way from a thread other than the GUI thread that created the control.
..... *[NumericUpDown]*	Local	NumericUpDown	NumericUpDown control on the GUI whose `enable` property should be changed.
..... *[value]*	Local	Boolean	Value the `enable` property should be changed to.
SetNumericUpDownState_ThreadSafe	Private	Void	This method does the actual invocation of the delegate in the thread that created the GUI controls.
..... *[NumericUpDown]*	Local	NumericUpDown	NumericUpDown control on the GUI whose `enable` property should be changed.
..... *[value]*	Local	Boolean	Value the `enable` property should be changed to.

Continued on next page...

Name	Modifier	Type/Return Value	Description
SetListBoxState_Delegate	Delegate	Void	Delegate to set the `enable` property of the ListBox control on the GUI. This is necessary for thread-safe enabling or disabling of the control from a thread other than the GUI thread that created the control.
····· *[ListBox]*	Local	ListBox	ListBox control on the GUI whose `enable` property should be changed.
····· *[value]*	Local	Boolean	Value the `enable` property should be changed to.
SetListBoxState_ThreadSafe	Private	Void	This method does the actual invocation of the delegate in the thread that created the GUI controls.
····· *[ListBox]*	Local	ListBox	ListBox control on the GUI whose `enable` property should be changed.
····· *[value]*	Local	Boolean	Value the `enable` property should be changed to.
SetTextboxState_Delegate	Delegate	Void	Delegate to set the `enable` property of the TextBox control on the GUI. This is necessary for thread-safe enabling or disabling of the control from a thread other than the GUI thread that created the control.
····· *[Textbox]*	Local	TextBox	TextBox control on the GUI whose `enable` property should be changed.
····· *[value]*	Local	Boolean	Value the `enable` property should be changed to.
SetTextboxState_ThreadSafe	Private	Void	This method does the actual invocation of the delegate in the thread that created the GUI controls.
····· *[Textbox]*	Local	TextBox	TextBox control on the GUI whose `enable` property should be changed.
····· *[value]*	Local	Boolean	Value the `enable` property should be changed to.
SetGroupBoxState_Delegate	Delegate	Void	Delegate to set the `enable` property of the GroupBox control on the GUI. This is necessary for thread-safe enabling or disabling of the control from a thread other than the GUI thread that created the control.
····· *[GroupBox]*	Local	GroupBox	GroupBox control on the GUI whose `enable` property should be changed.
····· *[value]*	Local	Boolean	Value the `enable` property should be changed to.
SetGroupBoxState_ThreadSafe	Private	Void	This method does the actual invocation of the delegate in the thread that created the GUI controls.
····· *[GroupBox]*	Local	GroupBox	GroupBox control on the GUI whose `enable` property should be changed.
····· *[value]*	Local	Boolean	Value the `enable` property should be changed to.
SetTextboxText_Delegate	Delegate	Void	Delegate to set the `text` property of the TextBox control on the GUI. This is necessary for changing the text of the TextBox control in a thread-safe way from a thread other than the GUI thread that created the control.
····· *[Textbox]*	Local	TextBox	TextBox control on the GUI whose `text` property should be changed.
····· *[text]*	Local	String	String the `text` property should be changed to.
SetTextboxText_ThreadSafe	Private	Void	This method does the actual invocation of the delegate in the thread that created the GUI controls.

Continued on next page...

Name	Modifier	Type/Return Value	Description
····· *[Textbox]*	Local	TextBox	TextBox control on the GUI whose `text` property should be changed.
····· *[text]*	Local	String	String the `text` property should be changed to.
SetLabelText_Delegate	Delegate	Void	Delegate to set the `text` property of the Label control on the GUI. This is necessary for changing the text of the Label control in a thread-safe way from a thread other than the GUI thread that created the control.
····· *[Label]*	Local	Label	Label control on the GUI whose `text` property should be changed.
····· *[text]*	Local	String	String the `text` property should be changed to.
SetLabelText_ThreadSafe	Private	Void	This method does the actual invocation of the delegate in the thread that created the GUI controls.
····· *[Label]*	Local	Label	Label control on the GUI whose `text` property should be changed.
····· *[text]*	Local	String	String the `text` property should be changed to.
SetTimerState_Delegate	Delegate	Void	Delegate to set the `enable` property of the Timer control on the GUI. This is necessary for thread-safe enabling or disabling of the control from a thread other than the GUI thread that created the control.
····· *[Timer]*	Local	Timer	Timer control on the GUI whose `enable` property should be changed.
····· *[value]*	Local	Boolean	Value the `enable` property should be changed to.
SetTimerState_ThreadSafe	Private	Void	This method does the actual invocation of the delegate in the thread that created the GUI controls.
····· *[Timer]*	Local	Timer	Timer control on the GUI whose `enable` property should be changed.
····· *[value]*	Local	Boolean	Value the `enable` property should be changed to.
setTimerState	Private	Void	Method to set the `enable` property of the Timer control on the GUI.
····· *[Timer]*	Local	Timer	Timer control on the GUI whose `enable` property should be changed.
····· *[value]*	Local	Boolean	Value the `enable` property should be changed to.
NumericUpDown_PollTime_ValueChanged	Private	Void	Method executed when the `ValueChanged` event of the control is raised. The method changes the interval of the polling timer to the value entered in the GUI.
····· *sender*	Local	System.Object	Object calling the method.
····· *e*	Local	System.EventArgs	Event arguments for the method call.
NumericUpDown_Temperature_ValueChanged	Private	Void	Method executed when the `ValueChanged` event of the control is raised. The method changes the temperature of the CEM to the value entered in the GUI.
····· *sender*	Local	System.Object	Object calling the method.
····· *e*	Local	System.EventArgs	Event arguments for the method call.
NumericUpDown_Port_ValueChanged	Private	Void	Method executed when the `ValueChanged` event of the control is raised. The method changes the port number for incoming network connections to the value entered in the GUI.

Continued on next page...

Name	Modifier	Type/Return Value	Description
····· *sender*	Local	System.Object	Object calling the method.
····· *e*	Local	System.EventArgs	Event arguments for the method call.
RadioButton_Network_CheckedChanged	Private	Void	Method executed when the `CheckedChanged` event of the control is raised. The method switches between the mode in which the program waits for network messages to change the flow and the mode in which the program uses the flow values from the table.
····· *sender*	Local	System.Object	Object calling the method.
····· *e*	Local	System.EventArgs	Event arguments for the method call.
TextBox_Status_TextChanged	Private	Void	Method executed when the `TextChanged` event of the control is raised. When new messages are displayed in the TextBox, the method scrolls the Textbox to the last line to show the latest messages.
····· *sender*	Local	System.Object	Object calling the method.
····· *e*	Local	System.EventArgs	Event arguments for the method call.
DataGridView_CellValidating	Private	Void	Method executed when the `CellValidating` event of the control is raised. The method performs a sanity check of the value entered in the cells of the DataGridView control and produces a warning if the data is incorrect.
····· *sender*	Local	System.Object	Object calling the method.
····· *e*	Local	DataGridViewCell ValidatingEventArgs	Event arguments for the method call.
DataGridView_KeyDown	Private	Void	Method executed when the `KeyDown` event of the control is raised, i.e., when a key is pressed while the control has the focus. The method checks for the key combination `Crtl+v`, i.e., pasting of data. It parses the data from the clipboard and tries to fill the cells of the DataGridView with it. This enables copy&paste functionality from Microsoft Excel.
····· *sender*	Local	System.Object	Object calling the method.
····· *e*	Local	System.EventArgs	Event arguments for the method call.
DataGridView_RowsAdded	Private	Void	Method executed when the `RowsAdded` event of the control is raised. When a new row is added, this method helps adopting the values from the previous row.
····· *sender*	Local	System.Object	Object calling the method.
····· *e*	Local	System.EventArgs	Event arguments for the method call.
DataGridView_Leave	Private	Void	Method executed when the `Leave` event of the control is raised. The method calls the `fillEmptyCells` method when the control loses the focus.
····· *sender*	Local	System.Object	Object calling the method.
····· *e*	Local	System.EventArgs	Event arguments for the method call.

Table 10.2: Overview of the methods of class `backgroundWorker`. Parameters for the methods are given under the method name in italic, indented by · · · · · · .

Name	Modifier	Type/Return Value	Description
receiveData	Public	Void	The method continuously checks for incoming data over the network socket until an abort request is made. It is the entry point for the `backgroundWorker` thread.
receive	Public	String	Wrapper method for reading data from the network socket. The return value is a String representation of the received network message without delimiter characters.
send	Public	Void	This method sends the specified message (with an appended delimiter character) over the network to the connected client.
· · · · · · *msg*	Local	String	The message that should be sent.
isClientConnected	Public	Boolean	The method checks whether a client is connected to the network socket. If there is a connection, it returns TRUE, otherwise, it returns FALSE.

10.2 Implementation of the Program “Bot”

10.2.1 Description and Purpose

The program “Bot” was written to make automatic data collection with the ellipsometer possible. It interacts with the program “Flow Controller” described in section 10.1, which enables the triggered change of flow parameters before ellipsometric measurements (see also Figure 10.1). Since the ellipsometer hardware is rather complex and a documentation of the interface to the hardware does not seem to be publically available, a work-around for measurement automatization was chosen. Instead of developing a program from scratch that interacts with the hardware directly (as it was done for the flow controllers, see section 10.1), a bot program was implemented which controls the proprietary measurement software provided by the manufacturer (“WVASE”) via emulated keystrokes. While this approach has the advantage of being relatively easy to implement and hence resulted in a short development time, there are some inherent drawbacks to this method, which will be discussed in more detail in section 10.2.3. Besides for conducting R&T scans, the “Bot” software also uses the “WVASE” program to export the data from the proprietary file format to a human-readable form (ASCII text), which can then be processed by a program written for Wolfram Mathematica 7, as briefly described in section 10.3.

10.2.2 Graphical User Interface

The Graphical User Interface (GUI) of the program “Bot” is shown in Figure 10.3. The GUI consists of three main parts. In the top part, the measurement mode can be chosen and the most commonly used parameters for the measurement can be set up. The second part allows for customizing more advanced settings. However, typically no changes to these values are required for standard measurements. The third part gives information about the progress and measurement time and has two buttons for starting and stopping the program.

The first option lets the user define the file name and path (the button “Browse” can be used to open a dialog and browse through the directories on the PC’s hard disk). The filename should include a complete path description, but no file extension (the extension will be appended by the program automatically, depending on whether the raw data is saved (`.dat`) or the data is exported in ASCII format (`.txt`)). During the measurements, an underscore followed by an automatically incremented counter will

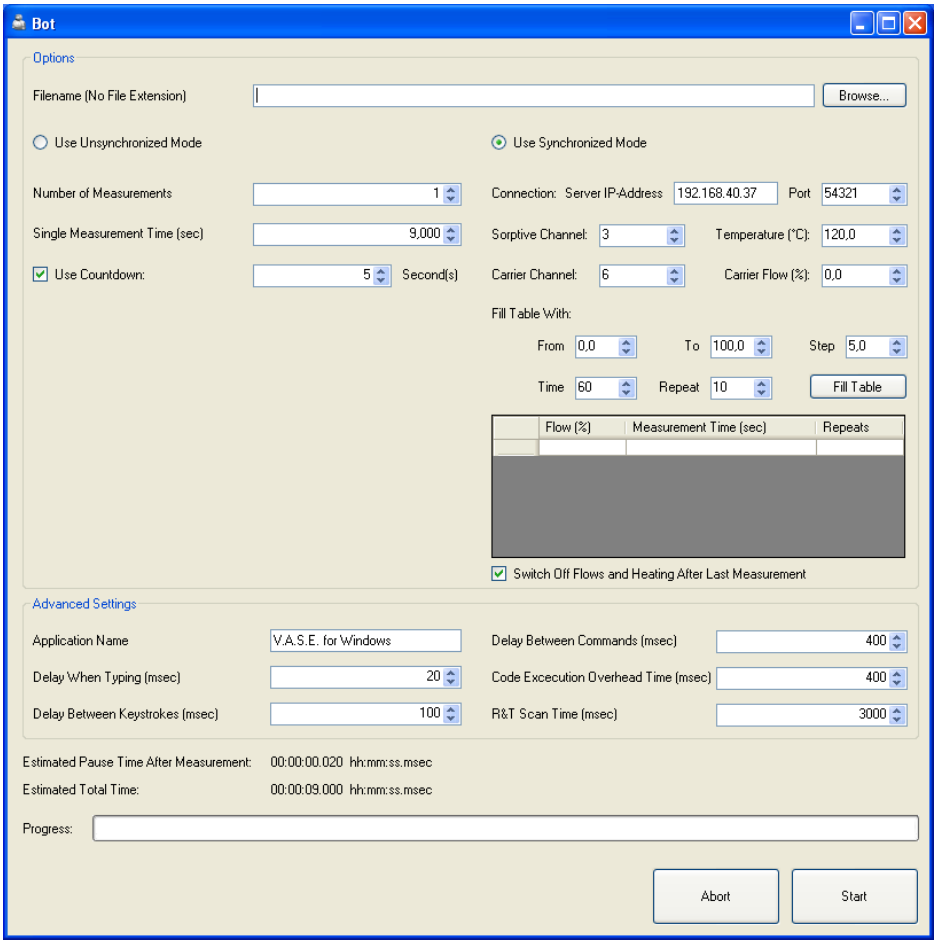

Figure 10.3: Screenshot of the Graphical User Interface (GUI) of the program "Bot".

be appended to the filename. When the "Synchronized Mode" is used, a description of the carrier gas flow and the sorptive flow will also be included in the filename. Next, the user can choose the measurement mode. There are two measurement modes available, an "Unsynchronized Mode" and a "Synchronized Mode". In the "Unsynchronized Mode", the software will simply perform R&T scans a given number of times without communication with another device. The available options for this mode are the number of measurements that should be performed and the time assigned to each measurement. For example, with the default parameters shown in Figure 10.3, one measurement would be performed and the time assigned to this measurement is 9 s. The measurement time includes the time necessary to perform all the operations and code execution plus a waiting time after all operations are completed to achieve the desired measurement intervals. In the example shown in Figure 10.3, the program estimates this waiting time to be 20 msec (as can be seen in the bottom part of the

GUI), i.e., the pure measurement time is 8.980 seconds. If a measurement was desired every 10 seconds or every minute, the actual measurement time would still be 8.980 seconds, but the program would automatically prolong the waiting time after the last operation to 1.020 seconds or 51.020 seconds, respectively. The last option available in this mode is to use a countdown with an optical and acoustic feedback before starting the first measurement, which allows for a manual synchronization with the start of another process (however, no further synchronization is carried out at later points in time).

The second mode, “Synchronized Mode”, uses network messages to communicate with the flow controller setup. This makes it possible to request a certain flow value before the ellipsometric measurement is made and ensures that the measurement is only carried out after the flow setpoint was changed successfully. There are more options available for this mode than for the “Unsynchronized Mode”, such as the possibility to enter the IP address of the PC that runs the server application (i.e., the program “Flow Controller”) and the port number that is used for network communication. Moreover, the channel number of the flow controller with the desired sorptive can be selected, the temperature of the CEM can be set (the CEM is hard-coded to be on channel 2, but this can easily be changed in the source code by altering the number of a public constant class member of the class `Form1`), and the channel number and flow value of the flow controller providing the carrier gas can be entered. The flow values of the sorptive flow controller, the time for a single measurement, and the number of measurements that should be performed at this flow setting can be entered in the table on the GUI. There are also controls that allow for the fast setup of simple, commonly used flow routines by filling the table with incrementing carrier flow values of a defined step size while using constant values for the number of measurements and the measurement time. Moreover, copy&paste functionality from and to Microsoft Excel was implemented for the table, making it possible to write and save more complex flow routines in Excel and reuse them at later points in time with this software. The last option available for this mode is the possibility to have the program set the setpoint of the flow controllers and the CEM to 0 after the last measurement was carried out.

In the “Advanced Settings” section of the program, some less commonly used parameters can be adjusted, mainly affecting the waiting times. Usually, these timings are long enough so that the “WVASE” software has enough time to react to the keystrokes sent by the “Bot” application. However, if measurements with a very high time resolution are required or if the waiting times turn out to be insufficient, they can be

adjusted here. Details on when the different waiting times are used during execution are given in Table 10.3. The textbox for the application name that can also be found in this section allows changing the name of the application the keys are sent to. In almost all cases this will be `V.A.S.E for Windows`, the default entry in this field. The string entered here has to correspond exactly to the name that is given in the taskbar for the application, otherwise the WinAPI function `FindWindow` will not be able to retrieve the correct window handle and hence the focus cannot be set to the right window. One case that makes it necessary to change this field is when an environment is loaded in the "WVASE" software. In this case, the title of the "WVASE" program changes to include the name of the environment, and hence this field has also to be adjusted to match the new title.

The bottom part of the GUI contains information about the estimated measurement time and the overall progress, as well as the buttons to start and stop execution of the program.

10.2.3 Implementation

The program contains the two public classes `Form1` and `backgroundWorker`. Again, the methods of the two classes run mainly in separate threads for keeping the GUI thread responsive during waiting times of the backgroundWorker thread. The class `Form1` provides methods for user interaction, controlling the GUI, and network communication, while the backgroundWorker thread contains methods for controlling the "WVASE" software, changing the focus of the active window, and emulating keystrokes. An overview of all the methods, types and parameters used by these two classes can be found in Tables 10.4 and 10.5 at the end of this section.

As already briefly described above, the "Bot" program controls the ellipsometer hardware by emulating user interaction, i.e., by sending keystrokes to the measurement software "WVASE" that is provided by the manufacturer. While this approach is rather simple to implement since nothing has to be known about hardware- or interface-specific commands (all the communication with the hardware is done by the software that was written by the manufacturer for this purpose), it has some inherent drawbacks. Most importantly, the whole interaction of the "Bot" program with the "WVASE" software is completely asynchronous, without any callbacks or feedback indicating the status of the operations requested by the "Bot" software through the keystrokes. This means that after requesting a certain operation from the "WVASE" software, an artificial waiting time (typically a few hundred milliseconds) had to be

implemented in the "Bot" application before the next command is issued, and the bot program simply has to rely on the fact that this waiting time was sufficient for the "WVASE" software to process the command and being ready to accept the next command (for a detailed list of the keystrokes that are sent, the waiting times after these commands, and a description of the issued commands, see Table 10.3). If the "WVASE" application is not ready yet or an error or unexpected event occurs, requesting the next command can result in uncontrolled or unintended operations. This is why great care has to be taken when choosing the waiting times and why it is very important to ensure that the "WVASE" software is configured correctly and that it is in the right state to accept the first command before starting the execution of the "Bot" program.

Another issue with the current implementation of the "Bot" software is the fact that for emulating the keystrokes, the WinAPI function `keybd_event` was used (a documentation of this method can be found online[283]). This method simply emulates a keyboard keystroke, i.e., the keystroke is sent to the application which currently has the keyboard focus. The "Bot" application tries to make sure that the right window has the keyboard focus before it starts sending the keys. In order to do so, the handle to the "WVASE" software is obtained from a call to the WinAPI function `FindWindow`[284], and this handle is passed to the WinAPI function `SetForegroundWindow`[285], or – if it is iconic (as determined by the WinAPI function `IsIconic`[286]) – to the WinAPI function `ShowWindow`[287] in order to set the keyboard focus to the correct application. If the focus of the window changes after this check was carried out (for example during emulated keystroke events), this can again result in unexpected behavior. However, since the main purpose of the "Bot" program is to perform automated measurements without the need for a user to be present and interact with the software, and since the PC that is running the program is exclusively used for ellipsometric measurements, this was not considered an important problem. Moreover, if this turns out to be problematic, it could probably be circumvented by using calls to the more powerful but more complex WinAPI function `SendMessage`[288] without the need for major modifications of the source code. `SendMessage` is able to send keystrokes to applications that do not have the keyboard focus. However, the exact names of the child windows and components of the "WVASE" software have to be known in order to retrieve their handles and address them with `SendMessage`.

Table 10.3: Overview of the keystrokes sent to the "WVASE" software, the commands they trigger, and the waiting times after execution.

Emulated Keystroke	Waiting Time[2]	Description
Alt + W	3	Opens the "Window" menu.
H	2	Selects "Hardware Window" from the "Window" menu.
Alt + A	3	Opens the "Acquire Data" menu.
R	2	Selects "R&T Scan" from the "Acquire Data" menu.
Return	2 + 3	Confirms the dialog asking whether the existing data should be replaced.
Arrow-Key Down (2x)	2 (2x)	Selects the option "Data only, using previous baseline".
Return	2 + 4	Starts the R&T Scan.
Return	2	Confirms the dialog asking whether the data should be saved.
<Filename>	1 (Nx)	Types in the filename chosen by the user (waiting time depends on the number of characters in the filename).
Return	2 (3x)	Confirms the saving dialog.
Return	2 (2x)	Closes the dialog asking for a comment.
Alt + W	3	Opens the "Window" menu.
R	2	Selects "Graph Window" from the "Window" menu.
Alt + F	3	Opens the "File" menu.
O	2	Selects the submenu "Output data points to textfile" from the "File" menu.
5	2 + 3	Selects "Curves in Columns, Single X-Column, With Headers" from the "Output data points to textfile" submenu.
<Filename>	1 (Nx)	Types in the filename chosen by the user (waiting time depends on the number of characters in the filename).
Return	2 (2x)	Confirms the saving dialog.

Table 10.4: Overview of the methods of class `Form1`. Parameters for the methods are given under the method name in italic, indented by · · · · · · .

Name	Modifier	Type[4]/Return Value	Description
Form1_Load	Private	Void	Method executed when the program starts. In this method, the GUI controls and global variables are initialized.

Continued on next page. . .

[3]The numbers in this column correspond to the following values given on the GUI: 1 = Delay When Typing, 2 = Delay Between Keystrokes, 3 = Delay Between Commands, 4 = R&T Scan Time.

[4]`System.Windows.Forms` Namespace is included in Object Types.

Name	Modifier	Type/Return Value	Description
····· *sender*	Local	Object	Object calling the method.
····· *e*	Local	System.EventArgs	Event arguments for the method call.
Start_Click	Private	Void	Method executed when pressing the "Start" Button. Disables GUI controls, checks whether the filenames generated during measurements are valid, initializes the backgroundWorker thread, and starts the timer for executing the measurements. Additionally, in "Synchronized Mode", the data from the flow table is parsed and the temperature of the CEM and the flow of the flow controller providing the carrier gas are set by sending a message over the network to the "Flow Controller" program.
····· *sender*	Local	System.Object	Object calling the method.
····· *e*	Local	System.EventArgs	Event arguments for the method call.
Button_Abort_Click	Public	Void	Method executed when pressing the "Abort" Button. Stops the measurement timer, re-enables the GUI controls, and does some clean-up.
····· *sender*	Local	System.Object	Object calling the method.
····· *e*	Local	System.EventArgs	Event arguments for the method call.
Button_Browse_Click	Private	Void	Method executed when pressing the "Browse" Button. Opens a dialog that lets the user define the path and filename of the files generated during measurements.
····· *sender*	Local	System.Object	Object calling the method.
····· *e*	Local	System.EventArgs	Event arguments for the method call.
Button_FillTable_Click	Private	Void	Method executed when pressing the "Fill Table" Button. Fills the table according to the data and options specified by the controls over the table.
····· *sender*	Local	System.Object	Object calling the method.
····· *e*	Local	System.EventArgs	Event arguments for the method call.
MeasurementTimer_Tick	Private	Void	Method executed when the "Measurement Timer" raises a `Tick` event. Sets up the parameters and the backgroundWorker thread for a new measurement. Additionally, in "Synchronized Mode", it is checked whether the flow needs to be changed and if so, a request is made by sending a message over the network to the "Flow Controller" program.
····· *sender*	Local	System.Object	Object calling the method.
····· *e*	Local	System.EventArgs	Event arguments for the method call.
Timer1_Tick	Private	Void	Method executed when the "Countdown Timer" raises a `Tick` event. In "Unsynchronized Mode", there is the option to have a countdown providing optical and acoustic feedback before starting the first measurement. This is done by this method.
····· *sender*	Local	System.Object	Object calling the method.
····· *e*	Local	System.EventArgs	Event arguments for the method call.

Continued on next page...

Name	Modifier	Type/Return Value	Description
sendMessage	Private	Void	This method sends the specified message (with an appended delimiter character) over the network to the server application and awaits an acknowledgment message.
····· *msg*	Local	String	The message that should be sent.
receiveMessage	Private	String	Wrapper method for reading data from the network socket. The return value is a String representation of the received network message without delimiter characters.
isClientConnected	Public	Boolean	The method checks whether a client is connected to the network socket. If there is a connection, it returns TRUE, otherwise, it returns FALSE.
getFlowSettings	Private	Boolean	Parses data and performs a sanity check of the values entered in the cells of the DataGridView control and produces a warning if the data is incorrect. If the method succeeds, it returns TRUE, otherwise, it returns FALSE.
complete	Private	Void	Re-enables the GUI controls and does some clean-up.
updateTimeLabels	Private	Void	Updates the labels on the GUI giving the approximate measurement time.
····· *setRepeatTime*	Local	Boolean	Optional value that indicates whether the minimal measurement time that can be chosen in the GUI should be set to the time that was estimated from the method (default value is TRUE).
getEstimatedMeasurementTime	Private	Double	Does the actual estimation of the measurement time based on the values entered in the GUI and returns it.
initializeThread	Private	Void	Creates a new thread and sets up the public class members.
isValidFileName	Private	Boolean	Checks whether the filename chosen by the user is valid, and whether files of the names that will be generated during the measurement already exist.
myEventHandler_ThreadAborted	Private	Void	Method executed when the backgroundWorker thread exited and raised the user-defined `threadAborted` event. This method stops the measurement timer, attempts to set the sorptive flow, the carrier gas flow, and the temperature of the CEM to 0, and re-enables some GUI controls.
myEventHandler_ProgressChanged	Private	Void	Method executed when the backgroundWorker thread completed a measurement and raised the user-defined `ProgressChanged` event. This method changes the GUI to reflect the current progress of the measurements.
····· *curNumber*	Local	Long	Number of the current measurement.
····· *maxNumber*	Local	Long	Total number of measurements.
DataGridView_CellValidating	Private	Void	Method executed when the `CellValidating` event of the control is raised. The method performs a sanity check of the value entered in the cells of the DataGridView control and produces a warning if the data is incorrect.
····· *sender*	Local	Object	Object calling the method.

Continued on next page...

Name	Modifier	Type/Return Value	Description
····· *e*	Local	DataGridViewCell ValidatingEventArgs	Event arguments for the method call.
DataGridView_KeyDown	Private	Void	Method executed when the `KeyDown` event of the control is raised, i.e., when a key is pressed while the control has the focus. The method checks for the key combination *Crtl+v*, i.e., pasting of data. It parses the data from the clipboard and tries to fill the cells of the `DataGridView` with it. This enables copy&paste functionality from Microsoft Excel.
····· *sender*	Local	Object	Object calling the method.
····· *e*	Local	KeyEventArgs	Event arguments for the method call.
TextBox_Filename_TextChanged	Private	Void	Method executed when the `TextChanged` event of the control is raised. The method forces a recalculation of the estimated measurement time.
····· *sender*	Local	System.Object	Object calling the method.
····· *e*	Local	System.EventArgs	Event arguments for the method call.
TextBox_IPAddress_Validating	Private	Void	Method executed when the `Validating` event of the control is raised. The method performs a sanity check on the entered IP address and produces a warning if the address is invalid.
····· *sender*	Local	Object	Object calling the method.
····· *e*	Local	System.ComponentModel. CancelEventArgs	Event arguments for the method call.
NumericUpDown_RepeatTime_ValueChanged	Private	Void	Method executed when the `ValueChanged` event of the control is raised. The method forces a recalculation of the estimated measurement time.
····· *sender*	Local	System.Object	Object calling the method.
····· *e*	Local	System.EventArgs	Event arguments for the method call.
NumericUpDown_FlowTime_ValueChanged	Private	Void	Method executed when the `ValueChanged` event of the control is raised. The method forces a recalculation of the estimated measurement time.
····· *sender*	Local	System.Object	Object calling the method.
····· *e*	Local	System.EventArgs	Event arguments for the method call.
NumericUpDown_MaxNumber_ValueChanged	Private	Void	Method executed when the `ValueChanged` event of the control is raised. The method forces a recalculation of the estimated measurement time.
····· *sender*	Local	System.Object	Object calling the method.
····· *e*	Local	System.EventArgs	Event arguments for the method call.
NumericUpDown_KeyDelay_ValueChanged	Private	Void	Method executed when the `ValueChanged` event of the control is raised. The method forces a recalculation of the estimated measurement time.
····· *sender*	Local	System.Object	Object calling the method.

Continued on next page...

Name	Modifier	Type/Return Value	Description
····· *e*	Local	System.EventArgs	Event arguments for the method call.
NumericUpDown_CommandDelay_ ValueChanged	Private	Void	Method executed when the `ValueChanged` event of the control is raised. The method forces a recalculation of the estimated measurement time.
····· *sender*	Local	System.Object	Object calling the method.
····· *e*	Local	System.EventArgs	Event arguments for the method call.
NumericUpDown_MeasurementTime_ ValueChanged	Private	Void	Method executed when the `ValueChanged` event of the control is raised. The method forces a recalculation of the estimated measurement time.
····· *sender*	Local	System.Object	Object calling the method.
····· *e*	Local	System.EventArgs	Event arguments for the method call.
NumericUpDown_Overhead_ValueChanged	Private	Void	Method executed when the `ValueChanged` event of the control is raised. The method forces a recalculation of the estimated measurement time.
····· *sender*	Local	System.Object	Object calling the method.
····· *e*	Local	System.EventArgs	Event arguments for the method call.
NumericUpDown_TypingDelay_ValueChanged	Private	Void	Method executed when the `ValueChanged` event of the control is raised. The method forces a recalculation of the estimated measurement time.
····· *sender*	Local	System.Object	Object calling the method.
····· *e*	Local	System.EventArgs	Event arguments for the method call.
CheckBox_Countdown_CheckedChanged	Private	Void	Method executed when the `ValueChanged` event of the control is raised. The method sets up the label that displays the countdown.
····· *sender*	Local	System.Object	Object calling the method.
····· *e*	Local	System.EventArgs	Event arguments for the method call.
RadioButton_UnsynchronizedMode_ CheckedChanged	Private	Void	Method executed when the `CheckedChanged` event of the control is raised. The method closes the network socket in case the "Unsynchronized Mode" is selected
····· *sender*	Local	System.Object	Object calling the method.
····· *e*	Local	System.EventArgs	Event arguments for the method call.
SetGroupBoxState_Delegate	Delegate	Void	Delegate to set the `enable` property of the GroupBox control on the GUI. This is necessary for thread-safe enabling or disabling of the control from a thread other than the GUI thread that created the control.
····· *[GroupBox]*	Local	GroupBox	GroupBox control on the GUI whose `enable` property should be changed.
····· *[value]*	Local	Boolean	Value the `enable` property should be changed to.
SetGroupBoxState_ThreadSafe	Private	Void	This method does the actual invocation of the delegate in the thread that created the GUI controls.
····· *[GroupBox]*	Local	GroupBox	GroupBox control on the GUI whose `enable` property should be changed.
····· *[value]*	Local	Boolean	Value the `enable` property should be changed to.

Continued on next page...

Name	Modifier	Type/Return Value	Description
SetButtonState_Delegate	Delegate	Void	Delegate to set the `enable` property of the Button control on the GUI. This is necessary for thread-safe enabling or disabling of the control from a thread other than the GUI thread that created the control.
····· *[Button]*	Local	Button	Button control on the GUI whose `enable` property should be changed.
····· *[value]*	Local	Boolean	Value the `enable` property should be changed to.
SetButtonState_ThreadSafe	Private	Void	This method does the actual invocation of the delegate in the thread that created the GUI controls.
····· *[Button]*	Local	Button	Button control on the GUI whose `enable` property should be changed.
····· *[value]*	Local	Boolean	Value the `enable` property should be changed to.
SetLabelText_Delegate	Delegate	Void	Delegate to set the `text` property of the Label control on the GUI. This is necessary for changing the text of the Label control in a thread-safe way from a thread other than the GUI thread that created the control.
····· *[Label]*	Local	Label	Label control on the GUI whose `text` property should be changed.
····· *[text]*	Local	String	String the `text` property should be changed to.
SetLabelText_ThreadSafe	Private	Void	This method does the actual invocation of the delegate in the thread that created the GUI controls.
····· *[Label]*	Local	Label	Label control on the GUI whose `text` property should be changed.
····· *[text]*	Local	String	String the `text` property should be changed to.
SetProgressBarValue_Delegate	Delegate	Void	Delegate to set the `value` property of the ProgressBar control on the GUI. This is necessary for thread-safe enabling or disabling of the control from a thread other than the GUI thread that created the control.
····· *[ProgressBar]*	Local	ProgressBar	ProgressBar control on the GUI whose `value` property should be changed.
····· *[value]*	Local	Decimal	Value the `value` property should be changed to.
SetProgressBarValue_ThreadSafe	Private	Void	This method does the actual invocation of the delegate in the thread that created the GUI controls.
····· *[ProgressBar]*	Local	ProgressBar	ProgressBar control on the GUI whose `enable` property should be changed.
····· *[value]*	Local	Decimal	Value the `value` property should be changed to.
SetFormText_Delegate	Delegate	Void	Delegate to set the `text` property of the Form control. This is necessary for changing the title of the Form control in a thread-safe way from a thread other than the GUI thread that created the control.
····· *[Form]*	Local	Form	Form control whose `text` property should be changed.
····· *[text]*	Local	String	String the `text` property should be changed to.
SetFormText_ThreadSafe	Private	Void	This method does the actual invocation of the delegate in the thread that created the GUI controls.

Continued on next page...

Name	Modifier	Type/Return Value	Description
····· *[Form]*	Local	Form	Form control whose `text` property should be changed.
····· *[text]*	Local	String	String the `text` property should be changed to.

Table 10.5: Overview of the methods of class "backgroundWorker". Parameters for the methods are given under the method name in italic, indented by ·····.

Name	Modifier	Type/Return Value	Description
startBot	Public	Boolean	This method checks whether the right window has the focus (and if not, it attempts to change the focus), and then executes the list of commands given in Table 10.3. This method is the entry point for the `backgroundWorker` thread.
pressKey	Private	Void	Wrapper method for emulating a keystroke.
····· *keyCode*	Local	String	KeyCode of the key for which the keystroke should be emulated.
····· *shift*	Local	Boolean	Optional value indicating whether the Shift key should be pressed together with the indicated key (used for emulating capital letters). Default value is FALSE.
····· *useShortKeyDelay*	Local	Boolean	Optional value indicating how long the application should wait after the keystroke for the target program to process the keystroke. Default value is FALSE.
pressKeyAndAlt	Private	Void	Wrapper method for emulating a keystroke when a key is pressed together with the `Alt` key.
····· *keyCode*	Local	String	KeyCode of the key for which the keystroke should be emulated.
writeFileName	Private	Void	This method parses the filename entered in the GUI and emulates keystrokes for each individual character of the string.
trySetForegroundWindow	Public	Boolean	This method tries to set the focus to the "WVASE" program.
····· *windowName*	Local	String	Title of the window that should receive the focus.

10.3 Data Analysis with Mathematica

10.3.1 Description and Implementation

The data collected from the R&T scans was further analyzed using a self-written Mathematica script, mainly for finding the positions of the stop band maxima. Those were needed for constructing the isotherms in which the stop band position was plotted against the partial pressure at which the measurement was performed. To find the maximum of the stop bands, the stop band of interest was fitted with the following empirical function:

$$y = c_0 + c_1 \cdot \exp\left[-\left(\sqrt{\left(\frac{\frac{1}{x} - \frac{1}{c_2}}{c_3}\right)^2}\right)^{c_4}\right],$$

where x and y correspond to the measured wavelength and intensity, and c_0 to c_4 are the fitting parameters. c_0 represents a constant offset, c_1 an amplitude value, c_2 the position of the stop band maximum, c_3 a measure for the width of the stop band, and c_4 an empirical exponent for varying the stop band shape. The function was chosen because for $c_4 = 2$, it resembles a Gaussian when plotting the data as a function of energy E instead of as a function of wavelength λ (since $E = \frac{hc}{\lambda} \Rightarrow E \propto \frac{1}{\lambda}$), with the fitting parameter c_2 corresponding directly to the position of the stop band maximum. Taking the squareroot of the argument squared before raising it to the power of c_4 was done to prevent the expression from becoming negative (and hence the argument of the exponential function possibly becoming imaginary when raising the negative value to a non-integer power) which causes the fitting algorithm to fail.

In brief, the Mathematica script first reads the data from the human-readable text files exported during ellipsometric measurements and transposes it to bring it into the right input format. It then searches for the beginning and the end of the stop band by looking for local minima and initializes the fitting parameters (for the first flow value, the user has to input some starting values, for all the following flow values, the parameters obtained from the last fit are taken and used as the starting point for the new fit). After that, it performs the fit using the Mathematica function "NonlinearModelFit" and calculates the standard errors of the fitting parameters, the root-mean-square deviation of the fitted data from the experimental data, and the x- and y-position of the maximum and exports them to a text file. It also plots the experimental data, the

fitting function, and the stop band position into a graph and exports it as an image file.

10.4 Photolithography Processing Parameters

The tables in this section summarize the processing parameters for the photolithography steps used in this work. Table 10.6 lists the shifts due to chromatic aberration of different objectives that were used. These shifts were determined experimentally by focusing a pattern onto a substrate using yellow light produced by a 500 nm LWP edge barrier filter, subsequently replacing the filter by a Brightline HC 370/36 band-pass excitation filter, adjusting the focus again, and recording the difference in the focal position as indicated by the scale on the focusing knob of the microscope.

Table 10.7 gives detailed experimental processing conditions for different photoresists and photolithographic methods used in this work.

Table 10.6: Overview of the corrections of the focal shift due to chromatic aberration when changing from yellow light to UV light.

Objective	Correction [scale units]
Plan Fluor 10x/0.30	+60
Plan APO 40x/0.95	-3
Plan APO 60x/1.20 Water	±0
Plan APO VC 100x/1.40 Oil	±0

10.5 Raw Data of Fluorescence Titration Experiments

Figure 10.4 contains the raw data of the fluorescence titration experiments that were used to construct the graphs in Figures 6.9, 6.10, 6.11.d, and 6.12, as explained in Section 6.5.5.

Table 10.7: Overview of the processing conditions for various photoresists used in this work.

Processing Step	"Standard" Photolithography				Microscope Projection Lithography		
	S1818 (pos.)	AZ5214E (pos.)	AZ5214E (IR)	SU8-10 (neg.)	AZ5214E (pos.)	AZ5214E (IR)	nLof2070 (neg.)
Spin-Speed[5]	2000 rpm	2000 rpm; 7000 rpm	2000 rpm; 7000 rpm	1000 – 2000 rpm	6000 rpm	6000 rpm	500 rpm; 4000 rpm
Spin Time	40 s	30 s; 6 s	30 s; 6 s	30 s	33 s	33 s	10 s; 40 s
Ramp	2	2; 1	2; 1	2	3	3	1; 1
Thickness	2.5 µm	2.5 µm	2.5 µm	8.4 µm-5.8 µm	1.1 µm	1.1 µm	6.5 µm
Pre-Bake[6]	15 min at 90 °C (O)	90 s at 90 °C (HP)	90 s at 90 °C (HP)	150 s at 90 °C (HP)	50 s at 110 °C (HP)	50 s at 110 °C (HP)	55 s at 110 °C (HP)
Exposure [s][7]	8 s	2 s	2 s	16 – 18 s	10x (ND2): 6 – 8 s	10x (ND2): 6 – 8 s	10x (ND2): 6 – 8 s
					40x (ND16): 6 – 8 s	40x (ND16): 6 – 8 s	40x (ND16): 6 – 8 s
					60x (ND16): 6 – 8 s	60x (ND16): 6 – 8 s	60x (ND16): 6 – 8 s
					100x (ND16): 5 – 7 s	100x (ND16): 5 – 7 s	100x (ND16): 5 – 7 s
Post-Exposure/IR Bake	n.a.	n.a.	30 s at 130 °C (HP)	4 min at 95 °C (HP)	n.a.	120 s at 110 °C (HP)	60 s at 110 °C (HP)
Flood Exposure[8]	n.a.	n.a.	30 s	n.a.	> 5 min	n.a.	n.a.
Developer[9]	AZ351B	AZ351B (1:5)	AZ351B (1:4)	SU-8 Developer	MIF726	MIF726	MIF726
Development Time	35 s	45 s	45 s	45 s	90 s	90 s	120 – 180 s
Hard Bake	n.a.	n.a.	3 h at 120 °C (O)	25 min at 220 °C (O)	n.a.	4 h at 130 °C (O)	4 h at 170 °C (O)

[5]When glass was used as the substrate, it was heated to 180 °C for 15 min prior to applying the resist in order to evaporate adsorbed water that can otherwise cause adhesion problems. In some cases, an adhesion promoter (hexamethyldisilazane, HMDS) was used that renders the surface more hydrophobic and thereby also helps with adhesion of the resist on hydrophilic substrates.

[6]O = Oven, HP = Hotplate

[7]For "Standard" photolithography, exposure times are given for a SUSS MicroTec MJB3 mask aligner. For Microscope Projection Lithography, exposure times are given for different objectives and ND filters as indicated. The aperture opening was adjusted to maximize the contrast (about 90 % closed). As a rule of thumb, the ND value of the employed filter combination needs to be 8x higher when using a fully opened aperture (however, fully opening the aperture results in a poorer contrast and hence in a stronger exposure of masked regions).

[8]Flood exposure was done with a HeroLab 2x4 W handheld UV lamp using 235 nm and 355 nm UV light, positioned about 1 – 2 cm above the substrates. In the case of transparent substrates, the substrate was turned over after half the time and illuminated from the backside as well.

[9]Dilutions are given in brackets as developer:water (v/v)

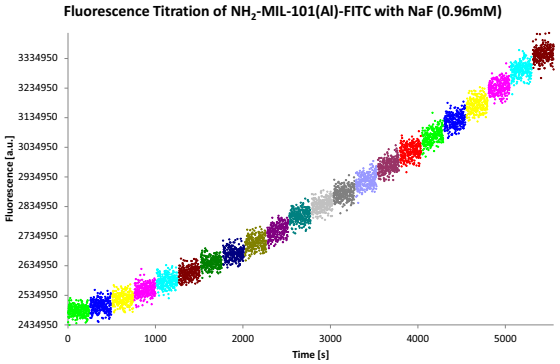
Fluorescence Titration of NH2-MIL-101(Al)-FITC with NaF (0.96mM)
Fluorescence [a.u.]
Time [s]

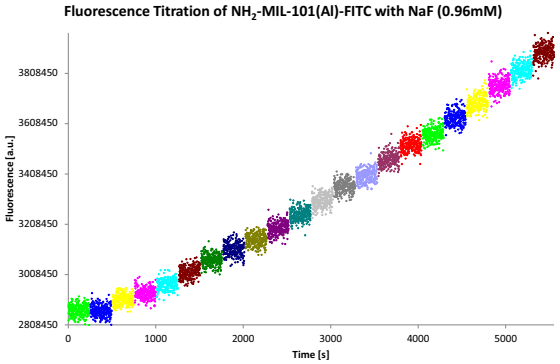
Fluorescence Titration of NH2-MIL-101(Al)-FITC with NaF (0.96mM)
Fluorescence [a.u.]
Time [s]

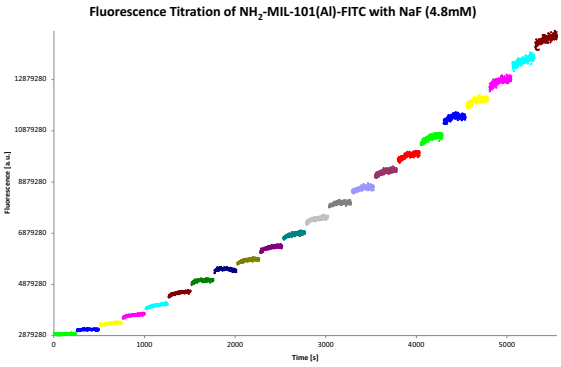
Fluorescence Titration of NH2-MIL-101(Al)-FITC with NaF (4.8mM)
Fluorescence [a.u.]
Time [s]

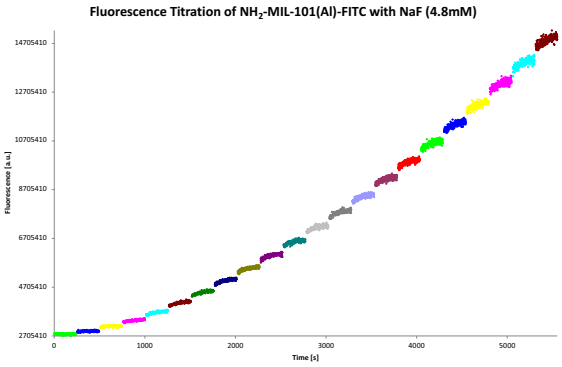
Fluorescence Titration of NH2-MIL-101(Al)-FITC with NaF (4.8mM)
Fluorescence [a.u.]
Time [s]

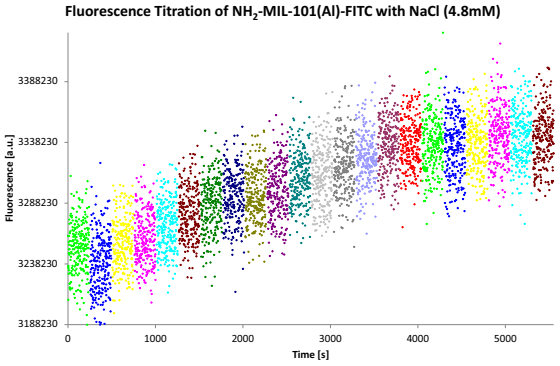
Fluorescence Titration of NH2-MIL-101(Al)-FITC with NaCl (4.8mM)
Fluorescence [a.u.]
Time [s]

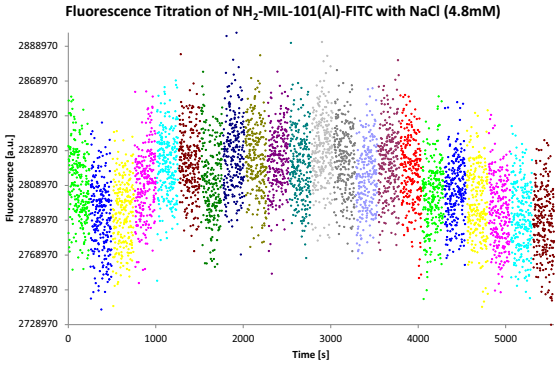
Fluorescence Titration of NH2-MIL-101(Al)-FITC with NaCl (4.8mM)
Fluorescence [a.u.]
Time [s]

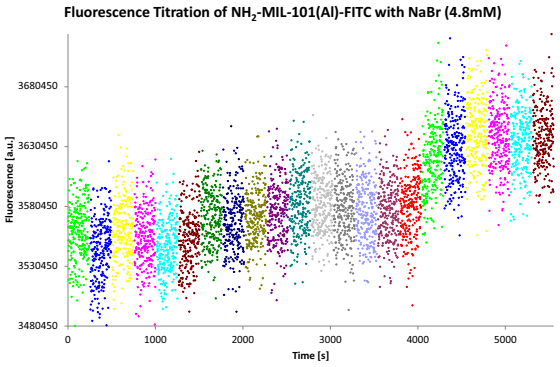
Fluorescence Titration of NH2-MIL-101(Al)-FITC with NaBr (4.8mM)
Fluorescence [a.u.]
Time [s]

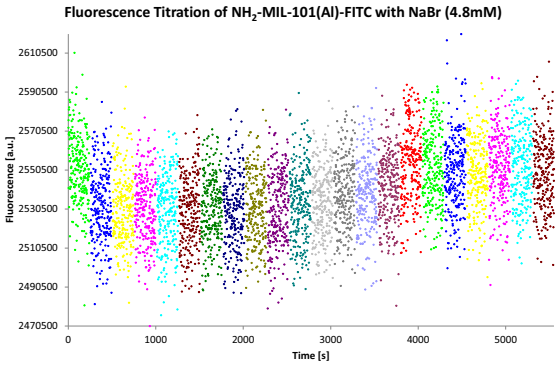
Fluorescence Titration of NH2-MIL-101(Al)-FITC with NaBr (4.8mM)
Fluorescence [a.u.]
Time [s]

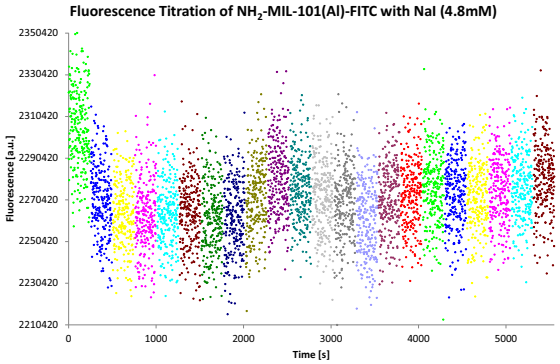
Fluorescence Titration of NH2-MIL-101(Al)-FITC with NaI (4.8mM)
Fluorescence [a.u.]
2350420
2330420
2310420
2290420
2270420
2250420
2230420
2210420
0
1000
2000
3000
4000
5000
Time [s]

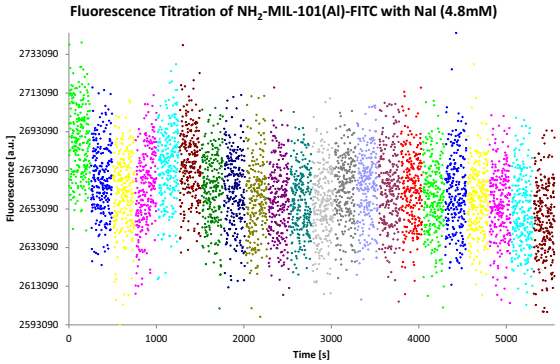
Fluorescence Titration of NH2-MIL-101(Al)-FITC with NaI (4.8mM)
Fluorescence [a.u.]
2733090
2713090
2693090
2673090
2653090
2633090
2613090
2593090
0
1000
2000
3000
4000
5000
Time [s]

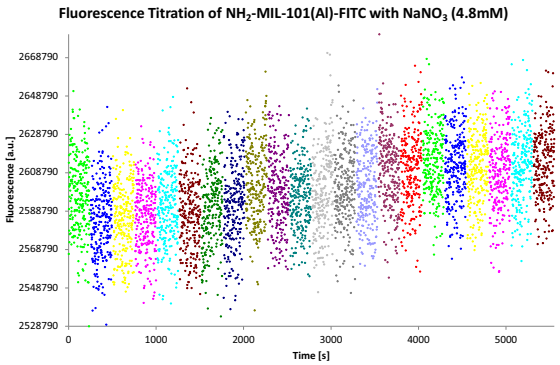
Fluorescence Titration of NH2-MIL-101(Al)-FITC with NaNO3 (4.8mM)
Fluorescence [a.u.]
2668790
2648790
2628790
2608790
2588790
2568790
2548790
2528790
0
1000
2000
3000
4000
5000
Time [s]

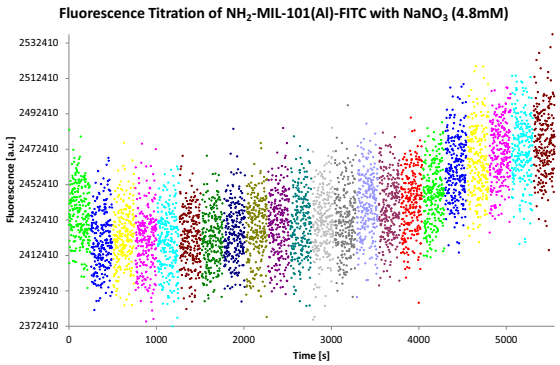
Fluorescence Titration of NH2-MIL-101(Al)-FITC with NaNO3 (4.8mM)
Fluorescence [a.u.]
2532410
2512410
2492410
2472410
2452410
2432410
2412410
2392410
2372410
0
1000
2000
3000
4000
5000
Time [s]

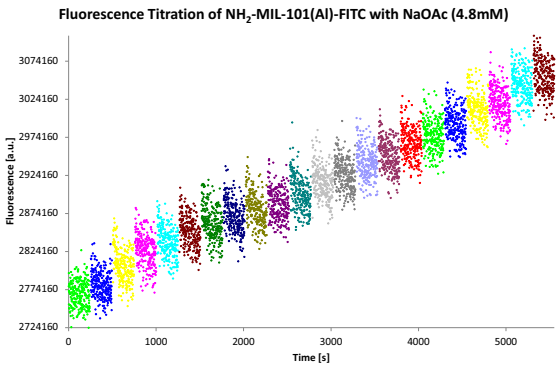
Fluorescence Titration of NH2-MIL-101(Al)-FITC with NaOAc (4.8mM)
Fluorescence [a.u.]
3074160
3024160
2974160
2924160
2874160
2824160
2774160
2724160
0
1000
2000
3000
4000
5000
Time [s]

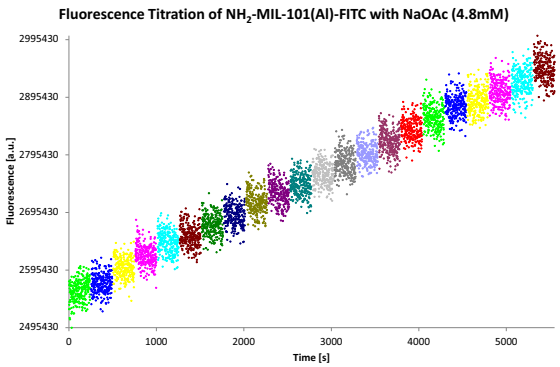
Fluorescence Titration of NH2-MIL-101(Al)-FITC with NaOAc (4.8mM)
Fluorescence [a.u.]
2995430
2895430
2795430
2695430
2595430
2495430
0
1000
2000
3000
4000
5000
Time [s]

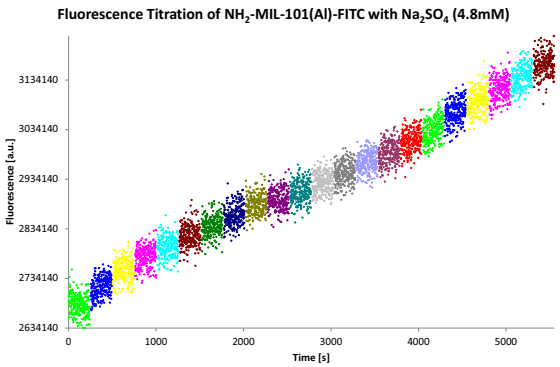
Fluorescence Titration of NH2-MIL-101(Al)-FITC with Na2SO4 (4.8mM)
Fluorescence [a.u.]
3134140
3034140
2934140
2834140
2734140
2634140
0
1000
2000
3000
4000
5000
Time [s]

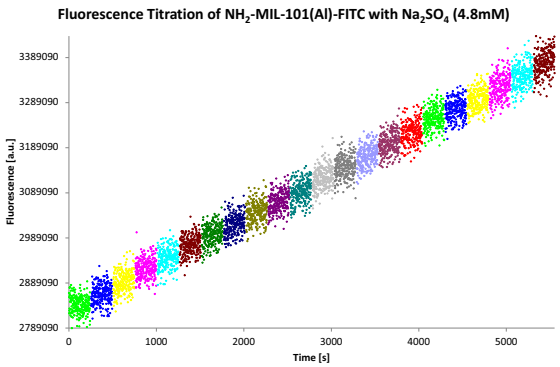
Fluorescence Titration of NH2-MIL-101(Al)-FITC with Na2SO4 (4.8mM)
Fluorescence [a.u.]
3389090
3289090
3189090
3089090
2989090
2889090
2789090
0
1000
2000
3000
4000
5000
Time [s]

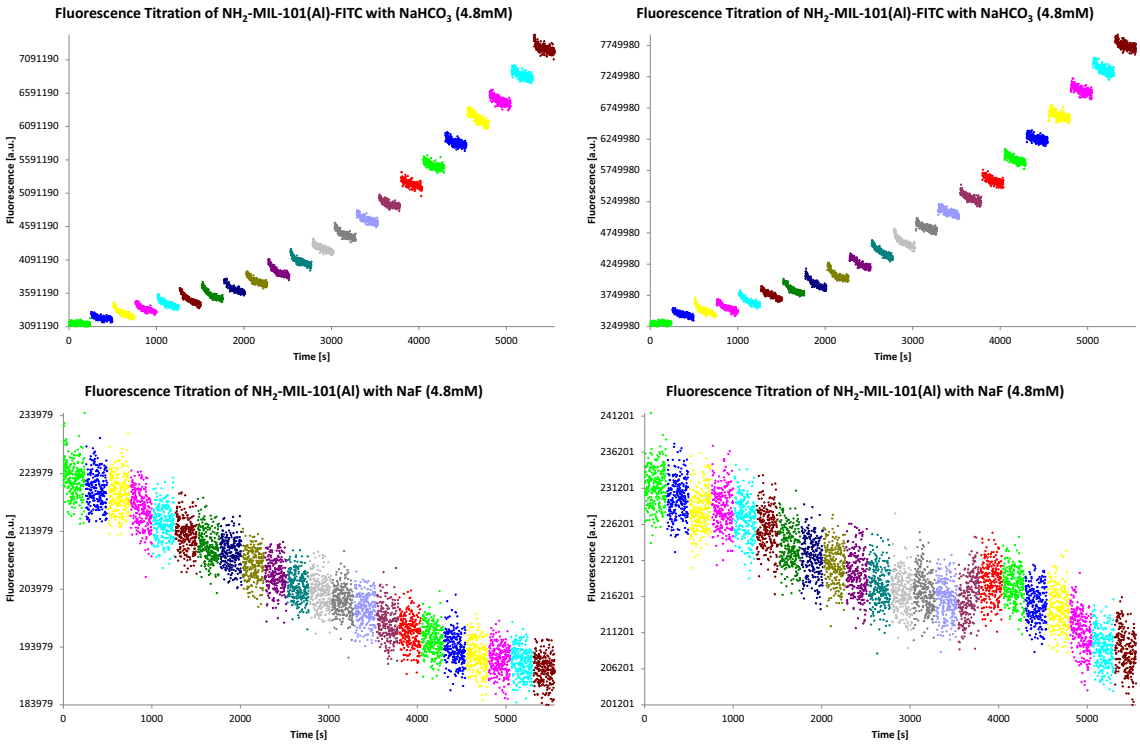

Figure 10.4: Raw fluorescence spectra. Shown are time-based fluorescence measurements (Ex: 485 nm, Em: 520 nm). For better visualization, a different color was chosen for each 4 minutes interval after a salt addition step of 2.5 µL, and the individual steps are separated by a time gap of 12 s (corresponding to the approximate time for dispensing 2.5 µL of salt solution from the syringe). Fluorescence titration curves were constructed from these data sets by taking the average value of the last 60 points for each salt addition step and plotting this value against the salt concentration in the cuvette, as described in Section 6.5.5. The concentration value in brackets in the titles denotes the concentration of the respective titration solution. For each salt, two spectra (measurement and reproduction) are shown.

10.6 Contents of the Supplementary CD

The following table lists the contents of the Supplementary CD that accompanies the printed version of this thesis.

Table 10.8: Contents of the Supplementary CD.

Path	Item	Description
\	`Dissertation.pdf`	This Document
`\Chapter3`	`M1.mov`	Movie recorded with a fluorescence microscope at a frame rate of 2.5 fps taken from sample 1 (false-colored in blue; scale bar is 5 µm; see also Figure 3.1 and Table 3.1)
`\Chapter3`	`M2.mov`	Movie recorded with a fluorescence microscope at a frame rate of 2.5 fps taken from sample 1 (false-colored in blue; scale bar is 5 µm; see also Figure 3.1 and Table 3.1)
`\Chapter3`	`M3.mov`	Movie recorded with a fluorescence microscope at a frame rate of 2.5 fps taken from sample 2 (false-colored in blue; scale bar is 5 µm; see also Figures 3.2 and 3.5 and Table 3.1)
`\Chapter3`	`M4.mov`	Movie recorded with a fluorescence microscope at a frame rate of 2.5 fps taken from sample 3 (false-colored in blue; scale bar is 5 µm; see also Figure 3.4 and Table 3.1)
`\Chapter3`	`M5.mov`	Movie recorded with a fluorescence microscope at a frame rate of 2.5 fps taken from sample 4 (false-colored in blue; scale bar is 5 µm; see also Figure 3.5 and Table 3.1)
`\Chapter3`	`M6.mov`	Movie recorded with a fluorescence microscope at a frame rate of 2.5 fps taken from sample 2 (false-colored in blue; scale bar is 5 µm; see also Figure 3.6 and Table 3.1)
`\Chapter3`	`M7.mov`	Movie recorded with a fluorescence microscope at a frame rate of 2.5 fps taken from sample 6 (false-colored in blue; scale bar is 5 µm; see also Figure 3.8 and Table 3.1)
`\Chapter3`	`M8.mov`	Movie recorded with a fluorescence microscope at a frame rate of 2.5 fps taken from sample 6 (false-colored in blue; scale bar is 5 µm; see also Figure 3.8 and Table 3.1)
`\Chapter3`	`M9.mov`	Movie recorded with a fluorescence microscope at a frame rate of 2.5 fps taken from sample 8 (false-colored in blue; scale bar is 5 µm; see also Figure 3.10 and Table 3.1)
`\Chapter3`	`M10.mov`	Movie recorded with a fluorescence microscope at a frame rate of 2.5 fps taken from sample 9 (false-colored in blue; scale bar is 5 µm; see also Figure 3.14 and Table 3.1)
`\Chapter3`	`M11.mov`	Movie recorded with a fluorescence microscope at a frame rate of 2.5 fps taken from sample 10 (false-colored in blue; scale bar is 5 µm; see also Figure 3.14 and Table 3.1)
`\Chapter4`	`M1.mov`	Movie recorded with a fluorescence microscope at a frame rate of 2.5 fps (false-colored in blue; scale bar is 5 µm; see also Figure 4.1.a)
`\Chapter4`	`M2.mov`	Movie recorded with a fluorescence microscope at a frame rate of 2.5 fps (false-colored in blue; scale bar is 5 µm; see also Figure 4.1.b)
`\Chapter4`	`M3.mov`	Movie recorded with a fluorescence microscope at a frame rate of 2.5 fps (false-colored in blue; scale bar is 5 µm; see also Figure 4.1.c)

Continued on next page...

Path	Item	Description
\Chapter4	M4.mov	Movie recorded with a fluorescence microscope at a frame rate of 2.5 fps (false-colored in blue; scale bar is 5 µm; see also Figure 4.2.b)
\Chapter4	M5.mov	Movie recorded with a fluorescence microscope at a frame rate of 2.5 fps (scale bar is 5 µm; see also Figure 4.2.a)
\Chapter4	M6.mov	Movie recorded with a fluorescence microscope at a frame rate of 2.5 fps (scale bar is 5 µm)
\Chapter4	M7.mov	Movie recorded with a fluorescence microscope at a frame rate of 2.5 fps (false-colored in blue; scale bar is 5 µm; see also Figure 4.3)
\Chapter4	M8.mov	Movie recorded with a fluorescence microscope at a frame rate of 2.5 fps (false-colored in blue; scale bar is 5 µm; see also Figure 4.5)
\Chapter4	M9.mov	Movie recorded with a fluorescence microscope at a frame rate of 2.5 fps (false-colored in blue; scale bar is 5 µm; see also Figure 4.6)
\Chapter4	M10.mov	Movie recorded with a fluorescence microscope at a frame rate of 2.5 fps (scale bar is 5 µm; see also Figure 4.7.a)
\Chapter6	M1.mov	Movie recorded with a fluorescence microscope at a frame rate of 0.2 fps (false-colored in blue; scale bar is 125 µm; see also Figure 5.6)
\Chapter11	Bot.txt	Source code of the "Bot" program (written in Visual Basic .NET; see also Section 10.2)
\Chapter11	FlowController.txt	Source code of the "FlowController" program (written in Visual Basic .NET; see also Section 10.1)
\Chapter11	MathematicaScript.txt	Source Code of the Mathematica script for R&T scan data analysis (written for Wolfram Mathematica 7; see also Section 10.3)
\Chapter11	Photomasks.txt	Source code of the Java program for generating gerber files of the photomask layouts (written for Java 6)
\Chapter11	FlowController	Project files of the "FlowController" program (compilable with Microsoft Visual Basic 2010 Express; see also Section 10.1)
\Chapter11	Bot	Project files of the "Bot" program (compilable with Microsoft Visual Basic 2010 Express; see also Section 10.2)

Publications and Presentations

Publications

C. L. McMullin, B. Rühle, M. Besora, A. G. Orpen, J. N. Harvey, N. Fey, "Computational study of (PBu3)-Bu-t as ligand in the palladium-catalysed amination of phenylbromide with morpholine", *J. Mol. Catal. A Chem.*, **2010**, 324 (1-2), 48-55.

B. Rühle[‡], M.Davies[‡], T. Lebold, C. Bräuchle, T. Bein, "Highly Oriented Mesoporous Silica Channels Synthesized in Microgrooves and Visualized with Single-Molecule Diffusion", *ACS Nano*, **2012**, 6 (3), 1948-1960.

F. M. Hinterholzinger[‡], A. Ranft[‡], J. M. Feckl, B. Rühle, T. Bein, B. V. Lotsch, "One-dimensional Metal–organic Framework Photonic Crystals Used as Platforms for Vapor Sorption", *J. Mater. Chem.*, **2012**, 22, 10356-10362.

B. Rühle[‡], F. M. Hinterholzinger[‡], S. Wuttke, K. Karaghiosoff, T. Bein, "Highly sensitive and selective fluoride detection in water through fluorophore release from a metal–organic framework", *submitted.*

B. Rühle[‡], M. Davies[‡], T. Bein, C. Bräuchle, "Fluorescence Microscopy Studies of Porous Silica Compounds", accepted for publication in *Zeitschrift für Naturforschung B.*

B. Rühle[‡], S. Wuttke[‡], F. M. Hinterholzinger, P. Roy, A. Godt, T. Bein, "Chemiluminescence in an Anthracene Based Metal–organic Framework", *in preparation.*

B. Rühle[‡], M. Davies[‡], T. Lebold, T. Bein, C. Bräuchle, "Electrophoresis of Single Dye Molecules in Highly Oriented Mesoporous Silica Channels", *in preparation.*

[‡] These authors contributed equally to the work.

Presentations

B. Rühle, T. Lebold, A. Zürner, C. Bräuchle, T. Bein, Poster presentation at the 22nd German Zeolite Conference, Munich (Germany), 2010

B. Rühle, T. Lebold, M. Davies, A. Zürner, C. Bräuchle, T. Bein, Poster presentation at the 16th International Zeolite Conference *joint with the* 7th International Mesostructured Materials Symposium, Sorrento (Italy), 2010

B. Rühle, M. Davies, C. Bräuchle, T. Bein, Poster presentation at the 4th Annual Symposium on Nanobiotechnology, Munich (Germany), 2010

M. Davies, B. Rühle, T. Bein, C. Bräuchle, Poster presentation at the 23rd German Zeolite Conference, Erlangen (Germany), 2011

B. Rühle, M. Davies, C. Bräuchle, T. Bein, Poster presentation at the conference on Nanomaterials for Biomedical Technologies, Frankfurt (Germany), 2012

F. M. Hinterholzinger, A. Ranft, J. M. Feckl, B. Rühle, B. V. Lotsch, T. Bein, Oral presentation at the 2012 MRS Spring Meeting & Exhibit, San Francisco (CA, USA), 2012

F. M. Hinterholzinger, B. Rühle, S. Wuttke, K. Karaghiosoff, T. Bein, Oral presentation at the 3rd International Conference on Metal–Organic Frameworks and Open Framework Compounds, Edinburgh (UK), 2012

A. Ranft, F. M. Hinterholzinger, J. Feckl, B. Rühle, T. Bein, B. V. Lotsch, Oral presentation at the 3rd International Conference on Metal–Organic Frameworks and Open Framework Compounds, Edinburgh (UK), 2012

B. Rühle, M. Davies, C. Bräuchle, T. Bein, Poster presentation at the 6th Annual Symposium on Nanobiotechnology, Kyoto (Japan), 2012

A. Schmidt, S. Niedermayer, C. Argyo, B. Rühle, V. Weiss, S. Mackowiak, C. von Schirnding, C. Bräuchle, T. Bein, Poster presentation at the joint SFB1032 and NIM meeting, Hohenkammer (Germany), 2013

B. Rühle, M. Davies, C. Bräuchle, T. Bein, Short oral presentation and poster presentation at the NIM Winterschool, Kirchberg (Austria), 2013

B. Rühle, M. Davies, S. Niedermayer, C. Bräuchle, T. Bein, Poster presentation at the SFB749 meeting, Wildbad Kreuth (Germany), 2013

Bibliography

[1] Wirth, M. J., Fairbank, R. W. P., and Fatunmbi, H. O. *Science* **275**(5296), 44–47 January (1997).

[2] Wirth, M. J., Swinton, D. J., and Ludes, M. D. *Journal of Physical Chemistry B* **107**(26), 6258–6268 June (2003).

[3] Corma, A. *Chemical Reviews* **97**(6), 2373–2420 October (1997).

[4] Jaroniec, M. *Journal of the American Chemical Society* **124**(48), 14506–14506 September (2002).

[5] Pandey, P., Upadhyay, S., and Pathak, H. *Sensors and Actuators B: Chemical* **60**(2-3), 83–89 November (1999).

[6] Lai, C.-Y., Trewyn, B. G., Jeftinija, D. M., Jeftinija, K., Xu, S., Jeftinija, S., and Lin, V. S.-Y. *Journal of the American Chemical Society* **125**(15), 4451–4459 March (2003).

[7] Bharali, D. J., Klejbor, I., Stachowiak, E. K., Dutta, P., Roy, I., Kaur, N., Bergey, E. J., Prasad, P. N., and Stachowiak, M. K. *Proceedings of the National Academy of Sciences of the United States of America* **102**(32), 11539–11544 (2005).

[8] Kukla, V., Kornatowski, J., Demuth, D., Girnus, I., Pfeifer, H., Rees, L. V. C., Schunk, S., Unger, K. K., and Kärger, J. *Science* **272**(5262), 702–704 May (1996).

[9] Terasaki, O., Liu, Z., Ohsuna, T., Shin, H. J., and Ryoo, R. *Microscopy and Microanalysis* **8**(01), 35–39 (2002).

[10] Benes, N. E., Jobic, H., and Verweij, H. *Microporous and Mesoporous Materials* **43**(2), 147–152 April (2001).

[11] Barrer, R. M. and Perry, G. S. *Journal of the Chemical Society* **0**, 842–849 (1961).

[12] Kresge, C. T., Leonowicz, M. E., Roth, W. J., Vartuli, J. C., and Beck, J. S. *Nature* **359**(6397), 710–712 October (1992).

[13] Soler-Illia, G. J. d. A. A., Sanchez, C., Lebeau, B., and Patarin, J. *Chemical Reviews* **102**(11), 4093–4138 October (2002).

[14] Goltner, C. G. and Antonietti, M. *Advanced Materials* **9**(5), 431–436 (1997).

[15] Zhao, D., Feng, J., Huo, Q., Melosh, N., Fredrickson, G. H., Chmelka, B. F., and Stucky, G. D. *Science* **279**(5350), 548–552 January (1998).

[16] Aksay, I. A., Trau, M., Manne, S., Honma, I., Yao, N., Zhou, L., Fenter, P., Eisenberger, P. M., and Gruner, S. M. *Science* **273**(5277), 892–898 August (1996).

[17] Ogawa, M. *Chemical Communications* **0**(10), 1149–1150 (1996).

[18] Yang, H., Kuperman, A., Coombs, N., Mamiche-Afara, S., and Ozin, G. A. *Nature* **379**(6567), 703–705 February (1996).

[19] Brinker, C. J., Lu, Y., Sellinger, A., and Fan, H. *Advanced Materials* **11**(7), 579–585 (1999).

[20] Lu, Y., Ganguli, R., Drewien, C. A., Anderson, M. T., Brinker, C. J., Gong, W., Guo, Y., Soyez, H., Dunn, B., Huang, M. H., and Zink, J. I. *Nature* **389**(6649), 364–368 September (1997).

[21] Ogawa, M. *Journal of the American Chemical Society* **116**(17), 7941–7942 August (1994).

[22] Doshi, D. A., Gibaud, A., Goletto, V., Lu, M., Gerung, H., Ocko, B., Han, S. M., and Brinker, C. J. *Journal of the American Chemical Society* **125**(38), 11646–11655 September (2003).

[23] Grosso, D., Babonneau, F., Albouy, P.-A., Amenitsch, H., Balkenende, A. R., Brunet-Bruneau, A., and Rivory, J. *Chemistry of Materials* **14**(2), 931–939 January (2002).

[24] Smarsly, B., Gibaud, A., Ruland, W., Sturmayr, D., and Brinker, C. J. *Langmuir* **21**(9), 3858–3866 March (2005).

[25] Grosso, D., Balkenende, A. R., Albouy, P. A., Ayral, A., Amenitsch, H., and Babonneau, F. *Chemistry of Materials* **13**(5), 1848–1856 April (2001).

[26] Beck, J. S., Vartuli, J. C., Roth, W. J., Leonowicz, M. E., Kresge, C. T., Schmitt, K. D., Chu, C. T. W., Olson, D. H., and Sheppard, E. W. *Journal of the American Chemical Society* **114**(27), 10834–10843 December (1992).

[27] Attard, G. S., Glyde, J. C., and Goltner, C. G. *Nature* **378**(6555), 366–368 November (1995).

[28] Wan, Y. and Zhao. *Chemical Reviews* **107**(7), 2821–2860 July (2007).

[29] Jung, C., Schwaderer, P., Dethlefsen, M., Kohn, R., Michaelis, J., and Bräuchle, C. *Nature Nanotechnology* **6**(2), 87–92 February (2011).

[30] Sanchez, C., Boissière, C., Grosso, D., Laberty, C., and Nicole, L. *Chemistry of Materials* **20**(3), 682–737 February (2008).

[31] Fan, R., Huh, S., Yan, R., Arnold, J., and Yang, P. *Nature Materials* **7**(4), 303–307 April (2008).

[32] Luo, H., Wang, D., He, J., and Lu, Y. *Journal of Physical Chemistry B* **109**(5), 1919–1922 February (2005).

[33] Yang, P., Wirnsberger, G., Huang, H. C., Cordero, S. R., McGehee, M. D., Scott, B., Deng, T., Whitesides, G. M., Chmelka, B. F., Buratto, S. K., and Stucky, G. D. *Science* **287**(5452), 465–467 (2000).

[34] Wu, C.-W., Ohsuna, T., Edura, T., and Kuroda, K. *Angewandte Chemie International Edition* **46**(28), 5364–5368 (2007).

[35] Daiguji, H., Tatsumi, N., Kataoka, S., and Endo, A. *Langmuir* **25**(19), 11221–11224 October (2009).

[36] Kim, E., Xia, Y., and Whitesides, G. M. *Nature* **376**(6541), 581–584 August (1995).

[37] Trau, M., Yao, N., Kim, E., Xia, Y., Whitesides, G. M., and Aksay, I. A. *Nature* **390**(6661), 674–676 (1997).

[38] Tolbert, S. H., Firouzi, A., Stucky, G. D., and Chmelka, B. F. *Science* **278**(5336), 264–268 (1997).

[39] Miyata, H. and Kuroda, K. *Journal of the American Chemical Society* **121**(33), 7618–7624 August (1999).

[40] Miyata, H., Kawashima, Y., Itoh, M., and Watanabe, M. *Chemistry of Materials* **17**(21), 5323–5327 October (2005).

[41] Zhao, D., Yang, P., Melosh, N., Feng, J., Chmelka, B. F., and Stucky, G. D. *Advanced Materials* **10**(16), 1380–1385 (1998).

[42] Naik, S. P., Yamakita, S., Ogura, M., and Okubo, T. *Microporous and Mesoporous Materials* **75**(1-2), 51–59 October (2004).

[43] Rühle, B., Davies, M., Lebold, T., Bräuchle, C., and Bein, T. *ACS Nano* **6**(3), 1948–1960 (2012).

[44] Miyata, H. and Kuroda, K. *Chemistry of Materials* **12**(1), 49–54 December (1999).

[45] Miyata, H., Noma, T., Watanabe, M., and Kuroda, K. *Chemistry of Materials* **14**(2), 766–772 January (2002).

[46] Lebold, T., Mühlstein, L. A., Blechinger, J., Riederer, M., Amenitsch, H., Köhn, R., Peneva, K., Müllen, K., Michaelis, J., Bräuchle, C., and Bein, T. *Chemistry - A European Journal* **15**(7), 1661–1672 (2009).

[47] Lebold, T., Schlossbauer, A., Schneider, K., Schermelleh, L., Leonhardt, H., Bein, T., and Bräuchle, C. *Advanced Functional Materials* **22**(1), 106–112 (2012).

[48] Feil, F., Cauda, V., Bein, T., and Bräuchle, C. *Nano Letters* **12**(3), 1354–1361 (2012).

[49] Burkett, S. L., Sims, S. D., and Mann, S. *Chemical Communications* **0**(11), 1367–1368 (1996).

[50] Macquarrie, D. J. *Chemical Communications* **0**(16), 1961–1962 (1996).

[51] Lim, M. H. and Stein, A. *Chemistry of Materials* **11**(11), 3285–3295 September (1999).

[52] Zürner, A., Kirstein, J., Döblinger, M., Bräuchle, C., and Bein, T. *Nature* **450**(7170), 705–708 (2007).

[53] Kirstein, J., Platschek, B., Jung, C., Brown, R., Bein, T., and Bräuchle, C. *Nature Materials* **6**(4), 303–310 April (2007).

[54] Feil, F., Jung, C., Kirstein, J., Michaelis, J., Li, C., Nolde, F., Müllen, K., and Bräuchle, C. *Microporous and Mesoporous Materials* **125**(1-2), 70 – 78 (2009).

[55] Moerner, W. E. and Kador, L. *Physical Review Letters* **62**(21), 2535–2538 May (1989).

[56] Orrit, M. and Bernard, J. *Physical Review Letters* **65**(21), 2716–2719 November (1990).

[57] 1st Nobel Conference of "Single Molecules in Physics, C. and Biology". *Single Molecule Spectroscopy: Nobel Conference Lectures*. Springer Berlin Heidelberg (2001), (1998).

[58] 2nd Nobel Conference of "Single Molecules in Physics, C. and Biology". *"Single Molecule Spectroscopy in Chemistry, Physics and Biology" Nobel Symposium*, volume 96. Springer Berlin Heidelberg (2001), (2010).

[59] Weiss, S. *Science* **283**(5408), 1676–1683 (1999).

[60] Tamarat, P., Maali, A., Lounis, B., and Orrit, M. *Journal of Physical Chemistry A* **104**(1), 1–16 December (1999).

[61] Moerner, W. E. *Journal of Physical Chemistry B* **106**(5), 910–927 January (2002).

[62] Yamaguchi, A., Uejo, F., Yoda, T., Uchida, T., Tanamura, Y., Yamashita, T., and Teramae, N. *Nature Materials* **3**(5), 337–341 May (2004).

[63] Platschek, B., Petkov, N., and Bein, T. *Angewandte Chemie International Edition* **45**(7), 1134–1138 (2006).

[64] Higgins, D. A., Collinson, M. M., Saroja, G., and Bardo, A. M. *Chemistry of Materials* **14**(9), 3734–3744 July (2002).

[65] Martin-Brown, S. A., Fu, Y., Saroja, G., Collinson, M. M., and Higgins, D. A. *Analytical Chemistry* **77**(2), 486–494 December (2004).

[66] Mei, E., Bardo, A. M., Collinson, M. M., and Higgins, D. A. *Journal of Physical Chemistry B* **104**(43), 9973–9980 October (2000).

[67] Cui, C., Kirkeminde, A., Kannan, B., Collinson, M. M., and Higgins, D. A. *Journal of Physical Chemistry C* **115**(3), 728–735 December (2010).

[68] Fu, Y., Ye, F., Sanders, W. G., Collinson, M. M., and Higgins, D. A. *Journal of Physical Chemistry B* **110**(18), 9164–9170 (2006).

[69] Ye, F., Higgins, D. A., and Collinson, M. M. *Journal of Physical Chemistry C* **111**(18), 6772–6780 April (2007).

[70] Hellriegel, C., Kirstein, J., Bräuchle, C., Latour, V., Pigot, T., Olivier, R., Lacombe, S., Brown, R., Guieu, V., Payrastre, C., Izquierdo, A., and Mocho, P. *Journal of Physical Chemistry B* **108**(38), 14699–14709 (2004).

[71] Hellriegel, C., Kirstein, J., and Bräuchle, C. *New Journal of Physics* **7**(1), 23 (2005).

[72] Jung, C., Hellriegel, C., Platschek, B., Wöhrle, D., Bein, T., Michaelis, J., and Bräuchle, C. *Journal of the American Chemical Society* **129**(17), 5570–5579 (2007).

[73] Jung, C., Kirstein, J., Platschek, B., Bein, T., Budde, M., Frank, I., Müllen, K., Michaelis, J., and Bräuchle, C. *Journal of the American Chemical Society* **130**(5), 1638–1648 (2008).

[74] Cremer, G. D., Bartholomeeusen, E., Pescarmona, P. P., Lin, K., Vos, D. E. D., Hofkens, J., Roeffaers, M. B., and Sels, B. F. *Catalysis Today* **157**(1-4), 236 – 242 (2010).

[75] Karwacki, L., Stavitski, E., Kox, M. H. F., Kornatowski, J., and Weckhuysen, B. M. *Angewandte Chemie International Edition* **46**(38), 7228–7231 (2007).

[76] Karwacki, L., Kox, M. H. F., Matthijs de Winter, D. A., Drury, M. R., Meeldijk, J. D., Stavitski, E., Schmidt, W., Mertens, M., Cubillas, P., John, N., Chan, A., Kahn, N., Bare, S. R., Anderson, M., Kornatowski, J., and Weckhuysen, B. M. *Nature Materials* **8**(12), 959–965 December (2009).

[77] Sommer, L., Svelle, S., Lillerud, K. P., Stöcker, M., Weckhuysen, B. M., and Olsbye, U. *Langmuir* **26**(21), 16510–16516 (2010).

[78] Roeffaers, M. B. J., Ameloot, R., Bons, A.-J., Mortier, W., De Cremer, G., de Kloe, R., Hofkens, J., De Vos, D. E., and Sels, B. F. *Journal of the American Chemical Society* **130**(41), 13516–13517 (2008).

[79] Roeffaers, M. B. J., De Cremer, G., Libeert, J., Ameloot, R., Dedecker, P., Bons, A.-J., Bueckins, M., Martens, J. A., Sels, B. F., De Vos, D. E., and Hofkens, J. *Angewandte Chemie International Edition* **48**(49), 9285–9289 November (2009).

[80] Kox, M. H. F., Mijovilovich, A., Sättler, J. J. H. B., Stavitski, E., and Weckhuysen, B. M. *ChemCatChem* **2**(5), 564–571 (2010).

[81] Chung, Y.-M., Mores, D., and Weckhuysen, B. M. *Applied Catalysis A: General* **404**(1-2), 12 – 20 (2011).

[82] Buurmans, I. L. C., Ruiz-Martinez, J., Knowles, W. V., van der Beek, D., Bergwerff, J. A., Vogt, E. T. C., and Weckhuysen, B. M. *Nat. Chem.* **3**(11), 862–867 November (2011).

[83] Karreman, M. A., Buurmans, I. L. C., Geus, J. W., Agronskaia, A. V., Ruiz-Marinez, J., Gerritsen, H. C., and Weckhuysen, B. M. *Angewandte Chemie International Edition* **51**(6), 1428–1431 (2012).

[84] Stavitski, E., Kox, M. H. F., and Weckhuysen, B. M. *Chemistry - A European Journal* **13**(25), 7057–7065 (2007).

[85] Kox, M. H. F., Stavitski, E., Groen, J. C., Pérez-Ramirez, J., Kapteijn, F., and Weckhuysen, B. M. *Chemistry - A European Journal* **14**(6), 1718–1725 (2008).

[86] Domke, K. F., Riemer, T. A., Rago, G., Parvulescu, A. N., Bruijnincx, P. C. A., Enejder, A., Weckhuysen, B. M., and Bonn, M. *Journal of the American Chemical Society* **134**(2), 1124–1129 (2012).

[87] Ruiz-Marinez, J., Buurmans, I. L., Knowles, W. V., van der Beek, D., Bergwerff, J. A., Vogt, E. T., and Weckhuysen, B. M. *Applied Catalysis A: General* **419-420**(0), 84 – 94 (2012).

[88] Mores, D., Stavitski, E., Verkleij, S. P., Lombard, A., Cabiac, A., Rouleau, L., Patarin, J., Simon-Masseron, A., and Weckhuysen, B. M. *Physical Chemistry Chemical Physics* **13**(35), 15985–15994 (2011).

[89] Parvulescu, A. N., Mores, D., Stavitski, E., Teodorescu, C. M., Bruijnincx, P. C. A., Gebbink, R. J. M. K., and Weckhuysen, B. M. *Journal of the American Chemical Society* **132**(30), 10429–10439 (2010).

[90] Bezrukov, S. M., Vodyanoy, I., and Parsegian, V. A. *Nature* **370**(6487), 279–281 July (1994).

[91] Kasianowicz, J. J., Brandin, E., Branton, D., and Deamer, D. W. *Proceedings of the National Academy of Sciences* **93**(24), 13770–13773 (1996).

[92] Venkatesan, B. M. and Bashir, R. *Nature Nanotechnology* **6**(10), 615–624 October (2011).

[93] Kumar, H., Lansac, Y., Glaser, M. A., and Maiti, P. K. *Soft Matter* **7**(13), 5898–5907 (2011).

[94] Sens, P. and Isambert, H. *Physical Review Letters* **88**(12), 128102– March (2002).

[95] Dekker, C. *Nature Nanotechnology* **2**(4), 209–215 April (2007).

[96] Chen, P., Gu, J., Brandin, E., Kim, Y.-R., Wang, Q., and Branton, D. *Nano Letters* **4**(11), 2293–2298 October (2004).

[97] Storm, A. J., Chen, J. H., Ling, X. S., Zandbergen, H. W., and Dekker, C. *Nature Materials* **2**(8), 537–540 August (2003).

[98] Chen, Z., Jiang, Y., Dunphy, D. R., Adams, D. P., Hodges, C., Liu, N., Zhang, N., Xomeritakis, G., Jin, X., Aluru, N. R., Gaik, S. J., Hillhouse, H. W., and Jeffrey Brinker, C. *Nature Materials* **9**(8), 667–675 August (2010).

[99] Mannion, J. T. and Craighead, H. G. *Biopolymers* **85**(2), 131–143 (2007).

[100] Lenne, P.-F., Rigneault, H., Marguet, D., and Wenger, J. *Histochemistry and Cell Biology* **130**(5), 795–805 (2008-11-01).

[101] Samiee, K., Foquet, M., Guo, L., Cox, E., and Craighead, H. *Biophysical Journal* **88**(3), 2145–2153 March (2005).

[102] Foquet, M., Korlach, J., Zipfel, W., Webb, W. W., and Craighead, H. G. *Analytical Chemistry* **74**(6), 1415–1422 February (2002).

[103] Zhang, B., Wood, M., and Lee, H. *Analytical Chemistry* **81**(13), 5541–5548 June (2009).

[104] Meistermann, L. and Tinland, B. *Phys. Rev. E* **62**(3), 4014–4017 September (2000).

[105] Lebold, T., Jung, C., Michaelis, J., and Bräuchle, C. *Nano Letters* **9**(8), 2877–2883 July (2009).

[106] Schlossbauer, A., Sauer, A. M., Cauda, V., Schmidt, A., Engelke, H., Rothbauer, U., Zolghadr, K., Leonhardt, H., Bräuchle, C., and Bein, T. *Advanced Healthcare Materials* **1**(3), 316–320 (2012).

[107] Cauda, V., Argyo, C., Schlossbauer, A., and Bein, T. *Journal of Materials Chemistry* **20**(21), 4305–4311 (2010).

[108] Schlossbauer, A., Dohmen, C., Schaffert, D., Wagner, E., and Bein, T. *Angewandte Chemie International Edition* **50**(30), 6828–6830 (2011).

[109] Schlossbauer, A., Warncke, S., Gramlich, P. M. E., Kecht, J., Manetto, A., Carell, T., and Bein, T. *Angewandte Chemie International Edition* **49**(28), 4734–4737 (2010).

[110] Schlossbauer, A., Kecht, J., and Bein, T. *Angewandte Chemie International Edition* **48**(17), 3092–3095 (2009).

[111] Sauer, A. M., Schlossbauer, A., Ruthardt, N., Cauda, V., Bein, T., and Bräuchle, C. *Nano Letters* **10**(9), 3684–3691 August (2010).

[112] Kecht, J., Schlossbauer, A., and Bein, T. *Chemistry of Materials* **20**(23), 7207–7214 November (2008).

[113] Cauda, V., Schlossbauer, A., Kecht, J., Zürner, A., and Bein, T. *Journal of the American Chemical Society* **131**(32), 11361–11370 July (2009).

[114] Cauda, V., Engelke, H., Sauer, A., Arcizet, D., Bräuchle, C., Rädler, J., and Bein, T. *Nano Letters* **10**(7), 2484–2492 June (2010).

[115] Yaghi, O. M., Li, G., and Li, H. *Nature* **378**(6558), 703–706 December (1995).

[116] Ferey, G. *Chemical Society Reviews* **37**(1), 191–214 (2008).

[117] Cook, T. R., Zheng, Y.-R., and Stang, P. J. *Chemical Reviews* **113**(1), 734–777 November (2012).

[118] Hoskins, B. F. and Robson, R. *Journal of the American Chemical Society* **111**(15), 5962–5964 July (1989).

[119] Fujita, M., Kwon, Y. J., Washizu, S., and Ogura, K. *Journal of the American Chemical Society* **116**(3), 1151–1152 February (1994).

[120] Kondo, M., Yoshitomi, T., Matsuzaka, H., Kitagawa, S., and Seki, K. *Angewandte Chemie International Edition* **36**(16), 1725–1727 (1997).

[121] Li, H., Eddaoudi, M., Groy, T. L., and Yaghi, O. M. *Journal of the American Chemical Society* **120**(33), 8571–8572 August (1998).

[122] Li, H., Eddaoudi, M., O'Keeffe, M., and Yaghi, O. M. *Nature* **402**(6759), 276–279 November (1999).

[123] Eddaoudi, M., Kim, J., Rosi, N., Vodak, D., Wachter, J., O'Keeffe, M., and Yaghi, O. M. *Science* **295**(5554), 469–472 (2002).

[124] Rowsell, J. L. and Yaghi, O. M. *Microporous and Mesoporous Materials* **73**(1-2), 3–14 August (2004).

[125] Rowsell, J. L. C. and Yaghi, O. M. *Angewandte Chemie International Edition* **44**(30), 4670–4679 (2005).

[126] Kitagawa, S., Okubo, T., Kawata, S., Kondo, M., Katada, M., and Kobayashi, H. *Inorganic Chemistry* **34**(19), 4790–4796 September (1995).

[127] Jhung, S. H., Lee, J.-H., Forster, P. M., Férey, G., Cheetham, A. K., and Chang, J.-S. *Chemistry - A European Journal* **12**(30), 7899–7905 (2006).

[128] Forster, P. M., Thomas, P. M., and Cheetham, A. K. *Chemistry of Materials* **14**(1), 17–20 December (2001).

[129] Mueller, U., Schubert, M., Teich, F., Puetter, H., Schierle-Arndt, K., and Pastre, J. *Journal of Materials Chemistry* **16**(7), 626–636 (2006).

[130] Furukawa, H., Ko, N., Go, Y. B., Aratani, N., Choi, S. B., Choi, E., Yazaydin, A. z., Snurr, R. Q., O'Keeffe, M., Kim, J., and Yaghi, O. M. *Science* **329**(5990), 424–428 (2010).

[131] Farha, O. K., Özgür Yazaydin A., Eryazici, I., Malliakas, C. D., Hauser, B. G., Kanatzidis, M. G., Nguyen, S. T., Snurr, R. Q., and Hupp, J. T. *Nat. Chem.* **2**(11), 944–948 November (2010).

[132] Cohen, S. M. *Chemical Science* **1**(1), 32–36 (2010).

[133] Cohen, S. M. *Chemical Reviews* **112**(2), 970–1000 September (2011).

[134] Tanabe, K. K. and Cohen, S. M. *Chemical Society Reviews* **40**(2), 498–519 (2011).

[135] Fei, H., Rogow, D. L., and Oliver, S. R. J. *Journal of the American Chemical Society* **132**(20), 7202–7209 April (2010).

[136] Dinca, M. and Long, J. R. *Journal of the American Chemical Society* **129**(36), 11172–11176 August (2007).

[137] Wu, C.-D., Hu, A., Zhang, L., and Lin, W. *Journal of the American Chemical Society* **127**(25), 8940–8941 June (2005).

[138] Kaye, S. S. and Long, J. R. *Journal of the American Chemical Society* **130**(3), 806–807 December (2007).

[139] Bae, Y.-S., Farha, O. K., Hupp, J. T., and Snurr, R. Q. *Journal of Materials Chemistry* **19**(15), 2131–2134 (2009).

[140] Wang, Z., Tanabe, K. K., and Cohen, S. M. *Inorganic Chemistry* **48**(1), 296–306 November (2008).

[141] Tanabe, K. K., Wang, Z., and Cohen, S. M. *Journal of the American Chemical Society* **130**(26), 8508–8517 June (2008).

[142] Garibay, S. J., Wang, Z., Tanabe, K. K., and Cohen, S. M. *Inorganic Chemistry* **48**(15), 7341–7349 July (2009).

[143] Goto, Y., Sato, H., Shinkai, S., and Sada, K. *Journal of the American Chemical Society* **130**(44), 14354–14355 October (2008).

[144] Gadzikwa, T., Lu, G., Stern, C. L., Wilson, S. R., Hupp, J. T., and Nguyen, S. T. *Chemical Communications* **0**(43), 5493–5495 (2008).

[145] Savonnet, M., Bazer-Bachi, D., Bats, N., Perez-Pellitero, J., Jeanneau, E., Lecocq, V., Pinel, C., and Farrusseng, D. *Journal of the American Chemical Society* **132**(13), 4518–4519 March (2010).

[146] Collins, D. J. and Zhou, H.-C. *Journal of Materials Chemistry* **17**(30), 3154–3160 (2007).

[147] Li, J.-R., Kuppler, R. J., and Zhou, H.-C. *Chemical Society Reviews* **38**(5), 1477–1504 (2009).

[148] Murray, L. J., Dinca, M., and Long, J. R. *Chemical Society Reviews* **38**(5), 1294–1314 (2009).

[149] Li, J.-R., Ma, Y., McCarthy, M. C., Sculley, J., Yu, J., Jeong, H.-K., Balbuena, P. B., and Zhou, H.-C. *Coordination Chemistry Reviews* **255**(15-16), 1791–1823 August (2011).

[150] Lee, J., Farha, O. K., Roberts, J., Scheidt, K. A., Nguyen, S. T., and Hupp, J. T. *Chemical Society Reviews* **38**(5), 1450–1459 (2009).

[151] Ma, L., Abney, C., and Lin, W. *Chemical Society Reviews* **38**(5), 1248–1256 (2009).

[152] Corma, A., Garcia, H., and Llabrés i Xamena, F. X. *Chemical Reviews* **110**(8), 4606–4655 April (2010).

[153] Horcajada, P., Gref, R., Baati, T., Allan, P. K., Maurin, G., Couvreur, P., Férey, G., Morris, R. E., and Serre, C. *Chemical Reviews* **112**(2), 1232–1268 December (2011).

[154] Cui, Y., Yue, Y., Qian, G., and Chen, B. *Chemical Reviews* **112**(2), 1126–1162 June (2011).

[155] Kreno, L. E., Leong, K., Farha, O. K., Allendorf, M., Van Duyne, R. P., and Hupp, J. T. *Chemical Reviews* **112**(2), 1105–1125 November (2012).

[156] Qiu, L.-G., Li, Z.-Q., Wu, Y., Wang, W., Xu, T., and Jiang, X. *Chemical Communications* **0**(31), 3642–3644 (2008).

[157] Zou, X., Zhu, G., Hewitt, I. J., Sun, F., and Qiu, S. *Dalton Transactions* **0**(16), 3009–3013 (2009).

[158] Qiu, Y., Deng, H., Mou, J., Yang, S., Zeller, M., Batten, S. R., Wu, H., and Li, J. *Chemical Communications* **0**(36), 5415–5417 (2009).

[159] Xie, Z., Ma, L., deKrafft, K. E., Jin, A., and Lin, W. *Journal of the American Chemical Society* **132**(3), 922–923 December (2009).

[160] Lan, A., Li, K., Wu, H., Olson, D. H., Emge, T. J., Ki, W., Hong, M., and Li, J. *Angewandte Chemie International Edition* **48**(13), 2334–2338 (2009).

[161] An, J., Shade, C. M., Chengelis-Czegan, D. A., Petoud, S., and Rosi, N. L. *Journal of the American Chemical Society* **133**(5), 1220–1223 January (2011).

[162] Pramanik, S., Zheng, C., Zhang, X., Emge, T. J., and Li, J. *Journal of the American Chemical Society* **133**(12), 4153–4155 (2011).

[163] Takashima, Y., Martinez, V. M., Furukawa, S., Kondo, M., Shimomura, S., Uehara, H., Nakahama, M., Sugimoto, K., and Kitagawa, S. *Nature Communications* **2**, 168– (2011).

[164] Doty, F. P., Bauer, C. A., Skulan, A. J., Grant, P. G., and Allendorf, M. D. *Advanced Materials* **21**(1), 95–101 (2009).

[165] Lu, Z.-Z., Zhang, R., Li, Y.-Z., Guo, Z.-J., and Zheng, H.-G. *Journal of the American Chemical Society* **133**(12), 4172–4174 March (2011).

[166] Lee, H., Jung, S. H., Han, W. S., Moon, J. H., Kang, S., Lee, J. Y., Jung, J. H., and Shinkai, S. *Chemistry - A European Journal* **17**(10), 2823–2827 (2011).

[167] Lu, G. and Hupp, J. T. *Journal of the American Chemical Society* **132**(23), 7832–7833 May (2010).

[168] Hinterholzinger, F. M., Ranft, A., Feckl, J. M., Ruhle, B., Bein, T., and Lotsch, B. V. *Journal of Materials Chemistry* **22**(20), 10356–10362 (2012).

[169] Kreno, L. E., Hupp, J. T., and Van Duyne, R. P. *Analytical Chemistry* **82**(19), 8042–8046 September (2010).

[170] Biemmi, E., Darga, A., Stock, N., and Bein, T. *Microporous and Mesoporous Materials* **114**(1-3), 380–386 September (2008).

[171] Ameloot, R., Stappers, L., Fransaer, J., Alaerts, L., Sels, B. F., and De Vos, D. E. *Chemistry of Materials* **21**(13), 2580–2582 May (2009).

[172] Allendorf, M. D., Houk, R. J. T., Andruszkiewicz, L., Talin, A. A., Pikarsky, J., Choudhury, A., Gall, K. A., and Hesketh, P. J. *Journal of the American Chemical Society* **130**(44), 14404–14405 October (2008).

[173] Sauer, M., Hofkens, J., and Enderlein, J. *Handbook of Fluorescence Spectroscopy and Imaging: From Ensemble to Single Molecules*. Wiley, (2010).

[174] Lakowicz, J. *Principles of Fluorescence Spectroscopy*. Springer London, Limited, (2009).

[175] McCain, K. S., Hanley, D. C., and Harris, J. M. *Anal. Chem.* **75**(17), 4351–4359 August (2003).

[176] Olympus, http://www.olympusmicro.com/primer/techniques/fluorescence/anatomy/fluoromicroanatomy.html. December (2012).

[177] Olympus, http://www.olympusmicro.com/primer/techniques/fluorescence/filters.html. December (2012).

[178] Hollas, J. *Modern Spectroscopy*. Wiley, (2004).

[179] Brundle, C., Evans, C., and Wilson, S. *Encyclopedia of Materials Characterization: Surfaces, Interfaces, Thin Films*. Butterworth-Heinemann Limited, (1992).

[180] Reimer, L. *Scanning electron microscopy*, volume 45. Springer, Berlin ; Heidelberg [u.a.], 2., completely rev. and updated ed. edition, (1998).

[181] Binnig, G., Quate, C. F., and Gerber, C. *Phys. Rev. Lett.* **56**(9), 930–933 March (1986).

[182] Eaton, P. and West, P. *Atomic Force Microscopy*. OUP Oxford, (2010).

[183] Patterson, A. L. *Phys. Rev.* **56**(10), 978–982 November (1939).

[184] Hesse, M., Meier, H., and Zeeh, B. *Spektroskopische Methoden in der organischen Chemie.* Thieme Georg Verlag, (2005).

[185] Haines, P. and of Chemistry (Gran Bretana), R. S. *Principles of Thermal Analysis and Calorimetry.* Royal Soc. of Chemistry, (2002).

[186] Sing, K. S. W., Everett, D. H., Haul, R. A. W., Moscou, L., Pierotti, R. A., Rouquerol, J., and Siemieniewska, T. *Pure and Applied Chemistry* **57**(4), 603–619 (1985).

[187] Rouquerol, J., Avnir, D., Fairbridge, C. W., Everett, D. H., Haynes, J. M., Pernicone, N., Ramsay, J. D. F., Sing, K. S. W., and Unger, K. K. *Pure and Applied Chemistry* **66**(8), 1739–1758 (1994).

[188] Atkins, P. W. *Physikalische Chemie.* Wiley-VCH, (1996).

[189] Santos, N. and Castanho, M. *Biophysical Journal* **71**(3), 1641–1650 September (1996).

[190] Malvern Intruments, *Zetasizer Nano Series - User Manual*, t.

[191] Madou, M. *Fundamentals of Microfabrication: The Science of Miniaturization, Second Edition.* CRC Press, (2002).

[192] Middleman, S. and Hochberg, A. *Process engineering analysis in semiconductor device fabrication.* McGraw-Hill, (1993).

[193] Daunton, R., Gallant, A. J., and Wood, D. *Journal of Micromechanics and Microengineering* **22**(7), 075016– (2012).

[194] Love, J. C., Wolfe, D. B., Jacobs, H. O., and Whitesides, G. M. *Langmuir* **17**(19), 6005–6012 September (2001).

[195] Brady, M. J. and Davidson, A. *Review Of Scientific Instruments* **54**(10), 1292–1295 (1983).

[196] Xia, Y. N. and Whitesides, G. M. *Annual Review Of Materials Science* **28**, 153–184 (1998).

[197] Campbell, D. J., Beckman, K. J., Calderon, C. E., Doolan, P. W., Ottosen, R. M., Ellis, A. B., and Lisensky, G. C. *Journal of Chemical Education* **76**(4), 537–541 APR (1999).

[198] Kumar, A. and Whitesides, G. M. *Applied Physics Letters* **63**(14), 2002–2004 October (1993).

[199] Wilbur, J. L., Kumar, A., Kim, E., and Whitesides, G. M. *Advanced Materials* **6**(7-8), 600–604 (1994).

[200] Delamarche, E., Michel, B., Biebuyck, H. A., and Gerber, C. *Advanced Materials* **8**(9), 719–729 (1996).

[201] Limpert, E., Stahel, W., and Abbt, M. *Bioscience* **51**(5), 341–352 May (2001).

[202] Holtrup, F. O., R. J. Müller, G., Quante, H., De Feyter, S., De Schryver, F. C., and Müllen, K. *Chemistry - A European Journal* **3**(2), 219–225 (1997).

[203] Sharma, V., Dhayal, M., Govind, Shivaprasad, S., and Jain, S. *Vacuum* **81**(9), 1094–1100 May (2007).

[204] Duez, C., Ybert, C., Clanet, C., and Bocquet, L. *Nature Physics* **3**(3), 180–183 March (2007).

[205] Nge, P. N., Pagaduan, J. V., Yu, M., and Woolley, A. T. *Journal of Chromatography A* **1261**(0), 129–135 October (2012).

[206] Sun, D., Wang, F., Wu, K., Chen, J., and Zhou, Y. *Microchimica Acta* **167**(1-2), 35–39 (2009).

[207] Zhao, J., Huang, W., and Zheng, X. *Journal of Applied Electrochemistry* **39**(12), 2415–2419– (2009).

[208] Zhou, C., Liu, Z., Dong, Y., and Li, D. *Electroanalysis* **21**(7), 853–858 (2009).

[209] Jung, C., Ruthardt, N., Lewis, R., Michaelis, J., Sodeik, B., Nolde, F., Peneva, K., Müllen, K., and Bräuchle, C. *ChemPhysChem* **10**(1), 180–190 (2009).

[210] Alexandridis, P. and Hatton, T. A. *Colloids and Surfaces A: Physicochemical and Engineering Aspects* **96**(1–2), 1 – 46 (1995).

[211] Almgren, M., Brown, W., and Hvidt, S. *Colloid and Polymer Science* **273**, 2–15 (1995).

[212] Wanka, G., Hoffmann, H., and Ulbricht, W. *Macromolecules* **27**(15), 4145–4159 (1994).

[213] Galarneau, A., Cambon, H., Di Renzo, F., Ryoo, R., Choi, M., and Fajula, F. *New Journal of Chemistry* **27**(1), 73–79 (2003).

[214] Gobin, O. C., Wan, Y., Zhao, D., Kleitz, F., and Kaliaguine, S. *Journal of Physical Chemistry C* **111**(7), 3053–3058 February (2007).

[215] Kocherbitov, V. and Alfredsson, V. *Langmuir* **27**(7), 3889–3897 March (2011).

[216] Kruk, M., Jaroniec, M., Ko, C. H., and Ryoo, R. *Chemistry of Materials* **12**(7), 1961–1968 July (2000).

[217] Ravikovitch, P. I. and Neimark, A. V. *Journal of Physical Chemistry B* **105**(29), 6817–6823 July (2001).

[218] Ryoo, R., Ko, C. H., Kruk, M., Antochshuk, V., and Jaroniec, M. *Journal of Physical Chemistry B* **104**(48), 11465–11471 November (2000).

[219] Kohl, C., Weil, T., Qu, J., and Müllen, K. *Chemistry - A European Journal* **10**(21), 5297–5310 (2004).

[220] Qu, J., Kohl, C., Pottek, M., and Müllen, K. *Angewandte Chemie International Edition* **43**(12), 1528–1531 (2004).

[221] Nolde, F., Qu, J., Kohl, C., Pschirer, N. G., Reuther, E., and Müllen, K. *Chemistry - A European Journal* **11**(13), 3959–3967 (2005).

[222] Kitagawa, S., Kitaura, R., and Noro, S.-i. *Angewandte Chemie International Edition* **43**(18), 2334–2375 (2004).

[223] Li, J.-R., Sculley, J., and Zhou, H.-C. *Chemical Reviews* **112**(2), 869–932 (2011).

[224] Faulkner, L. R. and Bard, A. J. *Journal of the American Chemical Society* **90**(23), 6284–6290 November (1968).

[225] Cavka, J. H., Jakobsen, S., Olsbye, U., Guillou, N., Lamberti, C., Bordiga, S., and Lillerud, K. P. *Journal of the American Chemical Society* **130**(42), 13850–13851 September (2008).

[226] Schaate, A., Roy, P., Godt, A., Lippke, J., Waltz, F., Wiebcke, M., and Behrens, P. *Chemistry - A European Journal* **17**(24), 6643–6651 (2011).

[227] Jiang, H.-L., Feng, D., Liu, T.-F., Li, J.-R., and Zhou, H.-C. *Journal of the American Chemical Society* **134**(36), 14690–14693 August (2012).

[228] Hinterholzinger, F. M., Wuttke, S., Roy, P., Preusse, T., Schaate, A., Behrens, P., Godt, A., and Bein, T. *Dalton Transactions* **41**(14), 3899–3901 (2012).

[229] Schaate, A., Roy, P., Preusse, T., Lohmeier, S. J., Godt, A., and Behrens, P. *Chemistry - A European Journal* **17**(34), 9320–9325 (2011).

[230] Chandross, E. A. *Tetrahedron Letters* **4**(12), 761–765 (1963).

[231] Schuster, G. B. *Accounts of Chemical Research* **12**(10), 366–373 October (1979).

[232] Stevani, C., Silva, S., and Baader, W. *European Journal of Organic Chemistry* **2000**(24), 4037–4046 (2000).

[233] Stevani, C. V., de Arruda Campos, I. P., and Baader, W. J. *Journal of the Chemical Society, Perkin Transactions 2* **0**(8), 1645–1648 (1996).

[234] Schleck, J. R. (Somerset, NJ), and Keyko, G. J. (Westfield, NJ), and Chopdekar, V. M. (Edison, NJ) *Patent US 5281367* (1994).

[235] McDonagh, C., Burke, C. S., and MacCraith, B. D. *Chemical Reviews* **108**(2), 400–422 (2008).

[236] Stich, M. I. J., Fischer, L. H., and Wolfbeis, O. S. *Chemical Society Reviews* **39**(8), 3102–3114 (2010).

[237] Wolfbeis, O. S. *Analytical Chemistry* **76**(12), 3269–3284 (2004).

[238] Schäferling, M. *Angewandte Chemie International Edition* **51**(15), 3532–3554 (2012).

[239] Wade, C. R., Broomsgrove, A. E. J., Aldridge, S., and Gabbai, F. P. *Chemical Reviews* **110**(7), 3958–3984 (2010).

[240] Galbraith, E. and James, T. D. *Chemical Society Reviews* **39**(10), 3831–3842 (2010).

[241] Kubik, S. *Chemical Society Reviews* **39**(10), 3648–3663 (2010).

[242] Jagtap, S., Yenkie, M. K., Labhsetwar, N., and Rayalu, S. *Chemical Reviews* **112**(4), 2454–2466 (2012).

[243] Dusemund, C., Sandanayake, K. R. A. S., and Shinkai, S. *Journal of the Chemical Society, Chemical Communications* **3**(3), 333–334 (1995).

[244] Wade, C. R. and Gabbai, F. P. *Dalton Transactions* **42**(42), 9169–9175 (2009).

[245] Kim, Y. and Gabbai, F. P. *Journal of the American Chemical Society* **131**(9), 3363–3369 (2009).

[246] Descalzo, A. B., Jimenez, D., Haskouri, J. E., Beltran, D., Amoros, P., Marcos, M. D., Martinez-Manez, R., and Soto, J. *Chemical Communications* **6**(6), 562–563 (2002).

[247] Guha, S. and Saha, S. *Journal of the American Chemical Society* **132**(50), 17674–17677 (2010).

[248] Boiocchi, M., Del Boca, L., Gomez, D. E., Fabbrizzi, L., Licchelli, M., and Monzani, E. *Journal of the American Chemical Society* **126**(50), 16507–16514 (2004).

[249] Zhao, H. and Gabbai, F. P. *Nat. Chem.* **2**(11), 984–990 (2010).

[250] Yaghi, O. M., O'Keeffe, M., Ockwig, N. W., Chae, H. K., Eddaoudi, M., and Kim, J. *Nature* **423**(6941), 705–714 (2003).

[251] Sumida, K., Rogow, D. L., Mason, J. A., McDonald, T. M., Bloch, E. D., Herm, Z. R., Bae, T.-H., and Long, J. R. *Chemical Reviews* **112**(2), 724–781 (2011).

[252] Ferey, G., Serre, C., Devic, T., Maurin, G., Jobic, H., Llewellyn, P. L., De Weireld, G., Vimont, A., Daturi, M., and Chang, J.-S. *Chemical Society Reviews* **40**(2), 550–562 (2011).

[253] Allendorf, M. D., Bauer, C. A., Bhakta, R. K., and Houk, R. J. T. *Chemical Society Reviews* **38**(5), 1330–1352 (2009).

[254] Yanai, N., Kitayama, K., Hijikata, Y., Sato, H., Matsuda, R., Kubota, Y., Takata, M., Mizuno, M., Uemura, T., and Kitagawa, S. *Nature Materials* **10**(10), 787–793 (2011).

[255] Lu, G., Farha, O. K., Kreno, L. E., Schoenecker, P. M., Walton, K. S., Van Duyne, R. P., and Hupp, J. T. *Advanced Materials* **23**(38), 4449–4452 (2011).

[256] Stylianou, K. C., Heck, R., Chong, S. Y., Bacsa, J., Jones, J. T. A., Khimyak, Y. Z., Bradshaw, D., and Rosseinsky, M. J. *Journal of the American Chemical Society* **132**(12), 4119–4130 (2010).

[257] Serra-Crespo, P., Ramos-Fernandez, E. V., Gascon, J., and Kapteijn, F. *Chemistry of Materials* **23**(10), 2565–2572 (2011).

[258] Imhof, A., Megens, M., Engelberts, J. J., de Lang, D. T. N., Sprik, R., and Vos, W. L. *Journal of Physical Chemistry B* **103**(9), 1408–1415 (1999).

[259] Bojarski, C., Grabowska, J., Kulak, L., and Kusba, J. *Journal of Fluorescence* **1**(3), 183–191 (1991).

[260] Agarwal, R. P. and Moreno, E. C. *Talanta* **18**(9), 873–880 (1971).

[261] Sur, S. K. and Bryant, R. G. *Zeolites* **16**(2-3), 118–124 (1996).

[262] Bodor, A., Toth, I., Banyai, I., Szabo, Z., and Hefter, G. T. *Inorganic Chemistry* **39**(12), 2530–2537 (2000).

[263] World Health Organization (WHO), Fawell, J., Bailey, K., Chilton, J., Dahi, E., Fewtrell, L., and Magara, Y. *Fluoride in Drinking-water*. IWA Publishing, London UK, (2006). ISBN: 1900222965.

[264] American Public Health Association, American Water Works Association, Water Environment Federation. *Standard methods for the examination of water and wastewater*. American Public Health Association, (1998).

[265] Ogston, A. G. *Transactions of the Faraday Society* **54**(0), 1754–1757 (1958).

[266] de Gennes, P. G. *Journal of Chemical Physics* **55**(2), 572–579 July (1971).

[267] Doi, M. and Edwards, S. F. *Journal of the Chemical Society, Faraday Transactions 2: Molecular and Chemical Physics* **74**(0), 1789–1801 (1978).

[268] Smisek, D. L. and Hoagland, D. A. *Science* **248**(4960), 1221–1223 June (1990).

[269] Nykypanchuk, D., Strey, H. H., and Hoagland, D. A. *Science* **297**(5583), 987–990 (2002).

[270] Turner, S. W. P., Cabodi, M., and Craighead, H. G. *Physical Review Letters* **88**(12), 128103– March (2002).

[271] Muthukumar, M. and Baumgaertner, A. *Macromolecules* **22**(4), 1937–1941 April (1989).

[272] Muthukumar, M. and Baumgaertner, A. *Macromolecules* **22**(4), 1941–1946 April (1989).

[273] Zimm, B. H. and Lumpkin, O. *Macromolecules* **26**(1), 226–234 January (1993).

[274] Yang, P. D., Deng, T., Zhao, D. Y., Feng, P. Y., Pine, D., Chmelka, B. F., Whitesides, G. M., and Stucky, G. D. *Science* **282**(5397), 2244–2246 (1998).

[275] Mandlmeier, B., Szeifert, J. M., Fattakhova-Rohlfing, D., Amenitsch, H., and Bein, T. *Journal of the American Chemical Society* **133**(43), 17274–17282 September (2011).

[276] Wang, T., Sel, O., Djerdj, I., and Smarsly, B. *Colloid and Polymer Science* **285**(1), 1–9 (2006).

[277] Kobler, J., Möller, K., and Bein, T. *ACS Nano* **2**(4), 791–799 March (2008).

[278] Wasserman, S. R., Tao, Y. T., and Whitesides, G. M. *Langmuir* **5**(4), 1074–1087 July (1989).

[279] Xia, Y., Zhao, X.-M., Kim, E., and Whitesides, G. M. *Chemistry of Materials* **7**(12), 2332–2337 December (1995).

[280] Microsoft, http://msdn.microsoft.com/en-us/library/d2se9adx(v=vs.71).aspx. March (2012).

[281] Microsoft, http://msdn.microsoft.com/en-us/library/windows/desktop/ff468832(v=vs.85).aspx. March (2012).

[282] Bronkhorst High-Tech B.V., http://www.bronkhorst.com/en/downloads/instruction_manuals. March (2012).

[283] Microsoft, http://msdn.microsoft.com/en-us/library/windows/desktop/ms646304(v=vs.85).aspx. March (2012).

[284] Microsoft, http://msdn.microsoft.com/en-us/library/windows/desktop/ms633499(v=vs.85).aspx. March (2012).

[285] Microsoft, http://msdn.microsoft.com/en-us/library/windows/desktop/ms633539(v=vs.85).aspx. March (2012).

[286] Microsoft, http://msdn.microsoft.com/de-de/library/windows/desktop/ms633527(v=vs.85).aspx. March (2012).

[287] Microsoft, http://msdn.microsoft.com/en-us/library/windows/desktop/ms633548(v=vs.85).aspx. March (2012).

[288] Microsoft, http://msdn.microsoft.com/en-us/library/windows/desktop/ms644950(v=vs.85).aspx. March (2012).